

Quantum Dots Coupled to Andreev Bound States

van Driel, D.

DOI

[10.4233/uuid:b906fd7b-4909-48cd-9fc4-2ceb2b7ca3da](https://doi.org/10.4233/uuid:b906fd7b-4909-48cd-9fc4-2ceb2b7ca3da)

Publication date

2024

Document Version

Final published version

Citation (APA)

van Driel, D. (2024). *Quantum Dots Coupled to Andreev Bound States*. [Dissertation (TU Delft), Delft University of Technology]. <https://doi.org/10.4233/uuid:b906fd7b-4909-48cd-9fc4-2ceb2b7ca3da>

Important note

To cite this publication, please use the final published version (if applicable).
Please check the document version above.

Copyright

Other than for strictly personal use, it is not permitted to download, forward or distribute the text or part of it, without the consent of the author(s) and/or copyright holder(s), unless the work is under an open content license such as Creative Commons.

Takedown policy

Please contact us and provide details if you believe this document breaches copyrights.
We will remove access to the work immediately and investigate your claim.

QUANTUM DOTS COUPLED TO ANDREEV BOUND STATES

David van Driel



QUANTUM DOTS COUPLED TO ANDREEV BOUND STATES

QUANTUM DOTS COUPLED TO ANDREEV BOUND STATES

Dissertation

for the purpose of obtaining the degree of doctor
at Delft University of Technology,
by the authority of the Rector Magnificus, prof. dr. ir. T.H.J.J. van der Hagen,
chair of the Board for Doctorates,
to be defended publicly on
Friday 4 October 2024 at 12:30 o'clock

by

David VAN DRIEL

Master of Science in Applied Physics,
Delft University of Technology, The Netherlands,
born in Eindhoven, The Netherlands.

This dissertation has been approved by the promotor.

Composition of the doctoral committee:

Rector Magnificus,	chairperson
Prof. dr. ir. L.P. Kouwenhoven,	Delft University of Technology, promotor
Prof. dr. A.F. Otte,	Delft University of Technology, promotor

Independent members:

Prof. dr. L. DiCarlo,	Delft University of Technology
Prof. dr. J.M. Thijssen,	Delft University of Technology
Dr. J. Paaske,	Niels Bohr Institute, Denmark
Dr. A. Chatterjee,	Delft University of Technology
Dr. A.R. Akhmerov,	Delft University of Technology, reserve member



Cover: *Phys. Pop. Art:* Silk screen of a Kitaev chain device.
By David van Driel.

Printed by: Gildeprint

Style: TU Delft House Style, with modifications by Moritz Beller
<https://github.com/Inventitech/phd-thesis-template>

Keywords: Semiconductor-superconductor hybrids, Majorana zero modes, charge sensing, spin, Kitaev chains

Copyright © 2024 by David van Driel

ISBN 978-94-6384-618-9

An electronic version of this dissertation is available at
<http://repository.tudelft.nl/>.

*Does it now seem worth all the color of skies?
To see the earth through painted eyes.*

- Nick Drake

CONTENTS

Summary	1
Samenvatting	3
1 Introduction	5
1.1 Intruding the Superconducting Gap	7
1.2 In Praise of Hybrids	10
1.3 Outline of This Thesis	11
References	12
2 Theory	15
2.1 Quantum Dots	17
2.1.1 Single-Electron Box	17
2.1.2 Double Quantum Dots	19
2.2 Sub-Gap States	24
2.2.1 Andreev Bound States	24
2.2.2 Superconducting Anderson Impurity Model	28
2.2.3 Yu-Shiba-Rusinov States	32
2.2.4 Andreev Bound State Yu-Shiba-Rusinov Crossover	35
2.3 Charge of Sub-Gap States	40
2.3.1 Single-Andreev Box	40
2.3.2 Electric Fields in Hybrids.	42
2.3.3 Charge Sensing Sub-Gap States	43
2.4 Minimal Kitaev Chains	45
2.4.1 Normal Quantum Dot Kitaev Chain	46
2.4.2 Proximitized Quantum Dot Kitaev Chain.	48
2.4.3 Andreev Bound State Quantum Dot Kitaev Chain	52
2.4.4 Charge Sensing a Minimal Kitaev Chain	54
References	59
3 Spin-Filtered Measurements of Andreev Bound States	65
3.1 Introduction	67
3.2 Results and discussion	69
3.2.1 Device fabrication and set-up	69
3.2.2 Zeeman-driven singlet-doublet transitions.	70
3.2.3 Gate-driven singlet-doublet transition	73
3.2.4 The Andreev bound state relaxation mechanism	74

3.3	Conclusion	76
3.4	Methods	76
3.4.1	Device set-up.	76
3.4.2	Quantum Dot Spin Filter	76
3.4.3	Analysis of spin-polarization.	77
3.5	Data availability	77
3.6	Extended Data	78
	References	87
4	Charge Sensing the Parity of an Andreev Molecule	93
4.1	Introduction	95
4.2	Results	95
4.2.1	Device characterization	95
4.2.2	ABS even ground state charge	97
4.2.3	Single ABS parity readout	98
4.2.4	Andreev molecule spectroscopy	100
4.2.5	Andreev molecule parity readout.	101
4.3	Conclusion.	103
4.4	Supplementary Information	103
4.4.1	Resonator characterization	103
4.4.2	Virtual gates and fig. 1 data processing.	103
4.4.3	Charge jumps	104
4.4.4	Extended range hybrid spectrum and charge sensing.	105
4.4.5	Fig. 2 charge sensor data processing	106
4.4.6	Andreev bound states in the atomic limit.	108
4.4.7	Fig. 3 dc transport and rf reflectometry comparison	110
4.4.8	Charge sensor SNR.	110
	References	112
5	Robust Poor Man's Majorana Zero Modes Using Yu-Shiba-Rusinov States	119
5.1	Fabrication and setup	122
5.2	YSR states in quantum dots.	123
5.3	Coupled YSR states.	124
5.4	Gate control of CAR and ECT	125
5.5	Majorana sweet spot	127
5.6	Conclusion.	129
5.7	Materials and Methods	129
5.7.1	Device fabrication	129
5.7.2	Transport measurements and data processing	129
5.7.3	Spinless PMM spectrum	130
5.7.4	Series resistance correction.	130
5.7.5	Device tune-up.	131
5.8	Supplementary Information	132
5.8.1	Theoretical model	132
5.8.2	Estimation of dephasing rates	133

5.9	Extended Data	135
	References	135
6	Cross-Platform Machine-Learning-Assisted Control of Minimal Kitaev Chains	149
6.1	Introduction	151
6.2	Device characterization	152
6.3	Tuning Algorithm	154
6.3.1	Theory Model	154
6.3.2	Model Validation.	155
6.3.3	Transfer Learning	156
6.3.4	Gradient Descent Voltage Optimization	157
6.4	Tuning Algorithm Performance	159
6.4.1	Zero Field Algorithm Performance	159
6.4.2	Finite Field Algorithm Performance	160
6.5	Discussion	162
6.6	Conclusion.	162
6.7	Supplementary information	163
6.7.1	CNN architecture	163
6.7.2	CNN training.	164
6.7.3	Kitaev Chain Effective Model.	164
6.7.4	Numerical Training Data.	166
6.7.5	Experimental Training Data	166
6.7.6	Data labeling procedure	169
6.7.7	CNN prediction limitations.	169
6.7.8	Regularization	170
6.7.9	Gradient descent algorithm	171
6.7.10	Choice of learning rate.	172
6.7.11	Choice of tolerance.	173
6.7.12	Pseudocode	174
6.7.13	Non-converged run example	174
	References	176
7	Conclusions and Outlook	181
7.1	Extending Kitaev Chains With a Single Superconductor	183
7.2	Beyond III-V Semiconductors.	185
7.3	Tuning a Minimal Kitaev Chain Without Normal Leads	186
7.4	Reading Out Parity Using Non-Local Quantum Capacitance	188
7.5	Yu-Shiba-Rusinov Singlet-Triplet Qubits	190
	References	193
	Acknowledgements	197
	Curriculum Vitæ	205
	List of Publications	207

SUMMARY

Andreev bound states arise in low-dimensional confined systems, coupled to superconductors. They show great similarity to the highly sought-after Majorana bound states, yet they lack the desirable non-Abelian statistics or topological protection. Except for these, Andreev bound states possess a multitude of unique and interesting properties. This thesis explores several of these properties, using semiconductor quantum dots as a measurement tool. In addition, quantum dots are hybridized with Andreev bound states to form novel systems, including Andreev molecules, and Kitaev chains.

In the theory section, we introduce several basic concepts, followed by a discussion of the properties of Andreev bound states and similar Yu-Shiba-Rusinov states. We then extend the concept of Andreev bound states to Kitaev chains in various implementations.

In the first chapter, we use a quantum dot as both a spin and energy filter to probe an Andreev bound state. We observe pure spin states despite the strong spin-orbit interaction in the host semiconductor. Utilizing a three-terminal measurement setup, we can change the spin-relaxation process of the Andreev bound state by changing tunnel barrier strengths.

Next, we configure a quantum dot as a charge sensor to study Andreev bound states. We observe smooth changes in ground state charge due to hybridization of the even-occupation states. We additionally detect abrupt loading of electrons during the singlet-doublet transition, which agrees with a change of ground state parity. Having used quantum dots as a measurement tool, we then hybridize them with Andreev bound states to form an Andreev molecule. We demonstrate readout of the ground state parity of the combined system using the charge sensor. We argue that parity-to-charge conversion in semiconductor-superconductor systems is a viable scheme for reading out Kitaev chains and associated qubits.

We proceed by strongly coupling two quantum dots to a single Andreev bound state. This coupling mediates tunneling and Cooper pair splitting processes between the quantum dots, effectively constituting a Kitaev chain. For each Andreev bound state, we can find two gate voltages at which the rates of these processes are equal and non-zero. Spectroscopic measurements reveal localized Majorana zero modes on the quantum dots that are robust against local electrostatic changes.

Engineering Kitaev chain-based qubits requires consistently finding Majorana zero modes. In the final experimental chapter of this thesis, we present an algorithm that tunes gate voltages until Majorana zero modes emerge in Kitaev chains. We employ a neural network to estimate the relative Cooper pair splitting and tunneling rates from spectroscopic measurements. These estimates are then input into a gradient descent algorithm until the rates are balanced, and Majorana zero modes emerge. We present statistics on the algorithm's performance and conclude that it is a vital tool in elevating Kitaev chains from the realm of fundamental study to quantum information.

We then propose a series of future experiments, based on our current findings. Notably, we explore the possibility of storing quantum information in the spin degree of freedom of a superconductor using Yu-Shiba-Rusinov states.

SAMENVATTING

Andreev-gebonden toestanden ontstaan in laag-dimensionale begrensde systemen die zijn gekoppeld aan supergeleiders. Ze vertonen grote gelijkenis met de veelgezochte Majorana-gebonden toestanden, maar missen de gewenste niet-Abeliaanse statistieken of topologische bescherming. Behalve deze karakteristieken bezitten Andreev-gebonden toestanden een veelvoud aan unieke en interessante eigenschappen. Dit proefschrift onderzoekt verschillende van deze eigenschappen met behulp van halfgeleider kwantumstippen als meetinstrument. Bovendien worden kwantumstippen gehybridiseerd met Andreev-gebonden toestanden om nieuwe systemen te vormen, waaronder Andreev-moleculen en Kitaev-ketens.

In de theoretische sectie introduceren we verschillende basisconcepten, gevolgd door een bespreking van de eigenschappen van Andreev-gebonden toestanden en vergelijkbare Yu-Shiba-Rusinov-toestanden. Vervolgens breiden we het concept van Andreev-gebonden toestanden uit naar Kitaev-ketens in verschillende implementaties.

In het eerste hoofdstuk gebruiken we een kwantumstip als zowel een spin- als energiefilter om een Andreev-gebonden toestand te onderzoeken. We observeren pure spintoestanden ondanks de sterke spin-baan koppeling in de gast-halfgeleider. Door gebruik te maken van een driepuntsmeting kunnen we het spin-relaxatieproces van de Andreev-gebonden toestand veranderen door de sterkte van de tunnelbarrières aan te passen.

Vervolgens configureren we een kwantumstip als een ladingensor om Andreev-gebonden toestanden te bestuderen. We observeren geleidelijke veranderingen in de grondtoestand-lading als gevolg van de hybridisatie van de even-bezettings toestanden. We detecteren ook abrupte belading van elektronen tijdens de singlet-doublet-overgang, wat overeenkomt met een verandering van de grondtoestand-pariteit. Na het gebruik van kwantumstippen als meetinstrument, hybridiseren we ze met Andreev-gebonden toestanden om een Andreev-molecuul te vormen. We demonstreren de uitlezing van de grondtoestand-pariteit van het gecombineerde systeem met behulp van de ladingensor. We stellen dat pariteit-naar-ladingconversie in halfgeleider-supergeleider-systemen een haalbaar schema is voor het uitlezen van Kitaev-ketens en de bijbehorende qubits.

We gaan verder door twee kwantumstippen sterk te koppelen aan een enkele Andreev-gebonden toestand. Deze koppeling bemiddelt tunneling- en Cooper-paar-splitsingsprocessen tussen de kwantumstippen, waardoor het geheel effectief een Kitaev-keten vormt. Voor elke Andreev-gebonden toestand kunnen we twee gate-spanningen vinden waarbij de tempo's van deze processen gelijk en niet-nul zijn. Spectroscopische metingen onthullen gelokaliseerde Majorana-nulmodi op de kwantumstip die robuust zijn tegen lokale elektrostatistische veranderingen.

Het ontwerpen van qubits op basis van Kitaev-ketens vereist dat Majorana-nulmodi consistent gevonden kunnen worden. In het laatste experimentele hoofdstuk van dit proefschrift presenteren we een algoritme dat gate-spanningen afstemt totdat Majorana-nulmodi verschijnen in Kitaev-ketens. We maken gebruik van een neurale netwerk om de relatieve

Cooper-paar-splitsing en tunneling-snelheden te schatten op basis van spectroscopische metingen. Deze schattingen worden vervolgens ingevoerd in een gradient-afdaal-algoritme totdat de tempo's in balans zijn en de Majorana-nulmodi verschijnen. We presenteren statistieken over de prestaties van het algoritme en concluderen dat het een vitaal hulpmiddel is voor het verheffen van Kitaev-ketens als subject van fundamenteel onderzoek naar een toepassing van kwantumtechnologie.

We stellen vervolgens een reeks toekomstige experimenten voor, gebaseerd op onze huidige bevindingen. In het bijzonder verkennen we de mogelijkheid om kwantuminformatie op te slaan in de spintoestand van een supergeleider met behulp van Yu-Shiba-Rusinov-toestanden.

1

INTRODUCTION

*Be like the rocky headland on which the waves constantly break.
It stands firm, and round it the seething waters are laid to rest.*

- Marcus Aurelius

1.1 INTRUDING THE SUPERCONDUCTING GAP

Sub-gap states are a *contradictio in terminis*; they are single-electronic states within an energy gap that excludes single-electronic states. Yet, their existence is ubiquitous, with physicists routinely observing sub-gap states, unwillingly at times. Sub-gap states emerge from the interplay between superconductivity and quantum confinement. Their study is deeply rooted in history and continues to have a lasting impact. When Heike Kamerlingh Onnes cooled down a wire fashioned from mercury to 4.2 K, he was stumped to find its electrical resistance dropped to zero. The year was 1911, and superconductivity had been discovered. It did not take the Nobel Committee long to recognize Kamerlingh Onnes' findings, as they awarded him the prize in 1913 "for his investigations on the properties of matter at low temperatures which led, inter alia, to the production of liquid helium". Many scientists will remember Kamerlingh Onnes as the founding father of superconductivity, as it remain a highly active field of research. Then in 1933, Meissner observed that superconductors can act as perfect diamagnets [1]. Two years later, the London brothers proposed equations that govern the electromagnetic behavior of superconductors, for which they had to introduce the penetration depth [2]. 24 years had passed since the discovery of superconductivity and there were only a handful of observations and phenomenological explanations.

It would take until 1950 for Ginzburg and Landau to propose their theory of superconductivity [3]. There was finally a systematic theory that could explain numerous phenomena in superconductors, though a microscopic interpretation was still lacking. Then in 1953, Pippard identified the need for a second length scale of superconductivity, which is now known as the coherence length [4]. A year later, Corak and co-workers performed specific heat measurements on superconductors. [5]. They realized that the specific heat was dominated by a term $e^{-\Delta/k_B T}$ at low temperatures, which suggests a gap in the single-electron density of states of size Δ . This energy gap was confirmed by the landmark, microscopic explanation of superconductivity by BCS in 1957 [6]. An attractive electron-electron interaction makes the Fermi surface of free electrons unstable. Electrons will then pair up within an energy window of size Δ around the Fermi level. The formation of Cooper pairs makes single-electronic sub-gap states energetically unfavorable. It is therefore unexpected to be able to inject electrons into a superconductor at energies below the superconducting gap.

In the same year that the BCS theory was published, Abrikosov detailed how magnetic fields can pierce superconductors when the penetration depth is larger than the coherence length [7]. He predicted the formation of a lattice of supercurrent vortices around field lines. A year later, Bogoliubov introduced his namesake transformation [8]. He showed that the excitations of a BCS ground state are superpositions of electrons and holes. Notably, there were no single-electron excitations below the gap. Later, the Bogoliubov transformation would be used to show that sub-gap states are in fact electron-hole superpositions. In 1960, Abrikosov and Gor'kov detailed how a finite concentration of paramagnetic impurities in a superconductor can close the energy gap [9]. Much of the research during this decade established the absence of electronic states in the superconducting gap. During the next decades, multiple physicists would predict the exact opposite.

In 1963, De Gennes and Saint-James predicted that transport resonances below Δ can occur in slabs of normal metal deposited on a superconductor [10]. A year later, Caroli, De

Gennes and Matricon predicted the existence of bound states in the vortices discovered by Abrikosov [11]. These sub-gap states are referred to as Caroli-deGennes-Matricon (CdGM) states. Then in 1964, Andreev proposed his titular “Andreev reflection” process, where an electron incident on a superconductor can reflect as a hole [12]. Not only did it explain the heat flow across a normal-superconductor (NS) interface, it also provided a convincing mechanism for sub-gap conductance.

Inspired by Abrikosov and Gor’kov’s work from 1960, Yu, Shiba and Rusinov independently considered how adding a single classical spin to a superconductor would influence the superconducting spectrum. Yu published his work in *Acta Physica Sinica* in 1965 [13]. Shiba published in *Progress of theoretical Physics* in 1968 [14]. Rusinov published in *JETP letters* in 1969 [15]. All three found that single ferromagnetic impurities could induce sub-gap states in the superconductor. The mechanism relies on an exchange coupling between the impurity and quasiparticles in the superconductor, similar to the Kondo effect [16]. These sub-gap states are now referred to as Yu-Shiba-Rusinov (YSR) states.

In the same year as Rusinov’s publication, Kulik showed that Andreev reflections in a superconductor-normal-superconductor (SNS) geometry can result in sub-gap states [17]. These are what we now refer to as Andreev bound states (ABSs). While originally identified in phase-biased systems, ABSs have become almost synonymous with sub-gap states. In 1972, Machida and Shibata also predicted sub-gap states for non-magnetic impurities without Coulomb interaction ($U = 0$) [18]. They write that “This new mechanism is caused by the resonance scattering due to localized impurities, though Shiba insists that there should not exist any bound state in this case”. They found that neither ferromagnetism, charging energy, nor phase differences are required for the formation of sub-gap states.

A year later, Rowell reported the experimental observation of sub-gap states in normal-superconductor-insulator-normal (NSIN) heterostructures [19]. They related their findings to the predictions made by De Gennes and Saint-James. In 1989, Hess et al. used the newly-found technique of scanning tunneling microscopy (STM) to perform tunneling spectroscopy in the center of vortices in a type-II superconductor [20]. As the experiment was performed using a metallic tip at 1.85 K, the temperature broadening of tunnel spectroscopy did not allow them to resolve discrete states. Soon after, the experimental data was reproduced theoretically by Shore et al., who found that the results could be explained by the sub-gap states predicted by Caroli, De Gennes and Matricon [21]. In 1993, Riedel and Bagwell calculated the current-voltage relation of NIS junctions [22]. Interestingly, they also considered an NIS system with an impurity in the metal, which also led to sub-gap states. In 1997, Yazdani et al. used STM to probe magnetic impurities on superconducting surfaces [23]. They found sub-gap states that were consistent with the predictions of Yu, Shiba and Rusinov. Then in 2001, Giazotto et al. reported resonant sub-gap transport in a GaAs-Nb heterostructure that was consistent with the predictions of De Gennes and Saint-James [24]. There was an additional transport resonance at the Fermi level, which they attributed to finite size effects.

Distinguishing a single, discrete sub-gap state from a sub-gap transport resonance can be non-trivial. For example, an induced gap in a normal metal also enters as a sub-gap resonance, but consists of a continuum of states. Obtaining a finite level spacing in a metal is challenging, as its dimensions would have to be smaller than the Fermi wavelength, which is on the order of Angstroms. STM was important in observing the first discrete

sub-gap states, as it allowed the study of individual atoms or vortices. Discrete states can also be found in semiconductors, as their low effective mass allows for finite level spacing. The experimental introduction of quantum dots made it more straightforward to create discrete states. In 2009, Grove-Rasmussen et al. observed sub-gap transport in superconductor-quantum dot-superconductor (S-QD-S) systems fabricated on carbon nanotubes [25]. They state that “the unusual sub-gap features observed in odd occupied dots are caused by an interplay between MAR [multiple Andreev reflections, red.] and quantum Shiba states”. This careful phrasing highlights the difficulty in telling transport resonances apart from sub-gap states. A year later, Pillet et al. found sub-gap states in carbon nanotubes as well, which they identified as Andreev bound states [26]. Since then, there have been many publications on sub-gap states which go far beyond their first observation. These include chains of ferromagnetic atoms on superconductors [27], CdGM states coupled to YSR states [28] and Andreev molecules in double quantum dots [29]. Interestingly, a hitherto undiscovered state was reported recently. In 2023, Schneider et al. observed sub-gap surface states on non-magnetic Ag islands on a bulk superconductor using STM [30]. They identified these as Machida-Shibata states, as there was no Coulomb interaction. It is debatable whether these states differ significantly from Andreev bound states. However, unlike the YSR states commonly observed in STM, they are non-magnetic. While sub-gap states are frequently observed in both impurities on superconductors and semiconductor-superconductor hybrids, the two communities remain relatively separated, and retain their own naming conventions.

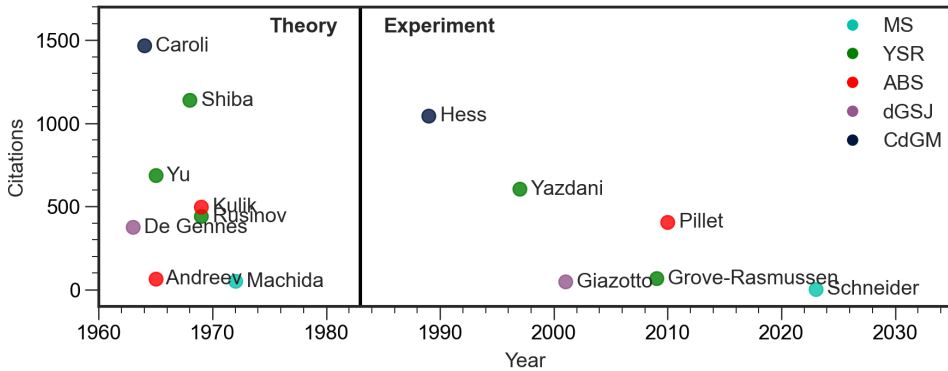


Figure 1.1: **Timeline of selected publications on sub-gap states.** We categorize the states as: Machida-Shibata (MS), Yu-Shiba-Rusinov (YSR), Andreev bound state (ABS), de Gennes Saint-James (dGSJ) and Caroli-deGennes-Matignon (CdGM).

Many sub-gap states have been predicted, named, and observed. They have been found in many device geometries, using different spectroscopic techniques. In figure 1.1, we show a timeline of selected publications on sub-gap states. While the distinction between these states can be arbitrary, there is historic value in understanding how they were proposed and observed for the first time. After all these years the paradox remains the same: why does a superconductor admit the addition of single electrons when its Fermi surface has become unstable due to an attractive electron-electron interaction? Fundamentally for

a state to become sub-gap, the total energy needs to be lowered upon coupling to the superconductor. This can happen due to a phase difference between superconductors, exchange-coupling, Coulomb interactions, resonant tunneling or vortex formation. Has every possible mechanism been explored, or are there still undiscovered sub-gap states in the wild?

1.2 IN PRAISE OF HYBRIDS

To confine a system is to impose rules on it. First and foremost, one limits the extent of the system to manually defined boundaries. If the system extent is small enough, i.e. on the order of the Fermi wavelength, additional rules are imposed on the system. These are given by quantum mechanics, where states can only exist at quantized energies. This can be seen in atoms, where one cannot add electrons outside the orbits. Fundamentally, these rules follow from many observations of our universe, which appears to behave according to principles. We focus on two important ones. The first being the Pauli exclusion principle, which states that every electronic quantum state can only be occupied by one electron. The second one is Heisenberg's uncertainty principle, which states that some pairs of observables cannot be known with high certainty simultaneously. The most famous example is the conjugate pair of position and momentum. In Bohr's model of atomic orbits, electrons orbit the nucleus at a fixed momentum and a fixed path. As this would require both to be known with high accuracy, it breaks in view of Heisenberg's uncertainty principle. Instead, we are left with a probability distribution of the electron location for any given momentum.

Confinement is not only restricted to atoms, but is also relevant in solid state physics. A semiconductor can also be confined, as its Fermi wavelength is typically around ~ 10 nm, which is readily accessible by modern electron lithography. The aforementioned rules apply here too, including electron level quantization, particle conservation and the Pauli exclusion principle. A confined semiconductor, a quantum dot, is therefore an excellent platform for quantum information processing. The large level spacing of electronic states makes it possible to decode quantum information into the spin degree of freedom. The Pauli exclusion principle prevents electrons in a single orbital from having the same spin state. As confinement can be changed using electrostatic gates, the information can move and interact with other qubits, allowing for two-qubit gates. Ultimately, it is the rules resulting from confinement that allows for quantum information to be well-defined in quantum dots.

Superconductivity, on the other hand, is nature's way of breaking rules. To start, one can have a current without any dissipation, which is impossible in normal conductors. For superconducting reservoirs, the total number of particles is conserved in a way that allows for fluctuations by pairs of electrons. Superconductors also break the concept of a Fermi surface, as it becomes unstable due to a positive attraction between electrons of arbitrary magnitude. As discussed in the section above, this results in a gap in the single-electronic states around the Fermi level. Heisenberg's uncertainty principle also applies to superconductors, only this time for the conjugate variables of phase and charge. This is ultimately the cause of the particle number fluctuations, as a grounded superconductor has a fixed phase.

Introducing superconductivity in a confined system presents physicists with an odd

dilemma: which rules are maintained and which are broken? Is charge well-defined, which is generally the case for a confined semiconductor. Is confinement maintained? The discrete, semiconducting states are ultimately only separated from a continuum of metallic states by the superconducting gap. Nature always finds a way of resolving conflict, which is illustrated by Andreev reflection. Here, an electron in a conductor is incident on an interface with a superconductor. There are no single-electronic states in the superconducting gap, so it cannot be transmitted across the interface. On the other hand, provided that momentum is conserved in the conductor, it cannot simply reverse its momentum. Andreev solved this apparent paradox by proposing that the electron retroreflects as a hole, creating a Cooper pair in the superconductor. This is allowed due to the particle number fluctuations in the superconductor.

When a confined semiconductor is tunnel-coupled to a superconducting reservoir, its discrete levels hybridize with the superconductor to form sub-gap states. This captures the information of the superconducting condensate, as well as the quasiparticles, in a single state in a semiconductor. Metaphorically, this is like having the whole world in a grain of sand. We emphasize that the sub-gap state remains coherent when coupled to a superconductor, in contrast to coupling a semiconductor to a normal lead, where the discrete state is drowned out by the continuum of metallic states. Sub-gap states acquire particle-hole symmetry from the parent superconductor. Their even states are now a superposition of an empty and fully-occupied orbital, due to Andreev reflection with the superconductor. As a result, the average charge of the even state can be anywhere between 0 and $2e$, where e is the electron charge. Depending on the charging energy of the semiconductor, sub-gap states can also have an odd ground state in the absence of a magnetic field. Crucially, sub-gap states can be manipulated via electrostatic gates, allowing for the fine-tuning of their electrochemical potential and coupling to the superconductor. This outlines the benefits of semiconductor-superconductor hybrids: controllable superconducting properties in a single state. It is this property that enables applications unique to hybrids, such as Andreev spin qubits, Kitaev chains, superconducting diodes, coupling spin qubits over large distances, triplet superconductivity and more.

1.3 OUTLINE OF THIS THESIS

In this thesis, we have studied quantum dots coupled to Andreev bound states in various forms. We first introduce the theoretical concepts relating to the experimental work in **chapter 2**. Here, we place the emphasis on quantum dots, sub-gap states, their charge and Kitaev chains.

In **chapter 3**, we detail how spin-polarized quantum dots can be used to probe the spin of sub-gap states. Based on spin-dependent transport we study individual Andreev bound states in a semiconductor-superconductor hybrid. We also study the relaxation mechanism of the excited states, as we can control the sub-gaps states' coupling to electron reservoirs.

In **chapter 4**, we study the charge of Andreev bound states using a quantum dot charge sensor. While sub-gap states usually refer to single-electronic states, we can directly probe the many-body ground state. While these states do not typically have a charging energy,

they can have well-defined charge. We find that the average charge can change by twice the electron charge without a change of ground state parity. Finally, we create an Andreev molecule by coupling a quantum dot to the hybrid. We see that the charge is coherently distributed over the two systems.

In **chapter 5**, we have coupled two quantum dots through an Andreev bound state. The strong coupling between each quantum dot and the Andreev bound state results in Andreev reflection on the quantum dots. We show that we can engineer a two-site Kitaev chain using this system, with stronger interaction strengths than for normal quantum dots.

Poor Man's Majorana zero modes can emerge in a two-site Kitaev chain in a parameter sweet spot. We can tune to this sweet spot by varying the Andreev bound state energy using an electrostatic gate. In **chapter 6**, we use a convolutional neural network to identify this sweet spot based on conductance measurements. We then use a gradient descent algorithm to vary the Andreev bound state energy until a sweet spot is reached.

We finally present conclusions from this thesis in **chapter 7**. In addition, we introduce possible research directions for the near future.

REFERENCES

- [1] Walther Meissner and Robert Ochsenfeld. Ein neuer effekt bei eintritt der supraleitfähigkeit. *Naturwissenschaften*, 21(44):787–788, 1933.
- [2] Fritz London and Heinz London. The electromagnetic equations of the supraconductor. *Proceedings of the Royal Society of London. Series A-Mathematical and Physical Sciences*, 149(866):71–88, 1935.
- [3] VL Ginzburg. Ginzburg, vl and landau, ld. *Zh. Eksp. Teor. Fiz*, 20(1064):1950, 1950.
- [4] Alfred Brian Pippard and William Lawrence Bragg. An experimental and theoretical study of the relation between magnetic field and current in a superconductor. *Proceedings of the Royal Society of London. Series A. Mathematical and Physical Sciences*, 216(1127):547–568, 1953.
- [5] WS Corak, BB Goodman, CB Satterthwaite, and A Wexler. Exponential temperature dependence of the electronic specific heat of superconducting vanadium. *Physical Review*, 96(5):1442, 1954.
- [6] John Bardeen, Leon N Cooper, and J Robert Schrieffer. Microscopic theory of superconductivity. *Physical Review*, 106(1):162, 1957.
- [7] Alexei A Abrikosov. On the magnetic properties of superconductors of the second group. *Soviet Physics-JETP*, 5:1174–1182, 1957.
- [8] N. N. Bogoljubov, V. V. Tolmachov, and D. V. Širkov. A new method in the theory of superconductivity. *Fortschritte der Physik*, 6(11-12):605–682, 1958.

- [9] Ai A Abrikosov and L Pr Gor'kov. Contribution to the theory of superconducting alloys with paramagnetic impurities. *Zhur. Eksptl'. i Teoret. Fiz.*, 39, 1960.
- [10] PG De Gennes and Daniel Saint-James. Elementary excitations in the vicinity of a normal metal-superconducting metal contact. *Phys. Letters*, 4, 1963.
- [11] C Caroli, PG De Gennes, and J Matricon. Bound fermion states on a vortex line in a type ii superconductor. *Physics Letters*, 9(4):307–309, 1964.
- [12] AF Andreev et al. Thermal conductivity of the intermediate state of superconductors ii. *Sov. Phys. JETP*, 20:1490, 1965.
- [13] L. Yu. Bound state in superconductors with paramagnetic impurities. *Acta Phys. Sin.*, 21:75–91, 1965.
- [14] Hiroyuki Shiba. Classical spins in superconductors. *Progress of theoretical Physics*, 40(3):435–451, 1968.
- [15] A.I. Rusinov. Superconductivity near a paramagnetic impurity. *JETP Lett.*, 9, 1969.
- [16] Jun Kondo. Resistance minimum in dilute magnetic alloys. *Progress of theoretical physics*, 32(1):37–49, 1964.
- [17] IO Kulik. Macroscopic quantization and the proximity effect in sns junctions. *Soviet Journal of Experimental and Theoretical Physics*, 30:944, 1969.
- [18] Kazushige Machida and Fumiaki Shibata. Bound states due to resonance scattering in superconductor. *Progress of Theoretical Physics*, 47(6):1817–1823, 1972.
- [19] JM Rowell. Tunneling observation of bound states in a normal metal–superconductor sandwich. *Physical Review Letters*, 30(5):167, 1973.
- [20] HF Hess, RB Robinson, RC Dynes, JM Valles Jr, and JV Waszczak. Scanning-tunneling-microscope observation of the abrikosov flux lattice and the density of states near and inside a fluxoid. *Physical review letters*, 62(2):214, 1989.
- [21] Joel D Shore, Ming Huang, Alan T Dorsey, and James P Sethna. Density of states in a vortex core and the zero-bias tunneling peak. *Physical review letters*, 62(26):3089, 1989.
- [22] Richard A Riedel and Philip F Bagwell. Current-voltage relation of a normal-metal–superconductor junction. *Physical Review B*, 48(20):15198, 1993.
- [23] Ali Yazdani, BA Jones, CP Lutz, MF Crommie, and DM Eigler. Probing the local effects of magnetic impurities on superconductivity. *Science*, 275(5307):1767–1770, 1997.
- [24] Francesco Giazotto, Pasqualantonio Pingue, Fabio Beltram, Marco Lazzarino, Daniela Orani, Silvia Rubini, and Alfonso Franciosi. Resonant transport in nb/gaas/algaas heterostructures: Realization of the de gennes–saint-james model. *Physical Review Letters*, 87(21):216808, 2001.

- [25] Kasper Grove-Rasmussen, Henrik Ingerslev Jørgensen, Brian Møller Andersen, Jens Paaske, Thomas Sand Jespersen, Jesper Nygård, Karsten Flensberg, and Poul Erik Lindelof. Superconductivity-enhanced bias spectroscopy in carbon nanotube quantum dots. *Physical Review B*, 79(13):134518, 2009.
- [26] JD Pillet, CHL Quay, P Morfin, C Bena, A Levy Yeyati, and P Joyez. Andreev bound states in supercurrent-carrying carbon nanotubes revealed. *Nature Physics*, 6(12):965–969, 2010.
- [27] Stevan Nadj-Perge, Ilya K Drozdov, Jian Li, Hua Chen, Sangjun Jeon, Jungpil Seo, Allan H MacDonald, B Andrei Bernevig, and Ali Yazdani. Observation of majorana fermions in ferromagnetic atomic chains on a superconductor. *Science*, 346(6209):602–607, 2014.
- [28] Zhaoen Su, Alexandre B Tacla, Moïra Hocevar, Diana Car, Sébastien R Plissard, Erik PAM Bakkers, Andrew J Daley, David Pekker, and Sergey M Frolov. Andreev molecules in semiconductor nanowire double quantum dots. *Nature communications*, 8(1):585, 2017.
- [29] Sunghun Park, Víctor Barrena, Samuel Mañas-Valero, José J Baldoví, Antón Fente, Edwin Herrera, Federico Mompeán, Mar García-Hernández, Ángel Rubio, Eugenio Coronado, et al. Coherent coupling between vortex bound states and magnetic impurities in 2d layered superconductors. *Nature Communications*, 12(1):4668, 2021.
- [30] Lucas Schneider, Khai That Ton, Ioannis Ioannidis, Jannis Neuhaus-Steinmetz, Thore Posske, Roland Wiesendanger, and Jens Wiebe. Proximity superconductivity in atom-by-atom crafted quantum dots. *Nature*, 621(7977):60–65, 2023.

2

2

THEORY

In het getal bezwijkt het verhaal en wordt geen beeld geboren.

- Johan Huizinga

This chapter serves to provide the reader with the necessary phenomena and models related to the experimental sections of the thesis. These include quantum dots, sub-gap states, charge sensing and Kitaev chains. While each of these topics comprises an expansive volume of literature, we introduce the reader to the bare minimum required to understand the subsequent chapters of this thesis. For the sections involving superconductivity, a BCS ground state is taken as a starting point, its derivation will not be reproduced.

2.1 QUANTUM DOTS

In condensed matter, quantum dots are metals or semiconductors that are confined in all three dimensions, effectively creating a zero-dimensional system. This confinement can be realized in two ways. First, quantum dots can be directly synthesized, in the form of nanometer sized structures. Second, they can be formed from a larger system, by electrostatically confining a small section. These electrostatically-defined quantum dots are isolated from their environments, allowing their electrostatic potential to be changed by voltage sources through gate electrodes. This leads to numerous effects, including one-by-one electron transport, Coulomb blockade and quantum fluctuations. Quantum dots can be tunnel-coupled to other systems, such as a superconductor or another quantum dot. If this coupling is controlled by a gate voltage, it allows for a tunable hybridization between the two systems. The resulting combined systems can take various forms, including double quantum dots, sub-gap states and Kitaev chains. A key characteristic of quantum dots is their sensitivity to changes in their electrostatic environment, making them highly effective as charge sensors. Given the prevalence of quantum dots in the chapters of this thesis, we provide a basic explanation in this introductory chapter.

2.1.1 SINGLE-ELECTRON BOX

When a conductor is confined to lower dimensions, two significant changes occur. First, the electronic energy levels become quantized as the system size approaches the Fermi wavelength. Second, the electrostatic cost of adding charges can exceed the thermal energy. While both effects are relevant for quantum dots, the latter is responsible for the quantization of charge on the dot, and is classical in nature. The “Single-Electron Box” (“SEB”) model captures the electrostatic effects of small conductors, and can reproduce certain phenomena associated with quantum dots.

In Figure 2.1a, we show a schematic drawing of a SEB. Here, a floating conductor (“the island”) is coupled to a grounded metal lead with a capacitance C . A tunnel barrier between the lead and island allows electrons to tunnel in and out. The island is also coupled to a metallic gate electrode with a capacitance C_g . This gate has an electrostatic potential, V_g , with respect to the grounded lead. As we change V_g using, for example, a voltage source, we are charging one of the capacitor plates, with the other being the island. An effective charge $q = C_g V_g$ is then induced on the island, which changes the electrostatic potential. For a parallel plate capacitor, the electrostatic potential is given by $U = Q^2 / 2C$. Similarly, we can write down the total electrostatic energy of the island as [1]:

$$E_{el} = \frac{E_C}{2} \left(N - \frac{q}{e} \right)^2 - \frac{q^2}{2C_g} \quad (2.1)$$

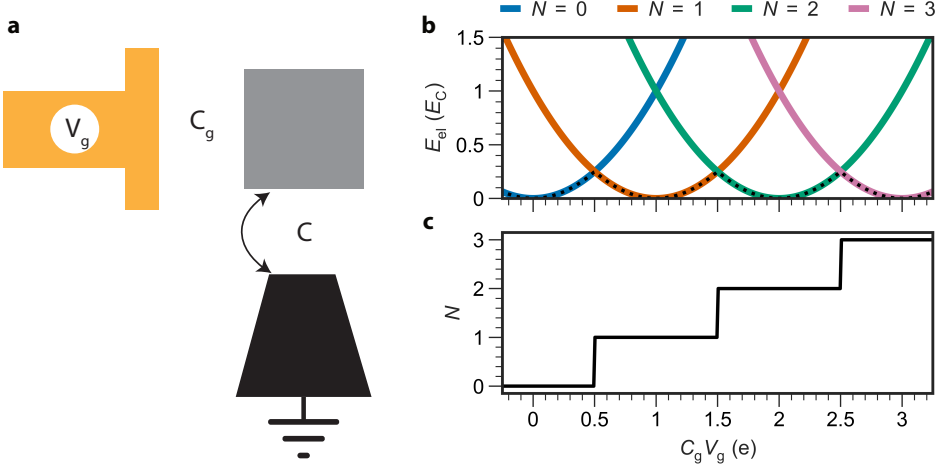


Figure 2.1: **Electrostatic energy and occupation values of a single-electron box.** **a.** Schematic overview of a single-electron box, showing a gate electrode (yellow) with an electrostatic potential, V_g , coupled to an island (gray) with a capacitance C_g . A grounded, metallic lead (black) has a capacitance C to the island, and allows electron to tunnel in or out. **b.** Electrostatic energy, E_{el} , for varying V_g for different amounts of excess electrons on the island, N . The black, dotted line indicates the lowest energy occupation of the island. **c.** N corresponding to the lowest E_{el} for varying V_g .

Where e is the elementary charge, N is the amount of excess electrons on the island, $q^2/2C_g$ is the work performed by the voltage source, and $E_C = e^2/(C + C_g)$ is the charging energy, which governs the energy cost of adding electrons to the island. In Figure 2.1b we show E_{el} , for varying V_g , for different occupations of the island. Note that we dropped the final term in Equation (2.1) as it does not depend on N . For a given N , the electrostatic energy increases parabolically with $C_g V_g$. This is equivalent to an ordinary capacitor, where changing V_g increases the electric field line density between the island and the gate, resulting in a greater electrostatic energy. Unlike a normal capacitor, electrons can tunnel between the lead and the island. The number of excess electrons on the island can therefore change to minimize E_{el} . The black, dotted line in Figure 2.1b indicates E_{el} of the lowest energy occupation.

Figure 2.1c shows N corresponding to the lowest E_{el} for varying V_g . N changes discontinuously at the charge-degeneracy points and is constant otherwise. This “Coulomb staircase” shows that the island is charged, one electron at a time, by an external voltage source. Note that the physics described here is largely classical in nature, except for the quantization of charge (electrons) and transport across a large potential barrier (tunneling). Electrons can be added at any energy, as long as the energy cost of charging the island is met. When the electronic levels in the island become discrete, electrons can only be added to discrete orbitals. The parabola’s of different N are then no longer equidistant, as the energy difference between orbitals becomes comparable to E_C .

ELECTROCHEMICAL POTENTIAL

We can define the electrochemical potential, which describes the energy difference between two subsequent occupations, as [2]:

$$\mu(N) = E_{\text{el}}(N) - E_{\text{el}}(N-1) = E_C \left(N - \frac{1}{2} - \frac{q}{e} \right) \quad (2.2)$$

We see that $\mu(N) = 0$ at $q/e = N - 1/2$, which is defined as the “charge-degeneracy point”, as the two charge states have the same energy. Here, a transport cycle is possible if the SEB has a second lead. An electron can then tunnel from the first lead into the island with $N - 1$ electrons, leaving it in the N occupation which has the same E_{el} at charge degeneracy. An electron can then tunnel out into the second lead, leaving the island in the $N - 1$ occupation again.

To understand the charge transfer mechanism, we compare the electrostatic cost of adding one or two electrons to the island. First, we simplify Equation (2.2) by setting $N = 1$ to consider the first electron added to the island and define:

$$\mu \equiv \mu(1) = E_{\text{el}}(1) - E_{\text{el}}(0) = E_C \left(\frac{1}{2} - \frac{q}{e} \right) \quad (2.3)$$

Throughout this thesis, we use μ to indicate the energy cost of adding an electron to an empty SEB or quantum dot. Likewise, the cost of adding the first two electrons at fixed q is:

$$E_{\text{el}}(2) - E_{\text{el}}(0) = E_C \left(2 - 2\frac{q}{e} \right) = 2\mu + E_C \quad (2.4)$$

This electrostatic energy cost can be supplied by the voltage source that charges the island by varying V_g . At fixed V_g , we can also add or remove electrons by applying a potential difference between the two leads, which is defined as the bias voltage V_{bias} . When the leads are biased, electrons are injected into or removed from the island with an energy $-eV_{\text{bias}}$. For $e|V_{\text{bias}}| < \mu$, the electrons do not have enough energy to change the island occupation. Energy conservation prevents a transport cycle, which places the island in Coulomb blockade. For $\mu < e|V_{\text{bias}}| < 2\mu + E_C$ a transport cycle between the leads and the island is possible. Electrons tunnel one-by-one, as the double occupation of the island is energetically forbidden. This is the reason why a SEB with a second lead is referred to as a single-electron transistor. For $2\mu + E_C < e|V_{\text{bias}}|$, the double occupation of the island lies in the bias window. Another transport channel opens in addition to one-by-one tunneling, which causes an increase in current.

We note that E_C sets the scale for the energy differences between island occupations. If temperature becomes on the order of the charging energy ($E_C \approx k_B T$), thermal excitation can overcome the energy differences between different occupations. Charge is then ill-defined in the island, as N can vary for any value of V_g .

2.1.2 DOUBLE QUANTUM DOTS

In the previous section, classical observables were sufficient for describing the electrostatics of a single-electron box. Here, we replace the excess charge, N , by the quantum mechanical number operator $N_i = c_i^\dagger c_i$. In this section, we provide a phenomenological

model that covers the most important aspects of double quantum dots. These systems consist of two quantum dots that are coupled by capacitance, tunneling, or both. We simplify the interactions of the two quantum dots using the constant interaction model, which has two assumptions [3]. First, the total capacitance sets the energy scale of the Coulomb interactions. Second, the single electron levels are independent of these interactions. We additionally assume that tunnel-coupling the QDs does not affect any of the capacitances. Figure 2.2a shows a schematic drawing of a double quantum dot, highlighting the relevant capacitances and voltages.

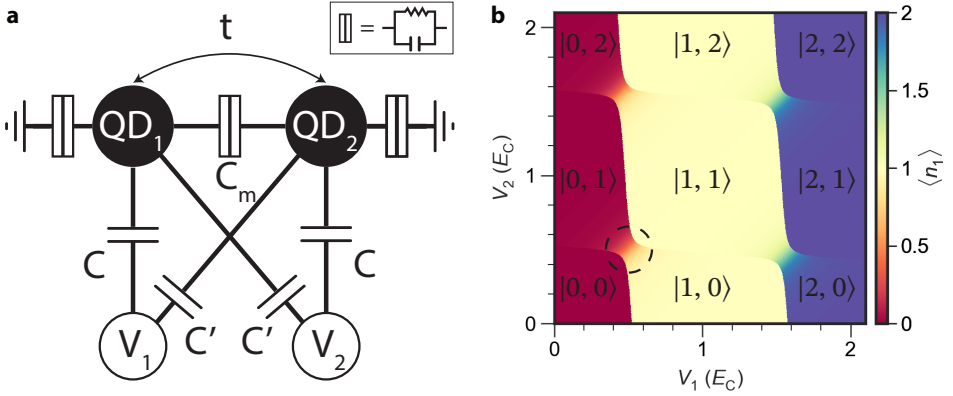


Figure 2.2: **The electron occupation of a double quantum dot.** **a.** Schematic diagram of a double quantum dot. Two quantum dots are coupled with a tunnel coupling, t , and a mutual capacitance, C_m . Each quantum dot has a gate electrode with an electrostatic potential, $V_{1/2}$ respectively. The gates have a capacitance C to their corresponding quantum dot, and a cross-capacitance C' to the other dot. Each quantum dot is connected to a grounded lead. **b.** Charge expectation value of the left quantum dot, $\langle N_1 \rangle$ for varying gate voltages V_1 and V_2 . Only a single orbital is considered for each quantum dot. For the calculations, we used: $C = 1$, $C' = 0.1$, $C_m \approx 0$, $t = 0.1$. The superimposed text indicates the ground state of the double quantum dot in the $|N_1, N_2\rangle$ basis. The dashed circle highlights the hybridization of the $|0, 1\rangle$ and $|1, 0\rangle$ states.

We can write the Hamiltonian of the total system as [4]:

$$\begin{aligned}
 H &= \sum_i H_{\text{QD}}^i + H_{\text{QD}}^m + H_T \\
 H_{\text{QD}}^i &= \frac{E_C^i}{2} \left(N_i - \frac{q_i}{e} \right)^2 \\
 H_{\text{QD}}^m &= \frac{E_C^m}{2} \left(N_1 - \frac{q_1}{e} \right) \left(N_2 - \frac{q_2}{e} \right) \\
 H_T &= t(c_1^\dagger c_2 + c_2^\dagger c_1)
 \end{aligned}$$

Where $E_C^i = \frac{e^2}{C_t} \left(\frac{1}{1 - (C_m^2/C_t^2)} \right)$ is the charging energy of the left/right quantum dot (QD) and $C_t = C + C' + C_m$. Here, C_m is the mutual capacitance between the two QDs. If $C_m \neq 0$, charge added to one QD affects the electrostatic energy of the other. We parametrize this part of the Hamiltonian, H_{QD}^m , by the mutual charging energy $E_C^m = \frac{e^2}{C_m} \left(\frac{1}{(C_t^2/C_m^2) - 1} \right)$. The

gate electrodes have a finite capacitance to both QDs, so we can write the induced charge as:

$$\begin{pmatrix} q_1 \\ q_2 \end{pmatrix} = \begin{pmatrix} C & C' \\ C' & C \end{pmatrix} \begin{pmatrix} V_1 \\ V_2 \end{pmatrix}$$

Where C is the capacitance between the gate and its corresponding QD, and C' is the cross-capacitance to the other dot. Finally, we add a phenomenological tunnel Hamiltonian, H_T , which is parametrized by the tunnel coupling, t , and allows electrons to hop between the two QDs [5].

In Figure 2.2b we show $\langle N_1 \rangle$ for varying gate voltages V_1 and V_2 , which is known as a “charge stability diagram”. We see that $\langle N_1 \rangle$ changes abruptly at $V_1 \approx 0.5E_C$ and $V_1 \approx 1.6E_C$. This behavior is comparable to Figure 2.1, where the gate voltage changes the electrostatic energy, causing a change in occupation of the island. However, $\langle N_1 \rangle$ is additionally affected by V_2 in two ways. First, the induced charge on QD1, q_1 , is directly changed by V_2 through the cross capacitance (C') or mutual capacitance (C_m). Second, the tunnel coupling between the two QDs causes the charge states to hybridize. This is emphasized by the dashed circle in Figure 2.2b, which shows an avoided crossing between the $|0, 1\rangle$ and $|1, 0\rangle$ states, known as an “interdot charge transition”. Here, a single electron is localized on both QDs, causing its energy to depend on both V_1 and V_2 . The two charge states hybridize to form bonding and anti-bonding states [4]:

$$\begin{aligned} \psi_B &= \alpha |0, 1\rangle + \beta |1, 0\rangle \\ \psi_A &= \beta |0, 1\rangle - \alpha |1, 0\rangle \end{aligned}$$

Where α and β depend on $V_{1,2}$ and t . The two charge states can lower their total energy up to an amount $|t|$ by forming a bonding state. If quantum dots are considered to be artificial atoms, then a double quantum dot is an artificial molecule. The hybridization of QD levels is the basis of many physical phenomena, including charge qubits, spin qubits, Kitaev chains, Andreev molecules and more.

SINGLE-ELECTRON BOX CHARGE SENSOR

When the interaction between two QDs is purely capacitive, electrons do not form (anti)-bonding states. However, the electrostatic potential of one QD does become directly sensitive to the occupation of the other. In Figure 2.3a, we show a double quantum dot system with a mutual capacitance, C_m , between the 2 QDs. Similar to Equation (2.3), we can define the electrochemical potentials of both QDs as:

$$\mu_1 \equiv E_{el}(1, 0) - E_{el}(0, 0) = \frac{E_C}{2} - \frac{1}{e}(CV_1E_C + CV_2E_C^m + C'V_2E_C) + E_C^m \langle N_2 \rangle \quad (2.5)$$

$$\mu_2 \equiv E_{el}(0, 1) - E_{el}(0, 0) = \frac{E_C}{2} - \frac{1}{e}(CV_2E_C + CV_1E_C^m + C'V_1E_C) + E_C^m \langle N_1 \rangle \quad (2.6)$$

Here, we use the same definitions as in Section 2.1.2 and limit ourselves to only the 0 and 1 occupations of the QDs. We can then define each QD's occupation as $\langle N_i \rangle = \text{sgn}(\mu_i)$. Each QD's electrochemical potential depends on the occupation of the other with proportionality given by E_C^m .

Figure 2.3b shows $\langle N_1 \rangle$ for varying V_1 and V_2 . For the calculation of $\langle N_1 \rangle$ and μ_2 , we have set $E_C^m \langle N_2 \rangle = 0$ in Equation (2.5) to prevent a self-consistent equation. This approximation

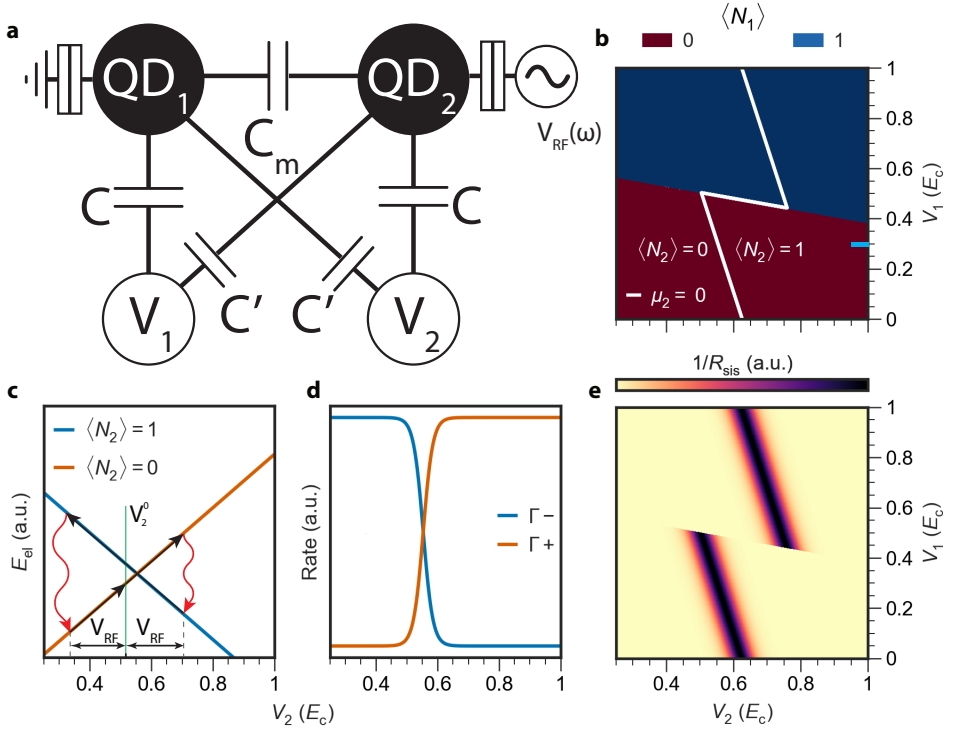


Figure 2.3: **Single-electron box charge sensor.** **a.** Schematic diagram of a capacitively-coupled double quantum dot. There is a mutual capacitance, C_m , between the two QDs. QD2 is tunnel coupled to a normal lead with a potential that varies with a frequency, ω , and amplitude, V_{RF} . **b.** The ground state occupation of QD1, $\langle N_1 \rangle$, for varying V_1 and V_2 . The superimposed white line indicates $\mu_2 = 0$, at which the 0 and 1 occupations of QD2 are degenerate. We have used $C = 1$, $C' = 0.05$ and $C_m = 0.25$ for the calculations. **c.** Schematic sketch of the electrostatic energy, E_{el} , of the 0 and 1 occupations of QD2 at $V_1 = 0V$. V_{RF} changes the occupation of the ground and excited states cyclically around the working point, V_2^0 . Black arrows indicate the work performed by the AC voltage, red arrows indicate the dissipative relaxation processes. **d.** The rates at which electrons tunnel into (Γ_+) and out of (Γ_-) the SEB for varying V_2 . **e.** The inverse of the Sisyphus resistance, $1/R_{sis}$, for varying V_1 and V_2 . For the calculation we used $\Gamma_0 = 0.1$, $k_B T = 0.01$ and $\omega = 0.02$. We have calculated μ_2 using the same capacitances used for panel b.

amounts to a lack of back-action of QD2 on QD1. We see that $\langle N_1 \rangle$ depends on both V_1 and V_2 because the cross-capacitance C' causes V_2 to directly affect the electrostatic potential of QD1. The white, superimposed line indicates $\mu_2 = 0$, for which QD2 is at charge degeneracy. Aside from cross-capacitance, μ_2 also depends on V_1 through the occupation of QD1, given by $E_C^m \langle N \rangle_1$. As $\langle N \rangle_1$ changes abruptly when an electron enters or leaves QD1, μ_2 changes abruptly too. An experimental measurement that probes μ_2 can be used to infer the ground state occupation of QD1, which is known as “charge sensing” [6]. One such technique requires a QD with a source and drain electrode. A change in electrochemical potential can then move the QD in or out of Coulomb blockade, causing a sharp change in current. In keeping with the SEB described in Section 2.1.1, we will detail how a QD with a single

lead can also be used as a charge sensor.

SISYPHUS RESISTANCE

We now couple the lead of QD2 in Figure 2.3a to an AC voltage source with an RMS amplitude, V_{RF} , and angular frequency, ω . We shall refer to QD2 as a single-electron box (SEB), considering it has a single lead. If we consider the circuit, we might naively expect the resistance to be $R = \Re\{Z_T + Z_\Sigma^C\}$, where Z_T is the impedance of the tunnel junction and Z_Σ^C is the summed impedance of the two parallel gate capacitances. The discrete nature of electron charge adds an extra source of dissipation however, which is referred to as “Sisyphus resistance” [7]. Figure 2.3c shows an energy diagram that highlights the origin of this dissipation. We fix the plunger gate voltage of QD2 at an arbitrary $V_2 = V_2^0$, at which the ground state occupation of SEB is 0. V_{RF} changes the electrostatic energy, E_{el} , of the 0 and 1 occupations of the SEB over time. We choose V_{RF} such that the AC voltage can change the ground state occupation, as indicated by the black arrows in Figure 2.3c. We model the SEB as a zero-dimensional system coupled to a three-dimensional electron reservoir and write the rate at which electrons tunnel into (Γ_+) and out of (Γ_-) the SEB as:

$$\Gamma_\pm = \frac{\Gamma_0}{1 + e^{\pm\mu_2/k_B T}} \quad (2.7)$$

Here, Γ_0 is the constant tunnel rate, which is weighted by the Fermi-Dirac distribution of the normal lead. $k_B T$ is the Boltzmann energy and μ_2 is the electrochemical potential of QD2 as defined in Equation (2.6). We calculate μ_2 using the parameters as used for Figure 2.3b and show (Γ_\pm) for varying V_2 in figure 2.3d. The system always remains in the ground state if $\omega \ll \Gamma_0$, leading to a change in occupation near the charge degeneracy point. If $\omega \sim \Gamma_0$, QD2 can remain in the same occupation, which becomes the excited state after crossing the charge-degeneracy point. When an electron tunnels between the lead and QD2, the SEB reaches its ground state again. The difference in E_{el} is then dissipated in the lead by the emission of a phonon, after which the cycle repeats. This leads to an average dissipation per cycle, P_{sis} , which mirrors the myth of Sisyphus.

For a resistor subject to a symmetrized noise spectrum, we can relate resistance and dissipation as: $R_{\text{sis}} = V_{\text{RF}}^2 / P_{\text{sis}}$. We note that this excludes the asymmetry between emission and absorption of bosons resulting from zero-point fluctuations. This implies that the Sisyphus dissipation vanishes at zero temperature. However, the residual rate of spontaneous emission ensures that bosons will continue being emitted at zero temperature [8]. We note that QD devices are typically operated at temperatures of ~ 10 mK, at which the stimulated emission rate is typically vanishing in size for weak coupling of the SEB to the photon bath [9]. For a broader discussion on the relevant impedances of a driven SEB, see Ref. [9]. We note that the authors of Ref. [9] mainly consider relaxation due to photons, yet the concept of Sisyphus dissipation applies broadly across all types of bosons. We neglect the dissipation due to spontaneous emission and write the Sisyphus resistance as [10]:

$$R_{\text{sis}} = \frac{k_B T}{(e\alpha)^2} \frac{1 + \Gamma_0^2/\omega^2}{\Gamma_0} \cosh^2\left(\frac{\mu_2}{2k_B T}\right) \quad (2.8)$$

Where α is the lever arm of the plunger gate and ω is the angular frequency of the AC voltage signal.

We show $1/R_{\text{sis}}$ for varying V_1 and V_2 in Figure 2.3e. We see that R_{sis} is highly gate-dependent, and reaches a minimum at the Coulomb resonance, which corresponds to $\mu_2 = 0$. When $\langle N_1 \rangle$ changes, there is an abrupt change in R_{sis} . If QD2 is embedded in a radio-frequency (RF) reflectometry circuit, this change in resistance can be observed as a dip in reflected signal amplitude [11]. Under suitable conditions, a change in reflected RF amplitude can then be related to a change in $\langle N_1 \rangle$, which allows SEBs to be used as charge sensors. We note that the resistive process described here goes hand-in-hand with a reactive process, resulting in a “tunneling capacitance”. This will affect the phase of the reflected RF signal in addition to the magnitude.

While we consider a system driven by a generic AC voltage, Sisyphus resistance is usually associated with RF reflectometry techniques. Typical lead-QD tunneling rates are on the order of $\sim 10 \mu\text{eV}$, which corresponds to a frequency of $\sim 2.4 \text{ GHz}$. If $f = \omega/2\pi \ll 2.4 \text{ GHz}$, the QD always remains in the ground state, meaning there will be negligible dissipation. SEB charge sensors are a good application when the addition of a drain electrode is not trivial, such as in 1D nanowires. We note that the absence of a DC current implies that SEB charge sensors are not affected by shot noise, unlike their source-drain charge sensor counterparts [12].

2.2 SUB-GAP STATES

In the previous section, we described the properties of quantum dots that arise due to confinement. This section deals with the effects of coupling confined systems to superconductors, which produces bound states within the superconducting energy gap. The emergence of sub-gap states has been derived by numerous physicists in numerous geometries. These include: non-magnetic impurities coupled to superconductors by Machida and Shibata [13], 2D normal metal-superconductor heterostructures by De Gennes and Saint James [14], classical spins coupled to superconductors by Yu, Shiba and Rusinov [15–17], vortices in type-II superconductors by Caroli, De Gennes and Matricon [18] and superconductor-normal-superconductor (SNS) interfaces by Andreev and Kulik [19, 20]. While terminology varies wildly, the physics that unifies these states is quite general. We can coarsely segment sub-gap states in semiconductor-superconductor systems into two types: interacting and non-interacting, which we refer to, for lack of better terms, as Yu-Shiba-Rusinov states and Andreev bound states, respectively.

2.2.1 ANDREEV BOUND STATES

Andreev bound states emerge as a result of Andreev reflection at the interface between a superconductor and a normal metal. An electron in a normal metal, incident on a superconductor cannot enter as there are no single-electronic states within the superconducting gap. To conserve momentum, a Cooper pair is created in the superconductor and a hole is retro-reflected in the normal metal. If the hole approaches a superconductor again, it is retro-reflected as an electron. This repeated process results in a bound state with a single-electron energy below the superconducting gap, which is defined as an Andreev bound state (ABS). These states were first observed in carbon nanotubes with two phase-biased, superconducting leads [21]. All device geometries presented in this thesis involve only semiconductors coupled to a single, grounded superconductor, which excludes a phase

difference.

Most descriptions of sub-gap states start from a superconducting Anderson impurity model. We postpone the discussion of this model to Section 2.2.2, and offer the simplest description of an ABS first. We consider a single electronic orbital in the basis: $|0\rangle, |\downarrow\rangle, |\uparrow\rangle, |2\rangle$. Then, we write the Hamiltonian as:

$$H_{\text{AL}} = \begin{bmatrix} 0 & 0 & 0 & \Gamma \\ 0 & \mu - \frac{E_Z}{2} & 0 & 0 \\ 0 & 0 & \mu + \frac{E_Z}{2} & 0 \\ \Gamma & 0 & 0 & 2\mu + E_C \end{bmatrix} \quad (2.9)$$

Here, μ is the electrochemical potential as defined in Equations (2.3) and (2.4), E_Z is the Zeeman energy, Γ is the coupling to the superconductor and E_C is the charging energy. By including Γ , we couple the 0 and 2 occupancies of the orbital. This can be seen heuristically as the result of Andreev reflection at the superconductor interface. While Γ conserves Fermion parity, it breaks particle conservation. To obtain this Hamiltonian, we have taken the parent gap to be the largest energy scale of the system: ($\Delta \rightarrow \infty$). This approximation is known as the “superconducting atomic limit”, where the proximity effect is parametrized by Γ [22, 23]. We note that equation (2.9) is a many-body Hamiltonian, which is convenient for including interactions such as E_C .

We can diagonalize this Hamiltonian by performing a *Bogoliubov transformation*, where we define new operators:

$$\begin{aligned} \gamma_{\uparrow}^{\dagger} &= u d_{\uparrow}^{\dagger} - v d_{\downarrow} \\ \gamma_{\downarrow}^{\dagger} &= v d_{\uparrow} + u d_{\downarrow}^{\dagger} \end{aligned} \quad (2.10)$$

The excitations described by these operators are defined as “Bogoliubons”. They have the same expression as the single-electronic excitations of a BCS ground state of a bulk superconductor. We find the following eigenstates in the even-parity sector after diagonalization:

$$\begin{aligned} |S_{-}\rangle &= u|0\rangle - v|2\rangle & u^2 &= \frac{1}{2} \left(1 + \frac{\mu + \frac{E_C}{2}}{\sqrt{(\mu + \frac{E_C}{2})^2 + \Gamma^2}} \right) \\ |S_{+}\rangle &= v|0\rangle + u|2\rangle & v^2 &= \frac{1}{2} \left(1 - \frac{\mu + \frac{E_C}{2}}{\sqrt{(\mu + \frac{E_C}{2})^2 + \Gamma^2}} \right) \end{aligned} \quad (2.11)$$

The 0 and 2 charge states hybridize into two singlet states with energies.

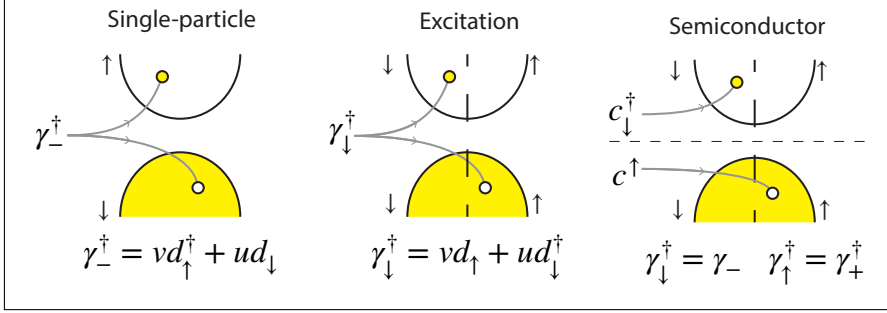
$$E_{\pm} = \frac{E_C}{2} + \mu \pm \sqrt{\left(\mu + \frac{E_C}{2}\right)^2 + \Gamma^2}$$

At the symmetric point ($\mu = -E_C/2$), we have $u^2 = v^2$, which means that the singlet states are a perfect combination of the 0 and 2 charge states. Here, the energy difference between the two singlet states has its minimum at 2Γ .

The odd-parity states, $\{|\downarrow\rangle, |\uparrow\rangle\}$, have energies $E_{\uparrow, \downarrow} = \mu \pm E_Z/2$ and are unaffected by superconductivity in the superconducting atomic limit. The Bogoliubon operators act on

the lower singlet state and describe transitions to the odd states:

$$\gamma_{\uparrow}^{\dagger} |S_{-}\rangle = |\uparrow\rangle \quad \gamma_{\downarrow}^{\dagger} |S_{-}\rangle = |\downarrow\rangle \quad (2.12)$$



This formalism is known as the **excitation picture**, where the lower singlet state is taken as the reference point [24]. Alternatively, we could define other Bogoliubon operators that act on $|\downarrow\rangle$ as a reference state:

$$\gamma_{\downarrow}^{\dagger} |\downarrow\rangle = |S_{-}\rangle \quad \gamma_{+}^{\dagger} |\downarrow\rangle = |S_{+}\rangle$$

This is known as the **single-particle picture**, which defines a filled spin-down band and an empty spin-up band as the vacuum state; $\gamma_{-} |\downarrow\rangle = \gamma_{+} |\downarrow\rangle = 0$ [25]. Here, γ_{-}^{\dagger} creates a quasiparticle at negative energy and γ_{+}^{\dagger} creates one at positive energy. As the vacuum state is not the BCS ground state, we consider the excitation picture as a better description of an ABS. The box at the top of the page provides a schematic comparison of the various pictures. The excitations described by equation (2.12) occur at energies:

$$\begin{aligned} E_{\uparrow}^{\text{ex}} &= E_{\uparrow} - E_{S_{-}} = \frac{E_Z}{2} + \sqrt{\left(\mu + \frac{E_C}{2}\right)^2 + \Gamma^2} - \frac{E_C}{2} \\ E_{\downarrow}^{\text{ex}} &= E_{\downarrow} - E_{S_{+}} = -\frac{E_Z}{2} + \sqrt{\left(\mu + \frac{E_C}{2}\right)^2 + \Gamma^2} - \frac{E_C}{2} \end{aligned} \quad (2.13)$$

We conclude that we started from a many-body Hamiltonian with interactions in equation (2.9) and arrived at a non-interacting Hamiltonian that describes single particle excitations from the singlet ground state:

$$H'_{\text{AL}} = E_{\text{ex}}^{\uparrow} \gamma_{\uparrow}^{\dagger} \gamma_{\uparrow} + E_{\text{ex}}^{\downarrow} \gamma_{\downarrow}^{\dagger} \gamma_{\downarrow} \quad (2.14)$$

We now define $|S\rangle \equiv |S_{-}\rangle$ and will only refer to this state as the singlet. The reason being that the $|S_{+}\rangle$ state is always higher in energy than the $|S_{-}\rangle$ state and does not participate in electron transport as a result.

ANDREEV BOUND STATE TRANSPORT

In tunneling spectroscopy, we observe four sub-gap resonances; at $\pm E_{\uparrow}^{\text{ex}}$ and at $\pm E_{\downarrow}^{\text{ex}}$. For describing electron transport through an ABS, we adopt the **semiconductor picture**. Here

we double the degrees of freedom and rewrite equation (2.14) such that it now has two positive energy and two negative energy excitations:

$$H_{\text{AL}}^{\text{SM}} = \begin{bmatrix} E_{\text{ex}}^{\uparrow} & 0 & 0 & 0 \\ 0 & E_{\text{ex}}^{\downarrow} & 0 & 0 \\ 0 & 0 & -E_{\text{ex}}^{\uparrow} & 0 \\ 0 & 0 & 0 & -E_{\text{ex}}^{\downarrow} \end{bmatrix}$$

We combine this semiconductor picture Hamiltonian with the *Mahaux-Weidenmuller* expression to compose a scattering matrix for a single, normal lead [26]:

$$S = \begin{bmatrix} r_{\text{ee}} & r_{\text{eh}} \\ r_{\text{he}} & r_{\text{hh}} \end{bmatrix} = 1 - 2\pi i W (E - H_{\text{AL}}^{\text{SM}} + i\pi W^{\dagger} W)^{-1} W^{\dagger} \quad (2.15)$$

$$W = t_{\text{lead}} \sqrt{\frac{1}{2\pi}} \begin{bmatrix} u & u & v & v \\ -v & -v & -u & -u \end{bmatrix}^T$$

Where $H'_{\text{AL}} = \text{diag}(E_{\text{ex}}^{\uparrow}, E_{\text{ex}}^{\downarrow}, -E_{\text{ex}}^{\uparrow}, -E_{\text{ex}}^{\downarrow})$. The scattering matrix relates incoming and outgoing modes in the leads: $\psi_{\text{out}} = S\psi_{\text{in}}$. Here, W describes the coupling of the ABS to modes in a single, normal lead in the wide-band limit. t_{lead} parametrizes the lead-ABS coupling, E is the excitation energy and u, v are defined according to Equation (2.11). The system described by this scattering matrix is shown in Figure 2.4a. Here, a normal island is coupled to a normal lead (yellow) and a superconducting lead (blue). Figure 2.4b shows the ground state of the ABS for varying μ and Γ . Because of the characteristic shape, this phase diagram is known as “the dome”. When the island-superconductor coupling is weak, the system can be in either a singlet or a doublet ground state, depending on μ . In the limit $\Gamma \rightarrow 0$, the 0 and 2 occupations are not coupled, and the system is effectively a quantum dot.

We show the ABS spectrum for $\Gamma = 0.15E_C$ in Figure 2.4c. Here, we compute the Andreev reflection rate, $|r_{\text{eh}}|^2$, for varying μ at each excitation energy, E . We see that the ABS crosses zero-energy, resulting in a characteristic “eye-shape”. Note that there is only a single, normal lead in the system, making Andreev reflection the only possible transport process. $|r_{\text{eh}}|^2$ vanishes at large $|\mu|$, which is explained by the u and v components of the singlet. In a single Andreev reflection process, an electron tunnels into the ABS with an amplitude u , while a hole tunnels out with an amplitude v . The combined amplitude of this process therefore scales with the product uv . The u and v components corresponding to Figure 2.4c are shown in panel f. We see that u and v change sharply when they cross over. The product uv is only finite around $-\mu = E_C/2$, meaning that the Andreev reflection rate is negligible elsewhere.

Figure 2.4d shows the spectrum for $\Gamma = E_C/2$. Here, the ABS has a single zero crossing at $-\mu = E_C/2$. From Figure 2.4g, we note that u and v change less sharply, allowing Andreev reflection over a larger range of μ . Figure 2.4e shows the spectrum for $\Gamma = E_C$. The ABS is now always in the even ground state, as the energy of the singlet state is significantly lowered by coupling to the superconductor. Figure 2.4h shows that u and v are both finite over the entire range of μ . In some semiconductor-superconductor devices, Γ can be changed directly by a tunnel gate, meaning that any point in the phase diagram can be accessed.

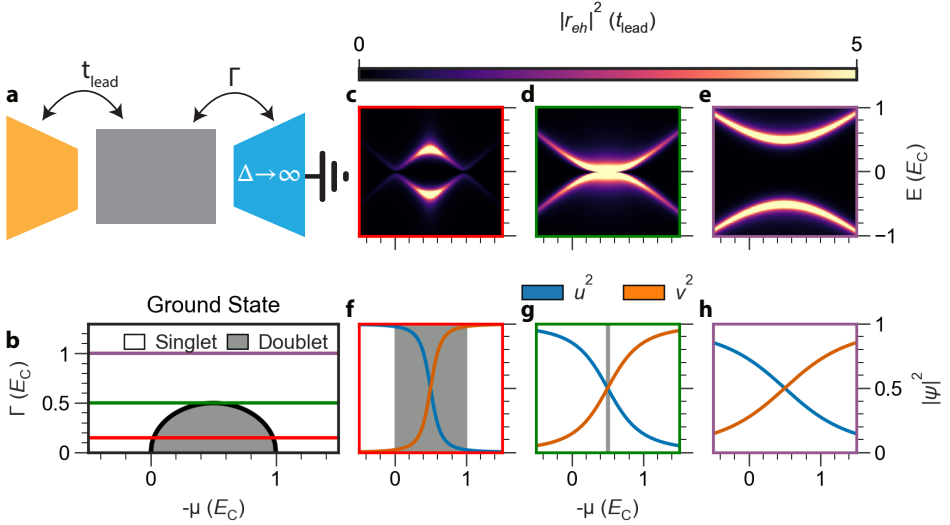


Figure 2.4: **Superconducting atomic limit transport and ground states** **a.** Schematic overview of the model, showing a normal lead (yellow) tunnel-coupled to an island (gray) with a coupling, t_{lead} . A grounded, superconducting lead (blue) with an infinite superconducting gap Δ is coupled to the conductor with a tunnel coupling Γ . **b.** The ground state of the island for varying Γ and electrochemical potential of the ABS, μ . The system can have an even, singlet ground state, or an odd, doublet ground state. **c-e.** Andreev reflection rate, $|r_{eh}|^2$, for varying μ and excitation energy, E . These are evaluated for different values of Γ , indicated by the colored horizontal lines in panel b. **f-h.** Wave functions components of the singlet, u^2 and v^2 , for varying μ . These are evaluated for different values of Γ , indicated by the colored horizontal lines in panel b. All calculations are performed for $t_{\text{lead}} = E_C/40$. The gray shading indicates the μ values for which the system has a doublet ground state, and the singlet is the excited state.

We conclude that the superconducting atomic limit provides a compact description of ABSs that can be utilized for calculating transport properties and composing phase diagrams. Note that we described Andreev bound states as non-interacting earlier, while we did add a charging energy term in this section. For a small E_C compared to the parent gap, Δ , this is justified. If Δ is not significantly larger, the atomic limit is not justified, and more complicated models are needed, such as the Anderson model. Note that we have completely omitted the states of the parent superconductor in Equation (2.9). This is a reasonable approximation when Δ is very large compared to E_C and quasiparticle occupation of the parent superconductor is too energetically expensive to consider. In realistic devices, E_C/Δ can become non-negligible, forcing us to consider the states of the superconductor explicitly. Because this breaks down the superconducting atomic limit, we have to start from a strongly interacting system.

2.2.2 SUPERCONDUCTING ANDERSON IMPURITY MODEL

While superconductivity stimulates the pairing of electrons, Coulomb repulsion quenches it, as phase and charge are conjugated variables $[N, \phi] = -2i$ [1]. This trade-off is captured well by the superconducting Anderson impurity model which describes a quantum dot

coupled to a superconductor [27]:

$$H = H_{\text{QD}} + H_{\text{T}} + H_{\text{SC}} \quad (2.16)$$

Here, H_{QD} describes a single orbital of a QD:

$$H_{\text{QD}} = \sum_{\sigma} \mu d_{\sigma}^{\dagger} d_{\sigma} + E_{\text{C}} d_{\downarrow}^{\dagger} d_{\downarrow} d_{\uparrow}^{\dagger} d_{\uparrow} + \frac{E_{\text{Z}}}{2} (d_{\uparrow}^{\dagger} d_{\uparrow} - d_{\downarrow}^{\dagger} d_{\downarrow}) \quad (2.17)$$

Where E_{Z} is the Zeeman energy, μ the electrochemical potential and E_{C} is the charging energy. Note that this is identical to the Hamiltonian defined in Equation (2.9), minus the term coupling the 0 and 2 occupations. The Hamiltonian of the superconductor is given by:

$$H_{\text{SC}} = \sum_{k\sigma} \xi_k c_{k\sigma}^{\dagger} c_{k\sigma} - \Delta \sum_k (c_{k\uparrow}^{\dagger} c_{-k\downarrow}^{\dagger} + \text{h.c.}) \quad (2.18)$$

Where ξ_k is the single-electronic energy at momentum k and Δ is the s-wave superconducting gap, which is taken to be real, constant and not affected by the quantum dot. We assume that the superconductor has a negligible Zeeman energy compared to the QD. The superconductor and semiconductor are coupled by:

$$H_{\text{T}} = t \sum_{k\sigma} (c_{k\sigma}^{\dagger} d_{\sigma} + \text{h.c.}) \quad (2.19)$$

Where H_{T} conserves spin and is parametrized by t . While the superconducting Anderson model is powerful enough to explain many phenomena of impurities coupled to superconductors, it is not analytically solvable. It is common to limit the sum over k in Equation (2.18) to a bandwidth given by the Debye frequency ω_{D} . Yet the simplest way to make Equation (2.16) exactly solvable, is to replace the sum over k by a single superconducting orbital. This is referred to as the “zero-bandwidth limit” and the resulting Hamiltonian of the superconductor is given by [28, 29]:

$$H_{\text{SC}}^0 = \sum_{\sigma} \xi c_{\sigma}^{\dagger} c_{\sigma} - \Delta (c_{\uparrow}^{\dagger} c_{\downarrow}^{\dagger} + \text{h.c.}) \quad (2.20)$$

We can then rewrite Equation (2.16) as:

$$H_{\text{ZBW}} = H_{\text{QD}} + H_{\text{T}} + H_{\text{SC}}^0 \quad (2.21)$$

Which is a 16 by 16 Hamiltonian, composed of the number states of the QD and the superconducting orbital. We will apply perturbation theory to reduce the basis and obtain a more intuitive picture of the states described by this Hamiltonian. First, we diagonalize H_{SC}^0 with a Bogoliubov transformation and write:

$$H_{\text{B}}^0 = \xi - \sqrt{\xi^2 + \Delta^2} + \sum_{\sigma} \sqrt{\xi^2 + \Delta^2} \gamma_{\sigma}^{\dagger} \gamma_{\sigma} \quad (2.22)$$

in the basis $\{|S_{-}\rangle, |\downarrow\rangle, |\uparrow\rangle, |S_{+}\rangle\}$. Where the Bogoliubov operators are defined according to Equation (2.10). We note that this Hamiltonian is identical to the excitation picture

of an ABS in the superconducting atomic limit, without Zeeman or charging energy, as defined in equation (2.12). This similarity is artificial, as we have created a discrete state in equation (2.22) by discarding all metallic orbitals but one. This is comparable to stating that a single orbital in a metal resembles the Hamiltonian of a QD without charging or Zeeman energy. Nevertheless, equation (2.22) has been used successfully in literature to describe ABSs in SNS devices [30]. Furthermore, equation (2.21) is a good approximation of a QD coupled to a single ABS, as seen in chapter 5.

We now fix the single-electronic level of the superconductor at the Fermi level ($\xi = 0$) and write:

$$H_{SC}^B \equiv H_B^0|_{\xi=0} = \begin{bmatrix} -\Delta & 0 & 0 & 0 \\ 0 & 0 & 0 & 0 \\ 0 & 0 & 0 & 0 \\ 0 & 0 & 0 & \Delta \end{bmatrix} \quad (2.23)$$

We now rewrite the Hamiltonian that couples the superconductor to the quantum dot to account for the Bogoliubon basis:

$$H_T^B = \frac{t}{\sqrt{2}} \left(d_{\downarrow}^{\dagger}(\gamma_{\downarrow} + \gamma_{\uparrow}^{\dagger}) + d_{\uparrow}^{\dagger}(\gamma_{\uparrow} - \gamma_{\downarrow}^{\dagger}) + \text{h.c.} \right) \quad (2.24)$$

And write the perturbed Hamiltonian, H_P , as:

$$H_P = H_{QD} + H_T^B + H_{SC}^B \quad (2.25)$$

Where the unperturbed part, $H_{QD} + H_{SC}^B$, is diagonal, and we consider H_T^B as a perturbation parametrized by the superconductor-semiconductor coupling, t . We partition the Hamiltonian into low-, and high-energy subspaces. Then, we integrate out the high-energy states of Equation (2.25) using the `pymablock` package [31]. This procedure is closely related to Schrieffer-Wolff transformations or Löwdin partitioning.

BCS SINGLET STATES

In section 2.2.1, we only considered the states of the QD, and neglected the state of the superconductor. We now aim to obtain the same Hamiltonian, while including states of the superconductor. We consider a single orbital in a QD, coupled using spin-conserving tunneling to a single orbital in a superconductor (equation (2.21)). We write the combined states of the QD and superconductor in the basis $|N_{QD}, N_{SC}\rangle$, where the superconductor states are written in the Bogoliubov basis: $\{|S_{-}\rangle, |\downarrow\rangle, |\uparrow\rangle, |S_{+}\rangle\}$. We include the full system when noting fermion parity, as opposed to only the QD states. First, we will consider the superconducting atomic limit, where $\Delta \gg E_C, t$. This allows us to compare our results directly with the superconducting atomic limit expression detailed in section 2.2.1. For large Δ , quasiparticle occupation of the superconductor is energetically expensive, so we exclude the states in which a single quasiparticle occupies the superconductor:

$$|\downarrow, \uparrow\rangle, |\uparrow, \downarrow\rangle, |\uparrow, \uparrow\rangle, |\downarrow, \downarrow\rangle \quad \text{even} \quad (2.26)$$

$$|0, \uparrow\rangle, |0, \downarrow\rangle, |2, \uparrow\rangle, |2, \downarrow\rangle \quad \text{odd} \quad (2.27)$$

We also exclude all the states involving the high-energy singlet $|S_+\rangle$ for the superconducting orbital, as they are $\sim 2\Delta$ higher in energy than the $|S\rangle$ state:

$$|0, S_+\rangle, |2, S_+\rangle \quad \text{even} \quad (2.28)$$

$$|\downarrow, S_+\rangle, |\uparrow, S_+\rangle \quad \text{odd} \quad (2.29)$$

This reduces our even-parity basis to only the $|0, S\rangle$ and $|2, S\rangle$ states, where the QD is empty or doubly-occupied and the superconductor is in the lowest-energy singlet state. Then, we find second order corrections in t and write down the effective Hamiltonian as:

$$H_{\text{AL}}^{\text{P}} = \begin{bmatrix} -\Delta + \frac{t^2}{-\Delta - \mu} & \Gamma \\ \Gamma & E_C - \Delta + 2\mu + \frac{t^2}{E_C - \Delta + \mu} \end{bmatrix} \quad (2.30)$$

$$\Gamma \equiv \frac{t^2 \left(\frac{E_C}{2} - \Delta \right)}{(\Delta + \mu)(E_C - \Delta + \mu)}$$

Here, Γ is an effective coupling between the 0 and 2 occupations of the QD, arising from virtual processes involving higher-energy states. For $\Delta \rightarrow \infty$ we obtain $\Gamma_{\text{AL}} \approx t^2/\Delta$ in leading order, which is a well-known result for the superconducting atomic limit [22, 23]. In Figure 2.5a, we compare the eigenstates of equation (2.30) with the results found in literature, as discussed in section 2.2.1. Figure 2.5a shows the wave function amplitudes of

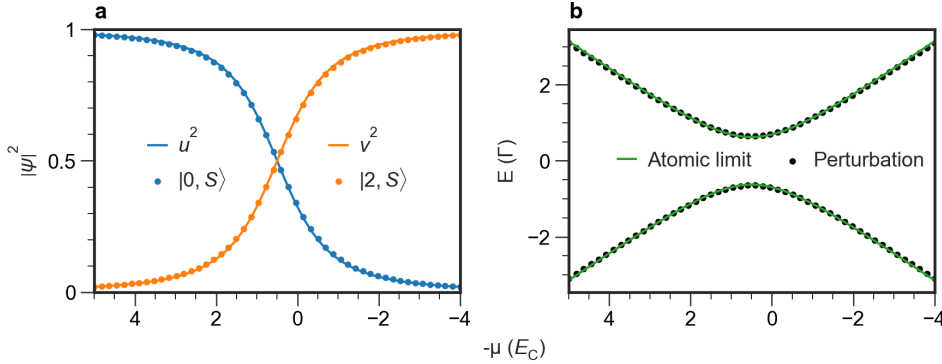


Figure 2.5: **Perturbative zero-bandwidth model eigenstates and excitation energies for large Δ .** The calculations were performed for $E_C = 0.1t$, $\Delta = 7.5t$. **a.** Wave function amplitudes of the singlet ground state for varying μ . The markers indicate the probability amplitudes of the $|0, S\rangle$ and $|2, S\rangle$ states found from perturbation theory. The lines show the BCS coefficients of the singlet state, as found from the superconducting atomic limit. **b.** Excitation energies of the lowest-energy even state to the lowest-energy odd state of the ABS. The markers indicate the energy difference between the lowest-energy even and odd-parity eigenstates found from perturbation theory. The lines show the excitation energy found from the superconducting atomic limit as defined in Equation (2.13).

the $|0, S\rangle$ and $|2, S\rangle$ states. The solid lines show u^2 and v^2 calculated from Equation (2.11) using the same parameters as the perturbative result, with $\Gamma_{\text{AL}} \approx t^2/\Delta$. We see that the agreement between the present result and the analytic expression for the superconducting atomic limit is excellent. Deviations are negligible for $E_C/2 \ll \Delta$, beyond which higher-order terms become relevant. To find the excitation energies, we first find the energies

of the $|\uparrow, S\rangle$ and $|\downarrow, S\rangle$ states. We diagonalize the odd-parity Hamiltonian, which includes corrections up to second order in t :

$$H_{\text{odd}} = \begin{bmatrix} -\Delta + \mu + \frac{t^2}{2(-E_C - \Delta - \mu)} + \frac{t^2}{2(-\Delta + \mu)} + \frac{E_Z}{2} & 0 \\ 0 & -\Delta + \mu + \frac{t^2}{2(-E_C - \Delta - \mu)} + \frac{t^2}{2(-\Delta + \mu)} - \frac{E_Z}{2} \end{bmatrix} \quad (2.31)$$

Where we set $E_Z = 0$ in the absence of an external magnetic field. Figure 2.5b shows the difference between the lowest-energy even and odd states. We conclude that we can reproduce the superconducting atomic limit results for an ABS using second order perturbation theory, starting from a zero-bandwidth Hamiltonian.

We have only considered eigenstates where the superconductor is in the singlet state. This is justified when Δ is the largest energy scale in the system, as the odd-occupancy states of the superconductor are Δ higher in energy than the singlet state. The solutions are only valid in the interval $-\Delta + E_C < \mu < \Delta - E_C$, as the denominators of the even and odd Hamiltonians will diverge otherwise. In the superconducting atomic limit, the excitation energy grows perpetually with increasing μ . This is a result of excluding states where a quasiparticle occupies the superconductor, which typically bound the energy of sub-gap states. By comparing the perturbation theory result with the superconducting atomic limit in equation (2.30), we have validated our model with a result that is known from literature in the limit $\Delta \gg E_C, t$. However, E_C and t can be non-negligible for realistic semiconductor-superconductor devices. When we introduce strong interactions on the QD ($E_C \sim \Delta$), we need to enlarge the basis to include quasiparticle occupation of the superconductor. Before studying this intermediate limit, we first consider the case $E_C \gg \Delta$.

2.2.3 YU-SHIBA-RUSINOV STATES

The superconducting atomic limit can be seen as a limiting case of a superconducting Anderson impurity model, where $\Delta \rightarrow \infty$. Yu, Shiba and Rusinov derived the emergence of sub-gap states in the opposite limit, where $E_C \rightarrow \infty$ [15–17]. To do so, they started from the s-d model, which was first used to propose the double-exchange mechanism of ferromagnetism [32]. Here, an impurity is tunnel-, and exchange-coupled to conduction band electrons in a metal. This can famously lead to an electron cloud in the metal that screens the impurity spin, known as the Kondo effect. If the metal becomes a superconductor, the magnetic impurity causes local Cooper pair breaking. A Yu-Shiba-Rusinov (YSR) state arises due to this interplay between a localized spin and superconductivity. We now explicitly write down the state of the superconductor in addition to the impurity in the basis $|N_{\text{impurity}}, N_{\text{SC}}\rangle$. The even state consists of an exchange singlet/triplet formed between an electron in the impurity and a quasiparticle in the superconductor: $|\downarrow, \uparrow\rangle \pm |\uparrow, \downarrow\rangle$. The odd state is a superposition of a single electron in the impurity and a single quasiparticle in the superconductor: $|\downarrow, S\rangle - |0, \downarrow\rangle$. The energy cost of exciting a quasiparticle in a superconductor is roughly Δ (see Equation (2.23)). In the superconducting atomic limit, this cost is taken to be infinite, meaning we do not consider the quasiparticle occupation of the superconductor. For YSR states, this approximation breaks down.

While originally derived for classical spins in superconductors, YSR states have been identified in ferromagnetic atoms on superconducting substrates [33], and quantum dots coupled to superconductors as well [34]. Because ABSs were already strongly associated

with low-dimensional semiconductors coupled to superconductors, the question arose as to their distinction. To obtain a state that is as different as possible from the ABSs shown in the previous section, we use perturbation theory to find Hamiltonians for sub-gap states in the limit $E_C \gg \Delta$. We note that a defining characteristic of YSR states is the existence of a superconducting, metallic screening cloud, which is not captured by the zero-bandwidth model. However, we can reproduce other signatures of YSR states by replacing this continuum of states with a single, superconducting orbital. Notably, the zero-bandwidth model predicts the formation of a singlet state with quasiparticle occupation of the superconductor. We shall refer to these as zero-bandwidth YSR (ZBW-YSR) states to distinguish them from the actual YSR states.

ZERO-BANDWIDTH YU-SHIBA-RUSINOV STATES

Starting from the full, 16×16 zero-bandwidth Hamiltonian of Equation (2.25), we will now derive a smaller Hamiltonian that captures the formation of ZBW-YSR states in the limit $E_C \gg \Delta, t$. The Hamiltonian conserves spin, and we limit ourselves to zero magnetic field. We first exclude the states from our basis where the spins of the QD and the superconducting orbital are aligned:

$$|\uparrow, \uparrow\rangle, |\downarrow, \downarrow\rangle$$

As before, we exclude all the states involving the high-energy $|S_+\rangle$ state for the superconducting orbital. Finally, we limit ourselves to $\mu \approx -E_C/2$, where the QD is at half-occupancy (i.e. in the middle of the dome shown in figure 2.4). The 0 and 2 occupations of the QD are then $E_C/2$ higher in energy than the 1 occupation, so we exclude the following states:

$$|\downarrow, \uparrow\rangle, |\uparrow, \downarrow\rangle \quad \text{even} \quad (2.32)$$

$$|0, \uparrow\rangle, |0, \downarrow\rangle, |2, \uparrow\rangle, |2, \downarrow\rangle \quad \text{odd} \quad (2.33)$$

We indicate these states in the higher energy subspace in figure 2.6a. For the low energy subspace, we consider states where the QD and superconductor spins are anti-parallel: $\{|\uparrow, \downarrow\rangle, |\downarrow, \uparrow\rangle\}$. We then write the Hamiltonian of the even-parity states that includes first and second order perturbations in t , and expand it around $\mu = -E_C/2$ to first order in μ :

$$H_{\text{YSR}}^E = \begin{bmatrix} \mu - J & J \\ J & \mu - J \end{bmatrix} \quad (2.34)$$

$$J \equiv \frac{4E_C t^2}{E_C^2 - 4\Delta^2}$$

Here, J is an effective exchange term that arises from virtual coupling through higher-energy states. It reduces to $(J = 4t^2/E_C)$ for $\Delta/E_C \rightarrow 0$, which is identical to the exchange constant of tunnel-coupled double quantum dots [35]. Diagonalizing the Hamiltonian yields two exchange-coupled states:

$$\begin{aligned} S(1, 1) &= \frac{1}{\sqrt{2}}(|\downarrow, \uparrow\rangle - |\uparrow, \downarrow\rangle) & E_S &= \mu - 2J \\ T_0(1, 1) &= \frac{1}{\sqrt{2}}(|\downarrow, \uparrow\rangle + |\uparrow, \downarrow\rangle) & E_T &= \mu \end{aligned} \quad (2.35)$$

These are the even-parity ZBW-YSR states, where an electron in the QD and a quasiparticle in the superconductor form a singlet or triplet state, respectively. We can see that the lowest-energy state is a singlet for $J > 0$ and a triplet for $J < 0$. At finite magnetic field, both the spins in the QD and the superconductor Zeeman-split. If the g -factors of the two are equal, the energy of the $S(1, 1)$ and $T_0(1, 1)$ states does not change. While comparable g -factors have been observed in Ge/SiGe QDs coupled to germanosilicide superconductors, this is not commonly the case [36]. In III-V semiconductors coupled to Al, the large g -factor difference creates an energy difference of $E_Z^{\text{QD}} - E_Z^{\text{SC}}$ between the $|\downarrow, \uparrow\rangle$ and $|\uparrow, \downarrow\rangle$. This makes the $|0, S\rangle$ and $|2, S\rangle$ states energetically favorable.

For the odd states, we limit the basis to the $|\downarrow, S\rangle$, $|\uparrow, S\rangle$ states and use the Hamiltonian defined in equation (2.31). Then, we diagonalize the even and odd parity Hamiltonians to obtain the eigenstates and eigenenergies. We calculate the excitation energies by subtracting the lowest-energy even and odd states.

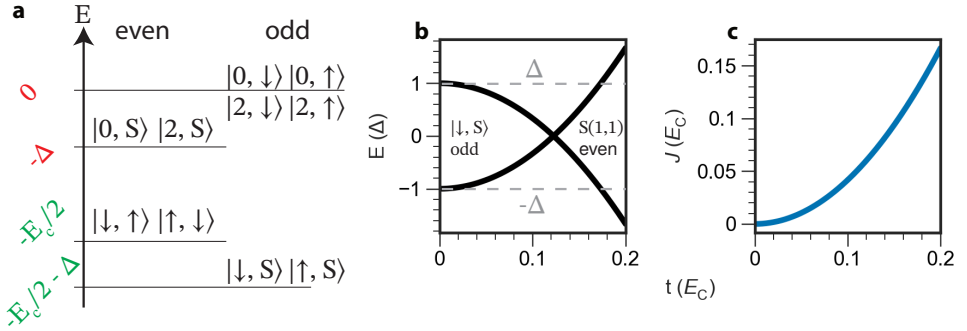


Figure 2.6: **Zero-bandwidth Yu-Shiba-Rusinov states in the large E_C limit.** The calculations were performed for $E_C = 10\Delta$ and $\mu = -E_C/2$, in the absence of an external magnetic field. **a.** Schematic diagram of the unperturbed states of the zero-bandwidth Hamiltonian at $\mu = -E_C/2$. Red (green) numbers indicate energies of the high (low) energy subspace. **b.** Excitation energies of the lowest-energy state for varying tunnel-coupling, t . The lines indicate the energy difference between the lowest-energy even and odd-parity eigenstates found from perturbation theory. The dashed, gray lines indicate the energy of the parent gap. The superimposed text indicates the ground state (parity). **c.** The effective exchange coupling, J , for varying t .

We show the excitation energy at $\mu = -E_C/2$ in Figure 2.6b for varying t . When $t = 0$, the superconductor and QD are decoupled, the ground state is $|\downarrow, S\rangle$ and the lowest excitation is at $E = \Delta$. When t increases, the energy of the even state is lowered, resulting in a sub-gap state. At $t \approx 0.15 E_C$, a phase transition occurs and the ZBW singlet, $S(1, 1)$, becomes the ground state. For ABSs, Andreev reflection couples the even states and results in a BCS singlet $u|0\rangle - v|2\rangle$. For YSR states, the formation of the screening cloud in a superconductor around an impurity results in an even-parity screened state. The mechanism is comparable to the Kondo effect, as it is an exchange process that lowers the energy of the bound state [37]. We conclude that a BCS singlet is not strictly necessary for the emergence of sub-gap states.

In Figure 2.6c we show the effective exchange coupling, J , for varying t . This exchange effectively flips the QD spin and couples the $|\uparrow, \downarrow\rangle, |\downarrow, \uparrow\rangle$ states. This is comparable to the spin of an impurity flipping due to scattering with conduction band electrons in the metal. J increases parabolically in t and is positive for $E_C > 2\Delta$, resulting in opposite spins for the

lowest-energy state. We note that the ZBW-YSR states closely resemble those found in two-electron double QDs [2]. We have purposefully labeled the exchange singlet and triplet states with $S(1, 1)$ and $T_0(1, 1)$ to make the analogy with double QDs. A major difference is the broken particle conservation in ZBW-YSR states, as the 0 and 2 occupations of the superconductor are coupled through Δ . Furthermore, the charging energy of most superconductors in hybrid systems is significantly lower than for QDs. In addition, the electrochemical potential is fixed for grounded superconductors. Despite these differences, certain concepts can carry over between ZBW-YSR states and double QDs. It might, for example, be possible to encode quantum information in the spin degree of freedom of quasiparticle states in a superconductor (see section 7.5).

We have used perturbation theory on the ZBW model to derive an effective model that captures a number of basic phenomena of YSR states, including exchange coupling and sub-gap excitation energies. A more accurate system description requires more superconducting orbitals, and different methods such as density matrix renormalization group. Also, we limited ourselves to the regime $E_C \gg \Delta, t$ to obtain eigenstates that are maximally different from the ones presented in Section 2.2.1. In realistic semiconductor-superconductor devices, the magnitude of Δ , t and E_C can become comparable. The distinction between YSR states and ABSs fades in those regimes, requiring a more complicated system description.

2.2.4 ANDREEV BOUND STATE YU-SHIBA-RUSINOV CROSSOVER

The states presented in Sections 2.2.1 and 2.2.3 have predictive value in certain regimes, but are both unphysical. The superconducting atomic limit finds a BCS singlet composed of the $|0, S\rangle$ and $|2, S\rangle$ states, mediated by virtual coupling through the $|\downarrow, \uparrow\rangle$ and $|\uparrow, \downarrow\rangle$ states. Conversely, the $E_C \rightarrow \infty$ limit finds a ZBW singlet composed of the $|\downarrow, \uparrow\rangle$ and $|\uparrow, \downarrow\rangle$ states, mediated by virtual coupling through the $|0, S\rangle$ and $|2, S\rangle$ states. While our discussion is limited by the approximations of the zero-bandwidth model, we will now look for an intermediate regime that might generalize to a crossover between ABSs and YSR states.

For $\Delta = E_C/2$, all the even parity states in figure 2.6a become degenerate at $\mu = -E_C/2$, meaning that we cannot partition them into low-, and high-energy subspaces anymore. We now include all the even states of figure 2.6a in our basis: $\{|0, S\rangle, |2, S\rangle, |\uparrow, \downarrow\rangle, |\downarrow, \uparrow\rangle\}$ and write down the Hamiltonian with perturbations up to second order in t .

$$H_E = \begin{bmatrix} -\Delta & 0 & -\frac{\sqrt{2}t}{2} & -\frac{\sqrt{2}t}{2} \\ 0 & E_C - \Delta + 2\mu & \frac{\sqrt{2}t}{2} & \frac{\sqrt{2}t}{2} \\ -\frac{\sqrt{2}t}{2} & \frac{\sqrt{2}t}{2} & \mu - J & J \\ -\frac{\sqrt{2}t}{2} & \frac{\sqrt{2}t}{2} & J & \mu - J \end{bmatrix} \quad (2.36)$$

$$J \equiv \frac{t^2 \left(\frac{E_C}{2} + \Delta \right)}{(\Delta - \mu)(E_C + \Delta + \mu)}$$

Here, J is an effective coupling between the $|\uparrow, \downarrow\rangle$ and $|\downarrow, \uparrow\rangle$ states, comparable to the term in Equation (2.34). We can perform a basis rotation of these states to further simplify the

Hamiltonian:

$$H'_E = U H_E U^\dagger = \begin{bmatrix} -\Delta & 0 & -t & 0 \\ 0 & U - \Delta + 2\mu & t & 0 \\ -t & t & -2J + \mu & 0 \\ 0 & 0 & 0 & \mu \end{bmatrix} \quad (2.37)$$

$$U \equiv \begin{bmatrix} 1 & 0 & 0 & 0 \\ 0 & 1 & 0 & 0 \\ 0 & 0 & \frac{\sqrt{2}}{2} & -\frac{\sqrt{2}}{2} \\ 0 & 0 & \frac{\sqrt{2}}{2} & \frac{\sqrt{2}}{2} \end{bmatrix}$$

Where the new basis is:

$$\begin{aligned} &|0, S\rangle \\ &|2, S\rangle \\ &S(1, 1) = \frac{1}{\sqrt{2}}(|\downarrow, \uparrow\rangle - |\uparrow, \downarrow\rangle) \\ &T_0(1, 1) = \frac{1}{\sqrt{2}}(|\downarrow, \uparrow\rangle + |\uparrow, \downarrow\rangle) \end{aligned} \quad (2.38)$$

We see that the $|0, S\rangle$ and $|2, S\rangle$ states are indirectly coupled through the $S(1, 1)$ state. The $T_0(1, 1)$ state is not coupled to any of the other states.

We now include all the odd states of figure 2.6a in the basis: $\{|\downarrow, S\rangle, |0, \downarrow\rangle, |2, \downarrow\rangle\}$. For clarity, we do not write the \uparrow states, as they are degenerate and completely decoupled from the \downarrow states, as the Hamiltonian conserves spin. We include perturbations in t up to first order and write the odd-parity Hamiltonian as:

$$H_O = \begin{bmatrix} -\Delta + \mu & \frac{\sqrt{2}t}{2} & -\frac{\sqrt{2}t}{2} \\ \frac{\sqrt{2}t}{2} & 0 & 0 \\ -\frac{\sqrt{2}t}{2} & 0 & E_C + 2\mu \end{bmatrix} \quad (2.39)$$

We see that the $|0, \downarrow\rangle$, $|2, \downarrow\rangle$ states are indirectly coupled through the $|\downarrow, S\rangle$ state. This implies that the odd ground state will be a superposition of single-spins in the QD and quasiparticles in the superconductor. We can then compute the spectrum and eigenstates of the even-, and odd-parity states. Figure 2.7a shows the excitation energy calculated from the lowest eigenenergies of the even-, and odd-parity Hamiltonians. We see a sub-gap state that crosses zero-energy, resulting in a characteristic eye-shape. Figure 2.7b shows the wave function components of the even-parity ground state, where we have omitted the $T_0(1, 1)$ state which is never occupied. The BCS singlet components, $|0, S\rangle$ and $|2, S\rangle$, cross-over at $\mu = -E_C/2$, which is consistent with the superconducting atomic limit description of ABSs. However, the $S(1, 1)$ component of the wave function also increases at $\mu = -E_C/2$, resulting in a nearly-perfect combination of ZBW and BCS singlet components. We have manually chosen the parameters of E_C , t , and Δ to find this ground state with nearly equal $|0, S\rangle$, $|2, S\rangle$ and $S(1, 1)$ components. We present this state as an illustration of the crossover between ABSs and YSR states, which we will discuss in more detail in the following section.

Figure 2.7c shows the wave function components of the odd-parity ground state. Here, the $|0, \downarrow\rangle$, $|2, \downarrow\rangle$ states have finite weight for all values of μ . This indicates that the single spin is delocalized between the QD and the superconducting orbital.

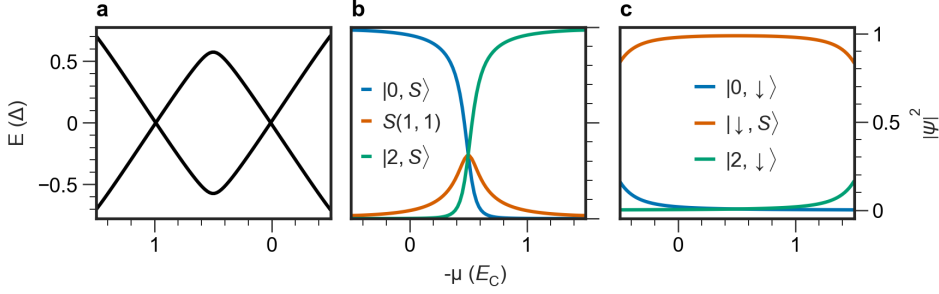


Figure 2.7: **Zero-bandwidth states in the ABS-YSR crossover regime.** The calculations were performed for $E_C = 7.5t$, and $\Delta = 5t$. **a.** Excitation energy for varying μ . **b.** Wave function amplitudes of the lowest-energy even state for varying μ . **c.** Wave function amplitudes of the lowest-energy odd state for varying μ .

ABS-YSR PHASE DIAGRAM FOR THE ZERO-BANDWIDTH MODEL

The combination of E_C , t and Δ in Figure 2.7 was chosen to find a cross-over state, which has properties belonging both to ABSs and YSR states. We can write down the state as: $|e\rangle = u|0, S\rangle + v|2, S\rangle - w|S(1, 1)\rangle$. It has the co-existence of BCS singlet correlations (0 and 2) and ZBW singlet correlations (\uparrow, \downarrow and \downarrow, \uparrow). To find the crossover between ABSs and YSR states, we can quantify these properties in a phase diagram. Figure 2.8a shows BCS

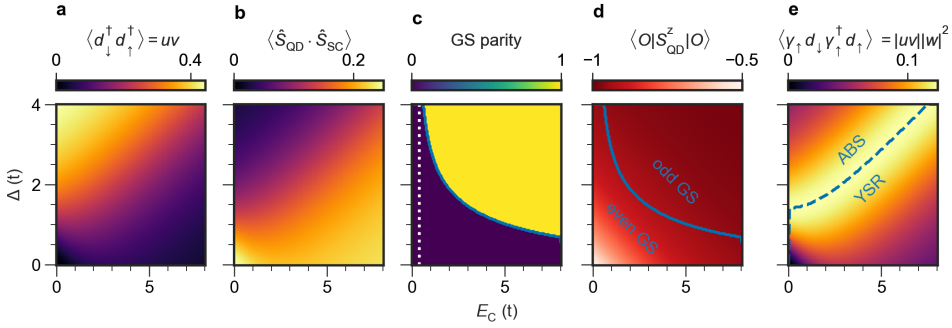


Figure 2.8: **ABS-YSR phase diagram for varying E_C and Δ .** The calculations were performed for $\mu = -E_C/2$, where the QD is at half-occupancy. **a.** BCS correlations of the lowest-energy even state, $\langle d_{\downarrow}^{\dagger} d_{\uparrow}^{\dagger} \rangle$, for varying E_C and Δ . **b.** Exchange coupling of the lowest-energy even state, $\langle \hat{S}_{QD} \cdot \hat{S}_{SC} \rangle$, for varying E_C and Δ . **c.** Ground state parity for varying E_C and Δ , where the blue line indicates the boundary between the even and odd ground states. The white dotted line indicates $E_C = 2\pi t^2$. **d.** Spin expectation value of the QD for the lowest-energy odd state, $\langle \sigma_{QD}^z \rangle$, for varying E_C and Δ . The blue line of panel c is included to indicate the ground state parity. **e.** Co-existence of BCS and exchange singlet correlations of the lowest-energy even state, $\langle \gamma_{\uparrow} d_{\downarrow} \gamma_{\uparrow}^{\dagger} d_{\uparrow}^{\dagger} + \text{h.c.} \rangle$, for varying E_C and Δ . The blue, dashed line indicates the values of E_C and Δ for which the combined BCS and exchange singlet correlations are largest.

correlations of the lowest-energy even state on the QD, defined as $\langle d_{\downarrow}^{\dagger} d_{\uparrow}^{\dagger} + \text{h.c.} \rangle$. We see that the BCS correlations are largest when Δ is greater than E_C . This is consistent with an Andreev bound state, which has weak interactions and a BCS singlet ground state.

Figure 2.8b shows the exchange coupling between the QD and the superconductor of the even state. The exchange term is largest when E_C is greater than Δ , which is consistent with an interacting YSR state where an electron in the QD and a quasiparticle in the superconductor form a singlet. Figure 2.8c shows the ground state parity of the system, where 0 denotes even and 1 denotes odd. We see that the phase boundary approaches $E_C = 2\pi t^2$ asymptotically, which is indicated by the white, dotted line. This value is known for the $\Delta \rightarrow \infty$ limit, and similar phase diagrams can be found in Fig. 3 of [29] and Fig. 9 of [28]. We note that the phase boundary behaves asymptotically for $E_C \rightarrow \infty$ as well, which is different from the aforementioned references. We attribute this difference to our usage of perturbation theory, which breaks down when $\Delta \approx t$, as in the bottom right corner of figure 2.8c. Figure 2.8d shows the spin expectation value of the lowest-energy odd state on the quantum dot, $\langle S_{\text{QD}}^z \rangle$. For low Δ/t and E_C/t , $\langle S_{\text{QD}}^z \rangle$ decreases up to a minimum of $-1/2$. Here, the spin is perfectly shared between the QD and the superconductor. Figure 2.8e quantifies the co-existence of the BCS and ZBW singlets, given by $\langle \gamma_1 d_{\downarrow} \gamma_1^\dagger d_{\uparrow} + \text{h.c.} \rangle$. This term is a product of all the wave function components of the lowest-energy even state, uvw , and is largest for the values of E_C and Δ that lie on the blue dashed line. At low t/Δ , this line roughly follows $E_C = 2\Delta$. The crossover term decreases when E_C becomes larger, as the state gradually evolves into a pure exchange singlet, associated with a ZBW-YSR state. This term also decreases for increasing Δ as the state becomes a pure BCS singlet associated with an ABS.

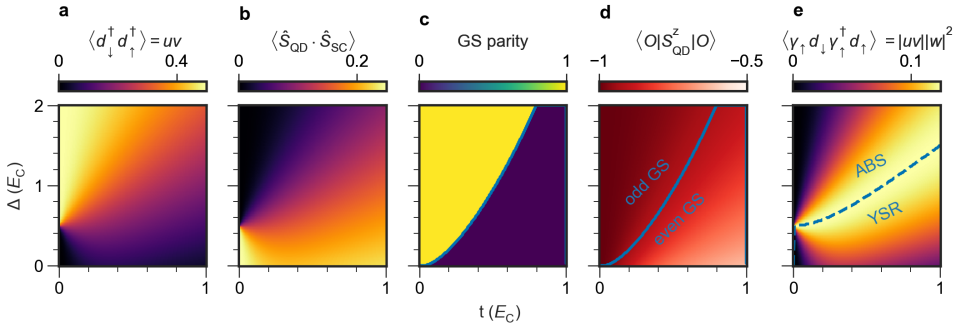


Figure 2.9: **ABS-YSR phase diagram for varying t and Δ .** The calculations were performed for $\mu = -E_C/2$, where the QD is at half-occupancy. **a.** BCS correlations of the lowest-energy even state, $\langle d_{\downarrow}^{\dagger} d_{\uparrow}^{\dagger} \rangle$, for varying t and Δ . **b.** Exchange coupling of the lowest-energy even state, $\langle \hat{S}_{\text{QD}} \cdot \hat{S}_{\text{SC}} \rangle$, for varying t and Δ . **c.** Ground state parity for varying t and Δ . **d.** Spin expectation value of the QD in the odd ground state, $\langle \sigma_{\text{QD}}^z \rangle$, for varying t and Δ . **e.** Co-existence of BCS and exchange singlet correlations of the lowest-energy even state, $\langle \gamma_1 d_{\downarrow} \gamma_1^{\dagger} d_{\uparrow} + \text{h.c.} \rangle$, for varying t and Δ . The blue, dashed line indicates the values of t and Δ for which the combined BCS and exchange singlet correlations are largest.

This phase diagram can also be studied for varying t and Δ at fixed E_C . We note that in reality, coupling a QD to a superconductor renormalizes the charging energy, which is not captured in this model. Figure 2.9a shows BCS correlations of the lowest-energy even state on the QD. For large Δ/t , quasiparticle occupation of the superconductor is energetically expensive, and the ground state is a BCS singlet. As t increases for low Δ/E_C , the BCS correlations increase initially. Here $\Delta < t$, for which the approximation

that t is a perturbation to the Hamiltonian is not justified anymore. The Kondo effect becomes relevant in this parameter regime, which the ZBW model does not capture. For large Δ/E_C , the ground state becomes a ZBW singlet for increasing t . This can be seen from the exchange correlations as well, as shown in Figure 2.9b. Figure 2.9c shows the ground state parity of the system, where 0 denotes even and 1 denotes odd. Increasing t favors an even-parity ground state, whereas increasing Δ results in an odd-parity ground state. Figure 2.9d shows the spin expectation value of the lowest-energy odd state on the quantum dot. For increasing t , the QD spin becomes localized more on the superconductor. Finally, Figure 2.9e shows the cross-over between the BCS and ZBW singlet components of the lowest-energy even state. As t increases, these correlations remain present for a larger range of Δ values.

We conclude that there is a gradual crossover from a BCS singlet to a ZBW singlet and that a phase diagram can be composed based on the nature of the even state. The phase diagram of the ground state parity shown in figure 2.8c shows good agreement with literature for $\Delta \rightarrow \infty$. Notably, our model uses only 3 basis states in the even parity subspace, and captures BCS correlations and spin-exchange of sub-gap states. While the conclusions are limited by the approximations of the zero-bandwidth model, we feel that the crossover behavior shown in this section can be expected for YSR states and ABSs.

THE ABS-YSR DIVIDE

Coupling confined electronic states to bulk superconductors remains a complicated problem. A complete description would require a full BCS density of states for the superconductor, and electron interactions for the normal system. The problem can be simplified for certain parameter regimes of the parent gap, the charging energy and the coupling to the superconductor. As a result, different device geometries are interpreted using different models. The interest in the Lutchyn-Oreg model motivated the study of quasi-one-dimensional semiconductors coupled to a bulk superconductor [38, 39]. The desire to probe the bulk of these systems led to the appearance of grounded superconductors, which quenches the charging energy of semiconductor states. This simplifies the system significantly, and motivated the usage of the superconducting atomic limit ($\Delta \gg E_C$), where the even ground state is a BCS singlet and the sub-gap states are referred to as ABSs. The superconducting atomic limit is straightforward to interpret, but fairly inaccurate when interactions appear on the QD.

On the other hand, electron-electron interactions were already studied within the context of the Kondo effect. This led to the study of quantum dots coupled to superconductors ($E_C \gg \Delta$), where superconductivity competes with the Kondo effect [40]. Here, interactions on the QD cannot be discarded, as in the case of semiconductors coupled to grounded superconductors. The system is well-described by the superconducting Anderson impurity model, which requires powerful mathematical techniques such as numerical renormalization group (NRG) to solve [41]. Here, the sub-gap states are referred to as YSR states, which are named in reference to ferromagnetic impurities in superconductors. The zero-bandwidth model can to a degree capture the interactions of the impurity with quasiparticle states in the superconductor. Recently, Baran et al. have shown that including a few superconducting orbitals gives results that are comparable to the NRG solution of the superconducting Anderson model [42]. YSR states are also found in superconductor-

QD-superconductor systems, in which the phase difference between the superconductors has to be considered too [43].

There are also quasi-one-dimensional semiconductors which are coupled to floating thin-film superconductors. Here, the semiconductor has a charging energy, though generally lower than in a quasi-zero-dimensional QD. The system is then referred to as an island, in which the superconducting gap and semiconducting charging energy can be comparable ($E_C \sim \Delta$). If the superconductor also acquires a charging energy, it leads to an interacting continuum [44]. As a result, the system needs to be described by a particle-conserving Hamiltonian, such as the Richardson model [45].

We have outlined three typical geometries in which sub-gap states are studied experimentally, i.e. grounded-superconductor hybrids, QDs coupled to superconductors and islands. While many phenomena are universal across these geometries, the terminology and models used can vary wildly. This echoes the time when sub-gap states were first predicted to exist in numerous geometries. Each model can give quantitatively different predictions for the singlet-doublet phase boundary. The zero-bandwidth model used in this section deviates significantly from the superconducting Anderson model in certain limits, such as $\Delta/t \rightarrow 0$. We do note that the zero-bandwidth model captures a QD coupled to an ABS quite well, as is discussed in chapter 5. Finally, we note that sub-gap states have been mostly studied using tunneling spectroscopy. Only recently have observables other than the spectrum been studied, including electronic compressibility, spin and ground state charge.

2.3 CHARGE OF SUB-GAP STATES

In the previous section, we discussed YSR states and ABSs, as well as their crossover. These states can undergo quantum phase transitions where the ground state parity changes. For QDs, a change in ground state parity leads to a change in charge of $1e$. This is not necessarily true for ABSs, where the even ground state is a superposition of an empty and a full orbital. In this section, we discuss the charge of sub-gap states.

2.3.1 SINGLE-ANDREEV BOX

To give an overview of the charge properties of sub-gap states, we create a toy model that is an extension of the single-electron box (see Section 2.1.1), and can be considered a variant of a Cooper pair box with $E_J = 0$ [46]. In Figure 2.10a, we show a sketch of the system that consists of a floating piece of conductor, tunnel coupled to a grounded, superconducting lead and capacitively coupled to a gate electrode, kept at a potential V_g . The capacitances between the gate and the lead to the island are C_g and C respectively. From Section 2.1.1, we recall that for a single-electron box (SEB):

$$E_C = \frac{e^2}{(C + C_g)}$$

$$\mu = E_C \left(\frac{1}{2} - \frac{C_g V_g}{e} \right)$$

The coupling to the superconductor induces sub-gap states in the island, which we consider in the superconducting atomic limit as described in Section 2.2.1. We now limit the

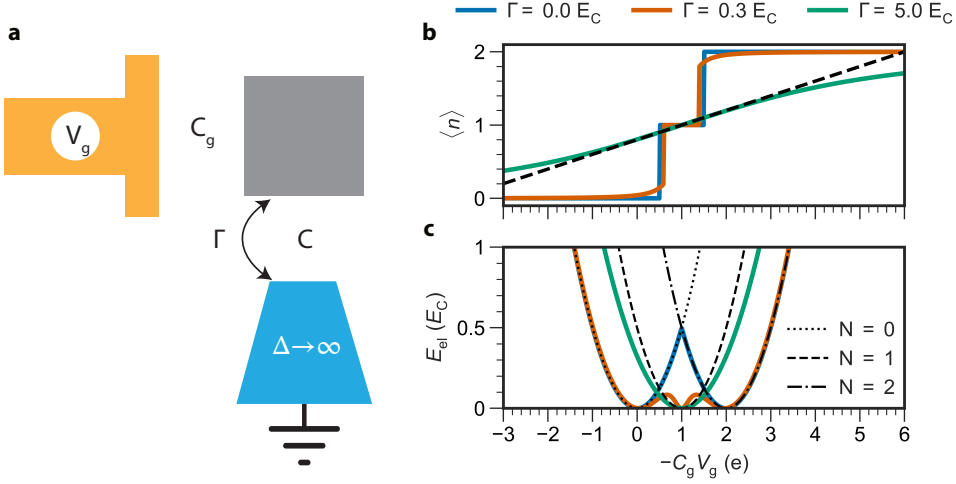


Figure 2.10: **Electrostatic energy and occupation values of a Single-Andreev Box.** **a.** Schematic overview of the model, showing a gate (yellow) with an electrostatic potential, V_g , coupled to an island (gray) with a capacitance C_g . A grounded, superconducting lead (blue) with an infinite superconducting gap Δ is coupled to the conductor with a tunnel coupling Γ and capacitance C . **b.** Fermion expectation value, $\langle n \rangle$, of the lowest energy even state of the island, for varying V_g , at different values of Γ/E_C . **c.** Electrostatic energy, E_{el} , for varying V_g of different occupations of the island. The black lines correspond to integer occupations of the island, disregarding superconductivity, with $N \in \{0, 1, 2\}$.

island to only hosting a single Andreev Bound State (ABS) that has a singlet ground state $|S\rangle = u|0\rangle - v|2\rangle$ or an odd ground state. We can then write down the occupation expectation value as:

$$\langle n \rangle = \begin{cases} \langle S|n|S \rangle = 2v^2 = 1 - \frac{\mu + \frac{E_C}{2}}{\sqrt{(\mu + \frac{E_C}{2})^2 + \Gamma^2}} & \text{even GS} \\ 1 & \text{odd GS} \end{cases} \quad (2.40)$$

Where Γ is the coupling to the superconductor. Figure 2.10 shows $\langle n \rangle$ for varying V_g , at different values of Γ/E_C . We see that when the superconductor is decoupled from the island ($\Gamma = 0$), $\langle n \rangle$ is always an integer, as for a normal SEB. When Γ is increased, $\langle n \rangle$ smoothly changes with V_g . This is due to the island exchanging charge with the superconductor due to Andreev reflection, which hybridizes the 0 and 2 occupations. When $\Gamma \gg |\mu + E_C|$, we can approximate the average occupation as $\langle n \rangle \approx 1 - (\mu + E_C/2)/\Gamma$. This is shown by the black, dashed line in figure 2.10b. In this regime, $d\langle n \rangle/dV_g \approx \text{const}$. The average charge of the ABS increases linearly with the gate voltage, similarly to the charge induced on the island by the gate, $-C_g V_g$.

We then calculate the electrostatic energy of the singlet state as:

$$E_{el} = \frac{E_C}{2} \left(2v^2 - \frac{q}{e} \right)^2 \quad (2.41)$$

We neglect any energetic contribution from superconductivity and show E_{el} for varying V_g in Figure 2.10c. Here, we see that as Γ increases, the energy of the singlet state starts

to match that of the 1 occupation. The hybridization between of the 0 and 2 occupations becomes stronger as the island-superconductor coupling increases.

In a normal SEB, charge in the island is well-defined if two conditions are met. First, $E_C \gg k_B T$, which ensures that the energy differences between charge states cannot be overcome by thermal fluctuations. It can be argued that charge is generally not well-defined for the single-Andreev box, as the even state does not have integer charge anymore. However, Fermion parity does remain well-defined. While E_C creates an energy difference between the even and odd occupations of a SEB, this is fulfilled by Γ in the single-Andreev box. Even for $E_C \ll \Gamma$, the energy difference between the ABS singlet and doublet occupations is still on the order of Γ . If $\Gamma \gg k_B T$, thermal fluctuations cannot change the ground state parity. Charge is then well-defined for the odd ground state, and bounded between 0 and $-2e$ for the even ground state. We do note that quasiparticle poisoning is required and inherent to superconducting devices, causing the Fermion parity of the island to flip over time. In figure 2.10, we neglected quasiparticle poisoning by assuming the ABS is always in its ground state.

To have well-defined charge in a SEB, the coupling between the island and the normal lead cannot be too strong. If a SEB is shorted to ground, there is no distinction between charge states in the island or in the ground itself. Therefore, N is no longer quantized and $E_{el} = 0$ can always be achieved by having $eN = q$ [1]. If the island is strongly coupled to the superconductor in a single-Andreev box ($\Gamma \gg E_C$), the occupation behaves as $e\langle n \rangle \sim -C_g V_g$, as shown by the dashed black line in Figure 2.10b. The island occupation, $\langle n \rangle$, is now a continuously changing variable, comparable to the case of the grounded single-electron box, except the single-Andreev box does have a finite E_{el} , and $0 \leq \langle n \rangle \leq 2$. For $\Gamma \rightarrow \infty$, the singlet state becomes a nearly perfect superposition of the 0 and 2 occupations for a larger range of V_g . The even state charge is then hard to distinguish from the odd state charge, even though the states have different energies. We note that in the limit $\Gamma \rightarrow \infty$ the assumptions of the superconducting atomic limit break down, and the even ground state becomes more than a BCS singlet, as discussed in Section 2.2.4.

2.3.2 ELECTRIC FIELDS IN HYBRIDS

We have seen that the coupling of a sub-gap state to a grounded superconductor affects its electrostatic properties. This distance also affects the electric field emanating from the state, because of screening by the superconductor. In Figure 2.11a we show the electrostatic potential of a point charge in a 2D InSb system with a grounded superconductor on top. We treat the superconductor as an infinite grounded plane, and calculate the electrostatic potential, V , at a location \mathbf{r} , using the method of images [47]:

$$V(\mathbf{r}) = \frac{1}{4\pi\epsilon_r\epsilon_0} \left(\frac{q}{|\mathbf{r} - d\hat{y}|} - \frac{q}{|\mathbf{r} + d\hat{y}|} \right) \quad (2.42)$$

Where ϵ_r is the dielectric constant of InSb, d is distance of the point charge to the superconductor, and we set $q = -e$. The black lines in Figure 2.11a indicate contours of constant V for $d = 9$ nm. The blue arrows show the electric field, $\hat{E} = -\nabla V$. As the point charge is closer to the superconductor, it starts to form an electric dipole with its image charge, and the potential drops off like $V \sim 1/r^2$. Figure 2.11b shows V for a point charge at a distance $d = 90$ nm away from the superconductor. We see that V decays more slowly away from

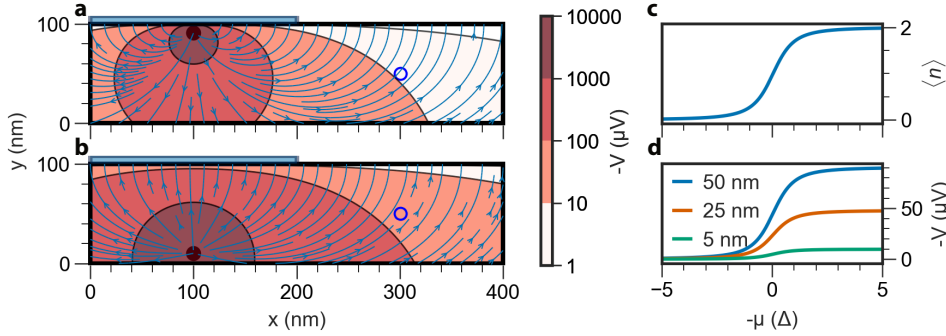


Figure 2.11: **Nanowire longitudinal section electrostatics.** **a.** Electrostatic potential, V , of a point charge in an InSb nanowire located 9 nm away from a grounded superconductor (blue). Blue arrows indicate the electric field, $\vec{E} = -\nabla V$. **b.** Same as **a.**, for a point charge 90 nm away from the superconductor. **c.** Fermion expectation value, $\langle n \rangle$ of the singlet ground state of an ABS, for varying chemical potential, μ . **d.** V at the location of the blue circle in panels **a** and **b**, for an ABS singlet ground state for varying μ , at different distances to the superconductor. The ABS is modeled as a point charge.

the point charge than in panel **a**. The larger d causes the point charge to act increasingly like an electric monopole as opposed to a dipole.

To estimate V resulting from an ABS in a hybrid nanowire, we replace the point charge $q = -e$ by the charge expectation value of an ABS in the singlet ground state, $q = -e\langle N \rangle$. Figure 2.11c shows $\langle N \rangle$ for varying chemical potential, μ . In Figure 2.11d, we show V calculated at the blue circle in panels **a** and **b**, for varying μ at three values of d . As the ABS charge becomes closer to the superconductor, the electrostatic potential at the blue circle decreases gradually. This implies that the charge of sub-gap states becomes harder to observe as they are localized closer to the interface with the superconductor. In these calculations, we have assumed that the ABS does not change for varying d .

2.3.3 CHARGE SENSING SUB-GAP STATES

When we introduced the charge of sub-gap states in the previous section, we limited the electrostatics to zero-dimensions. In truth, sub-gap states are found in quasi one-dimensional (nanowires) or two-dimensional (2DEG) systems. Because of confinement, the wave function of sub-gap states can be localized in different parts of the system. The distance of a sub-gap state to a grounded superconductor can affect its observable charge in two ways. Firstly, the charging energy (E_C) and coupling to the superconductor (Γ) are highly dependent on the distance, and affect how the ABS charge responds to a gate voltage. Secondly, the electrostatic potential decays more rapidly as the ABS is localized closer to the superconductor, as discussed in the previous section. While both will affect how a charge sensor can be used to measure the charge of a sub-gap state, we will disregard the dependence of Γ and E_C on distance as it highly depends on the microscopics of devices. We modify the constant interaction model of a double quantum dot (see Equations (2.5) and (2.6)) to make a phenomenological model of a SEB that is electrostatically coupled to

an ABS:

$$\mu_{\text{SEB}}(d) = \frac{E_{\text{C}}^{\text{SEB}}}{2} - e\alpha V_2 + V(d) - e\beta V_1 \quad (2.43)$$

$$\mu_{\text{ABS}} = E_{\text{C}}^{\text{ABS}} \left(\frac{1}{2} - \frac{C_{\text{g}} V_1}{e} \right) - e\beta V_2 \quad (2.44)$$

Where d is distance of the ABS to the superconductor, α is the lever arm of the SEB and β is the cross-capacitance. $V(d)$ is the electrostatic potential at the location of the SEB, which is calculated using Equation (2.42), where the ABS is approximated as a point charge in the middle of the hybrid segment. We calculate the charge of the ABS using the superconducting atomic limit (see Section 2.2.2 for details):

$$q = -e\langle n \rangle = \begin{cases} -2ev^2 = 1 - \frac{\mu_{\text{ABS}} + E_{\text{C}}^{\text{ABS}}/2}{\sqrt{(\mu_{\text{ABS}} + E_{\text{C}}^{\text{ABS}}/2)^2 + \Gamma^2}} & \text{even GS} \\ -e & \text{odd GS} \end{cases}$$

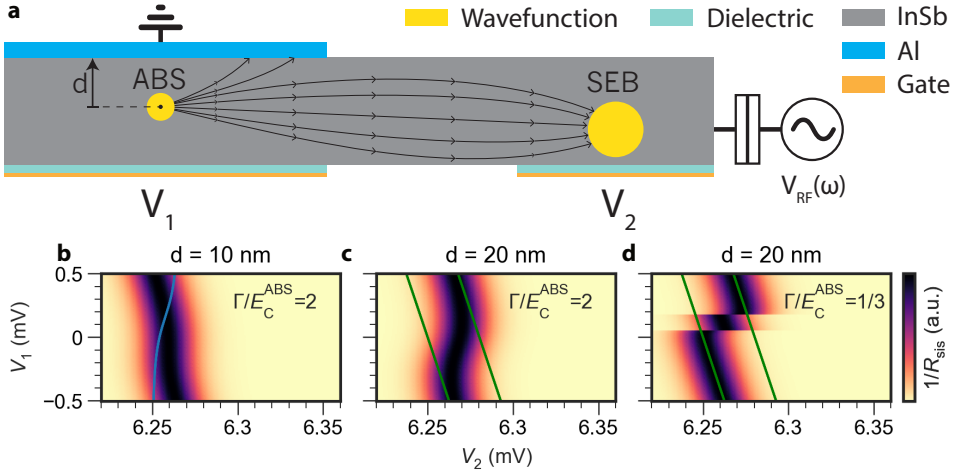


Figure 2.12: Charge Sensing Sub-Gap States with a single-electron box. **a.** Schematic sketch of a longitudinal cut of an InSb nanowire, with a grounded Al shell. The sub-gap state is modeled as a point charge in the hybrid segment, indicated by the yellow cylinder. The single-electron box (SEB) is modeled as a point charge in the bare InSb segment indicated by the yellow sphere. Electrical field lines between the ABS and the Al, and the ABS and the SEB are schematically sketched. The electrochemical potential of the sub-gap state and the SEB are controlled by two bottom gates with voltages $V_{1/2}$ respectively. d is the distance between the sub-gap state and the top facet of the nanowire. The hybrid section has a length $L = 250$ nm and a diameter $W = 100$ nm. For the ABS, we set $\Gamma = 80 \mu\text{eV}$ and $C_{\text{g}} = 0.001$ pF. For panels b and c, we use $E_{\text{C}}^{\text{ABS}} = 40 \mu\text{eV}$, and $E_{\text{C}}^{\text{ABS}} = 250 \mu\text{eV}$ for panel d. **b.-d.** The inverse of the Sisyphus resistance, $1/R_{\text{sis}}$, for varying V_1 and V_2 for $d = \{10 \text{ nm}, 20 \text{ nm}, 20 \text{ nm}\}$ and $\Gamma/E_{\text{C}}^{\text{ABS}} = \{2, 2, 1/3\}$ respectively. We have used $E_{\text{C}} = 5$ mV and a lever arm of $-e\alpha = 0.4$ for the SEB, and a cross-capacitance of $e\beta = 0.01$ between the sub-gap state and the SEB. The blue line in panel b indicates the position of the Coulomb resonance for $\langle n \rangle = 0$ and $\langle n \rangle = 2$. The green lines in panels c and d indicate the SEB Coulomb resonance for $\langle n \rangle = 0$ and $\langle n \rangle = 2$. We used Equation (2.8) for the calculations of the Sisyphus resistance, with: $T = 30$ mK, $f = \omega/2\pi = 300$ MHz and $\Gamma_0 = 40 \mu\text{eV}$.

The system is sketched in Figure 2.12a. Here, a longitudinal cross-cut of a semiconductor nanowire with a single Al top facet is shown. The ABS is modeled as a point charge in the hybrid, the SEB is located in the bare InSb segment. A normal lead is connected to an AC voltage and is tunnel-coupled to the SEB.

Figure 2.12b.-d. show the inverse of the Sisyphus resistance of the SEB, $1/R_{\text{sis}}$, for varying V_1 and V_2 , for different values of d . In Figure 2.12b, The ABS is localized 5 nm away from the grounded superconductor. We see that the Coulomb resonance of the SEB is changed gradually by V_1 . This shift can result from the change in occupation of the ABS, or the cross-capacitance, β . The superimposed, blue line shows the Coulomb resonance for $\beta = 0$. Here, we can faintly observe curvature in the shift of the resonance, in the absence of cross-capacitance. The small distance between the ABS and the grounded Al draws the electric field lines away from the SEB, which makes the ABS charge hard to distinguish from a more trivial shift due to cross-capacitance.

In Figure 2.12c, we can observe the curvature in the shift of the SEB Coulomb resonance more clearly, in addition to the linear shift from cross-capacitance. Here, the electric field lines between the ABS and SEB are screened less, due to the larger distance to the superconductor. The changing occupation of the ABS has a larger effect on the SEB's electrochemical potential as compared to panel b. The curvature stems from the gradual change of $\langle n \rangle$ from 0 to 2. The green lines indicate the SEB Coulomb resonance for $\langle n \rangle = 0$ and $\langle n \rangle = 2$.

In Figure 2.12d, we use the same distance as in panel c, but a larger $E_C^{\text{ABS}} = 250 \mu\text{eV}$. Because of the larger charging energy, the ABS now has a doublet ground state for a range of V_1 and V_2 values. The change in ground state parity of the ABS causes a discontinuous jump in the Coulomb resonance of the SEB. This is comparable to charge sensing of non-superconducting systems, where electrons are loaded one-by-one onto a quantum dot, see Figure 2.3. We note that for an ABS, the slope of the Coulomb resonance in the odd ground state is different from the one in the even ground state. This can be attributed to the gradual change of $\langle n \rangle$ in the singlet ground state, compared to $\langle n \rangle = 1$ for the odd ground state. Figure 2.12d implies that ground state parity can be inferred from charge sensing measurements. This is not universally true for sub-gap states, notably in Kitaev chains, which will be discussed in section 2.4.4

We note that the models used here are highly simplified. The electrostatic calculations are performed while assuming point charges and infinite ground planes, as opposed to finite systems. In reality, the charging energy and semiconductor-superconductor coupling depend strongly on the wave function profile. Furthermore, the ABS is modelled in the superconducting atomic limit, which is not valid as $E_C \sim \Delta$. Nevertheless, we conclude that the model predicts certain charge sensing signatures that will be shown in chapter 4.

2.4 MINIMAL KITAEV CHAINS

In sections 2.2.2 and 2.2.3 we discussed the effects of coupling quantum dots (QDs) to superconductors. We limited ourselves to a single QD to study the superconducting proximity effect on a confined system. When two QDs are coupled to the same superconductor, they both acquire particle-hole symmetry. A Cooper pair can then be split or formed in the superconductor, and the electrons can tunnel into or out of the dots. We also limited ourselves to zero magnetic field in the preceding chapters. When an external magnetic

field is applied, time-reversal symmetry is broken. Based on symmetries, systems can be categorized into certain classes. A system with particle-hole symmetry and broken time-reversal symmetry is a class D system. A one-dimensional, class D system has a \mathbb{Z}_2 topological invariant, meaning it can be described by a topological invariant with two possible values. At the transition from topologically trivial to non-trivial, Majorana zero-modes (MZMs) are predicted to appear at the ends of the one-dimensional class D system. In 2001, Kitaev proposed that this symmetry class can be realized in a spinless, infinite, one-dimensional tight-binding chain [48]. Unfortunately, an electronic implementation of the Kitaev chain is necessarily a spin-1/2 system with Kramer's degeneracy, and will have time-reversal symmetry. In 2010, the Lutchyn-Oreg model was introduced to find MZMs in semiconductor-superconductor hybrids with spin-orbit interaction and an external magnetic field [38, 39]. Whereas the Kitaev chain model is discrete, this model is continuous. In 2012, Sau and Das Sarma proposed a direct implementation of the Kitaev chain model in QDs coupled to superconductors [49]. Formally, this system will only be topological for an infinite number of QD. In the same year, Leijnse and Flensberg predicted that MZMs could even appear in a minimal chain, consisting of two QDs coupled through a single superconductor [50]. While these "Poor Man's Majorana zero modes" are not topologically protected, they do share properties with MZMs that appear in topologically non-trivial systems, including non-Abelian statistics, robustness to local perturbations and more. In this section, we will discuss minimal Kitaev chains realized in different geometries.

2.4.1 NORMAL QUANTUM DOT KITAEV CHAIN

Leijnse and Flensberg consider two fully spin-polarized QDs that are coupled through a grounded superconductor, which is shown in figure 2.13a. The system Hamiltonian is almost identical to the double QD detailed in section 2.1.2:

$$H = \mu_1 n_1 + \mu_2 n_2 + t d_1^\dagger d_2 + \Delta d_1^\dagger d_2^\dagger + \text{H.c.} \quad (2.45)$$

Here the subscripts 1 and 2 denote the left and right QDs, and t is the tunnel coupling. The term $\Delta d_1^\dagger d_2^\dagger$ describes the addition of an electron to both QDs simultaneously, and does not appear for normal double QDs. This is the "superconducting pairing" term as described by Kitaev, and can be realized by coupling the QDs through a superconductor. The processes associated with t and Δ are sketched in figure 2.13b,c.

We denote the combined state of the double QD in the number basis, $|n_{\text{QD1}}, n_{\text{QD2}}\rangle$, and write the Hamiltonian in the basis $\{|00\rangle, |10\rangle, |01\rangle, |11\rangle\}$:

$$H = \begin{pmatrix} 0 & 0 & 0 & \Delta \\ 0 & \mu_1 & t & 0 \\ 0 & t & \mu_2 & 0 \\ \Delta & 0 & 0 & \mu_1 + \mu_2 \end{pmatrix} \quad (2.46)$$

If we diagonalize the Hamiltonian for $t = \Delta$, we obtain the following eigenstates:

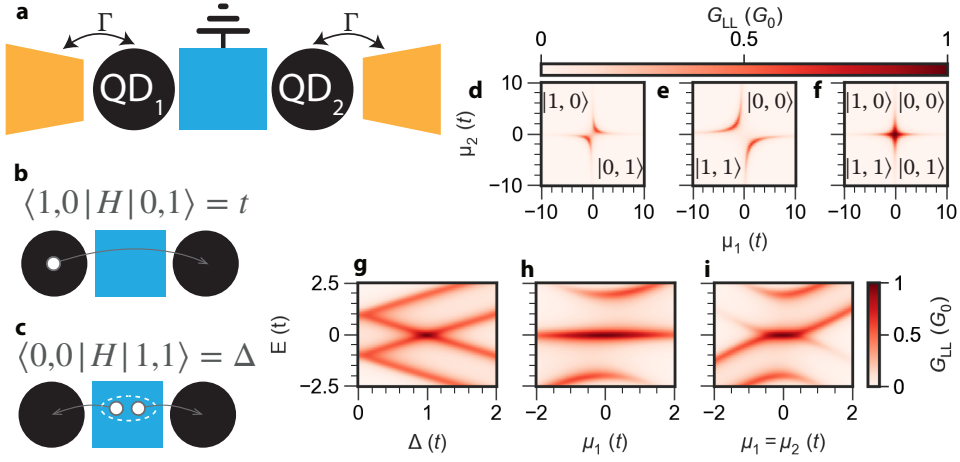


Figure 2.13: **A minimal Kitaev chain based on normal quantum dots.** **a.** A schematic diagram of the system. Two quantum dots (QDs) are tunnel coupled through a grounded superconductor. Each QD is coupled to a normal lead with magnitude Γ . **b.** Sketch of the tunneling process, t , between the QDs. **c.** Sketch of the superconducting pairing, Δ , between the QDs. **d-f.** Calculate conductance of the left lead, G_{LL} , for varying electrochemical potential of the QDs, μ_1 and μ_2 , for Δ/t values of $\{1/2, 2, 1\}$. The bias of both leads is 0. The superimposed text indicates the states that hybridize most strongly. **g.** G_{LL} , for varying Δ/t and bias of the left lead, E . Here, both QD levels are kept at the Fermi level: $\mu_1 = \mu_2 = 0$. **h.** G_{LL} , for varying μ_1 and E . Here, $\mu_2 = 0$ and $\Delta = t$. **i.** G_{LL} , for varying μ_1 and μ_2 , and E for $\Delta = t$.

$$\begin{aligned}
 |\alpha_e\rangle &= \frac{1}{\sqrt{2}}(|00\rangle + |11\rangle), & E_{\alpha_e} &= t \\
 |\alpha_o\rangle &= \frac{1}{\sqrt{2}}(|10\rangle + |01\rangle), & E_{\alpha_o} &= t \\
 |\beta_e\rangle &= \frac{1}{\sqrt{2}}(|00\rangle - |11\rangle), & E_{\beta_e} &= -t \\
 |\beta_o\rangle &= \frac{1}{\sqrt{2}}(|10\rangle - |01\rangle), & E_{\beta_o} &= -t
 \end{aligned} \tag{2.47}$$

At each energy $E = \pm t$, there is a degenerate even-parity and odd-parity state. An electron can be added or removed at the Fermi level to change the ground state parity of the system. To obtain a transport description of the system, we write the Hamiltonian in the semiconductor picture (see section 2.2.1):

$$h = \begin{pmatrix} \mu_1 & t & 0 & \Delta \\ t & \mu_2 & -\Delta & 0 \\ 0 & -\Delta & -\mu_1 & -t \\ \Delta & 0 & -t & -\mu_2 \end{pmatrix} \tag{2.48}$$

Having obtained a non-interacting single-electronic Hamiltonian, we can calculate the scattering matrix using the Mahaux-Weidenmuller formula:

$$S = 1 + 2i\pi W[h - E + i\pi W^\dagger W]^{-1} W^\dagger \tag{2.49}$$

Where E is the excitation energy and:

$$W = \sqrt{\frac{\Gamma}{2\pi}} \begin{pmatrix} 1 & 0 & 0 & 0 \\ 0 & 0 & -1 & 0 \\ 0 & 1 & 0 & 0 \\ 0 & 0 & 0 & -1 \end{pmatrix}$$

Here, Γ denotes the tunnel coupling between each QD and its respective lead. We calculate the conductance as $G_{LL}(E) = |S_{LL}^{ee}|^2 - |S_{LL}^{he}|^2 - 1$. In figure 2.13d we show G_{LL} at $E = 0$ for varying μ_1 and μ_2 for $\Delta/t = 0.5$. We see an avoided crossing between the Coulomb resonances of the QDs. There is only finite conductance for μ_1, μ_2 values close to resonance, which we attribute to transport processes involving both QDs. There is no local Andreev reflection process on the normal QDs, resulting in no local conductance when only one QD is on resonance with the lead. The avoided crossing seen in figure 2.13d indicates hybridization between the $|1, 0\rangle$ and $|0, 1\rangle$ states, which is commonly seen for interdot transitions in normal double QDs. In figure 2.13e, we show G_{LL} for varying μ_1 and μ_2 for $\Delta/t = 2$. Here, the avoided crossing is now oriented along the diagonal, indicating hybridization between the $|0, 0\rangle$ and $|1, 1\rangle$ states. This coupling violates particle conservation on the QDs, and is only possible due to the QDs exchanging charge with superconductor. This hybridization shows that Cooper pair splitting can coherently couple the even-parity states. In figure 2.13f, we show G_{LL} for varying μ_1 and μ_2 for $\Delta = t$. Here, the odd-parity and even-parity states hybridize with the same strength. The result is a degenerate even-, and odd-parity ground state as shown in equation (2.47), signaling the appearance of Poor man's Majorana zero modes.

In figure 2.13g we show G_{LL} for varying Δ and E , at $\mu_1 = \mu_2 = 0$. We see four particle-hole-symmetric peaks; two with energies $t - \Delta$ and two with energies $t + \Delta$. This shows the linear splitting of the zero-energy state with t/Δ , which is characteristic for a two-site Kitaev chain. In figure 2.13h we show G_{LL} for varying μ_1 and E , at $\mu_2 = 0$ and $t = \Delta$. Here, we see a zero-energy state that does not split upon changing μ_1 , which is a manifestation of the local protection of Poor Man's Majorana states. In figure 2.13i we show G_{LL} for varying μ_1, μ_2 and E , at $t = \Delta$. We see that the zero-energy state splits quadratically upon perturbing both QD electrochemical potentials. This quadratic protection is expected for a two-site chain, and increases polynomially for an increasing number of sites.

When more sites are added, the excited states (see equation (2.47)) form bands and the system becomes topological [49]. The minimal Kitaev chain model for normal QDs is a breakthrough work because of its bottom-up approach of topology. We can verify that $t = \Delta$ for each added pair, and see that the zero-energy state becomes more robust to global and local perturbations. However, it does require t and Δ to be mediated by a superconductor. In practice, these amplitudes are severely limited by the coherence length of the superconductor. Also, the model does not detail how the ratio of t and Δ can be changed electrostatically.

2.4.2 PROXIMITIZED QUANTUM DOT KITAEV CHAIN

In the previous section, we discussed the minimal Kitaev chain model based on normal QDs coupled through a grounded superconductor. As the superconducting coherence length can limit the tunneling amplitudes, it is desirable to find a different way of mediating

the even and odd coupling. One possibility is to replace the bulk superconductor by a semiconductor-superconductor system. The induced coherence length can be significantly longer than the bulk one, allowing for stronger coupling of the QDs [51]. Specifically, the combination of confinement and the proximity effect leads to Andreev Bound States (ABSs) appearing in the hybrid segment. The system of two QDs coupled through a semiconductor-superconductor section is sketched in figure 2.14a.

When the QDs are tunnel-coupled to an ABS (see section 2.2.2), their 0 and 2 occupations hybridize with an amplitude:

$$\Delta_{\text{ind}} = \frac{t^2 + t_{\text{SO}}^2}{2uvE_A} + O(t^4, t_{\text{SO}}^4) \quad (2.50)$$

Where t (t_{SO}) is the spin-conserving (flipping) tunnel rate between the QD and the ABS, E_A is the ABS' excitation energy, and u, v its singlet wave function components. We note that this is different from directly coupling a QD to a bulk superconductor, as the ABS is a single, discrete state. The result is the formation of zero-bandwidth states Yu-Shiba-Rusinov states on the QDs, see section 2.2.4 for discussion. We use the $\{|S\rangle, |\downarrow\rangle\}$ basis states for each QD and exclude the $|\uparrow\rangle$ state by assuming an infinitely large Zeeman energy. Assuming

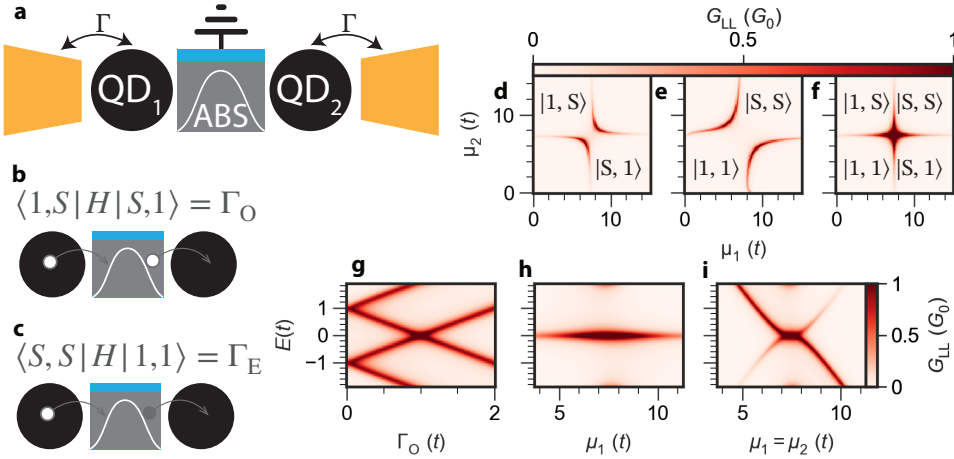


Figure 2.14: **A minimal Kitaev chain bases on proximitized quantum dots.** **a.** A schematic diagram of the system. Two quantum dots (QDs) are tunnel coupled to an ABS in a hybrid segment. Each QD is coupled to a normal lead with magnitude Γ . **b.** Sketch of an elastic co-tunneling process between the QDs. **c.** Sketch of a crossed Andreev reflection process between the QDs. **d-f.** Calculate conductance of the left lead, G_{LL} , for varying electrochemical potential of the QDs, μ_1 and μ_2 , for $\Delta_{\text{SO}}, t_{\text{SO}}$ values of $\{t/2, 2t, t\}$. The bias of both leads is 0. The superimposed text indicates the states that hybridize most strongly. **g.** G_{LL} , for varying Γ_E/t and bias of the left lead, E . Here, both QD levels are kept at the Fermi level: $\mu_1 = \mu_2 = 0$. **h.** G_{LL} , for varying μ_1 and E . Here, $\mu_2 = 0$ and $\Gamma_E = \Gamma_O$. **i.** G_{LL} , for varying μ_1 and μ_2 , and E for $\Gamma_E = \Gamma_O$.

$E_A \gg t, t_{\text{SO}}$, we can partition the odd occupations of the ABS into a high-energy subspace. We then assume that the ABS is always in the $|S\rangle$ ground state and do not explicitly write its state in our basis. Following Liu et al., we can then write an effective Hamiltonian for

the QDs [52]:

$$H_{\text{eff}} = \epsilon_1 n_1 + \epsilon_2 n_2 + \Gamma_O (f_L^\dagger f_R + f_R^\dagger f_L) + \Gamma_E (f_L^\dagger f_R^\dagger + f_R f_L) \quad (2.51)$$

Where $\epsilon_i = -E_C^i/2 - E_Z/2 + \sqrt{\mu_i^2 + \Delta_{i,\text{ind}}^2}$ is the energy cost of creating a Bogoliubon on QD i . Here, μ_i is the electrochemical potential, E_C^i is the charging energy, E_Z the Zeeman energy and $\Delta_{i,\text{ind}}$ is the induced gap. The effective couplings Γ_O and Γ_E are given by:

$$\Gamma_o = \langle S, \downarrow | H_{\text{coupling}}^{\text{eff}} | \downarrow, S \rangle = -t_{\uparrow\uparrow} v_L v_R + t_{\downarrow\downarrow} u_L u_R + \Delta_{\uparrow\downarrow} v_L u_R - \Delta_{\downarrow\uparrow} u_L v_R \quad (2.52)$$

$$\Gamma_e = \langle S, S | H_{\text{coupling}}^{\text{eff}} | \downarrow, \downarrow \rangle = -\Delta_{\uparrow\uparrow} v_L v_R + \Delta_{\downarrow\downarrow} u_L u_R + t_{\uparrow\downarrow} v_L u_R - t_{\downarrow\uparrow} u_L v_R \quad (2.53)$$

Where u_i, v_i are the singlet components of QD i . Here, t is now an elastic co-tunneling rate that involves virtual occupation of the ABS. The subscripts indicate the spin of the excitation on both QDs. Δ is a crossed Andreev reflection rate that is mediated by the ABS. For normal QDs, t exclusively couples the odd states, and Δ the even states. For QDs coupled to an ABS, this is no longer true. If a spin-up electron tunnels out of the left QD in the $|S\rangle$ state, it leaves it in the $|\downarrow\rangle$ state. If this electron rotates to spin-down and tunnels into the $|S\rangle$ state of the right QD, it leaves it in the $|\downarrow\rangle$ state too. In this way, spin-flipping tunneling, $t_{\uparrow\downarrow}$, can couple the $|S, S\rangle$ and $|\downarrow, \downarrow\rangle$ states. In addition, splitting a triplet Cooper pair over the QDs, $\Delta_{\downarrow\downarrow}$, also couples the $|S, S\rangle$ and $|\downarrow, \downarrow\rangle$ states. While both processes occur concomitantly, the elastic co-tunneling and crossed Andreev reflection rates depend on the ABS energy [53, 54]. For simplicity, we choose their amplitudes manually and set:

$$\begin{aligned} t_{\downarrow\downarrow} &= t_{\uparrow\uparrow} = t & \Delta_{\uparrow\downarrow} &= \Delta_{\downarrow\uparrow} = \Delta_0 \\ t_{\uparrow\downarrow} &= t_{\downarrow\uparrow} = t_{\text{SO}} & \Delta_{\uparrow\uparrow} &= \Delta_{\downarrow\downarrow} = \Delta_{\text{SO}} \end{aligned}$$

Here, t and t_{SO} are the spin-flipping, and spin-conserving tunneling rates. Δ_0 is the rate of splitting s -wave Cooper pairs. Δ_{SO} is the rate of splitting parallel spin Cooper pairs. To find a transport description of the system, we write the Bogoliubov-deGennes (BdG) Hamiltonian in the semiconductor picture as:

$$h_{\text{BdG}} = \begin{pmatrix} E_L & \Gamma_{\text{odd}} & 0 & \Gamma_{\text{even}} \\ \Gamma_{\text{odd}} & E_R & -\Gamma_{\text{even}} & 0 \\ 0 & -\Gamma_{\text{even}} & -E_L & -\Gamma_{\text{odd}} \\ \Gamma_{\text{even}} & 0 & -\Gamma_{\text{odd}} & -E_R \end{pmatrix} \quad (2.54)$$

The states of this Hamiltonian describe single-particle excitations from the $|S, S\rangle$ state. While the excitations of the system are Bogoliubons, the modes in the left and right leads are electrons or holes:

$$\Psi_{\text{in/out}} = (|Le \uparrow\rangle, |Le \downarrow\rangle, |Re \uparrow\rangle, |Re \downarrow\rangle, |Lh \uparrow\rangle, |Lh \downarrow\rangle, |Rh \uparrow\rangle, |Rh \downarrow\rangle)_{\text{in/out}}. \quad (2.55)$$

To couple the double QD system to the leads, we perform a Bogoliubov transformation of the lead modes:

$$(f_L^\dagger \quad f_R^\dagger \quad f_L \quad f_R)^T = \hat{M} (c_\uparrow^{L\dagger} \quad c_\downarrow^{L\dagger} \quad c_\uparrow^{R\dagger} \quad c_\downarrow^{R\dagger} \quad c_\uparrow^L \quad c_\downarrow^L \quad c_\uparrow^R \quad c_\downarrow^R)^T$$

We can then define the W -matrices that couple the leads to the system as:

$$W^\dagger = \sqrt{\frac{\Gamma}{2\pi}} \hat{M} = \sqrt{\frac{\Gamma}{2\pi}} \begin{pmatrix} 0 & u & 0 & 0 & -v & 0 & 0 & 0 \\ 0 & 0 & 0 & u & 0 & 0 & -v & 0 \\ -v & 0 & 0 & 0 & -v & u & 0 & 0 \\ 0 & 0 & -v & 0 & -v & 0 & 0 & u \end{pmatrix}$$

We then write the scattering matrix as:

$$S = 1 + 2i\pi W[h_{\text{BdG}} - V_{\text{bias}} + i\pi W^\dagger W]^{-1} W^\dagger \quad (2.56)$$

And we compute the conductance as: $G_{\text{LL}}(E) = |S_{\text{LL}}^{\text{ee}}|^2 - |S_{\text{LL}}^{\text{he}}|^2 - 1$.

In figure 2.14d we show G_{LL} at $E = 0$ for varying μ_1 and μ_2 for $\Delta_0 = t$, $t_{\text{SO}} = \Delta_{\text{SO}} = t/2$. We see an avoided crossing that indicates hybridization between the $|\downarrow, S\rangle$ and $|S, \downarrow\rangle$ states. There is now also finite conductance when only one QD is on resonance. We attribute this to local Andreev reflections resulting from the QD-ABS coupling. In figure 2.14e, we show G_{LL} for varying μ_1 and μ_2 for $\Delta_0 = t$, $t_{\text{SO}} = \Delta_{\text{SO}} = 2t$. Here, the avoided crossing is now oriented along the diagonal, indicating hybridization between the $|S, S\rangle$ and $|\downarrow, \downarrow\rangle$ states. In figure 2.14f, we show G_{LL} for varying μ_1 and μ_2 for $t_{\text{SO}} = \Delta_{\text{SO}} = \Delta_0 = t$. Here, the odd-parity and even-parity states hybridize with the same strength. The result is a degenerate even-, and odd-parity ground state.

In figure 2.14g we show G_{LL} for varying Γ_0 and E , at $\mu_1 = \mu_2 = 3E_C/2$. We see four particle-hole-symmetric peaks: two inner ones at energies $\pm|\Gamma_0 - \Gamma_E|$ and two outer ones at energies $\pm(\Gamma_0 + \Gamma_E)$. This shows the linear splitting of the zero-energy state with t/Δ , which is characteristic for a two-site Kitaev chain. In figure 2.14h we show G_{LL} for varying μ_1 and E , at $\mu_2 = 0$ and $\Gamma_0 = \Gamma_E$. Here, we see a zero-energy state that does not split upon changing μ_2 . This is the local protection of Poor Man's Majorana states. In figure 2.14i we show G_{LL} for varying $\mu_1 = \mu_2$ and E , at $\Gamma_0 = \Gamma_E$. We see that the zero-energy state splits quadratically upon perturbing both QD electrochemical potentials. This quadratic protection is expected for a two-site chain, and increases polynomially for an increasing number of sites.

Although these figure look almost identical to figure 2.13, there are differences between minimal Kitaev chains based on normal or proximitized QDs. First, the origin of the even and odd coupling. For normal QDs, these are given by Cooper pair splitting from a bulk superconductor, and direct tunneling. For proximitized QDs, the even and odd couplings are both mediated by an ABS. Furthermore, elastic co-tunneling and crossed Andreev reflection can couple both even-, and odd-parity states. Second, the even ground state is a superposition of the 0 and 2 occupations for proximitized QDs. This results in fractional charge differences between the even and odd states, as compared to the $1e$ difference for normal QDs. One effect of the proximity effect on the QDs is that the zero-energy state is stable over a larger range of μ_i values than for normal QDs. A Kitaev chain realized using QDs coupled to ABSs allows for a stronger coupling than using normal QDs. When this coupling becomes too strong (i.e. $E_A \sim t, t_{\text{SO}}$), the odd states of the ABS can form bonding/anti-bonding states with the QDs. They can then no longer be segmented into a high-energy subspace. As a result, the ABS states have to be explicitly included in the basis. An ABS then becomes a site of the chain, as opposed to a coupling element.

2.4.3 ANDREEV BOUND STATE QUANTUM DOT KITAEV CHAIN

In the previous section, we discussed how the even states of a QD can hybridize upon coupling it to an ABS. When the ABS excitation energy is larger than this coupling, its odd states do not hybridize strongly with the QD. However, an ABS can have an odd-parity ground state due to charging energy and/or an external magnetic field. When the ABS excitation is then coupled to a QD level, the odd states can also hybridize. We consider this process by starting from the $|\downarrow, S\rangle$ state, where the QD is occupied by a single spin and the ABS is in the singlet state. The spin-down electron can tunnel from the QD to the ABS, which forms the $|0, \downarrow\rangle$ state. We show a schematic drawing of this process in figure 2.15a. This spin-conserving tunneling process couples the global odd states of the QD-ABS system. The spin can also precess due to spin-orbit during tunneling. Starting from the $|0, S\rangle$ state, and up-electron can tunnel out of the ABS. If the electron rotates to down and tunnels into the QD, the $|\downarrow, \downarrow\rangle$ state is formed. This process couples the even states of the QD-ABS system and is sketched in figure 2.15b. In section 2.4.2 we discussed how an ABS can mediate elastic co-tunneling and crossed Andreev reflection between QDs. Here, we see that comparable odd and even couplings can also arise between an ABS and a single QD.

Following Miles et al. [55], we write the Hamiltonian of an ABS coupled to a QD as:

$$H = H_{\text{ABS}} + H_{\text{QD}} + H_t \quad (2.57)$$

We treat the ABS in the superconducting atomic limit, see equation (2.9) for the corresponding Hamiltonian. We also assume a large Zeeman energy to disregard all spin-up states, and write the QD Hamiltonian as:

$$H_{\text{QD}} = (\mu_{\text{QD}} - E_Z)c_{\downarrow}^{\dagger}c_{\downarrow} + E_C^{\text{QD}}c_{\uparrow}^{\dagger}c_{\uparrow}c_{\downarrow}^{\dagger}c_{\downarrow}. \quad (2.58)$$

H_t describes the tunnel coupling between the ABS and the QD and is given by:

$$H_t = t(c_{\downarrow}^{\dagger}d_{\downarrow} + c_{\uparrow}^{\dagger}d_{\uparrow} + h.c.) + t_{\text{so}}(-c_{\downarrow}^{\dagger}d_{\uparrow} + c_{\uparrow}^{\dagger}d_{\downarrow} + h.c.), \quad (2.59)$$

Where t is the spin-conserving tunneling amplitude, and t_{so} is the spin-flipping tunneling amplitude resulting from spin-orbit interaction. d_{\downarrow} removes a down-electron from the ABS.

The basis of equation (2.57) can be split into even and odd parity subspaces, where we consider the following states in the $|N, M\rangle = |N\rangle_{\text{QD}} \otimes |M\rangle_{\text{ABS}}$ basis:

$$\begin{aligned} \{|0, S\rangle, |2, S\rangle, |\downarrow, \downarrow\rangle\} & \text{ even} \\ \{|0, \downarrow\rangle, |\downarrow, S\rangle, |2, \downarrow\rangle\} & \text{ odd} \end{aligned} \quad (2.60)$$

Here $|S\rangle = u|0\rangle - v|2\rangle$ is the ABS singlet. Using equation (2.59), we can calculate the effective couplings between the global even-parity states:

$$\begin{aligned} \langle 2, S | H_t | 0, S \rangle &= 0 \\ \langle \downarrow, \downarrow | H_t | 0, S \rangle &= vt_{\text{so}} \\ \langle 2, S | H_t | \downarrow, \downarrow \rangle &= -ut_{\text{so}} \end{aligned}$$

For the couplings of the global odd-parity states we have:

$$\begin{aligned}\langle 0, \downarrow | H_t | \downarrow, S \rangle &= ut \\ \langle 0, \downarrow | H_t | 2, \downarrow \rangle &= 0 \\ \langle 2, \downarrow | H_t | \downarrow, S \rangle &= vt\end{aligned}$$

We can now segment the Hamiltonian into even-, and odd-parity subspace and write the Hamiltonians in the basis of equation (2.60):

$$H_E = \begin{bmatrix} E_S & 0 & vt_{SO} \\ 0 & 2\mu_{QD} + E_C^{QD} + E_S & -ut_{SO} \\ vt_{SO} & -ut_{SO} & \mu_{QD} - E_Z + E_{\downarrow} \end{bmatrix}$$

and

$$H_O = \begin{bmatrix} E_{\downarrow} & ut & 0 \\ ut & \mu_{QD} - E_Z + E_S & vt \\ 0 & vt & 2\mu_{QD} + E_C^{QD} + E_{\downarrow} \end{bmatrix}$$

Here $E_S = E_C/2 + \mu - \sqrt{(\mu + E_C/2)^2 + \Gamma^2}$ and $E_{\downarrow} = \mu - E_Z/2$ are the ABS singlet and spin-down state energies respectively. The Hamiltonian in the full basis of the even-, and odd-parity states is then given by:

$$H_{\text{total}} = \begin{bmatrix} H_E & 0 \\ 0 & H_O \end{bmatrix} \quad (2.61)$$

We then diagonalize both blocks of the Hamiltonian separately to find the lowest-energy eigenstates: $H_{E/O}\psi_{E/O}^0 = E_{E/O}^0\psi_{E/O}^0$.

In figure 2.15c we show $E_O^0 - E_E^0$ for varying μ_{QD} and μ_{ABS} for $t_{SO} = t/2$ where $t = E_C^{QD}/10$. We see an anti-diagonal avoided crossing that indicates hybridization between the $|0, \downarrow\rangle$ and $|\downarrow, S\rangle$ states, which signals $ut > vt_{SO}$. We note that the global parity can also change with μ_{ABS} when the QD is off-resonance (e.g. at $\mu_{QD} = 0$). This is a result of the ABS having an odd ground state without coupling to the QD, due to finite charging and Zeeman energies. In figure 2.15d we show $E_O^0 - E_E^0$ for $t_{SO} = 3.5t$. The diagonal avoided crossing shows the hybridization between the $|0, S\rangle$ and $|\downarrow, \downarrow\rangle$ states, indicating $vt_{SO} > ut$. The size of the avoided crossing is smaller than in panel c. This is because $v \ll u$ for the ABS, which means that the singlet is dominated by the $|2\rangle$ state at this μ_{ABS} value. Then, t_{SO} has to be significantly larger than t to satisfy $vt_{SO} > ut$. In figure 2.15e we show $E_O^0 - E_E^0$ for $t_{SO} = 2.94t$. Instead of an avoided crossing, the zero-energy lines intersect to form a cross. This is a sign of the even and odd couplings having the same magnitude: $ut = vt_{SO}$. Here, the QD-ABS system has a degenerate even-odd ground state with a gap of magnitude vt_{SO} . We can see from the zero-energy lines that local changes of μ_{ABS} or μ_{QD} do not split the state. Just as in the case of QDs coupled through an ABS or a bulk superconductor, we can find Poor Man's Majorana zero modes in the QD-ABS system.

We note that for the proximitized QDs discussed in section 2.4.2, there was a limit on the maximum QD-ABS coupling, given by $t, t_{SO} < E_A$. Stronger interaction or a lower ABS excitation energy would make the ABS an explicit site of the chain, which is the

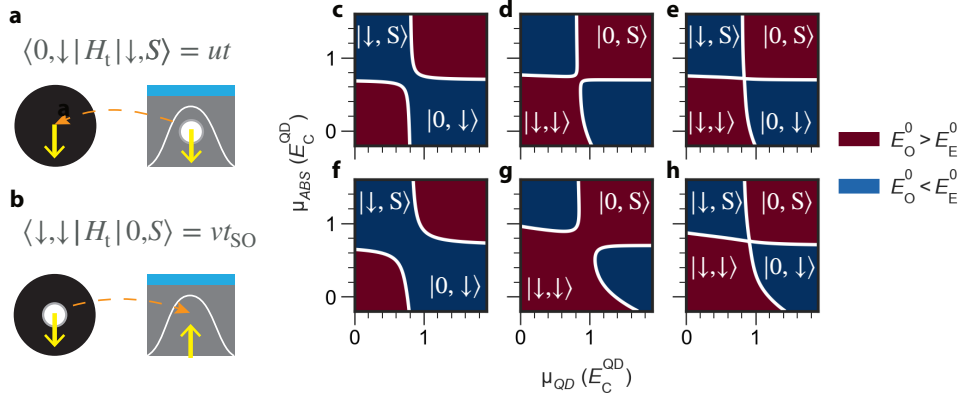


Figure 2.15: **A quantum dot-Andreev bound state minimal Kitaev chain.** **a.** Sketch of a spin-conserving tunneling process that couples the odd states of the QD-ABS system. **b.** Sketch of a spin-flipping process that couples the even states of the QD-ABS system. **c-e.** Difference between the lowest energy even-, and odd-parity states, $E_O^0 - E_E^0$, for varying μ_{QD} and μ_{ABS} for $t = E_C^{OD}/10$. We have used t_{SO}/t values of $\{1/2, 3.5, 3.22\}$. The superimposed text indicates the states that hybridize most strongly. The superimposed white lines indicate $E_O^0 = E_E^0$. **f-h.** $E_O^0 - E_E^0$ for varying μ_{QD} and μ_{ABS} for $t = E_C^{OD}/5$. We have used t_{SO}/t values of $\{1/2, 3.5, 2.94\}$.

principle of the QD-ABS Kitaev chain. In figure 2.15f-h., we show $E_O^0 - E_E^0$ for $t = E_C^{OD}/5$, which is twice as large as in panels c-e. We see that the zero-energy lines are more curved than in panel c. We attribute this to the larger total interaction strength, $t + t_{SO}$, which increases the induced gap of the QD due to coupling to the ABS (see equation (2.50)). In figure 2.15h, the zero-energy lines intersect to form a cross again. However, due to the curvature, a change of μ_{ABS} or μ_{QD} can now cause a splitting of the zero-energy state. The system is now so strongly hybridized, that a local perturbation has become a global perturbation. We can define a maximum coupling strength based on the spacing of the \downarrow and \uparrow excitations of the ABS. The energy difference of the two zero-crossings of the ABS is given by: $\Delta\mu_{ABS} = \sqrt{(E_C^{ABS} + E_Z)^2 - 4\Gamma^2}$. When $t, t_{SO} > \Delta\mu_{ABS}$, the QD-ABS hybridization becomes stronger than the level separation of the ABS. The system then becomes similar to a strongly-coupled double QD, where the system effectively acts as one large QD. Increasing t even more results in a larger induced gap on the QD, which can make an odd ground state energetically unfavorable.

The main advantage of a QD-ABS Kitaev chain over a proximitized QDs Kitaev chain is improved scalability. A three-site QD-ABS chain only needs 7 electrostatic gates, whereas a three-site chain with QDs as sites needs 4 extra gates. However, electrostatically tuning the QD-ABS chain to $ut = vt_{SO}$ is harder, as changes in gate voltages do not predictably affect t/t_{SO} . In a proximitized QD Kitaev chain, the elastic co-tunneling and crossed Andreev reflection rates can be tuned by changing the energy of the ABS that mediates them.

2.4.4 CHARGE SENSING A MINIMAL KITAEV CHAIN

In the previous sections, we have seen how a robust zero-energy excitation can emerge in various minimal Kitaev chain devices. This excitation signals the appearance of Poor Man's Majorana zero modes. Qubit states can be encoded in the parity of Majorana zero modes,

making parity readout crucial for quantum information experiments involving Poor Man's Majorana states. Proposed readout techniques include circuit quantum electrodynamics [56, 57], quantum capacitance [58] and charge sensing [59]. To read out parity using a charge measurement, it must first be converted into charge, and then sensed [60]. We can find the average charge of a proximitized QD Kitaev chain by computing the ground state occupation. We start by rewriting the Hamiltonian for two QDs coupled through an ABS (see section 2.4.2) in the interaction picture, and separating the even-, and odd-parity subspaces:

$$H_{\text{even}} = \begin{pmatrix} |S, S\rangle & |\downarrow\downarrow\rangle \end{pmatrix} \begin{pmatrix} 0 & \Gamma_E \\ \Gamma_E & \epsilon_L + \epsilon_R \end{pmatrix} \begin{pmatrix} |S, S\rangle \\ |\downarrow\downarrow\rangle \end{pmatrix} \quad (2.62)$$

$$H_{\text{odd}} = \begin{pmatrix} |\downarrow, S\rangle & |S, \downarrow\rangle \end{pmatrix} \begin{pmatrix} \epsilon_L & \Gamma_O \\ \Gamma_O & \epsilon_R \end{pmatrix} \begin{pmatrix} |\downarrow, S\rangle \\ |S, \downarrow\rangle \end{pmatrix} \quad (2.63)$$

We can then diagonalize each Hamiltonian and find the lowest-energy eigenstate:

$$H_{\text{even/odd}} \psi_{\text{even/odd}}^0 = E_{\text{even/odd}}^0 \psi_{\text{even/odd}}^0 \quad (2.64)$$

We show $E_{\text{odd}}^0 - E_{\text{even}}^0$ for varying μ_1 and μ_2 in figure 2.16a-c, for which we have used the same parameters as for figure 2.14e-f. As before, we see hybridization of different QD states

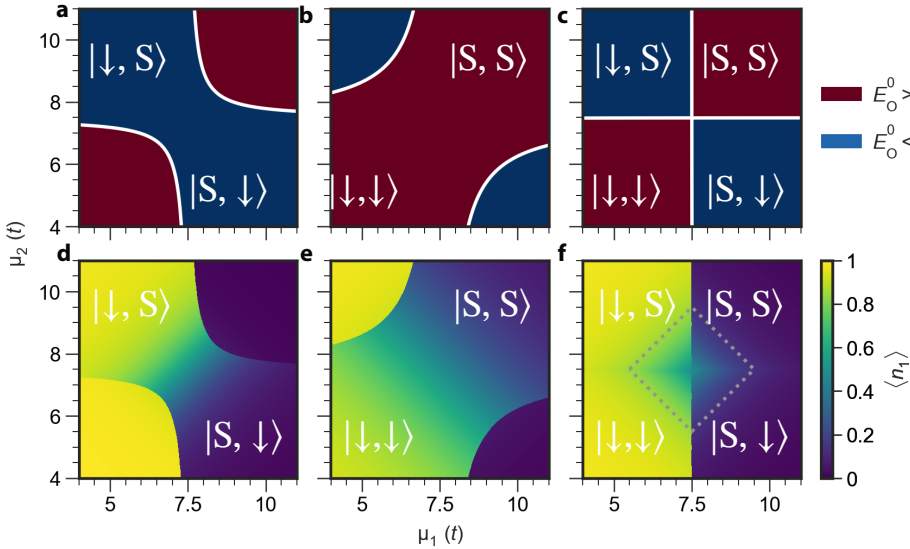


Figure 2.16: **Ground state parity and occupation of a proximitized quantum dot Kitaev chain.** a-c. Difference between the lowest energy even-, and odd-parity states, $E_O^0 - E_E^0$, for varying electrochemical potential of the QDs, μ_1 and μ_2 , for Δ_{SO}, t_{SO} values of $\{t/2, 2t, t\}$. The superimposed text indicates the states that hybridize most strongly. The superimposed white lines indicate $E_O^0 = E_E^0$. d-f. Ground state charge expectation of the left QD, $\langle n_1 \rangle$, for varying μ_1 and μ_2 corresponding to panels a-c. The superimposed rhombus indicates the region where $0.1 \leq \langle n_1 \rangle \leq 0.9$.

depending on the values of $t_{SO}, \Delta_{SO}, \Delta_0, t$. We can define operators for the local charge

expectation of the left QD as:

$$n_1^{\text{even}} = \begin{pmatrix} 2v_L \\ 1 \end{pmatrix} \quad (2.65)$$

$$n_1^{\text{odd}} = \begin{pmatrix} 1 \\ 2v_L \end{pmatrix} \quad (2.66)$$

Then we calculate the charge on the left QD depending on the ground state parity as:

$$\langle n_1 \rangle = \begin{cases} \psi_{\text{even}}^{0,\dagger} n_1^{\text{even}} \psi_{\text{even}}^0 & E_E^0 < E_O^0 \\ \psi_{\text{odd}}^{0,\dagger} n_1^{\text{odd}} \psi_{\text{odd}}^0 & E_E^0 > E_O^0 \end{cases}$$

We show $\langle n_1 \rangle$ corresponding to panels a-c in figure 2.16d-f. In panel d, we see that $\langle n_1 \rangle$ changes abruptly with μ_1 when μ_2 is off-resonance. This is due to the loading of electrons onto QD 1 as the QD level dips below the Fermi level. $\langle n_1 \rangle$ changes gradually along the anti-diagonal when QD2 is on resonance. This is due to the charge being localized on both QDs, as seen for the interdot transitions of normal double QDs (see section 2.1.2). In figure 2.16e, we see that $\langle n_1 \rangle$ changes gradually along the diagonal. This can be explained by the gradual evolution of the $|\downarrow, \downarrow\rangle$ state into the $|S, S\rangle$ state. A quasiparticle is removed from each QD, while their combined parity stays even. Unlike panel d, the total charge on the QDs is not conserved here. This is possible, as the QDs can exchange a Cooper pair with the grounded superconductor. In figure 2.16f we show $\langle n_1 \rangle$ for $\Gamma_E = \Gamma_O$. We see that $\langle n_1 \rangle$ changes abruptly due to μ_1 over most of the parameter space, except when QD2 is on resonance. There, a rhombus-shaped region where $\langle n_1 \rangle = 1/2$ is formed. For normal QDs, the region where $0.1 \leq \langle n_1 \rangle \leq 0.9$ is $8t$ by $8t$, which is indicated by the dashed gray line. Assuming a typical plunger gate lever arm for the QDs of $-\epsilon\alpha = 1/3$, and interaction strength, $2t = 2\Delta = 60 \mu\text{eV}$, this corresponds to a region in gate space of 0.72 mV by 0.72 mV , which is within the resolution of conventional digital-analog converters that are commonly used for voltage sources. This region corresponds to the cross formed by the Coulomb resonances of both QDs as seen in figure 2.16c. Here, there is a degenerate even-, and odd-parity ground state that signals the appearance of Majorana zero modes. For both parities, the charge expectation value is $1/2 \cdot 2v_L + 1/2$, as seen from equations (2.65) and (2.66). This means that parity can no longer be inferred from a charge measurement. To do so, we need to implement a parity-to-charge conversion procedure before measuring.

PARITY-TO-CHARGE CONVERSION

In a two-site Kitaev chain, the zero-energy state does not split upon changing the electrochemical potential of one QD. However, the wave function and charge expectation values do change. We illustrate this by considering a minimal Kitaev chain with normal QDs (see section 2.4.1) in the sweet spot ($t = \Delta$). When the left QD is at the Fermi level ($\mu_1 = 0$) and the right QD is detuned by an amount δ , we can write the Hamiltonian in the number basis

of the left and right QD: $\{|0,0\rangle, |1,0\rangle, |0,1\rangle, |1,1\rangle\}$ as:

$$H = \begin{bmatrix} 0 & 0 & 0 & t \\ 0 & 0 & t & 0 \\ 0 & t & \delta & 0 \\ t & 0 & 0 & \delta \end{bmatrix}$$

There is a doubly degenerate ground state with eigenvalues of $(\delta - \sqrt{\delta^2 + 4t^2})/2$, and corresponding eigenstates:

$$\begin{aligned} \psi_{\text{odd}} &= \begin{pmatrix} 0 & \frac{-\Lambda}{\sqrt{\Lambda^2+1}} & \frac{1}{\sqrt{|\Lambda|^2+1}} & 0 \end{pmatrix} \\ \psi_{\text{even}} &= \begin{pmatrix} \frac{-\Lambda}{\sqrt{\Lambda^2+1}} & 0 & 0 & \frac{1}{\sqrt{|\Lambda|^2+1}} \end{pmatrix} \end{aligned}$$

Here, we define $\Lambda \equiv (\delta + \sqrt{\delta^2 + 4t^2})/2t$, which can be interpreted as the degree to which the Majorana zero mode on the right QD is localized in different parts of the system. We can then write the charge expectation value of the left QD as:

$$\langle n_1 \rangle = \frac{1}{\Lambda^2 + 1} \begin{cases} 1 & \text{even GS} \\ \Lambda^2 & \text{odd GS} \end{cases}$$

In the odd ground state, detuning the right QD increases $\langle n_1 \rangle$. This is caused by the Majorana wave function “leaking” to the left QD, which is required for the particle conservation which is inherent to the odd ground state. In the even ground state, $\langle n_1 \rangle$ decreases upon increasing δ . The right QD becomes unoccupied as its energy is moved above the Fermi level. Because the $|0,0\rangle$ and $|1,1\rangle$ states are paired in the even ground state, the left QD will also become unoccupied, which violates particle conservation. In other words: ψ_{even} respects exchange symmetry when detuning one QD, while ψ_{odd} does not. Defining the operator \hat{P} that exchanges the electrons in the QDS, we find: $\psi_{\text{odd}} \hat{P} \psi_{\text{odd}}^\dagger = 2\Lambda/(\Lambda^2 + 1)$. Fundamentally, this means that the electrons in the QDs are indistinguishable particles only for $t = \delta$ when both QDs are kept at the Fermi level. The electrons in the QDs remain indistinguishable in the even ground state for $\delta \neq 0$. However, the even ground state does break particle conservation upon detuning one QD: $\psi_{\text{even}}(n_1 + n_2) \psi_{\text{even}}^\dagger = 2/(\Lambda^2 + 1)$. The condition $t = \Delta$ is special as both the even- and odd-parity ground state respect particle-conservation and exchange symmetry. To summarize: we can create a charge difference between the even and odd ground state by detuning one QD. The ground state parity can then be inferred by measuring charge on the other QD. We stress that the zero-energy does not split in the process.

We now apply this parity-to-charge conversion protocol to the proximitized QD Kitaev chain. In figure 2.17a, we schematically show a device design in which parity can be inferred from a local charge measurement using a single-lead QD as a charge sensor (see figure 2.3 for details). In figure 2.17b we show $\langle n_1 \rangle$, for varying μ_1 and μ_2 for $\Gamma_E = \Gamma_O$. We see the diamond-shaped region where $\langle n_1 \rangle = 1/2$ that signals a degenerate even-, and odd-parity ground state. In figure 2.17c we show $\langle E | n_1 | E \rangle$ and $\langle O | n_1 | O \rangle$, for varying μ_2 where we fix the left QD at the Fermi level $\mu_1 = E_C/2 = 7.5t$. Here, E and O are the degenerate even-, and odd-parity ground states. At $\mu_2 = E_C/2$ (gray hexagon), the even and odd ground states

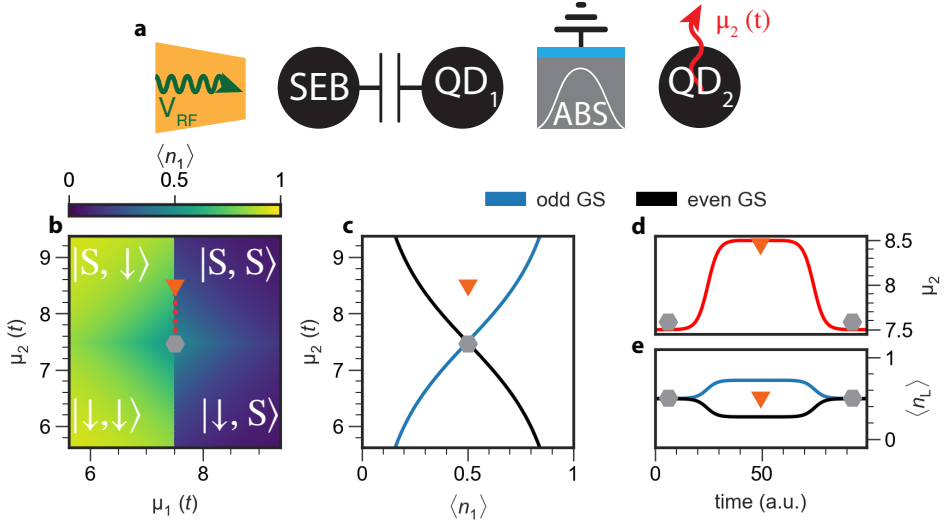


Figure 2.17: **Parity-to-charge conversion protocol in a minimal Kitaev chain using proximitized quantum dots.** **a.** A schematic diagram of the system. Two QDs are tunnel coupled to an ABS in a hybrid segment. The left QD is capacitively coupled to a single-electron box (SEB) charge sensor. The right QD is detuned over time with an amplitude $\mu_2(t)$. The SEB is tunnel-coupled to a normal lead which is connected to an RF-reflectometry set-up used to probe the resistance of the SEB. **b.** Ground state charge expectation of the left QD, $\langle n_1 \rangle$, for varying μ_1 and μ_2 for $\Gamma_E = \Gamma_O$. The superimposed text indicates the ground states. The orange triangle and gray hexagon indicate the readout and starting point of the protocol respectively. **c.** $\langle n_1 \rangle$ for the odd-, and even-parity ground states for varying μ_2 at $\mu_1 = E_C/2$. **d.** Schematic diagram of a readout pulse, where μ_2 is changed over time. **e.** $\langle n_1 \rangle$ for the odd-, and even-parity ground states as μ_2 changed over time.

have the same $\langle n_1 \rangle$. Heuristically, this can be seen as a manifestation of topology, where a local measurement of the system cannot detect Majorana zero modes. When the right QD is detuned, a difference in $\langle n_1 \rangle$ is created between the even- and odd-parity ground states. For $\mu_2 > 7.5t$, the right QD level is above the Fermi level, which causes it to become unoccupied. In the odd ground state, the left QD becomes occupied, as the total charge is conserved. In the even ground state, the left QD becomes unoccupied as well, as a Cooper pair is formed from an electron in each QD. In figure 2.17d, we show a pulse sequence of μ_2 that moves the right QD from the Fermi level (gray hexagon) to the readout point (orange triangle) and back again. We show the corresponding values of $\langle n_1 \rangle$ over the course of the pulse in figure 2.17e. At the readout point, the difference in $\langle n_1 \rangle$ between the even-, and odd-parity ground states can be observed. At this point, an RF reflectometry measurement of the SEB can infer the parity based on the measured charge. We note that away from the starting point (gray hexagon), a small change in μ_1 will split the zero-energy state. As the parity becomes easier to distinguish, charge noise will also affect the parity states more.

REFERENCES

- [1] Yuli V Nazarov and Yaroslav M Blanter. *Quantum transport: introduction to nanoscience*. Cambridge university press, 2009.
- [2] Ronald Hanson, Leo P Kouwenhoven, Jason R Petta, Seigo Tarucha, and Lieven MK Vandersypen. Spins in few-electron quantum dots. *Reviews of modern physics*, 79(4):1217, 2007.
- [3] H Van Houten, CWJ Beenakker, and AAM Staring. Coulomb-blockade oscillations in semiconductor nanostructures. *Single charge tunneling: Coulomb blockade phenomena in nanostructures*, pages 167–216, 1992.
- [4] Wilfred G Van der Wiel, Silvano De Franceschi, Jeroen M Elzerman, Toshimasa Fujisawa, Seigo Tarucha, and Leo P Kouwenhoven. Electron transport through double quantum dots. *Reviews of modern physics*, 75(1):1, 2002.
- [5] Jasper Van Veen, Damaz De Jong, Lin Han, Christian Prosko, Peter Krogstrup, John D Watson, Leo P Kouwenhoven, and Wolfgang Pfaff. Revealing charge-tunneling processes between a quantum dot and a superconducting island through gate sensing. *Physical Review B*, 100(17):174508, 2019.
- [6] Ph Lafarge, H Pothier, Edwin R Williams, D Esteve, C Urbina, and Michel H Devoret. Direct observation of macroscopic charge quantization. *Zeitschrift für Physik B Condensed Matter*, 85:327–332, 1991.
- [7] Fredrik Persson, CM Wilson, Martin Sandberg, Göran Johansson, and Per Delsing. Excess dissipation in a single-electron box: The sisyphus resistance. *Nano letters*, 10(3):953–957, 2010.
- [8] Ramón Aguado and Leo P Kouwenhoven. Double quantum dots as detectors of high-frequency quantum noise in mesoscopic conductors. *Physical Review Letters*, 84(9):1986, 2000.
- [9] L Peri, GA Oakes, L Cochrane, CJB Ford, and MF Gonzalez-Zalba. Beyond-adiabatic quantum admittance of a semiconductor quantum dot at high frequencies: Rethinking reflectometry as polaron dynamics. *arXiv preprint arXiv:2307.16725*, 2023.
- [10] MF Gonzalez-Zalba, S Barraud, AJ Ferguson, and AC Betz. Probing the limits of gate-based charge sensing. *Nature communications*, 6(1):6084, 2015.
- [11] Florian Vigneau, Federico Fedele, Anasua Chatterjee, David Reilly, Ferdinand Kuemmeth, M Fernando Gonzalez-Zalba, Edward Laird, and Natalia Ares. Probing quantum devices with radio-frequency reflectometry. *Applied Physics Reviews*, 10(2), 2023.
- [12] MG House, Ian Bartlett, Prasanna Pakkiam, Matthias Koch, Eldad Peretz, Joost van der Heijden, Takashi Kobayashi, Sven Rogge, and MY Simmons. High-sensitivity charge detection with a single-lead quantum dot for scalable quantum computation. *Physical Review Applied*, 6(4):044016, 2016.

- [13] Kazushige Machida and Fumiaki Shibata. Bound states due to resonance scattering in superconductor. *Progress of Theoretical Physics*, 47(6):1817–1823, 1972.
- [14] PG De Gennes and Daniel Saint-James. Elementary excitations in the vicinity of a normal metal-superconducting metal contact. *Phys. Letters*, 4, 1963.
- [15] L. Yu. Bound state in superconductors with paramagnetic impurities. *Acta Phys. Sin.*, 21:75–91, 1965.
- [16] Hiroyuki Shiba. Classical spins in superconductors. *Progress of theoretical Physics*, 40(3):435–451, 1968.
- [17] A.I. Rusinov. Superconductivity near a paramagnetic impurity. *JETP Lett.*, 9, 1969.
- [18] C Caroli, PG De Gennes, and J Matricon. Bound fermion states on a vortex line in a type ii superconductor. *Physics Letters*, 9(4):307–309, 1964.
- [19] AF Andreev et al. Thermal conductivity of the intermediate state of superconductors ii. *Sov. Phys. JETP*, 20:1490, 1965.
- [20] IO Kulik. Macroscopic quantization and the proximity effect in sns junctions. *Soviet Journal of Experimental and Theoretical Physics*, 30:944, 1969.
- [21] JD Pillet, CHL Quay, P Morfin, C Bena, A Levy Yeyati, and P Joyez. Andreev bound states in supercurrent-carrying carbon nanotubes revealed. *Nature Physics*, 6(12):965–969, 2010.
- [22] Alexandre Assouline, Cheryl Feuillet-Palma, Alexandre Zimmers, Hervé Aubin, Marco Aprili, and Jean-Christophe Harmand. Shiba Bound States across the Mobility Edge in Doped InAs Nanowires. *Physical Review Letters*, 119(9):097701, August 2017.
- [23] J. Barański and T. Domański. In-gap states of a quantum dot coupled between a normal and a superconducting lead. *Journal of Physics: Condensed Matter*, 25(43):435305, October 2013. Publisher: IOP Publishing.
- [24] Landry Bretheau. *Localized excitations in superconducting atomic contacts: probing the Andreev doublet*. PhD thesis, Ecole Polytechnique X, 2013.
- [25] Supriyo Datta and Philip F Bagwell. Can the bogoliubov–de gennes equation be interpreted as a ‘one-particle’ wave equation? *Superlattices and microstructures*, 25(5-6):1233–1250, 1999.
- [26] Jeroen Danon, Anna Birk Hellenes, Esben Bork Hansen, Lucas Casparis, Andrew P Higginbotham, and Karsten Flensberg. Nonlocal conductance spectroscopy of andreev bound states: symmetry relations and bcs charges. *Physical Review Letters*, 124(3):036801, 2020.
- [27] Philip Warren Anderson. Localized magnetic states in metals. *Physical Review*, 124(1):41, 1961.

- [28] Johannes Bauer, A Oguri, and AC Hewson. Spectral properties of locally correlated electrons in a bardeen–cooper–schrieffer superconductor. *Journal of Physics: Condensed Matter*, 19(48):486211, 2007.
- [29] Tobias Meng, Serge Florens, and Pascal Simon. Self-consistent description of andreev bound states in josephson quantum dot devices. *Physical Review B*, 79(22):224521, 2009.
- [30] Landry Bretheau, ÇÖ Girit, C Urbina, D Esteve, and H Pothier. Supercurrent spectroscopy of andreev states. *Physical Review X*, 3(4):041034, 2013.
- [31] Isidora Araya Day, Sebastian Miles, Daniel Varjas, and Anton R. Akhmerov. Pymablock, 6 2023.
- [32] V Yu Irkhin and SV Streltsov. S. vonsovsky and the dawn of the theory of strongly correlated systems. *Journal of Superconductivity and Novel Magnetism*, 35(8):2135–2140, 2022.
- [33] Ali Yazdani, BA Jones, CP Lutz, MF Crommie, and DM Eigler. Probing the local effects of magnetic impurities on superconductivity. *Science*, 275(5307):1767–1770, 1997.
- [34] Kasper Grove-Rasmussen, Henrik Ingerslev Jørgensen, Brian Møller Andersen, Jens Paaske, Thomas Sand Jespersen, Jesper Nygård, Karsten Flensberg, and Poul Erik Lindelof. Superconductivity-enhanced bias spectroscopy in carbon nanotube quantum dots. *Physical Review B*, 79(13):134518, 2009.
- [35] Daniel Loss and David P DiVincenzo. Quantum computation with quantum dots. *Physical Review A*, 57(1):120, 1998.
- [36] Lazar Lakic, Will Lawrie, et al. A proximitized quantum dot in germanium [forthcoming]. *arXiv preprint arXiv:2402.19382*, 2024.
- [37] Jun Kondo. Resistance minimum in dilute magnetic alloys. *Progress of theoretical physics*, 32(1):37–49, 1964.
- [38] Roman M Lutchyn, Jay D Sau, and S Das Sarma. Majorana fermions and a topological phase transition in semiconductor-superconductor heterostructures. *Physical review letters*, 105(7):077001, 2010.
- [39] Yuval Oreg, Gil Refael, and Felix Von Oppen. Helical liquids and majorana bound states in quantum wires. *Physical review letters*, 105(17):177002, 2010.
- [40] Eduardo JH Lee, Xiaocheng Jiang, Ramón Aguado, Charles M Lieber, Silvano De Franceschi, et al. Scaling of subgap excitations in a superconductor-semiconductor nanowire quantum dot. *Physical Review B*, 95(18):180502, 2017.
- [41] Jong Soo Lim, Rosa López, Ramón Aguado, et al. Shiba states and zero-bias anomalies in the hybrid normal-superconductor anderson model. *Physical Review B*, 91(4):045441, 2015.

- [42] Virgil V Baran, Emil JP Frost, and Jens Paaske. Surrogate model solver for impurity-induced superconducting subgap states. *Physical Review B*, 108(22):L220506, 2023.
- [43] Luka Pavešić, Ramón Aguado, and Rok Žitko. Quantum dot josephson junctions in the strong-coupling limit. *arXiv preprint arXiv:2304.12456*, 2023.
- [44] Rok Zitko. Superconducting quantum dot and the sub-gap states. *arXiv preprint arXiv:1901.01039*, 2019.
- [45] Luka Pavešić, Daniel Bauernfeind, et al. Subgap states in superconducting islands. *Physical Review B*, 104(24):L241409, 2021.
- [46] Vincent Bouchiat, D Vion, Ph Joyez, D Esteve, and MH Devoret. Quantum coherence with a single cooper pair. *Physica Scripta*, 1998(T76):165, 1998.
- [47] David J Griffiths. Introduction to electrodynamics, 2005.
- [48] A Yu Kitaev. Unpaired majorana fermions in quantum wires. *Physics-uspekhi*, 44(10S):131, 2001.
- [49] Jay D Sau and S Das Sarma. Realizing a robust practical majorana chain in a quantum-dot-superconductor linear array. *Nature communications*, 3(1):964, 2012.
- [50] Martin Leijnse and Karsten Flensberg. Parity qubits and poor man’s majorana bound states in double quantum dots. *Physical Review B*, 86(13):134528, 2012.
- [51] Hoi-Yin Hui, Jay D Sau, and S Das Sarma. Bulk disorder in the superconductor affects proximity-induced topological superconductivity. *Physical Review B*, 92(17):174512, 2015.
- [52] Chun-Xiao Liu, A Mert Bozkurt, Francesco Zatelli, Sebastiaan LD ten Haaf, Tom Dvir, and Michael Wimmer. Enhancing the excitation gap of a quantum-dot-based kitaev chain. *arXiv preprint arXiv:2310.09106*, 2023.
- [53] Chun-Xiao Liu, Guanzhong Wang, Tom Dvir, and Michael Wimmer. Tunable superconducting coupling of quantum dots via andreev bound states in semiconductor-superconductor nanowires. *Physical review letters*, 129(26):267701, 2022.
- [54] Alberto Bordin, Guanzhong Wang, Chun-Xiao Liu, Sebastiaan LD Ten Haaf, Nick Van Loo, Grzegorz P Mazur, Di Xu, David Van Driel, Francesco Zatelli, Sasa Gazibegovic, et al. Tunable crossed andreev reflection and elastic cotunneling in hybrid nanowires. *Physical Review X*, 13(3):031031, 2023.
- [55] Sebastian Miles, David van Driel, Michael Wimmer, and Chun-Xiao Liu. Kitaev chain in an alternating quantum dot-andreev bound state array. *arXiv preprint arXiv:2309.15777*, 2023.
- [56] LC Contamin, Matthieu R Delbecq, B Douçot, Audrey Cottet, and Takis Kontos. Hybrid light-matter networks of majorana zero modes. *npj Quantum Information*, 7(1):171, 2021.

- [57] M Hinderling, SC ten Kate, DZ Haxell, M Coraiola, S Paredes, E Cheah, F Krizek, R Schott, W Wegscheider, D Sabonis, et al. Flip-chip-based fast inductive parity readout of a planar superconducting island. *arXiv preprint arXiv:2307.06718*, 2023.
- [58] Stephan Plugge, Asbjørn Rasmussen, Reinhold Egger, and Karsten Flensberg. Majorana box qubits. *New Journal of Physics*, 19(1):012001, 2017.
- [59] David Aasen, Michael Hell, Ryan V Mishmash, Andrew Higginbotham, Jeroen Danon, Martin Leijnse, Thomas S Jespersen, Joshua A Folk, Charles M Marcus, Karsten Flensberg, et al. Milestones toward majorana-based quantum computing. *Physical Review X*, 6(3):031016, 2016.
- [60] Gábor Széchenyi and András Pályi. Parity-to-charge conversion for readout of topological majorana qubits. *Physical Review B*, 101(23):235441, 2020.

3

3

SPIN-FILTERED MEASUREMENTS OF ANDREEV BOUND STATES

Scientist alone is true poet he gives us the moon.

- Allen Ginsberg

Semiconductor nanowires coupled to superconductors can host Andreev bound states with distinct spin and parity, including a spin-zero state with an even number of electrons and a spin-1/2 state with odd-parity. Considering the difference in spin of the even and odd states, spin-filtered measurements can reveal the underlying ground state. To directly measure the spin of single-electron excitations, we probe an Andreev bound state using a spin-polarized quantum dot that acts as a bipolar spin filter, in combination with a non-polarized tunnel junction in a three-terminal circuit. We observe a spin-polarized excitation spectrum of the Andreev bound state, which can be fully spin-polarized, despite strong spin-orbit interaction in the InSb nanowires. Decoupling the hybrid from the normal lead causes a current blockade, by trapping the Andreev bound state in an excited state. Spin-polarized spectroscopy of hybrid nanowire devices, as demonstrated here, is proposed as an experimental tool to support the observation of topological superconductivity.

3.1 INTRODUCTION

Low-dimensional III-V semiconductors proximitized via coupling to superconductors have been researched extensively in recent decades [1, 2]. Interest in these hybrid systems is a result of their gate-tunability, strong response to magnetic fields, and large spin-orbit interaction, all combined with superconductivity [3, 4]. This makes superconductor-semiconductor hybrids a candidate for creating a topological superconducting phase hosting Majorana zero modes. However, the intrinsic disorder in these systems can lead to localized Andreev bound states (ABSs) that reproduce many of the proposed Majorana signatures [5]. Proximitized InSb nanowires, such as those used in this work, can be tuned between three regimes of superconductor-semiconductor coupling using electrostatic gates [6, 7]. When the electron wavefunction is pushed toward the superconductor by negative gate voltage, the nanowire is fully proximitized and the density of states exhibits a hard superconducting gap. When the electron wavefunction is drawn into the semiconductor away from the superconductor by positive gate voltage, the proximity effect weakens and the density of states becomes gapless, i.e., the gap is soft. In the intermediate regime between these two, a confined hybrid nanowire hosts discrete subgap ABSs, whose electrochemical potential is controlled by gate. It was recently shown that an ABS spanning the entire superconductor-nanowire hybrid length gives rise to non-local transport phenomena [8–12], including equal-spin crossed-Andreev reflection [13], which enables the formation of a minimal Kitaev chain hosting Majorana bound states [14].

A confined semiconductor can host discrete quantum levels. Coupling the semiconductor to a superconductor allows the two to exchange a pair of electrons in a process known as Andreev reflection. This couples the even-occupation levels of the semiconductor, whereby they become ABSs with an induced pairing gap Γ [15–20]. While this exchange of electrons does not conserve charge, the parity of an ABS remains well-defined: even or odd. In the case of even parity, the ABS is in a singlet state which, within the atomic limit [15], is of the form:

$$|S\rangle = u|0\rangle - v|2\rangle \quad (3.1)$$

where $|0\rangle$ denotes the state in which the ABS is unoccupied and $|2\rangle$ the state in which it is occupied by two electrons. u and v are the relevant BCS coefficients [15, 21]. The odd-parity manifold consists of a doublet of two states, $|\downarrow\rangle$ and $|\uparrow\rangle$, which are degenerate

in the absence of an external magnetic field B . The energies of the even singlet and odd doublet states, as well as u and v , depend on μ_H , the energy of the uncoupled quantum level with respect to the superconductor Fermi energy. Both are shown schematically in Fig. 3.1a,b for Zeeman energy $E_Z = 3\Gamma$. A finite Zeeman energy E_Z splits the doublet states in energy, while the singlet does not disperse (Fig. 3.1c). An ABS can be excited from its ground state to an excited state of opposite parity by receiving or ejecting a single electron from a nearby reservoir. This parity-changing process requires an energy ξ , the energy difference between the ground and excited states, as indicated in Fig. 3.1a,c. These excitation energies are detected as conductance resonances in conventional tunneling spectroscopy measurements [8, 22–26]. The ABS resonances split with an applied magnetic field when the ground state is even and disperse to higher energy with an odd ground state [23]. These ABS excitations are believed to be spin-polarized as they arise from transitions between spinless and spin-polarized many-body states. Spin polarization weakens in the presence of spin-orbit coupling, where ABSs become admixtures of both spins and different orbital levels [27]. A pseudo-spin replaces spin as the quantum number defining the doublet states, and complete spin-polarization along the applied field direction is no longer expected [28]. Measurement of the spin polarization of ABS excitations may thus reveal the presence of spin-orbit coupling in hybrid systems. So far, spin-polarized spectroscopy of comparable Yu-Shiba-Rusinov states [29–31] has indeed revealed signatures of finite spin polarization on ferromagnetic adatoms [32–35]. It was further argued that the observation of fully spin-polarized zero-energy edge modes in ferromagnetic chains is a strong signature of a topological phase [36, 37].

In this work, we measure the spin-polarized excitation spectrum of a hybrid InSb nanowire hosting an ABS. This is done using a three-terminal setup consisting of a grounded superconductor–semiconductor hybrid tunnel-coupled on one side to a spin-polarized quantum dot (QD) and on the other side to a conventional tunnel junction. At low magnetic fields, we show complete spin polarization of the ABS, which reverses with increasing fields. At even higher fields, we observe a persistent, spin-polarized zero-bias peak. Furthermore, we show that the complete spin polarization of the ABS is responsible for a transport blockade that can be lifted by coupling the ABS to a non-polarized electron reservoir. We refer readers to a simultaneous submission by Danilenko et al. [38] for another report reaching complementary conclusions.

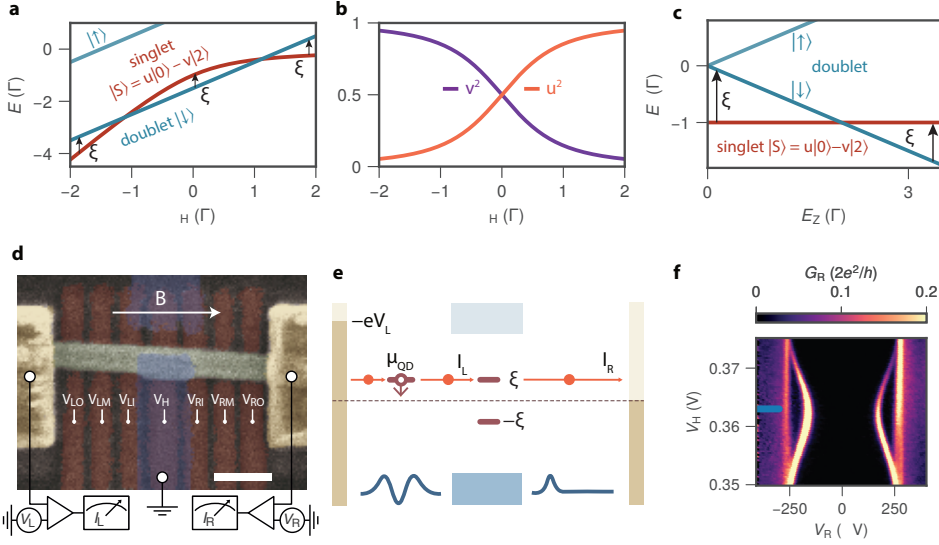


Figure 3.1: **Tunnel spectroscopy in a three-terminal InSb-Al nanowire.** **a.** Energy diagram showing the evolution of the many-body Andreev bound state (ABS) spectrum with electrochemical potential μ_H for $E_Z = 3\Gamma$. The arrows illustrate the parity-changing transition energies ξ from the ground state to the first excited state. **b.** The dependence of u^2 and v^2 on μ_H under the same conditions as **a.** **c.** Energy diagram showing the ABS spectrum with the applied magnetic field creating Zeeman splitting E_Z , at $\mu_H = 0$. All calculations in **a-c** are made in the atomic limit approximation with zero charging energy [15]. **d.** False-colored SEM image showing the device studied throughout the paper. Normal leads are yellow, bottom gates red, the InSb nanowire green and the grounded Al shell is blue. The normal contacts can be biased independently with respect to the grounded Al, the current is measured left and right simultaneously. Scale bar is 200 nm. **e.** Schematic diagram of electron transport using a quantum dot (QD) as a spin filter. Finger gates define a QD and a tunnel junction in the nanowire (blue lines at the bottom sketch their potential profiles). Lead electrochemical potentials are indicated by the dark yellow rectangles. The left lead is biased at a voltage V_L with respect to the grounded superconductor (blue). The QD states are at a gate-tunable energy μ_{QD} . ABS excitation energies are shown as brown, horizontal lines. The blue rectangles indicate the Al quasiparticle continuum. The potential landscape created by the gates is shown schematically by the blue lines at the bottom of the panel. **f.** Tunneling spectroscopy result G_R of the investigated ABS for varying gate voltage V_H for $V_{RO} = 500$ mV.

3.2 RESULTS AND DISCUSSION

3.2.1 DEVICE FABRICATION AND SET-UP

The fabrication of the reported device follows Ref. [13]. An InSb nanowire was placed on an array of bottom gates which are separated from the nanowire by a thin bilayer of atomic-layer-deposited (ALD) Al_2O_3 and HfO_2 dielectric of ~ 10 nm each. A thin Al segment of length roughly 200 nm was evaporated using a shadow-wall lithography technique [39, 40]. Normal Cr/Au contacts were fabricated on both sides of the device (more details on substrate fabrication can be found in Ref. [41]). Fig. 3.1d shows the device along with its gates. Throughout the experiment, we keep the middle superconductor grounded. Both left and right leads are voltage-biased independently with biases V_L and V_R , respectively. Similarly, the currents on the left and right leads (I_L and I_R , respectively) are measured simultaneously. The full circuit is shown in Supplementary Fig. 1 and is discussed in the methods.

Fig. 3.1e sketches the energy diagram of electron transport in the device. The left three gates define a QD in the InSb segment above them, whose electrochemical potential μ_{QD} is controlled linearly by V_{LP} . The three gates on the right side define a conventional tunnel junction. Using this circuit, the hybrid can be probed in two ways. When the QD is off-resonance and the left side does not participate in transport, conventional tunnel spectroscopy can be performed from the right. The resulting $G_{\text{R}} = dI_{\text{R}}/dV_{\text{R}}$ is shown in Fig. 3.1f, revealing a discrete sub-gap ABS, described by the intermediate regime of superconductor-semiconductor coupling [7]. The energy of the ABS disperses with V_{H} , which linearly relates to μ_{H} . All further results are obtained at $V_{\text{H}} = 363 \text{ mV}$ as indicated by the blue line unless otherwise specified. This places the ABS in the vicinity of its energy minimum. The second way of examining the ABS is performing QD spectroscopy from the left, by applying a fixed V_{L} and varying the probed energy by scanning μ_{QD} . Setting $-eV_{\text{L}} > \mu_{\text{QD}} = |\xi| > 0$ injects electrons into the ABS, while $-eV_{\text{L}} < \mu_{\text{QD}} = -|\xi| < 0$ extracts electrons from the ABS. In the presence of a Zeeman field, the QD charge transitions become spin-polarized when $2E_{\text{Z}} > e|V_{\text{L}}|$, allowing only spins of one type to tunnel across it [42]. As a result, the QD is operated as a bipolar spin filter with a finite energy resolution (see Methods and Supplementary Fig. 2). We use \uparrow, \downarrow to represent the two spin polarities and label the QD chemical potentials $\mu_{\text{QD}\uparrow, \downarrow}$ to distinguish between them where necessary.

We note that our spin probe consists of only a single quantum state which becomes fully spin-polarized under the presence of a large Zeeman field. This is different from conventional spin-polarized tunneling in scanning tunneling microscopy experiments, where an exemplary Fe tip achieves 40-45% polarization [43]. In a more recent study using a YSR-state on a STM tip as a spin probe, the filtering mechanism using a single quantum state is comparable to that reported in this paper [35].

3.2.2 ZEEMAN-DRIVEN SINGLET-DOUBLET TRANSITIONS

Fig. 3.2a shows tunneling spectroscopy of the particular ABS shown in Fig. 3.1f for varying B . The ABS conductance peak at $|V_{\text{R}}| \approx 200 \mu\text{V}$ Zeeman-splits into two resonances, one moving to higher and the other to lower energies. At $B \approx 300 \text{ mT}$, the low-energy states cross at zero energy. This crossing has been identified earlier [23] as a singlet-doublet transition, where the ground state of the hybrid becomes the odd-parity $|\downarrow\rangle$ state. Next, we perform QD spectroscopy by measuring I_{L} as a function of V_{LP} with fixed $V_{\text{L}} = \pm 400 \mu\text{V}$. For each spin, the spectrum is obtained by converting V_{LP} to μ_{QD} and then combining the two bias polarities (see Methods and Supplementary Fig. 2). Fig. 3.2b and c show the resulting QD spectroscopy for varying B . The QD functions as a \downarrow -filter (panel b) or \uparrow -filter (panel c) for $B > 100 \text{ mT}$ (blue dashed lines), where the QD Zeeman energy splitting exceeds $|eV_{\text{L}}|$ and only one spin is available for transport. The white triangle in Fig. 3.2b indicates missing data for $V_{\text{L}} > 0$. Finite current within this triangle arises due to peak-broadening in $V_{\text{L}} < 0$ data (see Supplementary Fig. 4 for details).

The peaks observed in QD spectroscopy are also visible in tunneling spectroscopy (see Supplementary Fig. 5 for comparison), although only one branch of the particle-hole-symmetric peaks in G_{R} remains for each QD spin. The down-filtered ABS feature (panel b) disperses with a negative slope. We understand this by examining the energy diagram in Fig. 3.1c. For $|B| < 300 \text{ mT}$, the non-dispersing singlet is the ground state and the first excited state is $|\downarrow\rangle$. Probing the ABS at positive energies injects spin-down electrons, which

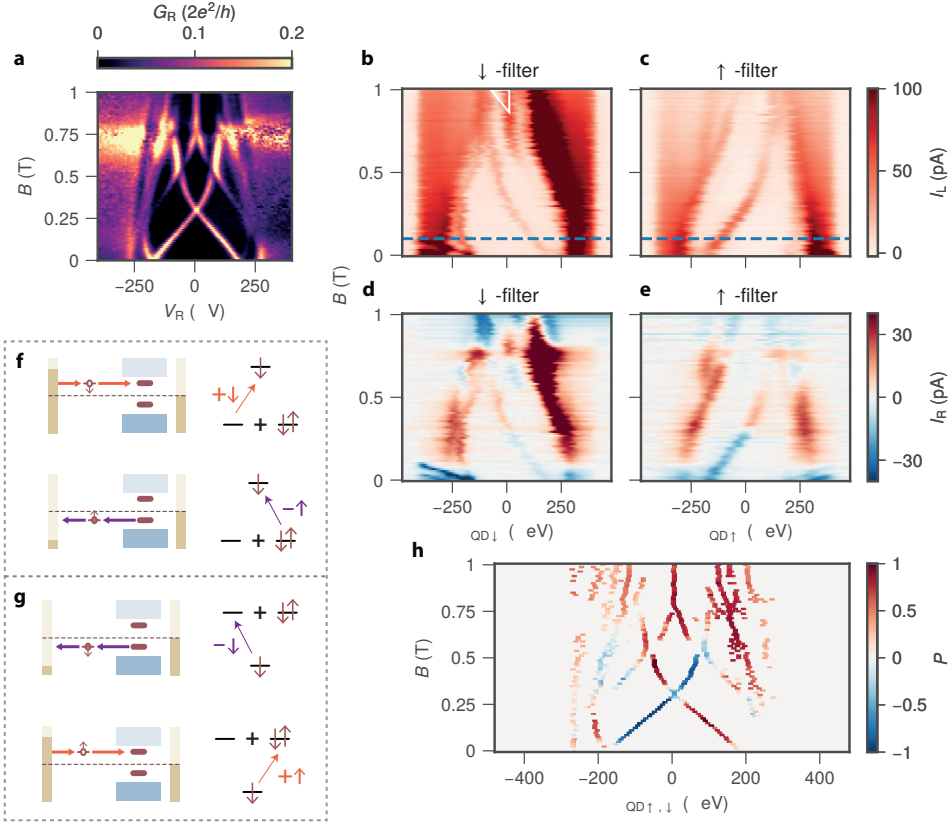


Figure 3.2: **Spin-polarized quantum dot spectroscopy of an Andreev bound state across the Zeeman-driven singlet-doublet transition.** **a.** Tunneling spectroscopy of the hybrid for B applied along the nanowire axis for $V_{RO} = 500$ mV and $V_H = 363$ mV. **b., c.** I_L vs μ_{QD} and B using the quantum dot (QD) as a \downarrow -filter (panel b) and \uparrow -filter (panel c). The blue dashed line at $B = 100$ mT indicates the field above which the QD becomes a spin filter. **d., e.** I_R vs μ_{QD} and B using the QD as a \downarrow -filter (panel d) and \uparrow -filter (panel e). **f.** Schematic energy diagram of spin-polarized excitations for the singlet ground state Andreev bound state (ABS). A down spin can tunnel into the ABS (upper) or an up spin can tunnel out (lower). **g.** Schematic energy diagram of spin-polarized excitations for the doublet ground state ABS. A down spin can tunnel out of the ABS (upper) or an up spin can tunnel into it (lower). **h.** The spin-polarization $P = (I^\downarrow - I^\uparrow)/(I^\downarrow + I^\uparrow)$ calculated from panels b and c at ABS energies found from panel a [44].

excites the singlet to $|\downarrow\rangle$ as illustrated in the upper part of Fig. 3.2f. Hence, these peaks in electron transport move down with increasing B . At $B \approx 300$ mT, the ABS undergoes a quantum phase transition, after which the ground state is $|\downarrow\rangle$. To transition from $|\downarrow\rangle$ to $|S\rangle$ without participation of spin-up electrons, a down-polarized electron must be first removed from the ABS, as shown in the upper part of Fig. 3.2g. Thus, the peak in current is found only for $\mu_{QD} < 0$. For $B < 0.6$ T, the \uparrow -filter data in panel c mirrors that of panel b. This symmetry is understood by comparing the lower parts of Fig. 3.2f, g to the respective upper ones. When the ABS allows injecting spin-down electrons, it also allows removing

spin-up ones, due to $|S\rangle$ being a superposition of empty and doubly-occupied states.

Thus far, we have focused on the excitation of the ABS. To complete a transport cycle, the ABS must also be able to relax back to the ground state. This can be done by either emitting or accepting electrons from the right lead through the tunnel junction. As a consequence, finite QD-current I_L is generally accompanied by finite I_R at the corresponding energy and field, as shown in fig 3.2d, e. We observe the same sub-gap features as in panels b,c confirming that these are extended ABSs that couple to both normal leads. Upon crossing the singlet-doublet transition, the ABS relaxation requires an opposite direction of electron flow, giving rise to the sign switching of I_R at $B = 0.3$ T [8, 10–13, 45]. The precise sign of I_R depends on μ_H as discussed in more detail in below.

We further quantify the spin-polarization of the ABS in Fig. 3.2h. We calculate the spin polarization $P = (I^\downarrow - I^\uparrow)/(I^\uparrow + I^\downarrow)$, where I^\uparrow, I^\downarrow indicates the current measured using the down- or up-polarized configuration, using the data from Fig. 3.2b, c (see Supplementary Fig. 5 for details and Methods for the definition of I^\uparrow, I^\downarrow). Before the singlet-doublet transition, we see a fully spin-polarized ABS with $P = \pm 1$. The spin polarization reverses immediately after the transition. At the singlet-doublet transition, we observe a zero-bias peak with $|P| < 1$ as both spins can participate in transport. The non-vanishing calculated P may be due to microscopic details in QD transport (see Methods).

We emphasize that we report on complete spin polarization, i.e., the rate of exciting the ABS to the $|\downarrow\rangle$ by injecting an up-polarized electron is below noise level, which is ~ 1 pA. This indicates that no noticeable spin rotation occurs during tunneling between the QD and ABS and their spin must be co-linear. Spin rotation is predicted to arise in the presence of strong spin-orbit coupling, which was observed in a similar setup in our previous work [13] (See Supplementary Fig. 7 for spin-polarized measurements conducted with that device, showing incomplete spin-polarization). We attribute the absence of spin rotation for this particular ABS to the large level spacing in both the QD (Supplementary Fig. 3) and the ABS (Fig. 3.1d) preventing efficient spin-mixing between different orbital states [27]. See Supplementary Fig. 9 for a large gate range measurement of QD levels splitting in field.

The presence of spin-flip tunneling, induced by the spin-orbit interaction, could also result in the lifting of the observed blockade [46]. Previously, such spin-flip tunneling in InAs-based double quantum dots was modulated by controlling the barrier separating the QDs [47]. In Supplementary Fig. 10 we present spin-polarized spectroscopy taken with a more positive tunnel gate value V_{LT} , showing a small lifting of the spin blockade. Since we do not expect the change in the tunnel gate voltage to significantly affect the QD or the ABS levels, we interpret the partial lifting of the spin blockade as resulting from spin-flip tunneling.

At higher fields ($B > 0.6$ T), we observe another low-energy ABS in tunneling spectroscopy. Above $B \approx 0.75$ T, this ABS sticks to zero energy and is completely down-polarized (Fig. 3.2h). While a persistent, spin-polarized zero-bias peak is a predicted signature of Majorana bound states [48–50], the short length of our hybrid section excludes this interpretation [51]. The interplay of spin-orbit coupling and confinement is a known mechanism for the formation of persistent zero-bias conductance peaks in QDs coupled to superconductors, given precise tuning of the QD chemical potential [28]. Such states develop a spin texture that has a global vanishing magnetic moment but is locally spin-polarized [52]. Our observation of a spin-polarized, persistent zero-bias peak is consistent with this inter-

pretation. We emphasize that this state is fine-tuned using V_H (see Supplementary Fig. 8 where for a different value of V_H the zero-bias peak does not persist over a large range of B) and further study is required to fully characterize such states.

3.2.3 GATE-DRIVEN SINGLET-DOUBLET TRANSITION

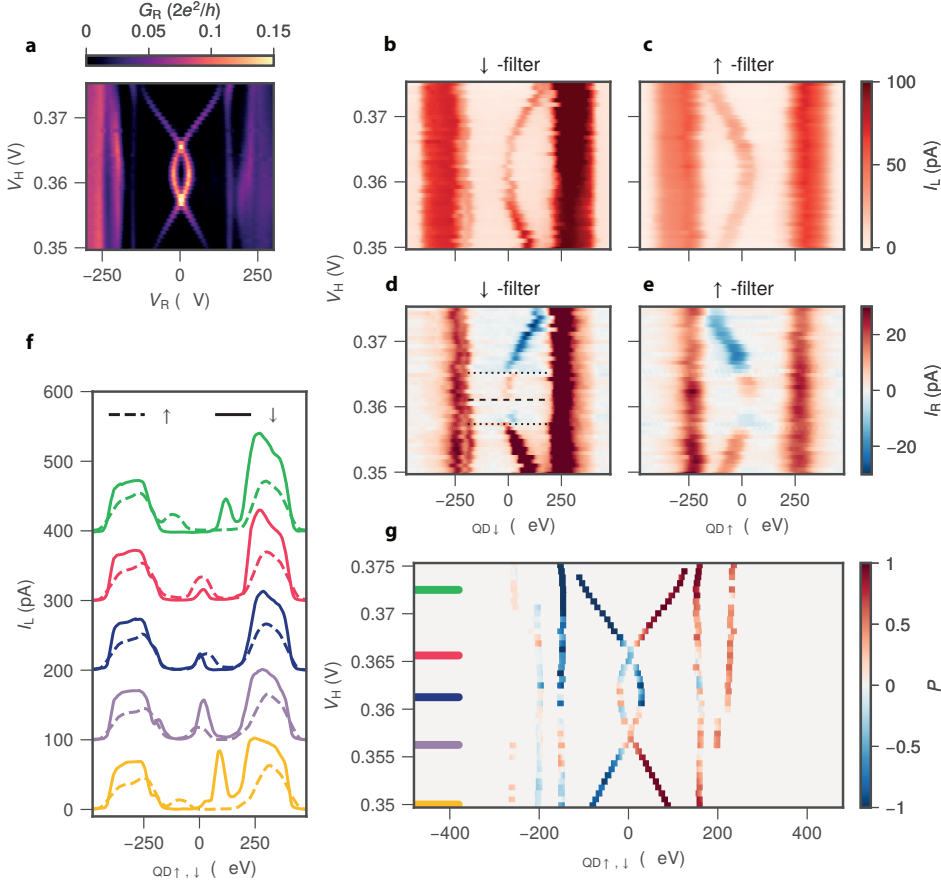


Figure 3.3: **Spin-polarized quantum dot spectroscopy of an Andreev Bound State during the gate-driven singlet-doublet transition.** **a.** Tunneling spectroscopy of the hybrid for varying V_H . The external magnetic field is fixed at $B = 350$ mT and $V_{RO} = 500$ mV. **b., c.** I_L vs μ_{QD} and V_H using the quantum dot (QD) as a \downarrow -filter (panel b) and \uparrow -filter (panel c). **d., e.** I_R vs μ_{QD} and V_H using the QD as a \downarrow -filter (panel d) and \uparrow -filter (panel e). The non-local current changes sign three times, twice at the singlet-doublet transitions (black dotted lines) and once at the Andreev bound state energy minimum (black dashed line). **f.** Linecuts of panels b and c at values of V_H indicated by the lines in g. Each pair of traces is offset by 100 pA for readability. **g.** The spin-polarization $P = (I^\downarrow - I^\uparrow)/(I^\downarrow + I^\uparrow)$ found from panels b and c.

The singlet-doublet phase transition reported above can also occur upon gate-tuning the electrochemical potential of the ABS, as illustrated in Fig. 3.1a. Fig. 3.3a shows tunneling spectroscopy for varying V_H at $B = 350$ mT. The ABS crosses zero at $V_H = 0.357$ V and

$V_H = 0.366$ V. Between these two crossings, the ground state of the ABS is $|\downarrow\rangle$. At higher and lower values of V_H , the ground state is the singlet $|S\rangle$. This is observed in the spin-polarized spectroscopy shown in Fig. 3.3b,c. $|S\rangle$ can only be excited to $|\downarrow\rangle$ when spin-down electrons tunnel into the hybrid or when spin-up electrons tunnel out. The doublet ground state shows the opposite: The \downarrow -filter peak in current is found only for $\mu_{QD} < 0$ and the \uparrow -filter peak only for $\mu_{QD} > 0$.

The non-local relaxation current I_R (panels d and e) shows three alternations between positive and negative currents, for both spin polarizations. At lower values of V_H , $|u|^2 \gg |v|^2$ and $|S\rangle \approx |0\rangle$. Therefore, the dominant relaxation mechanism from the excited $|\downarrow\rangle$ state to the ground state $|S\rangle$ is an electron tunneling out of the ABS to the right lead, giving rise to positive I_R . At high V_H , $|S\rangle \approx |2\rangle$ and relaxation entails electrons tunneling into the ABS and thus $I_R < 0$. At the two singlet-doublet transitions (dotted lines in panel d), the current sign reverses for the same reason discussed in Fig. 3.2d, e. At $V_H = 361$ mV (dashed line in panel d), μ_H crosses zero and the effective charge of the ABS, $|u|^2 - |v|^2$, switches sign. The non-local current also reverses direction, an effect investigated in detail in literature [8, 10–13, 45].

Fig. 3.3g shows the corresponding spin polarization that was computed likewise to Fig. 3.2h. Transport at positive μ_{QD} is seen to be fully down-polarized in the singlet ground state. Likewise, states are up-polarized for negative μ_{QD} . Polarization appears as incomplete in the $|\downarrow\rangle$ ground state. This is a measurement artifact due to using QDs as spin filters. The up-, and down-filter transport peaks have finite broadening due to temperature and coupling to the leads. For ABSs close to zero, this can result in peaks at negative and positive μ_{QD} overlapping, as seen in the dark blue linecut of Fig. 3.3f, giving imperfect polarization.

A similar problem occurs for states close to the gap edge. We see that the higher energy ABS always appears down-polarized at positive μ_{QD} and up-polarized at negative μ_{QD} . Close to the gap edge, broadening results in tunneling into the Al density of states, in addition to the ABS. The inability to distinguish between tunneling into the metallic and semiconductor density of states makes the interpretation of spin polarization at higher energies unreliable.

3.2.4 THE ANDREEV BOUND STATE RELAXATION MECHANISM

To emphasize the role of the right lead in relaxing the ABS, we show the effect of decoupling it from the hybrid. Fig. 3.4a shows G_R for varying V_R and V_{RO} at $B = 200$ mT, for which the ground state is singlet. Lowering the gate voltage V_{RO} gradually decouples the hybrid from the right normal lead, evident in the decay of G_R . For $V_{RO} < 0.28$ V, the right junction is fully pinched off. Fig. 3.4b shows the corresponding QD spectroscopy using the \uparrow -filter. The transport at energies exceeding the superconducting gap is virtually unaffected by the pinching-off of the normal lead. Strikingly, transport between the QD and the ABS is completely blocked for $V_{RO} < 0.28$ V. In addition, the non-local transport is suppressed at all energies once the right lead is pinched off (Fig. 3.4c). To understand this blockade, we first consider the full transport cycle. Fig. 3.4d, e illustrate the ABS excitation and relaxation processes. The ABS is excited from the singlet ground state to the $|\downarrow\rangle$ excited state by ejecting an electron into the \uparrow -filter QD (panel d). The spin-down electron in $|\downarrow\rangle$, however, cannot tunnel out into the spin-up left QD again. For the ABS to transition back into the

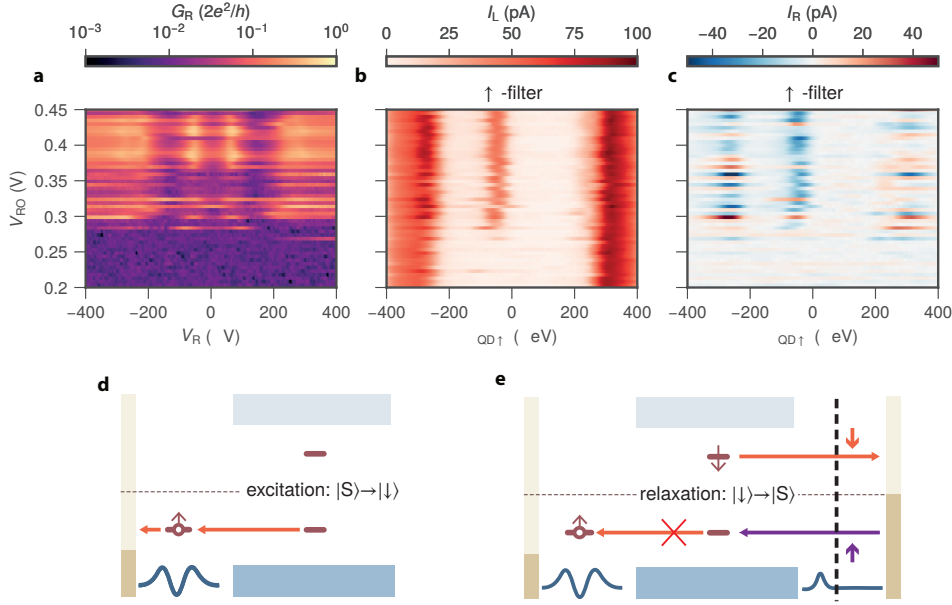


Figure 3.4: **Blocking the Andreev bound state excited state relaxation.** **a.** Tunneling-spectroscopy G_R as a function of V_R and V_{RO} at $B = 200$ mT for $V_H = 363$ mV. Transport through the right tunnel junction is pinched off for $V_{RO} \leq 0.28$ V. **b.** Quantum dot (QD) spectroscopy I_L for the \uparrow -filter for varying V_{RO} . Transport through the Andreev bound state (ABS) stops when the tunnel junction is pinched off. **c.** QD-spectroscopy I_R for the up-polarized QD level for varying V_{RO} . All non-local transport stops when the tunnel junction is pinched off. **d.** Schematic illustration of ABS excitation under the spin and bias setting in b, c. The ABS can only be excited from $|S\rangle$ to $|\downarrow\rangle$ via ejecting an electron into the QD. **e.** Schematic illustration of the ABS relaxation process. Transitioning from $|\downarrow\rangle$ back to $|S\rangle$ is only possible via electron exchange with the right lead and becomes blocked when parts to the right of the vertical black dashed line are pinched off.

ground state and restart the transport cycle, the right side has to participate in its relaxation. This is done by either receiving an up electron from the non-spin-polarized right lead or, interestingly, by emitting a down electron to the right lead (panel e). As discussed above, the singlet state is a superposition $|0\rangle$ and $|2\rangle$, coupled via Andreev reflection. Decoupling the non-polarized right lead from the hybrid removes the only source of relaxation of the ABS, resulting in the transport blockade seen in panel b. We emphasize that this differs from the spin-filtering effects discussed in previous sections, where incompatible spin states between the QD and the ABS prevent the excitation of the ABS. It is instead similar to the so-called Andreev blockade [53] where the excitation is allowed, but the relaxation process is suppressed. Our current noise level of ~ 1 pA gives a lower bound for the spin-relaxation time of ~ 100 ns. ABS parity lifetimes of $10\ \mu\text{s}$ or slower have been observed [54], which is significantly slower than we can resolve. We interpret this to mean that there are no mechanisms in our system that can relax the ABS in less than 100 ns.

3.3 CONCLUSION

In conclusion, we use a spin-polarized QD to characterize the spin-polarization of an ABS. We show complete spin polarization of the ABS excitation process, signaling the absence of significant spin-orbit coupling in the measured regime. We further observe the reversal of the ABS spin and charge when driving it through the singlet–doublet transition using applied magnetic field or gate voltage. Furthermore, we note the appearance of a spin-polarized zero-bias peak at higher magnetic fields. This work establishes the use of spin-polarized QDs as a spectroscopic tool allowing the study of the spin degree of freedom. This can be utilized in the future to study topological superconductors, where a reversal of the bulk spin-polarization is expected when the system is tuned to the topological regime [55]. The predicted spin polarization of the arising Majorana zero modes can also be observed in this way [56].

3.4 METHODS

3.4.1 DEVICE SET-UP

Supplementary Fig. 1 shows a sketch of the device with the electrical circuit used for the experiment. The Al was evaporated at two angles relative to the nanowire: 5 nm at 45° and 4.5 nm at 15°, forming a superconductor-semiconductor hybrid underneath. The Al shell is kept grounded during the experiment. Voltage bias is applied on either the left lead (V_L) or the right (V_R) while keeping the other lead grounded. The currents on both leads (I_L and I_R on the left and right leads, respectively) are measured simultaneously. A small RMS AC amplitude $V_R^{\text{AC}} = 4 \mu\text{eV}$ is applied on top of V_R for the tunneling spectroscopy measurements. All measurements are performed in a dilution refrigerator with a base temperature of 30 mK. The magnetic field is applied along the wire length. The quantum dot on the left was formed by creating two tunnel junctions using V_{LT} and V_{LO} . Its electrochemical potential is controlled by V_{LP} . The tunnel junction on the right is formed by creating a single tunnel junction with V_{RT} . The electrochemical potential of the hybrid section is set using V_H . Pinching off the tunnel junction as explained in Figure 4 was done by changing the value of V_{RO} .

3.4.2 QUANTUM DOT SPIN FILTER

The QD is characterized by measuring the current on the left lead (I_L) as a function of V_L and V_{LP} . Supplementary Fig. 2a shows a single Coulomb diamond with an orbital level spacing of $\delta = 3.5 \text{ meV}$, much larger than the superconducting gap and Zeeman energy used throughout the experiment. The large level spacing allows us to treat the QD as a single orbital near the Fermi energy, which is occupied by zero, one, or two electrons, as indicated in the figure (see measurement with an extended range of V_L and V_{LP} in Supplementary Fig. 3). From this measurement we find a lever-arm for V_{LP} of $\alpha = 0.4$. The current I_L is completely suppressed for $|eV_L| < 170 \mu\text{eV}$, indicating a hard gap and no local Andreev reflection for these gate settings [57]. The current on the right lead, I_R , which was measured simultaneously, shows similar features (Supplementary Fig. 2b). To analyze the data, we first convert V_{LP} to the electrochemical potential of the QD (μ_{QD}) at a fixed negative or positive $V_L = \pm 400 \mu\text{V}$ (orange and purple lines in panel a, respectively). For a given negative bias $-eV_L > 0$ (see schematic drawing in Supplementary Fig. 2c), the Fermi

energy of the lead lies above that of the hybrid segment. Hence, electrons are injected into the hybrid when μ_{QD} is within the transport window: $-eV_{\text{L}} > \mu_{\text{QD}} > 0$. We then convert the value of V_{LP} to μ_{QD} through $\mu_{\text{QD}} = -(\alpha e(V_{\text{LP}} - V_{\text{LP}}^0) + eV_{\text{L}})$, where V_{LP}^0 is the gate voltage at which the dot level is aligned with the applied bias. Note that $\mu_{\text{QD}} = -eV_{\text{L}}$ when the QD is aligned with the bias edge $V_{\text{LP}} = V_{\text{LP}}^0$. See Supplementary Fig. 4 for a comparison of raw and processed data. In Supplementary Fig. 2d we plot $|I_{\text{L}}|$ vs μ_{QD} . The current shows two peaks at $\sim 270 \mu\text{eV}$ and $\sim 170 \mu\text{eV}$, which we interpret as the bulk superconducting gap and the ABS energy, respectively. Similarly, for positive bias, the Fermi energy of the lead lies below that of the hybrid segment and electrons tunnel out of the hybrid segment when μ_{QD} is within the transport window (see schematic drawing in Supplementary Fig. 2e). In Supplementary Fig. 2f, we plot $|I_{\text{L}}|$ vs μ_{QD} and see features that are symmetric to those shown in panel d. We use the positive-bias data for $\mu_{\text{QD}} < 0$ and negative-bias data for $\mu_{\text{QD}} > 0$. Juxtaposing the two halves yields the full spectrum in Supplementary Fig. 2g. The spectrum obtained in this way is in qualitative agreement with the superimposed tunneling spectroscopy results at the same V_{H} . Therefore, measuring the current through the QD enables us to obtain the ABS spectrum [58, 59]. Next, we apply an external magnetic field to polarize the QD excitations. The even-to-odd QD charge transition ($V_{\text{LP}} \approx 369 \text{ mV}$) now involves only the addition and removal of electrons with spin \downarrow , while the odd-to-even transition ($V_{\text{LP}} \approx 379 \text{ mV}$) involves the addition and removal of electrons with spin \uparrow [27, 60]. As a result, the QD becomes a spin filter, allowing spin-polarized spectroscopy [42, 61].

3.4.3 ANALYSIS OF SPIN-POLARIZATION

To compute P for Fig. 3.2h and 3.3h, we first find peaks in tunneling spectroscopy using a standard peak-finding procedure provided by the SciPy python package [62]. The peak energies found from Fig. 3.2a are indicated by white dots in Supplementary Fig. 5a. Supplementary Fig. 5b,c shows these peak energies, overlaid on the \downarrow and \uparrow -filter data of Fig. 3.2. For each of these energies, we finally calculate $P = (I^{\downarrow} - I^{\uparrow}) / (I^{\downarrow} + I^{\uparrow})$. The data processing is done similarly for Fig. 3.3h.

This procedure correctly produces $P = \pm 1$ when spin-polarization is complete, i.e., $I^{\uparrow} = 0$ while $I^{\downarrow} \neq 0$ at a given μ_{QD} or vice versa. When polarization is incomplete, however, our calculated P may differ quantitatively from the true spin composition of the ABS. For example, measuring an entirely non-polarized $P = 0$ requires $I^{\uparrow} = I^{\downarrow}$. In practice, since the two spin filters are different QD charge degeneracies and differ in gate voltage, I^{\uparrow} is often different from I^{\downarrow} even at zero field due to electrostatic effects on the tunnel rate, leading to finite calculated $|P|$. This is indeed the case in Fig. 3.2b, c. From Fig. 3.2h, we see $|P| < 1$ at $B \approx 300 \text{ mT}$. Because the ABS has $P = \pm 1$ before and directly after the singlet-doublet transition, we conclude that its spin polarization, if any, must be weak.

3.5 DATA AVAILABILITY

The data generated in this study, as well as the code used to analyse and plot it have been deposited in a Zenodo repository that can be accessed freely at: <https://doi.org/10.5281/zenodo.7220682>.

3.6 EXTENDED DATA

3

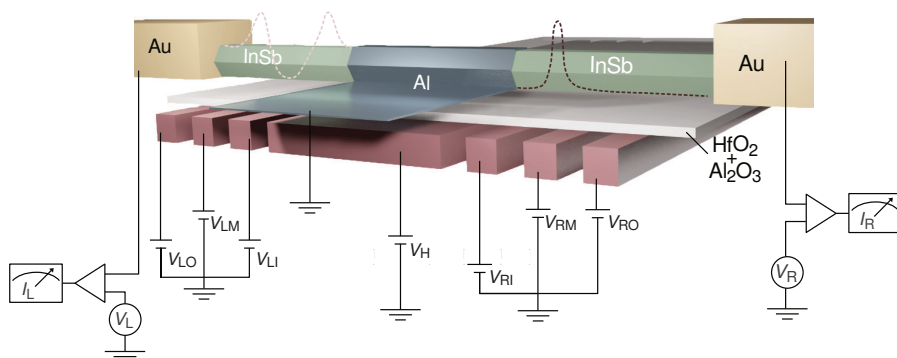


Figure 1: **Device schematic and measurement setup.** A quantum dot (QD) is defined by the three leftmost finger gates, V_{LO} , V_{LP} and V_{LI} , below the nanowire. The middle gate V_H controls the electrochemical potential of the hybrid InSb-Al nanowire. A tunnel junction is defined using V_{RT} . The voltages applied on each group of finger gates are schematically represented by the height of the voltage sources in the circuit diagram.

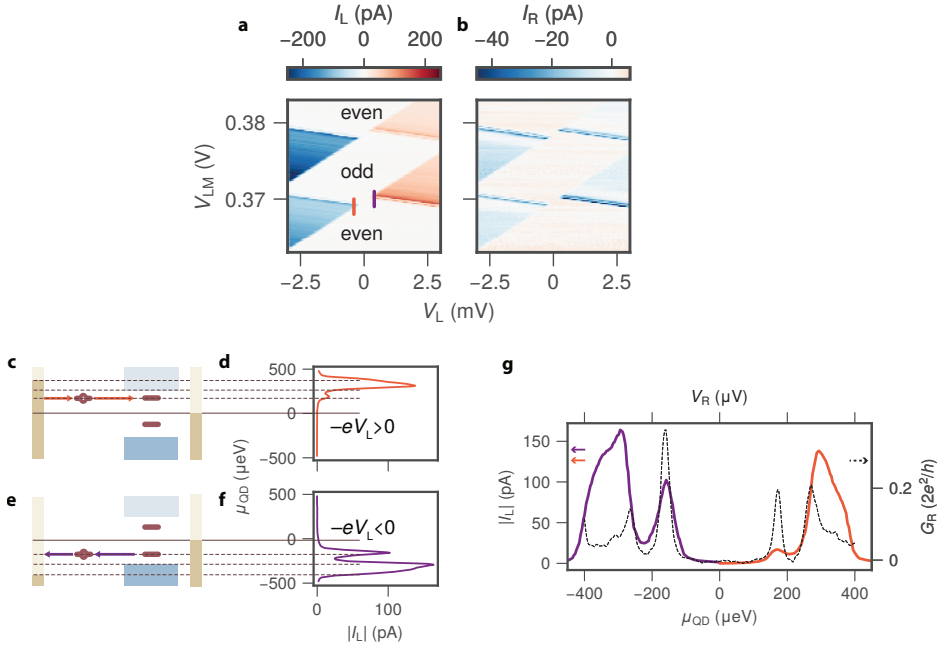


Figure 2: Quantum dot spectroscopy. **a.**, **b.** I_L and I_R vs V_L and V_{LP} with $V_R = 0$ showing the Coulomb diamond structure of the quantum dot (QD). **c.**, **e.** Energy diagrams schematically depicting QD spectroscopy. Negative (panel c) or positive (panel e) V_L is set to fix the left lead potential above the bulk gap ($e|V_L| > \Delta_{Al}$). μ_{QD} is tuned by varying V_{LP} . Current flows through the system when μ_{QD} aligns with the ABS or when aligned with the continuum states in the hybrid segment. **d.** **f.** Line-cut of $|I_L|$ taken from panel **a** at $V_L = \pm 400 \mu\text{eV}$. The gate voltage V_{LP} has been converted to the electrochemical potential of the QD μ_{QD} . **g.** The positive energy section of panel **d.** (orange line), the negative energy section of panel **f.** (purple line) merged to show the full density of states measured by QD spectroscopy. In addition, we show a linecut of G_R vs V_R (black dashed line), which was obtained with the tunnel junction when the QD was off-resonance and its lead grounded. See 4 for measurements of both polarities $V_L = \pm 400 \mu\text{eV}$ presented separately.

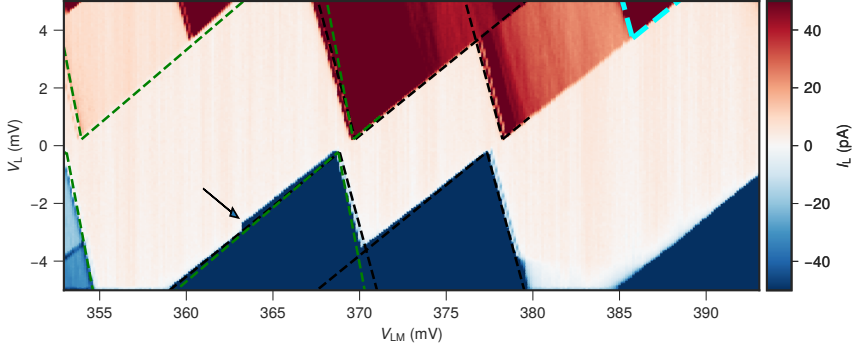


Figure 3: Local Coulomb diamonds A measurement of I_L for the quantum dot (QD) on the left side of the hybrid for $B = 0$. The bias V_L and dot gate V_{LP} are varied. There is a conversion factor between the QD electrochemical potential and the gate voltage. This is given by the capacitance between gate and dot relative to the total capacitance: $\alpha = C_G/C_{tot}$. Because Coulomb blockade blocks transport in a specific bias-gate window, it is possible to find this conversion factor. The black, dashed lines are a constant interaction model overlay for the $N + 1$ Coulomb diamond, whose transitions are used as a spin filter throughout the paper [63]. From the constant interaction model we obtain $\alpha = 0.4 \pm .01$ and a charging energy $E_C = 3.4$ meV. The cyan lines indicate the next orbital level, for which we find an orbital level spacing of $\delta = 3.5$ meV. The green, dashed lines are a constant interaction model overlay for the N th Coulomb diamond. From this model, we estimate an addition energy $E_{add} = E_C + \delta \approx 6.9$ meV. This is in agreement with the previously mentioned level spacing and charging energy. We do note that the slopes of the green and black dashed lines do not completely agree. We attribute this to a gate jump that occurred at the voltage indicated by the arrow.

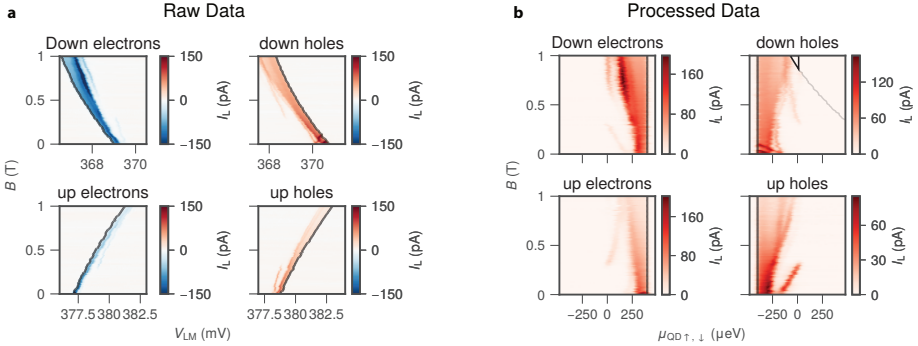


Figure 4: Quantum dot (QD) spectroscopy data processing. **a.** The raw data corresponding to main text Fig. 2. All electron data was measured at $-400 \mu\text{eV}$, the hole data at $400 \mu\text{eV}$. Magnetic field changes both the Andreev bound state (ABS) and QD level energies, hence, a slope between V_D and B is observed. I_L drops rapidly after the gate aligns the QD level with the bias window edge. This gate value V_{LP}^0 is used as a reference to convert the gate voltage to the electrochemical potential of the QD using $\mu_{QD} = -(\alpha e(V_{LP} - V_{LP}^0) + eV_L)$. The values found for V_{LP}^0 are indicated by the black line in the plots. Note that the QD resonance moves out of the measurement range for high fields for spin-down holes. This results in missing data after converting V_{LP}^0 to μ_{QD} . **b.** The processed data after the gate voltage is converted to the QD electrochemical potential. The field-dependence of the QD level energy is captured by V_{LP}^0 , which allows us to arrive at a spectrum of the ABS. The black lines indicate $\mu_{QD} = -eV_L$. Everything above the gray line in the spin-down hole data is out of range for V_{LP} . For the most part, this is no problem, considering there is no hole transport for $\mu_{QD} > 0$. However, the gray line crosses zero for high fields, which leads to the missing data as indicated by the black triangle. This corresponds to the white triangle in main text Fig. 2.

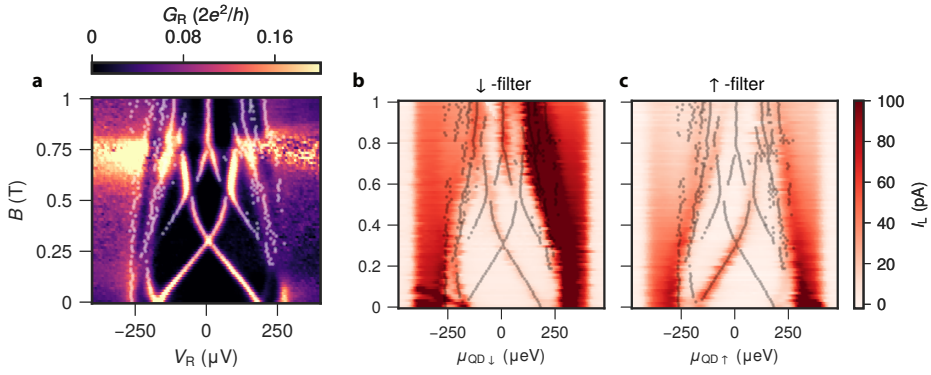


Figure 5: **Correlated quantum dot and tunneling spectroscopy (main text Fig. 2).** **a.** Tunneling spectroscopy of the hybrid for varying external field strength. Positions of peaks in tunneling spectroscopy are found using a standard peak-finding procedure provided by the SciPy python package [62]. **b., c.** I_L vs μ_{QD} and B using the \downarrow -filter (panel b) and \uparrow -filter (panel c). Both are overlaid with the peak energies found from tunneling spectroscopy in panel a.

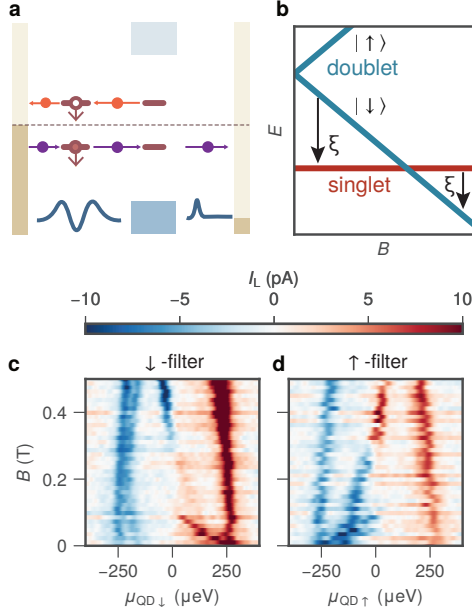


Figure 6: **Spin-polarization of the Andreev bound state relaxation.** **a.** Schematic of the transport cycle when the quantum dot (QD) lead is grounded and the tunnel junction bias is fixed at $eV_R = -400 \mu\text{V}$. The non-polarized tunnel junction can both excite and relax the Andreev bound state (ABS). When the QD is on-resonance with the ABS, it provides a second path for the excited ABS to relax. **b.** Schematic energy diagram showing the evolution of the many-body spectrum with the applied magnetic field. The arrows illustrate the transitions from the first excited state to the ground state. **c., d.** I_L for varying B and μ_{QD} using the QD as a \downarrow -filter (panel c) and \uparrow -filter (panel d). Similar to the results shown in Fig. 2, the spin-polarized measurement of the ABS shows only a single sub-gap peak traveling to lower energy and crossing zero at $B \approx 300 \text{ mT}$. At low fields, when the ground state of the ABS is singlet, and the excited state is $|\downarrow\rangle$, the ABS can relax by emitting a down-polarized electron or an up-polarized hole. At higher applied fields, when the ground state becomes doublet, the selection rules reverse. Contrary to our discussion so far, the absence of current when the ABS and QD spin are opposite is not associated with a transport blockade, as the tunneling between the normal lead and the ABS proceeds regardless of the presence of the QD.

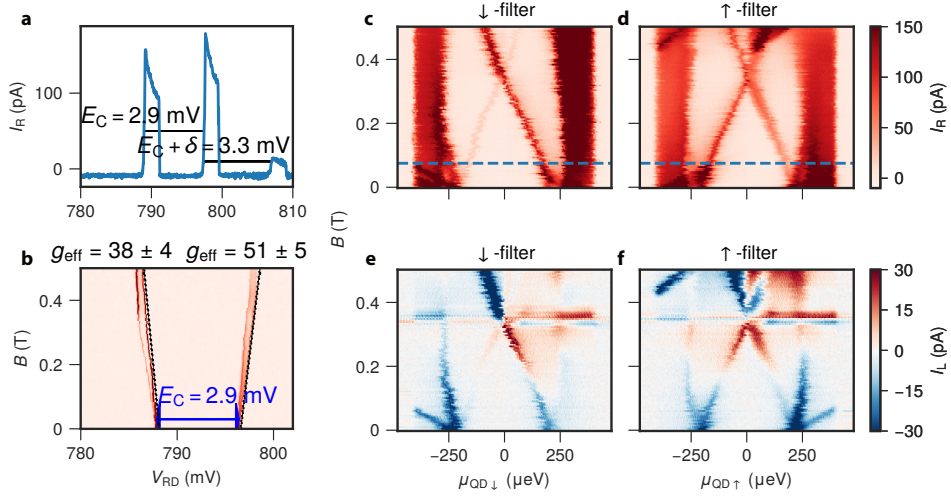


Figure 7: Spin-polarized spectroscopy of a second device. Measurements conducted on the device reported on in Ref. [13], which has an Al length of 180 nm, with an additional 2 Å of Pt grown at 30°. Here, the quantum dot (QD) formed on the right side of the Andreev bound state (ABS) served as the spin-filter for the spin-polarized spectroscopy. Compared to Ref. [13], here the barrier between the spin-polarized QD and the ABS was tuned to be much higher, reducing the transport between the QD and the ABS, and reducing the amount of spin-flip tunneling. **a.** The current through the QD I_R as a function of V_{RD} , for fixed $V_R = 1$ mV. The two resonances observed around $V_{RD} = 790$ mV and $V_{RD} = 798$ mV serve as our \downarrow and \uparrow spin filters respectively. Note the additional resonance at $V_{RD} = 808$ mV, that we attribute to the next orbital level. Spin-orbit coupling on the QD can give rise to spin mixing decreasing the efficiency of the \uparrow spin filter. **b.** The current through the QD I_R as a function of V_{RD} and B , for fixed $V_R = 0.3$ mV. The two resonances evolve with the expected trajectory showing their spin polarization. We determine E_C and g_{eff} using a lever arm of 0.34 for the \downarrow -filter and 0.37 for the \uparrow -filter. These are also used for panels c-f. **c., d.** I_R vs μ_{QD} and B using the QD as a \downarrow -filter (panel c) and \uparrow -filter (panel d). The QD acts as a spin filter for $B > 75$ mT, indicated by the blue line. Below the blue line, both QD spins are within the bias window and participate in transport. We note that the \downarrow filter shows the expected behavior as discussed in the main text, with some leakage current resulting from spin-flip tunneling or spin-orbit effect in the ABS itself. The \uparrow filter shows little signs of polarization. We attribute this to strong spin mixing within the QD making it a poor spin-filter. **e., f.** I_L vs μ_{QD} and B using the QD as a \downarrow -filter (panel e) and \uparrow -filter (panel f).

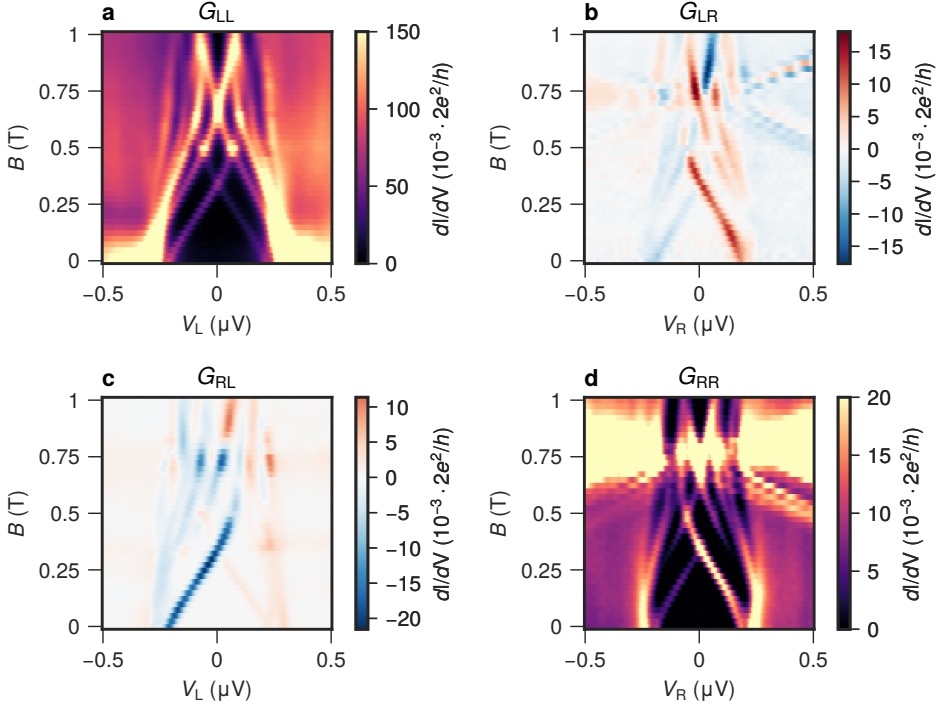


Figure 8: Full conductance matrix of the Andreev bound state studied in the main text for different gate settings. See ref [10] for details on the measurement technique. The gates forming a quantum dot to the left of the hybrid are reconfigured as a tunnel junction to measure non-local conductance. **a.** Local tunneling spectroscopy on the left of the hybrid $G_{LL} = dI_L/dV_L$ for varying B . **b.** Non-local conductance $G_{LR} = dI_L/dV_R$ for varying B . **c.** Non-local conductance $G_{RL} = dI_R/dV_L$ for varying B . **d.** Local tunneling spectroscopy on the right of the hybrid $G_{RR} = dI_R/dV_R$ for varying B .

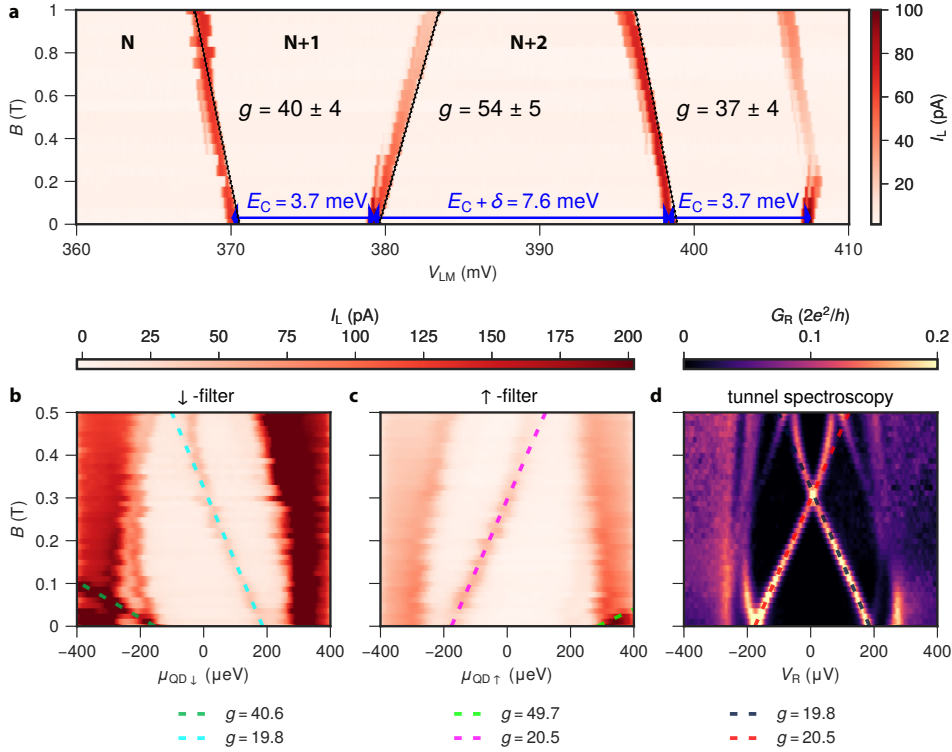


Figure 9: **g factors and quantum dot level spacing.** **a.** A measurement of I_L for the quantum dot (QD) on the left side of the hybrid for varying B and dot gate V_{LP} . Horizontal lines estimate spacing between adjacent QD levels. A lever arm of 0.4 found from Fig. 3 is used to convert gate values into units of energy, and calculate addition energies. The sloped lines estimate the g factor of the QD levels. **b., c.** A zoom in of Fig. 2b, c with dashed lines estimating the g factor of the QD and lowest-lying Andreev bound state (ABS). **d.** The lines corresponding to the ABS g factor overlaid on top of the tunnel spectroscopy of Fig. 2a.

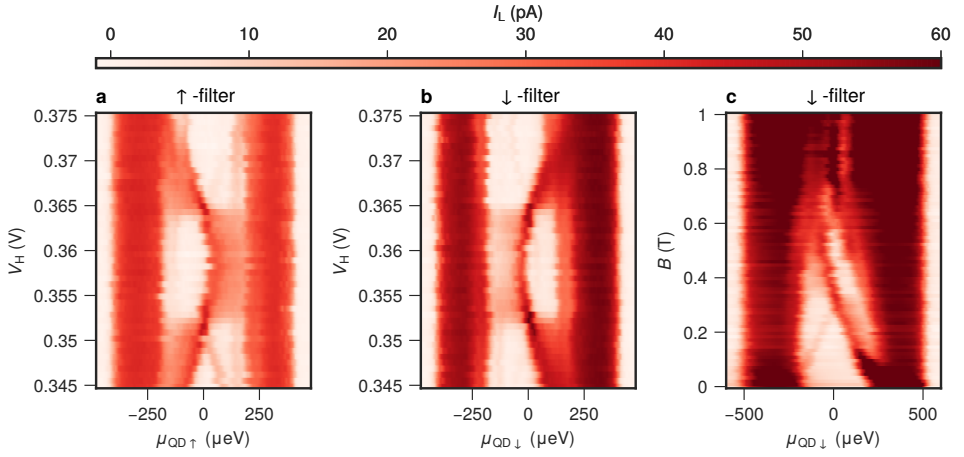


Figure 10: **Spin-polarized quantum dot spectroscopy of an Andreev bound state for different gate settings.** All main text figures were obtained for $V_{LT} = 135$ mV, while here we set $V_{LT} = 168$ mV.

a., b. I_L vs μ_{QD} and V_H using the quantum dot (QD) as a \downarrow -filter (panel a) and \uparrow -filter (panel b) for $B = 400$ mT. Peaks in I_L can be seen for both negative and positive μ_{QD} , indicating incomplete spin-polarization. We further see signatures of inelastic tunneling compatible with the higher tunneling rate between the QD and the Andreev bound state [64]. **c.** I_L vs μ_{QD} and B at using the QD as a \downarrow -filter for $V_H = 356$ mV. We observe incomplete spin-polarization as in panels a and b.

REFERENCES

- [1] Morteza Aghaee, Arun Akkala, Zulfi Alam, Rizwan Ali, Alejandro Alcaraz Ramirez, Mariusz Andrzejczuk, Andrey E. Antipov, Pavel Aseev, Mikhail Astafev, Bela Bauer, Jonathan Becker, Srinu Boddapati, Frenk Boekhout, Jouri Bommer, Tom Bosma, Leo Bourdet, Samuel Boutin, Philippe Caroff, Lucas Casparis, Maja Cassidy, Sohail Chatoor, Anna Wulf Christensen, Noah Clay, William S. Cole, Fabiano Corsetti, Ajuan Cui, Paschalis Dalampiras, Anand Dokania, Gijs de Lange, Michiel de Moor, Juan Carlos Estrada Saldaña, Saeed Fallahi, Zahra Heidarnia Fathabad, John Gamble, Geoff Gardner, Deshan Govender, Flavio Griggio, Ruben Grigoryan, Sergei Gronin, Jan Gukelberger, Esben Bork Hansen, Sebastian Heedt, Jesús Herranz Zamorano, Samantha Ho, Ulrik Laurens Holgaard, Henrik Ingerslev, Linda Johansson, Jeffrey Jones, Ray Kallaher, Farhad Karimi, Torsten Karzig, Cameron King, Maren Elisabeth Kloster, Christina Knapp, Dariusz Kocon, Jonne Koski, Pasi Kostamo, Peter Krogstrup, Mahesh Kumar, Tom Laeven, Thorvald Larsen, Kongyi Li, Tyler Lindemann, Julie Love, Roman Lutchyn, Morten Hannibal Madsen, Michael Manfra, Signe Markussen, Esteban Martinez, Robert McNeil, Elvedin Memisevic, Trevor Morgan, Andrew Mullally, Chetan Nayak, Jens Nielsen, William Hvidtfelt Padkær Nielsen, Bas Nijholt, Anne Nurmohamed, Eoin O'Farrell, Keita Otani, Sebastian Pauka, Karl Petersson, Luca Petit, Dmitry I. Pikulin, Frank Preiss, Marina Quintero-Perez, Mohana Rajpalke, Katrine Rasmussen, Davyd Razmadze, Outi Reentila, David Reilly, Richard Rouse, Ivan Sadovskyy, Lauri Sainiemi, Sydney Schreppler, Vadim Sidorkin, Amrita Singh, Shilpi Singh, Sarat Sinha, Patrick Sohr, Toma š Stankevič, Lieuwe Stek, Henri Suominen, Judith Suter, Vicky Svidenko, Sam Teicher, Mine Temuerhan, Nivetha Thiagarajah, Raj Tholapi, Mason Thomas, Emily Toomey, Shivendra Upadhyay, Ivan Urban, Saulius Vaitiekėnas, Kevin Van Hoogdalem, David Van Woerkom, Dmitrii V. Viazmitinov, Dominik Vogel, Steven Waddy, John Watson, Joseph Weston, Georg W. Winkler, Chung Kai Yang, Sean Yau, Daniel Yi, Emrah Yucelen, Alex Webster, Roland Zeisel, and Ruichen Zhao. Inas-al hybrid devices passing the topological gap protocol. *Phys. Rev. B*, 107:245423, Jun 2023.
- [2] Elsa Prada, Pablo San-Jose, Michiel WA de Moor, Attila Geresdi, Eduardo JH Lee, Jelena Klinovaja, Daniel Loss, Jesper Nygård, Ramón Aguado, and Leo P Kouwenhoven. From andreev to majorana bound states in hybrid superconductor–semiconductor nanowires. *Nature Reviews Physics*, 2(10):575–594, 2020.
- [3] Roman M Lutchyn, Erik PAM Bakkers, Leo P Kouwenhoven, Peter Krogstrup, Charles M Marcus, and Yuval Oreg. Majorana zero modes in superconductor–semiconductor heterostructures. *Nature Reviews Materials*, 3(5):52–68, 2018.
- [4] Yuval Oreg, Gil Refael, and Felix Von Oppen. Helical liquids and majorana bound states in quantum wires. *Physical review letters*, 105(17):177002, 2010.
- [5] Haining Pan and S Das Sarma. Physical mechanisms for zero-bias conductance peaks in majorana nanowires. *Physical Review Research*, 2(1):013377, 2020.

- [6] Andrey E Antipov, Arno Bargerbos, Georg W Winkler, Bela Bauer, Enrico Rossi, and Roman M Lutchyn. Effects of gate-induced electric fields on semiconductor majorana nanowires. *Physical Review X*, 8(3):031041, 2018.
- [7] N van Loo, GP Mazur, T Dvir, G Wang, RC Dekker, J-Y Wang, M Lemang, C Sfiligoj, A Bordin, D van Driel, et al. Electrostatic control of the proximity effect in the bulk of semiconductor-superconductor hybrids. *arXiv preprint arXiv:2211.06709*, 2022.
- [8] J. Schindele, A. Baumgartner, R. Maurand, M. Weiss, and C. Schönenberger. Nonlocal spectroscopy of Andreev bound states. *Physical Review B*, 89(4):045422, 2014.
- [9] G. Fülöp, F. Domínguez, S. d’Hollós, A. Baumgartner, P. Makk, M. H. Madsen, V. A. Guzenko, J. Nygård, C. Schönenberger, A. Levy Yeyati, and S. Csonka. Magnetic Field Tuning and Quantum Interference in a Cooper Pair Splitter. *Physical Review Letters*, 115(22):227003, 2015.
- [10] G. C. Ménard, G. L. R. Anselmetti, E. A. Martinez, D. Puglia, F. K. Malinowski, J. S. Lee, S. Choi, M. Pendharkar, C. J. Palmstrøm, K. Flensberg, C. M. Marcus, L. Casparis, and A. P. Higginbotham. Conductance-Matrix Symmetries of a Three-Terminal Hybrid Device. *Physical Review Letters*, 124(3):036802, 2020.
- [11] Jeroen Danon, Anna Birk Hellenes, Esben Bork Hansen, Lucas Casparis, Andrew P. Higginbotham, and Karsten Flensberg. Nonlocal Conductance Spectroscopy of Andreev Bound States: Symmetry Relations and BCS Charges. *Physical Review Letters*, 124(3):036801, 2020.
- [12] Andreas Pöschl, Alisa Danilenko, Deividas Sabonis, Kaur Kristjuhan, Tyler Lindemann, Candice Thomas, Michael J Manfra, and Charles M Marcus. Nonlocal conductance spectroscopy of andreev bound states in gate-defined inas/al nanowires. *arXiv preprint arXiv:2204.02430*, 2022.
- [13] Guanzhong Wang, Tom Dvir, Grzegorz P Mazur, Chun-Xiao Liu, Nick van Loo, Sebastiaan LD Ten Haaf, Alberto Bordin, Sasa Gazibegovic, Ghada Badawy, Erik PAM Bakkers, et al. Singlet and triplet cooper pair splitting in hybrid superconducting nanowires. *Nature*, pages 1–6, 2022.
- [14] Tom Dvir, Guanzhong Wang, Nick van Loo, Chun-Xiao Liu, Grzegorz P Mazur, Alberto Bordin, Sebastiaan LD Ten Haaf, Ji-Yin Wang, David van Driel, Francesco Zatelli, et al. Realization of a minimal kitaev chain in coupled quantum dots. *Nature*, 614(7948):445–450, 2023.
- [15] J Bauer, A Oguri, and A C Hewson. Spectral properties of locally correlated electrons in a Bardeen–Cooper–Schrieffer superconductor. *Journal of Physics: Condensed Matter*, 19(48):486211, 2007.
- [16] A Martín-Rodero and A Levy Yeyati. The Andreev states of a superconducting quantum dot: mean field versus exact numerical results. *Journal of Physics: Condensed Matter*, 24(38):385303, 2012.

- [17] J Barański and T Domański. In-gap states of a quantum dot coupled between a normal and a superconducting lead. *Journal of Physics: Condensed Matter*, 25(43):435305, 2013.
- [18] Nils Wentzell, Serge Florens, Tobias Meng, Volker Meden, and Sabine Andergassen. Magnetoelectric spectroscopy of Andreev bound states in Josephson quantum dots. *Physical Review B*, 94(8):085151, 2016.
- [19] Alexandre Assouline, Cheryl Feuillet-Palma, Alexandre Zimmers, Hervé Aubin, Marco Aprili, and Jean-Christophe Harmand. Shiba bound states across the mobility edge in doped inas nanowires. *Physical Review Letters*, 119(9):097701, 2017.
- [20] Rok Žitko. Superconducting quantum dot and the sub-gap states. *Spintronics XI*, 10732:107321N, 2018.
- [21] Michael Tinkham. *Introduction to superconductivity*. Courier Corporation, 2004.
- [22] R. S. Deacon, Y. Tanaka, A. Oiwa, R. Sakano, K. Yoshida, K. Shibata, K. Hirakawa, and S. Tarucha. Tunneling Spectroscopy of Andreev Energy Levels in a Quantum Dot Coupled to a Superconductor. *Physical Review Letters*, 104(7):076805, 2010.
- [23] Eduardo J. H. Lee, Xiaocheng Jiang, Manuel Houzet, Ramón Aguado, Charles M. Lieber, and Silvano De Franceschi. Spin-resolved Andreev levels and parity crossings in hybrid superconductor–semiconductor nanostructures. *Nature Nanotechnology*, 9(1):79–84, 2014.
- [24] Anders Jellinggaard, Kasper Grove-Rasmussen, Morten Hannibal Madsen, and Jesper Nygård. Tuning Yu-Shiba-Rusinov states in a quantum dot. *Physical Review B*, 94(6):064520, 2016.
- [25] J. Gramich, A. Baumgartner, and C. Schönenberger. Andreev bound states probed in three-terminal quantum dots. *Physical Review B*, 96(19):195418, 2017.
- [26] Tom Dvir, Marco Aprili, Charis H. L. Quay, and Hadar Steinberg. Zeeman tunability of Andreev bound states in van der Waals tunnel barriers. *Physical Review Letters*, 123(21):217003, 2019.
- [27] R. Hanson, L. P. Kouwenhoven, J. R. Petta, S. Tarucha, and L. M. K. Vandersypen. Spins in few-electron quantum dots. *Reviews of Modern Physics*, 79(4):1217–1265, 2007.
- [28] Christopher Reeg, Olesia Dmytruk, Denis Chevallier, Daniel Loss, and Jelena Klinovaja. Zero-energy Andreev bound states from quantum dots in proximitized Rashba nanowires. *Physical Review B*, 98(24):245407, 2018.
- [29] L Yu. Bound state in superconductors with paramagnetic impurities. *Acta Phys. Sin.*, 21:75–91, 1965.
- [30] Hiroyuki Shiba. Classical spins in superconductors. *Progress of theoretical Physics*, 40(3):435–451, 1968.
- [31] AI Rusinov. Superconductivity near a paramagnetic impurity. *JETP Lett.*, 9, 1969.

- [32] Dongfei Wang, Jens Wiebe, Ruidan Zhong, Genda Gu, and Roland Wiesendanger. Spin-polarized yu-shiba-rusinov states in an iron-based superconductor. *Physical Review Letters*, 126(7):076802, 2021.
- [33] L Cornils, A Kamlapure, L Zhou, Saurabh Pradhan, AA Khajetoorians, Jonas Fransson, J Wiebe, and R Wiesendanger. Spin-resolved spectroscopy of the yu-shiba-rusinov states of individual atoms. *Physical review letters*, 119(19):197002, 2017.
- [34] Alexander V Balatsky, Ilya Vekhter, and Jian-Xin Zhu. Impurity-induced states in conventional and unconventional superconductors. *Reviews of Modern Physics*, 78(2):373, 2006.
- [35] Lucas Schneider, Philip Beck, Jens Wiebe, and Roland Wiesendanger. Atomic-scale spin-polarization maps using functionalized superconducting probes. *Science Advances*, 7(4):eabd7302, 2021.
- [36] Stevan Nadj-Perge, Ilya K Drozdov, Jian Li, Hua Chen, Sangjun Jeon, Jungpil Seo, Allan H MacDonald, B Andrei Bernevig, and Ali Yazdani. Observation of majorana fermions in ferromagnetic atomic chains on a superconductor. *Science*, 346(6209):602–607, 2014.
- [37] Sangjun Jeon, Yonglong Xie, Jian Li, Zhijun Wang, B Andrei Bernevig, and Ali Yazdani. Distinguishing a majorana zero mode using spin-resolved measurements. *Science*, 358(6364):772–776, 2017.
- [38] Alisa Danilenko, Andreas Pöschl, Deividas Sabonis, Vasileios Vlachodimitropoulos, Candice Thomas, Michael J Manfra, and Charles M Marcus. Spin-resolved spectroscopy using a quantum dot defined in inas 2deg. *arXiv preprint arXiv:2212.10175*, 2022.
- [39] Sebastian Heedt, Marina Quintero-Pérez, Francesco Borsoi, Alexandra Fursina, Nick van Loo, Grzegorz P. Mazur, Michał P. Nowak, Mark Ammerlaan, Kongyi Li, Svetlana Korneychuk, Jie Shen, May An Y. van de Poll, Ghada Badawy, Sasa Gazibegovic, Nick de Jong, Pavel Aseev, Kevin van Hoogdalem, Erik P. A. M. Bakkers, and Leo P. Kouwenhoven. Shadow-wall lithography of ballistic superconductor–semiconductor quantum devices. *Nature Communications*, 12(1):4914, 2021.
- [40] Francesco Borsoi, Grzegorz P. Mazur, Nick van Loo, Michał P. Nowak, Léo Bourdet, Kongyi Li, Svetlana Korneychuk, Alexandra Fursina, Ji-Yin Wang, Vukan Levajac, Elvedin Memisevic, Ghada Badawy, Sasa Gazibegovic, Kevin van Hoogdalem, Erik P. A. M. Bakkers, Leo P. Kouwenhoven, Sebastian Heedt, and Marina Quintero-Pérez. Single-Shot Fabrication of Semiconducting–Superconducting Nanowire Devices. *Advanced Functional Materials*, 31(34):2102388, 2021.
- [41] Grzegorz P. Mazur, Nick van Loo, Ji-Yin Wang, Tom Dvir, Guanzhong Wang, Aleksei Khindanov, Svetlana Korneychuk, Francesco Borsoi, Robin C. Dekker, Ghada Badawy, Peter Vinke, Sasa Gazibegovic, Erik P. A. M. Bakkers, Marina Quintero-Pérez, Sebastian Heedt, and Leo P. Kouwenhoven. Spin-mixing enhanced proximity effect in

- aluminum-based superconductor–semiconductor hybrids. *Advanced Materials*, page 2202034, 2022.
- [42] R. Hanson, L. M. K. Vandersypen, L. H. Willems van Beveren, J. M. Elzerman, I. T. Vink, and L. P. Kouwenhoven. Semiconductor few-electron quantum dot operated as a bipolar spin filter. *Physical Review B*, 70(24):241304, 2004.
- [43] Roland Wiesendanger. Spin mapping at the nanoscale and atomic scale. *Reviews of Modern Physics*, 81(4):1495, 2009.
- [44] RJ Soulen Jr, JM Byers, MS Osofsky, B Nadgorny, T Ambrose, SF Cheng, Pr R Broussard, CT Tanaka, J Nowak, JS Moodera, et al. Measuring the spin polarization of a metal with a superconducting point contact. *science*, 282(5386):85–88, 1998.
- [45] Andrea Maiani, Max Geier, and Karsten Flensberg. Conductance-matrix symmetries of multiterminal semiconductor-superconductor devices. *arXiv*, 2022.
- [46] J Danon and Yu V Nazarov. Pauli spin blockade in the presence of strong spin-orbit coupling. *Physical Review B*, 80(4):041301, 2009.
- [47] A Pfund, I Shorubalko, K Ensslin, and R Leturcq. Suppression of spin relaxation in an inas nanowire double quantum dot. *Physical Review Letters*, 99(3):036801, 2007.
- [48] Doru Sticlet, Cristina Bena, and Pascal Simon. Spin and majorana polarization in topological superconducting wires. *Physical Review Letters*, 108(9):096802, 2012.
- [49] James J He, Tai Kai Ng, Patrick A Lee, and Kam Tuen Law. Selective equal-spin andreev reflections induced by majorana fermions. *Physical review letters*, 112(3):037001, 2014.
- [50] Arbel Haim, Erez Berg, Felix von Oppen, and Yuval Oreg. Signatures of majorana zero modes in spin-resolved current correlations. *Physical Review Letters*, 114(16):166406, 2015.
- [51] Tudor D. Stanescu, Roman M. Lutchyn, and S. Das Sarma. Dimensional crossover in spin-orbit-coupled semiconductor nanowires with induced superconducting pairing. *Phys. Rev. B*, 87:094518, Mar 2013.
- [52] Christian Jünger, Raphaëlle Delagrangé, Denis Chevallier, Sebastian Lehmann, Kimberly A Dick, Claes Thelander, Jelena Klinovaja, Daniel Loss, Andreas Baumgartner, and Christian Schönenberger. Magnetic-field-independent subgap states in hybrid rashba nanowires. *Physical Review Letters*, 125(1):017701, 2020.
- [53] Po Zhang, Hao Wu, Jun Chen, Sabbir A Khan, Peter Krogstrup, David Pekker, and Sergey M Frolov. Signatures of andreev blockade in a double quantum dot coupled to a superconductor. *Physical Review Letters*, 128(4):046801, 2022.
- [54] Gerbold C Ménard, Filip K Malinowski, Denise Puglia, Dmitry I Pikulin, Torsten Karzig, Bela Bauer, Peter Krogstrup, and Charles M Marcus. Suppressing quasiparticle poisoning with a voltage-controlled filter. *Physical Review B*, 100(16):165307, 2019.

- [55] Paweł Szumniak, Denis Chevallier, Daniel Loss, and Jelena Klinovaja. Spin and charge signatures of topological superconductivity in Rashba nanowires. *Physical Review B*, 96(4):041401, 2017.
- [56] Marcel Serina, Daniel Loss, and Jelena Klinovaja. Boundary spin polarization as a robust signature of a topological phase transition in Majorana nanowires. *Physical Review B*, 98(3):035419, 2018.
- [57] J. Gramich, A. Baumgartner, and C. Schönenberger. Subgap resonant quasiparticle transport in normal-superconductor quantum dot devices. *Applied Physics Letters*, 108(17):172604, 2016.
- [58] Christian Jünger, Andreas Baumgartner, Raphaëlle Delagrangé, Denis Chevallier, Sebastian Lehmann, Malin Nilsson, Kimberly A. Dick, Claes Thelander, and Christian Schönenberger. Spectroscopy of the superconducting proximity effect in nanowires using integrated quantum dots. *Communications Physics*, 2(1):76, 2019.
- [59] T. R. Devidas, Itai Keren, and Hadar Steinberg. Spectroscopy of NbSe₂ Using Energy-Tunable Defect-Embedded Quantum Dots. *Nano Letters*, 21(16):6931–6937, 2021.
- [60] R. M. Potok, J. A. Folk, C. M. Marcus, V. Umansky, M. Hanson, and A. C. Gossard. Spin and polarized current from Coulomb blockaded quantum dots. *Physical Review Letters*, 91(1):016802, 2003.
- [61] Patrik Recher, Eugene V. Sukhorukov, and Daniel Loss. Quantum Dot as Spin Filter and Spin Memory. *Physical Review Letters*, 85(9):1962–1965, 2000.
- [62] Pauli Virtanen, Ralf Gommers, Travis E Oliphant, Matt Haberland, Tyler Reddy, David Cournapeau, Evgeni Burovski, Pearu Peterson, Warren Weckesser, Jonathan Bright, et al. Scipy 1.0: fundamental algorithms for scientific computing in python. *Nature Methods*, 17(3):261–272, 2020.
- [63] Leo P Kouwenhoven, DG Austing, and Seigo Tarucha. Few-electron quantum dots. *Reports on Progress in Physics*, 64(6):701, 2001.
- [64] Toshimasa Fujisawa, Tjerk H Oosterkamp, Wilfred G Van der Wiel, Benno W Broer, Ramón Aguado, Seigo Tarucha, and Leo P Kouwenhoven. Spontaneous emission spectrum in double quantum dot devices. *Science*, 282(5390):932–935, 1998.

4

CHARGE SENSING THE PARITY OF AN ANDREEV MOLECULE

4

Yet, as has been said of him before, no theory of life seemed to him to be of any importance compared with life itself. He felt keenly conscious of how barren all intellectual speculation is when separated from action and experiment.

- Oscar Wilde

The proximity effect of superconductivity on confined states in semiconductors gives rise to various bound states such as Andreev bound states (ABSs), Andreev molecules and Majorana zero modes. While such bound states do not conserve charge, their Fermion parity is a good quantum number. One way to measure parity is to convert it to charge first, which is then sensed. In this work, we sense the charge of ABSs and Andreev molecules in an InSb-Al hybrid nanowire using an integrated quantum dot operated as a charge sensor. We show how charge sensing measurements can resolve the even and odd states of an Andreev molecule, without affecting the parity. Such an approach can be further utilized for parity measurements of Majorana zero modes in Kitaev chains based on quantum dots.

4.1 INTRODUCTION

Majorana zero modes (MZMs) are predicted to appear at the ends of a 1D chain of spin-polarized, electronic sites with superconducting pairing [1–3], which can be implemented using quantum dots (QDs) coupled to superconductors [4, 5]. Even a minimal, two-site Kitaev chain hosts MZMs in a parameter sweet spot [6–8], and was recently realized in a semiconductor-superconductor hybrid nanowire [9]. MZMs in Kitaev chains are predicted to be robust to local perturbations and obey non-Abelian statistics, allowing for the demonstration of Ising anyon fusion rules and braiding [10, 11]. Qubit states can be encoded in the parity of pairs of MZMs, making parity readout crucial for any quantum information experiment involving MZMs. Proposed readout techniques include circuit quantum electrodynamics [12, 13], quantum capacitance [14] and charge sensing [15]. To read out parity using a charge measurement, it must first be converted into charge, and then sensed [16]. Although charge sensing has been applied to semiconductor-superconductor hybrids before, it has never been used to detect fractional charge differences [17, 18]. This can potentially be necessary for parity readout in Kitaev chains, given that the charge difference between the even and odd ground states can range from 0 to $1e$. In this work, we present charge sensing measurements of a hybrid semiconductor-superconductor system. First, we measure the charge of an Andreev bound state (ABS) in its even and odd Fermion parity ground states. Then, we couple a QD to an ABS to form an Andreev molecule, and infer its ground state parity from tunnel spectroscopy and charge sensing measurements. As opposed to transport, charge sensing does not alter the parity itself, highlighting its potential as a tool for MZM parity readout in Kitaev chains.

4.2 RESULTS

4.2.1 DEVICE CHARACTERIZATION

figure 1a shows an SEM image of the device measured in this work. An InSb nanowire is placed on a thin layer of gate dielectric, below which are finger gates. See Refs. [19, 20] for details on device fabrication. The middle section of the wire, the hybrid segment, is contacted by a grounded Al thin film and hosts ABSs. We define a QD to the left of the hybrid segment by setting V_{LO} and V_{TL} to create tunnel junctions in the nanowire. We control the QD's electrochemical potential using V_{CS} and operate it as a single lead QD charge sensor (CS) [21]. The tunnel gate between the CS and hybrid segment is kept at a negative voltage $V_{TL} = -100$ mV to fully quench transport and ensure their coupling is only capacitive. The nanowire section to the right of the hybrid segment can be either a

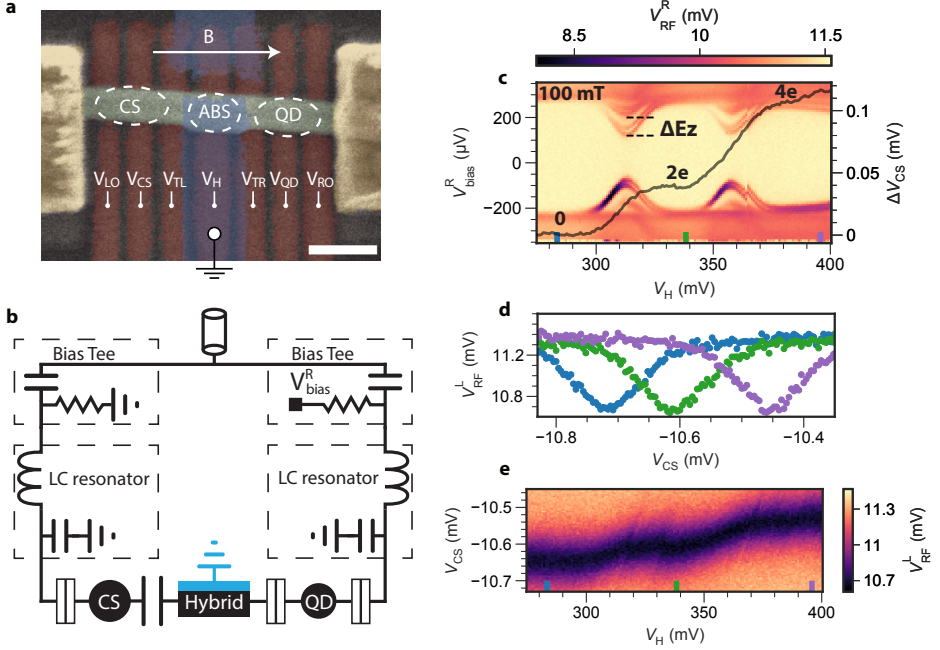


Figure 1: Device set-up and characterization. **a.** False color SEM micrograph of our device. An InSb nanowire (green) is placed on an array of bottom gates (brown) and contacted by normal Cr/Au leads (yellow). We define a quantum dot (QD) to the left of the hybrid segment, and operate it as a charge sensor (CS). Another QD can be formed using the gates to the right of the hybrid segment. The names of the gate voltages are indicated in the respective gates. The scale bar is 200 nm. **b.** DC equivalent circuit of our device. Both normal leads of the hybrid segment are connected to off-chip LC resonators, which are multiplexed. Each LC resonator has a bias tee that can be used to bias the leads with respect to the grounded Al. **c.** Amplitude of the reflected RF signal of the right lead, V_{RF}^R , for varying voltage on the hybrid plunger gate, V_H and the right bias, V_R , for an external magnetic field $B = 100$ mT, $V_{TR} = 0$, $V_{QD} = 500$ mV and $V_{RO} = 500$ mV. **Superimposed line:** Shift of the gate voltage corresponding to the Coulomb resonance of the CS, ΔV_{CS} , for each V_H setting, extracted from **e**. The Zeeman splitting of the first ABS is indicated by ΔE_Z . 0, 2e and 4e indicate additional charge accumulated on the hybrid. **d.** Amplitude of the reflected RF signal of the left lead, V_{RF}^L , for varying voltage on the CS plunger gate, V_{CS} , at fixed values of V_H indicated by the colored bars in panels **c** and **e**. **e.** V_{RF}^L for varying V_{CS} and V_H .

tunnel barrier or a QD, depending on the tunnel gate voltages V_{RO} and V_{TR} .

The nanowire is contacted by two normal Cr/Au leads that can be used for DC transport and radio frequency (RF) reflectometry measurements. figure 1b shows the DC equivalent circuit of the device and its connections. Both normal leads are connected to LC resonators with bias tees, allowing us to independently voltage bias them with respect to the grounded Al. The LC resonators are off-chip and multiplexed, see Ref. [22] for details. Further details on the reflectometry circuit can be found in Ref. [23]; for resonator characterization, see section 4.4.1. Experiments are performed in a dilution refrigerator at a base temperature of 30 mK.

4.2.2 ABS EVEN GROUND STATE CHARGE

The hybrid segment hosts ABSs that can have an odd, doublet ground state ($\{|\downarrow\rangle, |\uparrow\rangle\}$) or an even ground state. We consider an ABS in the atomic limit, where the even ground state is a singlet: $|S\rangle = u|0\rangle - v|2\rangle$, with 0 and 2 denoting the occupation of a single orbital [24, 25]. The singlet state changes between being mostly unoccupied (0-like) or doubly occupied (2-like) when the electrochemical potential of the ABS changes. Note that this is a gradual change of ground state, as opposed to changing a QD ground state by occupying additional electrons. When the semiconductor-superconductor coupling is stronger than the charging energy, the ABS has an even ground state with a doublet excited state [26].

To characterize the hybrid segment, we set $V_{RO} = 500$ mV and $V_{QD} = 500$ mV to accumulate electrons, and create a tunnel barrier by setting $V_{TR} = 0$ mV to perform tunneling spectroscopy from the right lead. Figure 1c shows amplitude of the reflected RF signal of the right lead, V_{RF}^R , for varying hybrid plunger gate voltage, V_H , and right voltage bias, V_R . A dip in V_{RF}^R can be related to a peak in differential conductance [23]. The hybrid segment has a hard-gapped density of states with two well-separated ABSs of which the energy can be controlled with V_H . Each ABS excitation is split into two resonances, because we apply 100 mT along the nanowire axis. From the Zeeman splitting $\Delta E_Z = 80 \mu\text{eV}$, we obtain an effective g -factor of $g = 13.8$ for the ABS. The ABS excitations do not cross zero bias, signalling an even ground state for the entire V_H range. We note that there is a switch in the signal at $V_H \approx 365$ mV, which we attribute to a charge jump in the hybrid segment.

Figure 1d shows amplitude of the reflected RF signal of the left lead, V_{RF}^L , for varying plunger gate voltage of the CS, V_{CS} , taken at three different values of V_H . A Coulomb resonance of the CS is seen as a dip in V_{RF}^L whenever a CS level is aligned with the Fermi level of the left lead [27]. We see that the V_{CS} value corresponding to the V_{RF}^L minimum changes due to V_H , which has two possible causes. First, V_H directly gates the CS due to cross-capacitance. Second, V_H can change the occupation of the hybrid segment and the resulting charge is sensed by the CS. To extract the charge sensing signal only, we define virtual gates that are linear combinations of the physical gate voltages, to compensate for cross-capacitances between gates (for details see section 4.4.2).

In figure 1e, we show one particular CS Coulomb resonance for varying V_{CS} and V_H . We have subtracted a global slope from the data, which we attribute to imperfect virtual gate settings. The global slope was chosen such that the CS resonance is roughly constant in V_H up to 300 mV, for which there are no sub-gap states (for details and raw data, see section 4.4.2). We note the presence of switches in the CS signal at $V_H = 320$ mV and $V_H = 365$ mV. The latter switch occurs at the same V_H value as the one observed in figure 1c. We attribute the switches in the CS signal to charge jumps in the hybrid segment (for more discussion, see section 4.4.3).

The superimposed black line of figure 1c shows the shift of the CS Coulomb resonance, ΔV_{CS} , as found from figure 1e. We see that ΔV_{CS} depends on V_H and changes most strongly when there is an ABS at sub-gap energies. The absence of sharp jumps in ΔV_{CS} shows that there are no abrupt changes of charge, which is consistent with an even ground state for the entire V_H range as found from figure 1c. We interpret the change in ΔV_{CS} at $V_H = 310$ mV and $V_H = 360$ mV as the CS sensing the charge of the ABSs changing continuously from 0 to $2e$, where e is the charge of the electron.

Gradual change of charge without change of parity, as seen here, has been observed

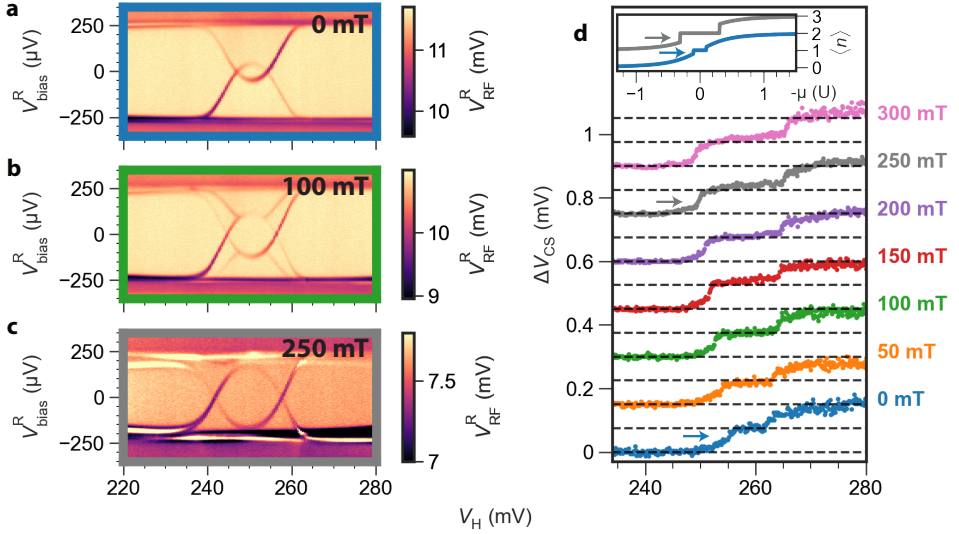


Figure 2: **Charge sensing the even and odd ground states of an ABS.** **a-c.** Amplitude of the reflected RF signal of the right lead, V_{RF}^{R} , for varying hybrid gate voltage V_{H} and right bias V_{R} , taken at $B = 0 \text{ mT}$ (a.), $B = 100 \text{ mT}$ (b.) and $B = 250 \text{ mT}$ (c.) for $V_{\text{TR}} = 0 \text{ mV}$, $V_{\text{TL}} = -100 \text{ mV}$, $V_{\text{LO}} = 170 \text{ mV}$ and $V_{\text{RO}} = 500 \text{ mV}$. **d.** Shift of the CS Coulomb resonance, ΔV_{CS} , at different B values for $V_{\text{TL}} = -140 \text{ mV}$ and $V_{\text{LO}} = 172 \text{ mV}$. The horizontal lines are offset by $75 \mu\text{V}$, which corresponds to a charge difference of approximately $1e$. The arrows indicate the even-odd transition at $B = 0 \text{ mT}$ and $B = 250 \text{ mT}$ respectively. **inset.** The occupation expectation value of the ABS ground state, $\langle n \rangle$, for varying chemical potential, μ , at different B values, calculated in the atomic limit. The arrows indicate the even-odd transition.

before in normal double quantum dots [28, 29]. In our case, however, the ABS exchanges charge with a large Al reservoir and becomes a coherent superposition of 0 and $2e$.

4.2.3 SINGLE ABS PARITY READOUT

To use our charge sensor for parity readout, we focus on an ABS with a ground state that can be changed from even to odd parity using V_{H} . figure 2a shows spectroscopy of such an ABS in a different V_{H} range than figure 1, for $B = 0 \text{ mT}$. We see a sub-gap state that crosses zero energy twice for changing V_{H} , give rising to a characteristic ABS eye-shape [30, 31]. The ABS ground state between the zero-energy crossings is a spin doublet $|D\rangle = |\downarrow\rangle, |\uparrow\rangle$ [26]. Having a doublet ground state at $B = 0 \text{ mT}$ signals that the ABS has a charging energy that is non-negligible. We note that this is uncommon among most ABSs in the hybrid segment, as can be seen from measurements in a larger V_{H} range (see section 4.4.4). We choose this particular ABS as it allows us to measure charge in both the even and odd ground state. figure 2b and c show spectroscopy of the ABS at $B = 100 \text{ mT}$ and $B = 250 \text{ mT}$, respectively. The magnetic field Zeeman splits the doublet states, making the odd state lower in energy than the even state over a larger V_{H} range.

In figure 2d we show the processed shift of the CS Coulomb resonance, ΔV_{CS} , for varying V_{H} at different B values. To obtain ΔV_{CS} for each B value, we first set the CS on Coulomb resonance using V_{CS} and measure V_{RF}^{L} for varying V_{H} . We then convert the

measured V_{RF}^{L} to the corresponding shift of the CS Coulomb resonance, resulting in ΔV_{CS} . For details, see section 4.4.5.

For each B value, we identify three distinct V_{H} regions where the ΔV_{CS} response is roughly flat. The middle region of these around $V_{\text{H}} \approx 260 \text{ mV}$ occupies a larger V_{H} range for increasing B . This is consistent with $|\downarrow\rangle$ being the ground state for a larger V_{H} range, as inferred from figure 2a-c (note that the V_{H} values for which the ABS has an odd ground state differ slightly between panels a-c. and d. due to different V_{LO} and V_{TL} gate voltages, which were chosen to optimize the sensitivity of the charge sensor). We interpret the three distinct ΔV_{CS} values for increasing V_{H} as corresponding to the 0-like even, singly occupied odd, and 2-like even states of the ABS.

We observe finite curvature in ΔV_{CS} for the even ground state, which we attribute to mixing of the 0 and 2 occupations, similar to figure 1e. The curvature is most visible close to the even-odd transition, and becomes less apparent with increasing B . At $B = 0 \text{ mT}$, the even-odd transition (indicated by the blue arrow) occurs when the ABS is near its energy minimum, where the average ABS charge is $1e$ for both the even and odd states [32, 33]. The even state charge gradually changes from 0 to almost $1e$ in the V_{H} range before the transition. At $B = 250 \text{ mT}$, the even-odd transition occurs when the ABS is no longer close to its energy minimum. The difference in charge between the even and odd states is then greater, resulting in a sharper change of ΔV_{CS} , as indicated by the gray arrow.

If the curvature of ΔV_{CS} is exclusive to the even ground state, we can use it to infer the parity of the ABS using charge sensing only. To illustrate this point, we calculate and show the charge of an ABS in the inset of figure 2d. Here, the average occupation, $\langle n \rangle$, is shown for varying chemical potential, μ , at two different values of B (for more details see section 4.4.6). At low B , curvature in $\langle n \rangle$ is a characteristic sign of an ABS in a singlet ground state, provided that the parent gap is much larger than the charging energy. To infer the ABS parity from the curvature of ΔV_{CS} experimentally, the ABS cannot be strongly coupled to another discrete state or orbital. In the coupled system, changing the gate voltage can transfer charge between the states. This can result in curvature of ΔV_{CS} for the odd ground state in addition to the even one.

So far, we have established that charge sensing measurements can resolve the charge differences between the even and odd ground states of a single ABS. In a two-site Kitaev chain, however, it is the combined parity of two hybridized QDs that has to be detected. We create a proxy system by hybridizing a QD with an ABS and charge sense it to give a minimal demonstration of parity readout for Kitaev chains. Parity readout of Majorana zero modes requires extra steps, which we detail in the discussion. We note that an alternating ABS-QD array can also constitute a Kitaev chain [34, 35].

4.2.4 ANDREEV MOLECULE SPECTROSCOPY

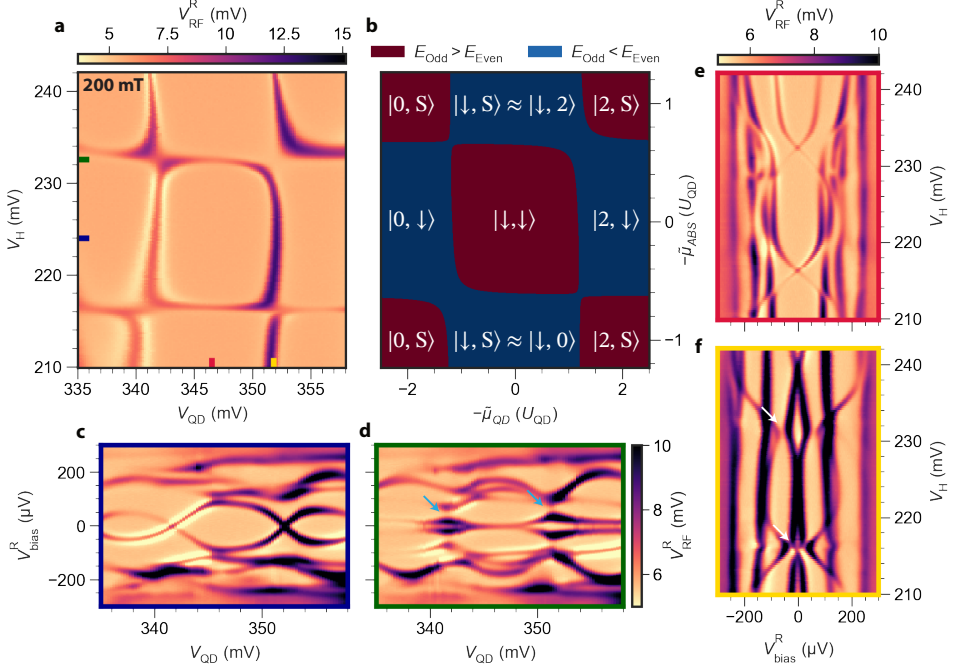


Figure 3: **Spectroscopy of a hybridized ABS-QD system.** **a.** Amplitude of the reflected RF signal of the right lead, V_{RF}^R for varying QD plunger gate voltage, V_{QD} , and V_H taken at $V_R = 0$ V, $B = 200$ mT, $V_{TR} = 215$ mV and $V_{RO} = 340$ mV. **b.** Parity of the lowest energy eigenstate of a coupled ABS-QD system for varying QD and ABS chemical potential $\tilde{\mu}_{QD}$ and $\tilde{\mu}_{ABS}$, computed in the atomic limit. We designate the ground state parity as even if $E_{Odd} > E_{Even}$ and odd if $E_{Odd} < E_{Even}$. The superimposed text indicates the ground states in the $|N, M\rangle = |N\rangle_{QD} \otimes |M\rangle_{ABS}$ basis of the ABS-QD system. We denote the ABS singlet state by $|S\rangle$, and highlight its dominant occupation for the $|\downarrow, S\rangle$ state. **c., d.** V_{RF}^R for varying V_{QD} and V_R , taken at two different values of V_H indicated by the blue and green horizontal bars in panel a. **e., f.** V_{RF}^R for varying V_H and V_R , taken at two different values of V_{QD} indicated by the red and yellow vertical bars in panel a.

To create the ABS-QD system, we define a QD to the right of the hybrid segment by creating a tunnel barrier using V_{RO} (see figure 1a). We then lower the tunnel barrier between the QD and the hybrid segment by increasing V_{TR} .

figure 3a shows a charge stability diagram measured in V_{RF}^R for varying V_H and QD plunger gate, V_{QD} . We see avoided crossings that indicate hybridization of the QD and ABS. The QD resonance can be seen when the ABS is off-resonance (blue bar), which we attribute to local Andreev reflection on the QD and the usage of RF reflectometry instead of differential conductance (for details see section 4.4.7). Similarly, the ABS can be observed when the QD is off-resonance (e.g., red bar). Because of the strong hybridization between the QD and ABS, the latter can always be seen in spectroscopy upon probing the QD.

figure 3b shows the ground state parity of a QD coupled to an ABS, computed in the atomic limit. States are indicated in the ABS-QD number basis, with $|S\rangle$ denoting the ABS

singlet. We emphasize that the singlet is dominantly 0-like or 2-like at $-\tilde{\mu}_{\text{ABS}} = \pm 1 U_{\text{QD}}$. The avoided crossings have different sizes in figure 3b, which is caused by the mixing of 0 and 2 occupations of the ABS (for details on the model, see section 4.4.6). We see that figure 3b qualitatively reproduces most of the features of figure 3a.

figure 3c and d show spectroscopy of the QD for varying V_{QD} and V_{R} at fixed values of V_{H} indicated by the horizontal lines in figure 3a. When the ABS in the hybrid segment is not at zero-energy (blue bar, panel c), we see multiple sub-gap states, where the lowest one forms a typical eye-shape. This indicates the formation of Yu-Shiba-Rusinov (YSR) states on the QD, due to its strong coupling to the hybrid segment [36–40]. figure 3d (green bar) shows spectroscopy of the QD when the ABS excitation is at zero energy, i.e., on-resonance. Here we see that the ABS and QD states form sub-gap bonding and anti-bonding states when they are on resonance, indicated by the blue arrows. Two hybridized sub-gap states are often referred to as an “Andreev molecule”, which usually designates two coupled YSR states [41–47] or phase-tunable ABSs in Josephson junctions [48–50]. Because our ABS-QD system shows hybridization of an ABS in a hybrid with a YSR state in a QD, we categorize it as an Andreev molecule.

figure 3e and f show spectroscopy of the QD for varying V_{H} at fixed values of V_{QD} indicated by the vertical lines in figure 3a. When the QD is off-resonance (red bar, panel e) the lowest sub-gap state crosses zero energy twice, and the excited states are close in energy to the superconducting gap. figure 3f (yellow bar) shows spectroscopy when the QD excitation is at zero-energy. When the ABS is on resonance, it splits the zero-bias peak of the QD, indicated by the white arrows. This effect is known to occur for QDs strongly coupled to ABSs [51–53].

4.2.5 ANDREEV MOLECULE PARITY READOUT

Next, we sense the charge of the ABS within the ABS-QD system. figure 4a shows the phase of the reflected RF signal of the left lead, $\phi_{\text{RF}}^{\text{L}}$, for varying V_{QD} and V_{H} , at different gate and field settings from figure 3. We set the CS on Coulomb resonance using V_{CS} , at the V_{QD} and V_{H} settings that correspond to the bottom left corner of figure 4a. Globally, we observe three horizontal regions where $\phi_{\text{RF}}^{\text{L}}$ depends almost only on V_{H} , which we interpret as the 0-like even, singly occupied $|\downarrow\rangle$ and 2-like even states of the ABS. In addition, there are 4 regions where V_{RF}^{L} depends visibly on V_{QD} , which we attribute to the QD hybridizing with the ABS. These regions are highlighted using dashed rectangles.

In figure 4b we show a zoom-in of panel a corresponding to the black rectangle. Here, the CS was gated to be on the steepest slope of the Coulomb peak using V_{CS} at the start of the measurement. We see an off-diagonal avoided crossing, which signals an interdot transition [54]. Because this is the first interdot transition of this QD orbital and ABS, we label the bottom left corner of figure 4b with $|0, S\rangle$, where the QD orbital is unoccupied, and the ABS is in the 0-like singlet state. The other states are labeled by counting the added electrons. Although the QD is proximitized by coupling to the hybrid, as seen in figure 3c, we retain the number basis for clarity.

figure 4c shows the numerical derivative of panel b, $d\phi_{\text{RF}}^{\text{L}}/dV_{\text{H}}$, after processing with a Savgol filter. The dips in $d\phi_{\text{RF}}^{\text{L}}/dV_{\text{H}}$ form two blue hyperbolas that indicate where the even and odd ground states are degenerate [29]. Based on the states inferred from panel b, we label the region between the hyperbolas as odd (“O”) and the two areas outside as even

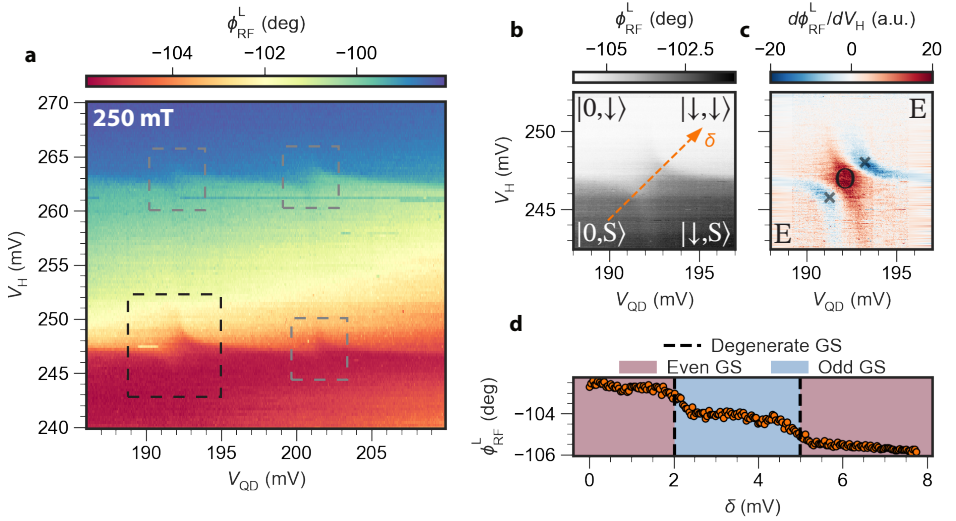


Figure 4: Charge sensing measurements of the ABS-QD system. All data was taken for $V_{TR} = 255$ mV, $V_{RO} = 230$ mV and $B = 250$ mT. **a.** Phase of the reflected RF signal of the left lead, ϕ_{RF}^L , for varying V_{QD} and V_H . **b.** Zoom in of **a.** for the range indicated by the dashed rectangle. The superimposed text indicates the ground state of the ABS-QD system in the same basis as in figure 3b. **c.** The numerical derivative, $d\phi_{RF}^L/dV_H$, of **b.** The superimposed text indicates the parity of the states in panel **b**, where "O" and "E" indicate an odd and even ground state, respectively. The two crosses indicate negative peaks of $d\phi_{RF}^L/dV_H$ found from peak-finding for the cut along the orange diagonal line shown in panel **b**. **d.** ϕ_{RF}^L for a cut along the orange diagonal line shown in panel **b**. Here, V_{QD} and V_H are changed in parallel, indicated by δ . The vertical black lines correspond to the V_{QD} and V_H values of the black crosses in panel **c**, from which we infer a parity change. The red and blue shading indicate even and odd ground states, respectively.

("E").

figure 4d shows a linecut of ϕ_{RF}^L taken along the orange line in panel **b**, where V_{QD} and V_H are changed in parallel, indicated by δ . The two vertical, dashed black lines correspond to the gate values of the superimposed crosses in panel **c**, which we use to divide the range of δ into even and odd ground states. We note that there are three regions where ϕ_{RF}^L is roughly constant, and that these coincide with even and odd parity sectors. From this we conclude that we can read out the parity of the ABS-QD system by measuring its charge.

Extending parity readout using charge sensing to a two-site Kitaev chain requires an additional step however. In the "Poor Man's Majorana" sweet spot, the degenerate even and odd parity ground states have the same charge [8]. Detuning one QD creates a charge difference between the even and odd ground states on the other QD, while the states remain degenerate [55]. A local charge sensing measurement on the non-detuned QD can then tell the parity based on charge. This protocol of detuning and measuring charge has to be performed within the quasi-particle poisoning time, otherwise the parity flips during the measurement. We note that our RF integration time of $\tau = 9.3$ ms is on the order of quasiparticle poisoning times typically found in hybrid systems, although estimates vary strongly depending on device design [56, 57]. This results in the CS predominantly sensing

the average occupation of our system. We show SNR values for different integration times in section 4.4.8.

4.3 CONCLUSION

In conclusion, we have operated a QD as a charge sensor and measured the charge of ABSs in a hybrid semiconductor-superconductor nanowire. We have found that the charge of an ABS can change by $2e$ while remaining in the even ground state. The charge difference between the even and odd states can be less than $1e$ due to the ABS exchanging charge with the superconductor. We have coupled a QD to an ABS to form a hybridized state, which we categorize as an Andreev molecule. Using the charge sensor, we can infer the parity of the ABS-QD system when the even and odd ground states have different charges. For a two-site Kitaev chain, both parities have the same charge in the sweet spot, and require an additional step for parity-to-charge conversion. We demonstrate that charge sensing can be used to read out parity in hybrid systems -without affecting it- and is promising for usage in Kitaev chains.

DATA AVAILABILITY

All raw data in the publication and the analysis code used to generate figures are available at <https://doi.org/10.5281/zenodo.10067038>.

4.4 SUPPLEMENTARY INFORMATION

4.4.1 RESONATOR CHARACTERIZATION

Both normal contacts of the device presented in this work are bonded to off-chip LC resonators. figure 5a,b show the amplitude of the reflected RF signal of the left and right lead $V_{\text{RF}}^{\text{L/R}}$ for varying frequency, f , at $B = 0$ mT. We fit the resonator responses using a model for asymmetric resonances by Khalil et al. [58]. From the fit, we obtain the internal and external Q-factors listed in the figure. For all other measurements in this work, we fix the frequencies at $f_{\text{L}} = 364$ MHz and $f_{\text{R}} = 264$ MHz. All RF measurements were performed using a Zurich Instruments UHFLI.

4.4.2 VIRTUAL GATES AND FIG. 1 DATA PROCESSING

figure 6 shows the gates and cross-capacitance matrix \hat{C} used for the virtual gates in this work. The matrix \hat{C} allows us to estimate the actual electrochemical potential change due to cross-capacitance, using: $\vec{V}' = \hat{C}\vec{V}$. Here, the vector \vec{V} contains all the physical gate voltages and \vec{V}' is the resulting voltage on parts of the device. This allows us to change gates in a way that, for example, affects only the QD and not the CS electrochemical potential. For more details on virtual gates, see Refs. [59, 60].

Our virtual gate implementation was imperfect, leading to a residual cross-capacitance between V_{H} and V_{CS} . figure 7a shows that the CS resonance is also gated by V_{H} . We attribute the residual cross-coupling to the non-linearity of the device and an inaccurate choice of \hat{C} . We correct for this in post-processing by subtracting a global slope, until the CS resonance does not depend on V_{H} up to $V_{\text{H}} = 300$ mV. This result is presented in Fig. 1e

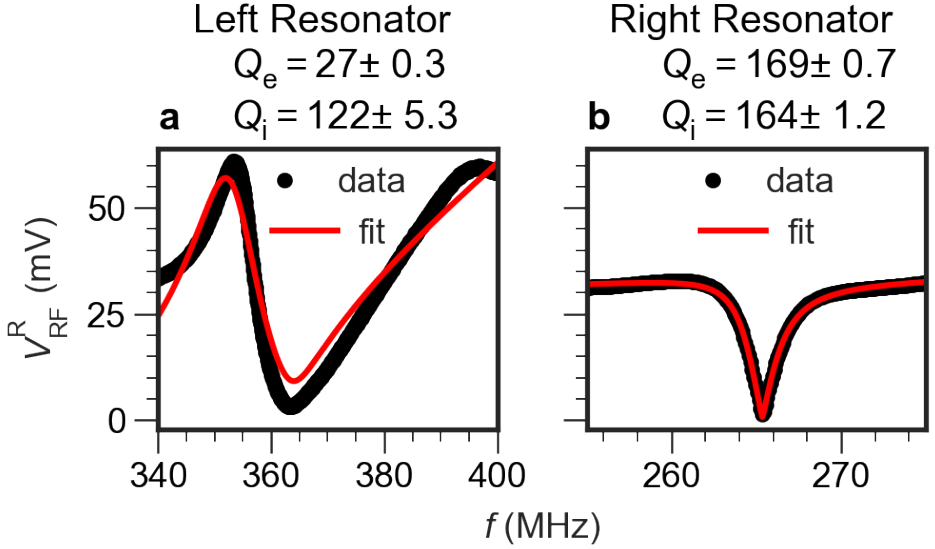


Figure 5: **Resonator characterization.** Fits of off-chip resonators performed according to the model described in Ref. [58]. **a.** Amplitude of the reflected RF signal of the left lead, V_{RF}^L , versus the frequency of the RF output signal, f . **b.** Amplitude of the reflected RF signal of the right lead, V_{RF}^R , versus the frequency of the RF output signal, f .

and in figure 7b. In figure 7d we show the minima of the Coulomb dip for each V_H value, extracted from panels a., b. The processed data is seen to be devoid of a global slope. The line in figure 6d is superimposed in Fig. 1c.

4.4.3 CHARGE JUMPS

In figure 1c, there is a switch in the tunnel spectroscopy measurement of the hybrid segment at $V_H \approx 365$ mV, which is also observed in figure 8a. These abrupt switches are referred to as "charge jumps", and are attributed to the filling and emptying of charge traps in the nanowire in the vicinity of the ABS. This changes the electrochemical potential of the ABS, which leads to a change in excitation energy as seen in figure 1c. Charge jumps have been observed at reproducible gate voltages in semiconductor-superconductor nanowire devices [61, 62].

We attribute the switches in the charge sensor signal in figure 1e to the emptying and filling of charge traps in the hybrid segment as well. As the electrochemical potential of the ABS changes due to a charge jump, so does its average charge in the singlet ground state. The Coulomb resonance of the charge sensor will shift abruptly as a result. We note that as the change in ABS charge is a fraction of $1e$, the shift of the charge sensor will be comparatively small.

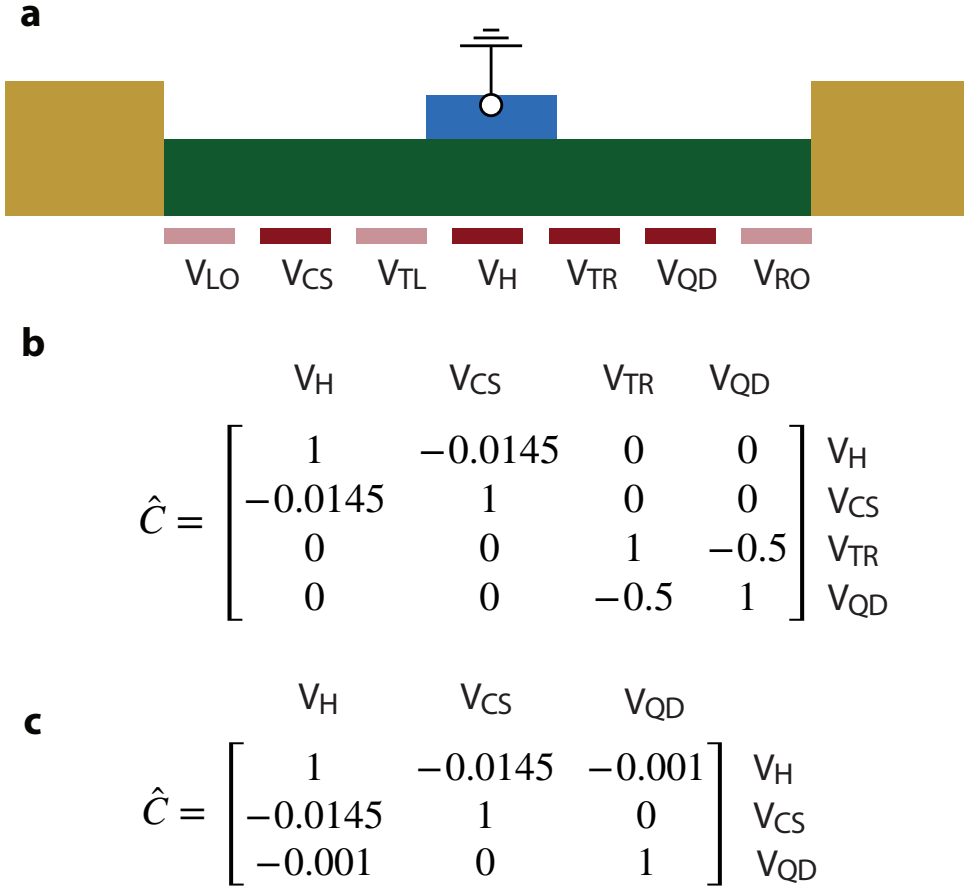


Figure 6: **Virtual gates.** **a.** Device sketch that highlights the physical gates used to define the new virtual gates **b.** The cross-capacitance matrix for the gates highlighted in **a.** Off-diagonal numbers indicate a finite cross-coupling between physical gates, which is corrected for using the virtual gates. This setting is used for Fig. 1 and 2. **c.** Same as panel **b**, but corresponding to the data from figure 4 of the main text.

4.4.4 EXTENDED RANGE HYBRID SPECTRUM AND CHARGE SENSING

figure 8a shows spectroscopy of the hybrid for a larger range of V_H than shown in Fig. 1c. The ABSs shown in Fig. 1 are indicated by the blue marks. The ABS of Fig. 2 is indicated by the white marks. Panel **b** shows the corresponding charge sensor measurement.

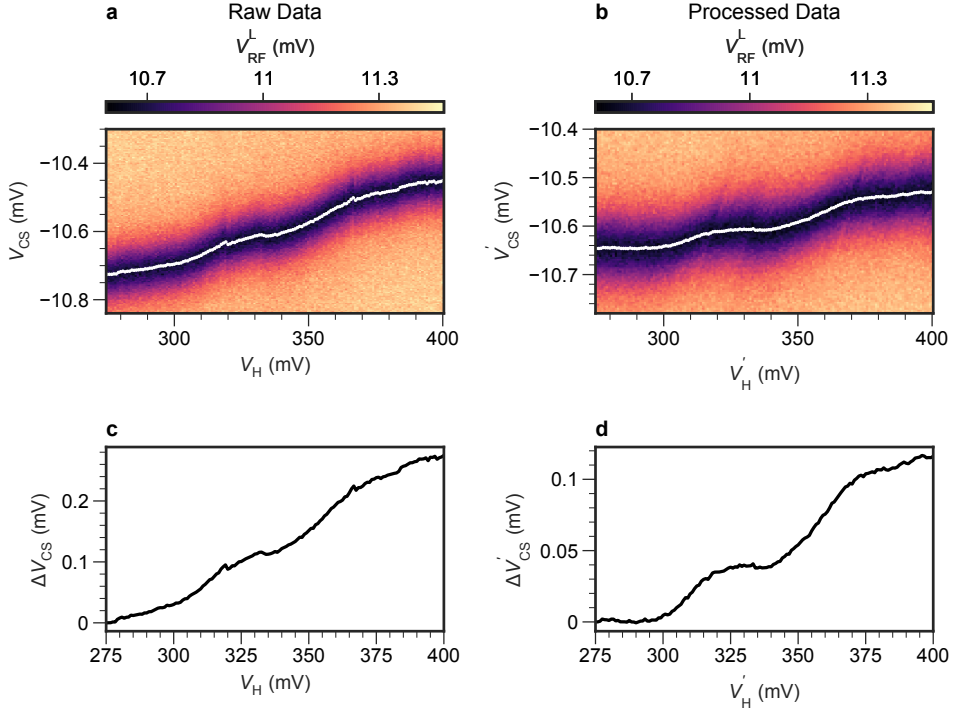


Figure 7: **Data processing of Fig. 1.** **a.** Amplitude of the reflected RF signal of the left lead, V_{RF}^L , for varying V_{CS} and V_H . White markers indicate the minimum of the Coulomb resonance for each V_H value. **b.** Same as **a.**, but after removing a global slope between V_{CS} and V_H . **c.,d.** Shift of the CS Coulomb resonance, ΔV_{CS} , for each V_H setting, extracted from **a.** and **b.** respectively. These correspond to the white markers in panels **a** and **b**. The line of panel **d** is superimposed on Fig. 1c.

4.4.5 FIG. 2 CHARGE SENSOR DATA PROCESSING

A change of the ABS charge results in a linear shift of the CS electrochemical potential, proportional to their mutual capacitance. The resulting change in reflected signal V_{RF}^L is not linear due to the shape of the Coulomb dip. To compensate for this, we first perform a characterization measurement of V_{RF}^L for varying V_{CS} for each B value as shown in figure 9a-g. We then fix the V_{CS} gate value such that the CS is on Coulomb resonance and measure V_{RF}^L while varying V_H , which is shown in figure 9h-n. For each measured V_{RF}^L value per V_H , we find the closest V_{RF}^L value in the characterization measurement. We then map the measured V_{RF}^L value to V_{CS} , which is indicated by the orange markers in figure 9a-g. Finally, we subtract a global slope from the resulting V_{CS} value that we attribute to remaining cross-capacitance to V_H and show the resulting ΔV_{CS} in figure 9o-u. We note that the vertical difference between the three plateaus is now roughly equal, as compared to figure 9h-n. Therefore, we interpret the processed data as being proportional to the ABS charge.

Finally, we see from figure 9a-g. that the noise in V_{RF}^L is larger for some magnetic field values, such as $B = 300$ mT, than for others, such as $B = 250$ mT. This noise affects the processed data (figure 9o-u) mostly for $V_H \approx 275$ mV, as the charge sensor is already almost

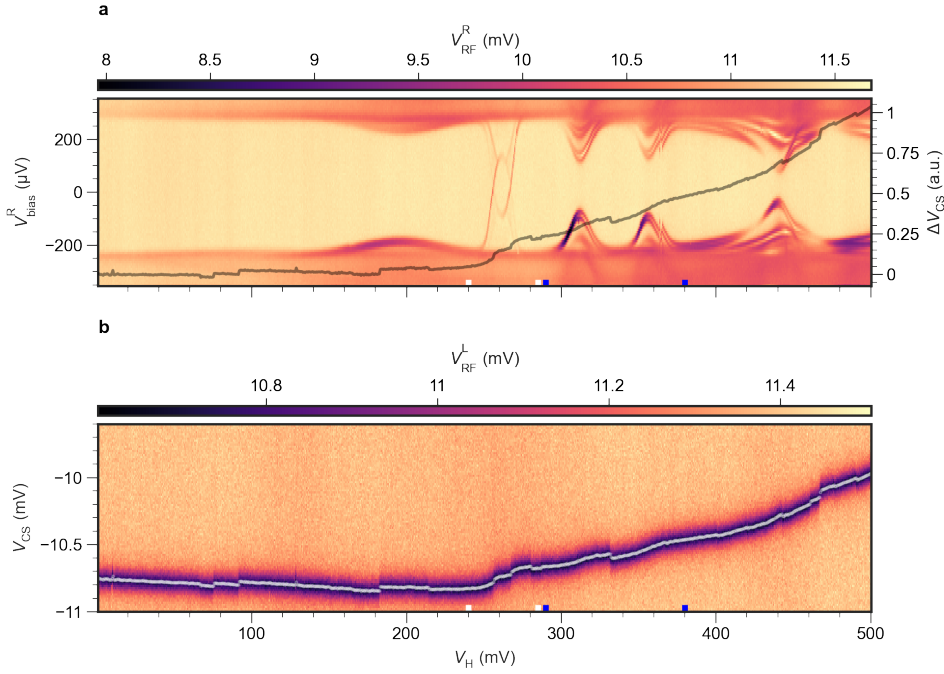


Figure 8: **Extended V_H range measurement of Fig. 1.** **a.** Amplitude of the reflected RF signal of the right lead, V_{RF}^R for varying hybrid gate voltage V_H and right bias V_R at $B = 100$ mT, $V_{TR} = 0$ and $V_{RO} = 500$ mV. **Superimposed line.** Shift of the CS Coulomb resonance for each V_H setting, extracted from b. A global slope is subtracted for clarity. **b.** Amplitude of the reflected RF signal of the left lead, V_{RF}^L , for varying V_{CS} and V_H . White dots indicate the CS resonance found from peak-finding. The ABSs shown in Fig. 1 are indicated by the blue marks. The ABS of Fig. 2 is indicated by the white marks. Panel b shows the corresponding charge sensor measurement.

in Coulomb blockade, where the noise is largest. While we are not completely certain about the cause, it has been proposed that magnetic fields can affect charge traps, which changes the charge noise [63].

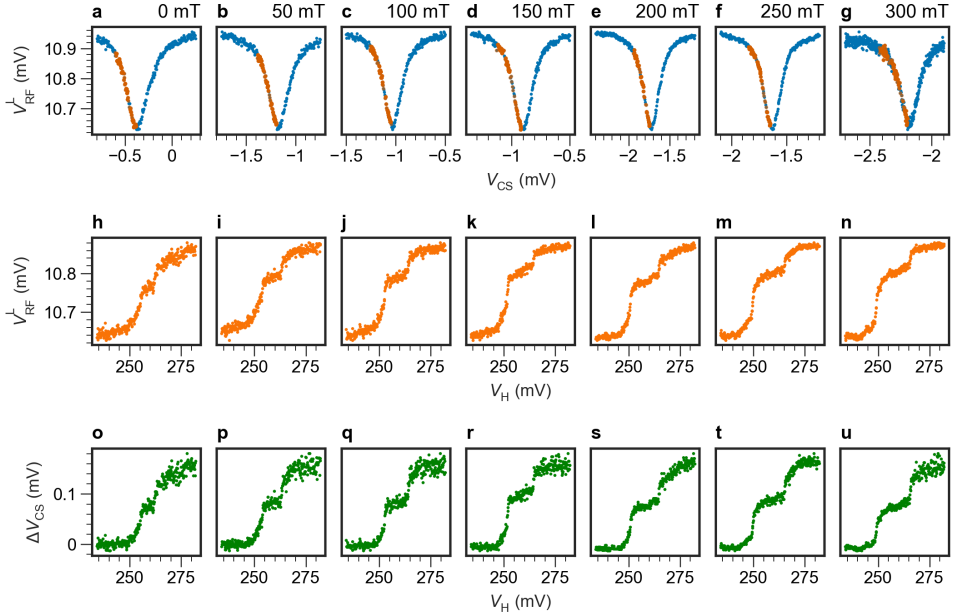


Figure 9: **Data processing of Fig. 2.** **a-g.** Amplitude of the reflected RF signal of the left lead, V_{RF}^{L} , for varying V_{CS} at $V_{\text{H}} = 234 \text{ mV}$ for values of B indicated in the title. These measurements are used to map a measured V_{RF}^{L} value to the closest V_{CS} value. **Orange markers.** The V_{RF}^{L} values from the data shown in panels h-n, mapped to V_{CS} . For each V_{H} setpoint, the measured V_{RF}^{L} is compared to the full V_{RF}^{L} v.s. V_{CS} curve of panels a-g. Each measured V_{RF}^{L} value from panels h-n is then mapped to a V_{CS} value from panels a-g. **h-n.** V_{RF}^{L} for varying V_{H} at fixed V_{CS} for values of B indicated in the title. At each value of V_{H} , the measured V_{RF}^{L} is compared to the corresponding measurement of panels a-g. for the same B . The closest matching value of V_{CS} is then chosen, resulting in a mapping of V_{H} to V_{CS} , which is plotted in orange in panels a-g. **o-u.** Shift of the gate voltage corresponding to the Coulomb resonance of the CS, ΔV_{CS} , for varying V_{H} . These correspond to the orange markers of panels a-g. after subtracting a global slope.

4.4.6 ANDREEV BOUND STATES IN THE ATOMIC LIMIT

The inset of Fig. 2d shows the occupation of an ABS modeled in the atomic limit. In the many-body basis of a single orbital $\{|0\rangle, |2\rangle, |\downarrow\rangle, |\uparrow\rangle\}$ the Hamiltonian is:

$$H_{\text{ABS}} = \begin{bmatrix} 0 & -\Gamma & 0 & 0 \\ -\Gamma & 2\mu + U & 0 & 0 \\ 0 & 0 & \mu + E_Z & 0 \\ 0 & 0 & 0 & \mu - E_Z \end{bmatrix}$$

Where μ is the electrochemical potential of the uncoupled orbital, Γ is the coupling to the superconductor, U is the charging energy and E_Z is the Zeeman energy. We diagonalize the Hamiltonian, obtain the eigenvectors and calculate the ABS ground state occupation $\langle n \rangle$. For Fig. 2d, we use $\Gamma = 2.45$, $U = 5$ and $E_Z = 0, 0.25, 0.6$. For more details on the model, see Refs. [64, 65].

For Fig. 3, we combine an atomic-limit ABS with a QD (see Ref. [34] for more details):

$$H = H_{\text{ABS}} + H_{\text{QD}} + H_t \quad (4.1)$$

Where for the QD we have:

$$H_{\text{QD}} = (\mu_{\text{QD}} - E_Z)c_{\downarrow}^{\dagger}c_{\downarrow} + U_{\text{QD}}c_{\uparrow}^{\dagger}c_{\uparrow}c_{\downarrow}^{\dagger}c_{\downarrow}. \quad (4.2)$$

H_t describes the tunnel coupling between the ABS and the QD and is given by:

$$H_t = t(c_{\downarrow}^{\dagger}d_{\downarrow} + c_{\uparrow}^{\dagger}d_{\uparrow} + h.c.) + t_{\text{so}}(-c_{\downarrow}^{\dagger}d_{\uparrow} + c_{\uparrow}^{\dagger}d_{\downarrow} + h.c.), \quad (4.3)$$

Where t is the spin-conserving tunneling amplitude, and t_{so} is the spin-flipping tunneling amplitude resulting from spin-orbit interaction.

The basis of equation (4.1) can be split into even and odd parity subspaces, where we consider the following states in the $|N, M\rangle = |N\rangle_{\text{QD}} \otimes |M\rangle_{\text{ABS}}$ basis:

$$\begin{array}{ll} \{|0, S\rangle, |2, S\rangle, |\downarrow, \downarrow\rangle\} & \text{even} \\ \{|0, \downarrow\rangle, |\downarrow, S\rangle, |2, \downarrow\rangle\} & \text{odd} \end{array}$$

4

Here $|S\rangle = u|0\rangle - v|2\rangle$ is the ABS singlet. Using equation (4.3), we can calculate the effective coupling terms between the basis states of the system. We only consider transitions with a fixed global parity, i.e. only transitions between two odd occupation states or transitions between two even occupation states. The effective coupling between the different even occupation states of the system is given by:

$$\langle 2, S | H_t | 0, S \rangle = 0 \quad (4.4)$$

$$\langle \downarrow, \downarrow | H_t | 0, S \rangle = vt_{\text{so}} \quad (4.5)$$

$$\langle 2, S | H_t | \downarrow, \downarrow \rangle = -ut_{\text{so}} \quad (4.6)$$

For the odd occupation states we have:

$$\langle 0, \downarrow | H_t | \downarrow, S \rangle = ut \quad (4.7)$$

$$\langle 0, \downarrow | H_t | 2, \downarrow \rangle = 0 \quad (4.8)$$

$$\langle 2, \downarrow | H_t | \downarrow, S \rangle = vt \quad (4.9)$$

We can now write down Equation (4.1) in the even and odd parity subspace matrix representation:

$$H_{\text{even}} = \begin{bmatrix} E_S & 0 & vt_{\text{so}} \\ 0 & 2\mu_{\text{QD}} + U_{\text{QD}} + E_S & -ut_{\text{so}} \\ vt_{\text{so}} & -ut_{\text{so}} & \mu_{\text{QD}} - E_Z + E_{\downarrow} \end{bmatrix}$$

and

$$H_{\text{odd}} = \begin{bmatrix} E_{\downarrow} & ut & 0 \\ ut & \mu_{\text{QD}} - E_Z + E_S & vt \\ 0 & vt & 2\mu_{\text{QD}} + U_{\text{QD}} + E_{\downarrow} \end{bmatrix}$$

Here E_S and E_{\downarrow} are the ABS singlet and doublet energies respectively. The full many-body matrix describing the system is given by the following block-diagonal matrix:

$$H_{\text{total}} = \begin{bmatrix} H_{\text{even}} & 0 \\ 0 & H_{\text{odd}} \end{bmatrix} \quad (4.10)$$

The ground state of the system corresponds to the eigenstate of the lowest eigenenergy of equation (4.10). Fig. 3b was computed for $U_{\text{ABS}} = 0.03$, $U_{\text{QD}} = 1$, $\Gamma = 0.3$, $E_Z = 0.7$, $t = 0.15$, $t_{\text{so}} = 0.01$.

4.4.7 FIG. 3 DC TRANSPORT AND RF REFLECTOMETRY COMPARISON

In figure 10 we compare the charge stability diagram of Fig. 3a as measured in RF reflectometry and DC transport. Most of the features seen in figure 10a are also seen in figure 10b. In V_{RF}^{R} , some features are more visible than in DC transport. While there is only a finite current when the QD undergoes Andreev reflection or hybridizes with the ABS, there is always a dip in V_{RF}^{R} when the normal lead and QD are on resonance. This can be explained by the excess dissipation known as "Sisyphus resistance", which originates from the QD level and Fermi level of the normal lead being detuned with an AC voltage [27]. We attribute the measured current at zero-bias in figure 10b to a finite voltage offset.

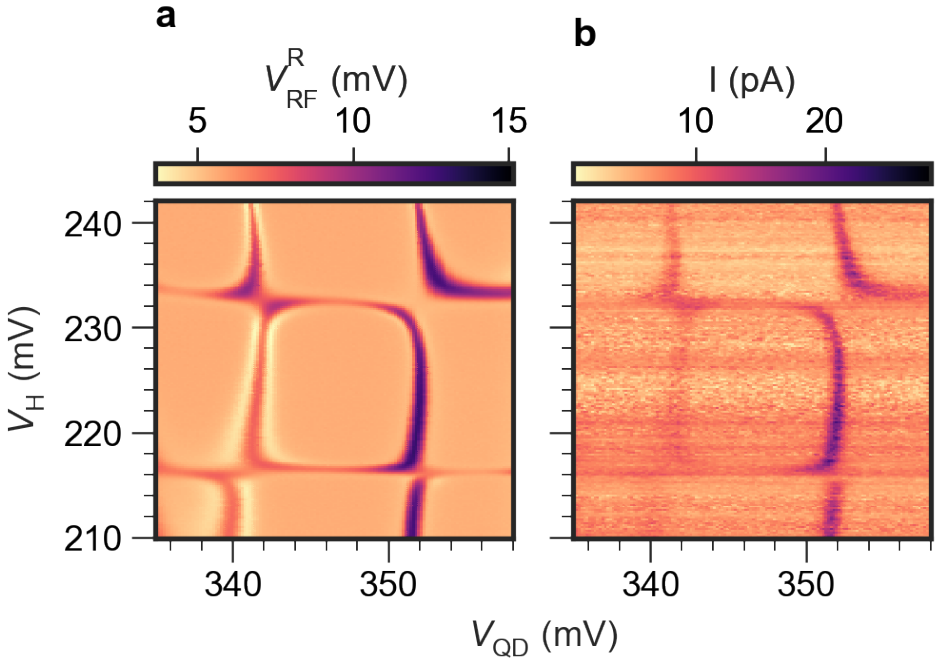


Figure 10: **Comparison of DC transport and RF reflectometry of Fig. 3.** at $V_{\text{R}} = 0$. **a.** Amplitude of the reflected RF signal of the right lead, V_{RF}^{R} for varying QD plunger gate voltage, V_{QD} , and V_{H} . **a.** Current measured at the right lead, I , for varying QD plunger gate voltage, V_{QD} , and V_{H} .

4.4.8 CHARGE SENSOR SNR

To estimate the SNR of the charge sensor, we measure the in-phase response and quadrature, I and Q , of the left resonator for the ABS of Fig. 2 at $B = 100$ mT. We measure the I and Q signals over time at different V_{H} values and plot the result in histograms, as shown in figure 11a. For each histogram, we compute the average IQ response μ_i and the standard

deviation σ_i . Then, we define the SNR for two charge states as:

$$\text{SNR}_{i,j} = \frac{|\mu_i - \mu_j|}{\sigma_i + \sigma_j}$$

See Supplemental Material of Ref. [66] for details. The red and purple lines in figure 11a show $|\mu_i - \mu_j|$ for the 0 and 1, and 1 and 2 occupations of the ABS. Dividing by the sum of the standard deviations results in the SNR. figure 11b shows SNR calculated for varying integration time, t_{int} . figure 11c shows SNR calculated for varying RF output power. It reaches a maximum of 39.5 for -26 dBm for the SNR of the 0-like singlet and 1 occupations. figure 11d shows SNR calculated for varying tunnel gate voltage V_{LO} . We fit the resulting Coulomb peak and extract the ratio of peak height and full width at half maximum. We see that a sharper Coulomb peak results in a higher SNR.

4

100 mT

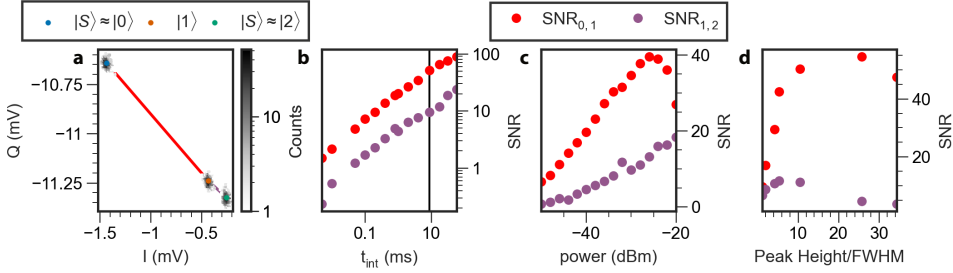


Figure 11: **Charge Sensor SNR measurements for a single ABS.** **a.** Example histograms of the in-phase response and quadrature, I and Q of the left resonator, for the 0-like even, 1 and 2-like even occupations of the ABS. The colored markers indicate the charge state of the ABS that corresponds to each histogram. The red and purple lines show the distance between the histograms that we use to calculate the SNR. **b.** The SNR calculated from IQ-histograms for the 0-like singlet and doublet states (red), and 2-like singlet and doublet states (purple) for varying integration time t_{int} . The vertical black line indicates, $t_{\text{int}} = 9.3$ ms, which is the integration time used in the main text. The RF out signal had a power of -30 dBm for every t_{int} . **c.** Same as panel b., for varying power of the RF input signal and at fixed $t_{\text{int}} = 9.3$ ms. **d.** Same as panel c., for varying shape of the CS Coulomb resonance at fixed $t_{\text{int}} = 9.3$ ms and power -30 dBm. Each data point is taken for a different gate voltage V_{LO} , resulting in Coulomb peaks of different width. We present the SNR versus Coulomb peak height, divided by the full width at half maximum.

REFERENCES

- [1] A. Yu Kitaev. Unpaired Majorana fermions in quantum wires. *Physics-Uspekhi*, 44(10S):131, October 2001.
- [2] Yuval Oreg, Gil Refael, and Felix von Oppen. Helical Liquids and Majorana Bound States in Quantum Wires. *Physical Review Letters*, 105(17):177002, October 2010.
- [3] Roman M. Lutchyn, Jay D. Sau, and S. Das Sarma. Majorana Fermions and a Topological Phase Transition in Semiconductor-Superconductor Heterostructures. *Physical Review Letters*, 105(7):077001, August 2010.
- [4] Jay D. Sau and S. Das Sarma. Realizing a robust practical Majorana chain in a quantum-dot-superconductor linear array. *Nature Communications*, 3(1):964, July 2012. Number: 1 Publisher: Nature Publishing Group.
- [5] Ion C. Fulga, Arbel Haim, Anton R. Akhmerov, and Yuval Oreg. Adaptive tuning of Majorana fermions in a quantum dot chain. *New Journal of Physics*, 15(4):045020, April 2013. Publisher: IOP Publishing.
- [6] Martin Leijnse and Karsten Flensberg. Parity qubits and poor man’s Majorana bound states in double quantum dots. *Physical Review B*, 86(13):134528, October 2012.
- [7] Chun-Xiao Liu, Guanzhong Wang, Tom Dvir, and Michael Wimmer. Tunable superconducting coupling of quantum dots via andreev bound states in semiconductor-superconductor nanowires. *Physical review letters*, 129(26):267701, 2022.
- [8] Athanasios Tsintzis, Rubén Seoane Souto, and Martin Leijnse. Creating and detecting poor man’s Majorana bound states in interacting quantum dots. *Physical Review B*, 106(20):L201404, November 2022.
- [9] Tom Dvir, Guanzhong Wang, Nick Van Loo, Chun-Xiao Liu, Grzegorz P. Mazur, Alberto Bordin, Sebastiaan L. D. Ten Haaf, Ji-Yin Wang, David Van Driel, Francesco Zatelli, Xiang Li, Filip K. Malinowski, Sasa Gazibegovic, Ghada Badawy, Erik P. A. M. Bakkers, Michael Wimmer, and Leo P. Kouwenhoven. Realization of a minimal Kitaev chain in coupled quantum dots. *Nature*, 614(7948):445–450, February 2023.
- [10] Péter Boross and András Pályi. Braiding-based quantum control of a Majorana qubit built from quantum dots, May 2023. arXiv:2305.08464 [cond-mat, physics:quant-ph] version: 1.
- [11] Chun-Xiao Liu, Haining Pan, F. Setiawan, Michael Wimmer, and Jay D. Sau. Fusion protocol for Majorana modes in coupled quantum dots, December 2022. arXiv:2212.01653 [cond-mat].
- [12] L. C. Contamin, M. R. Delbecq, B. Douçot, A. Cottet, and T. Kontos. Hybrid light-matter networks of Majorana zero modes. *npj Quantum Information*, 7(1):171, December 2021.

- [13] M. Hinderling, S. C. ten Kate, D. Z. Haxell, M. Coraiola, S. Paredes, E. Cheah, F. Krizek, R. Schott, W. Wegscheider, D. Sabonis, and F. Nichele. Flip-chip-based fast inductive parity readout of a planar superconducting island, July 2023. arXiv:2307.06718 [cond-mat].
- [14] Stephan Plugge, Asbjørn Rasmussen, Reinhold Egger, and Karsten Flensberg. Majorana box qubits. *New Journal of Physics*, 19(1):012001, January 2017. Publisher: IOP Publishing.
- [15] David Aasen, Michael Hell, Ryan V. Mishmash, Andrew Higginbotham, Jeroen Danon, Martin Leijnse, Thomas S. Jespersen, Joshua A. Folk, Charles M. Marcus, Karsten Flensberg, and Jason Alicea. Milestones Toward Majorana-Based Quantum Computing. *Physical Review X*, 6(3):031016, August 2016.
- [16] Gábor Széchenyi and András Pályi. Parity-to-charge conversion for readout of topological Majorana qubits. *Physical Review B*, 101(23):235441, June 2020.
- [17] Deividas Sabonis, David van Zanten, Judith Suter, Torsten Karzig, Dmitry I. Pikulin, Jukka I. Väyrynen, Eoin O’Farrell, Davydas Razmadze, Peter Krogstrup, and Charles M. Marcus. Comparing tunneling spectroscopy and charge sensing of Andreev bound states in a semiconductor-superconductor hybrid nanowire structure, May 2021. arXiv:2105.08871 [cond-mat].
- [18] Davydas Razmadze, Deividas Sabonis, Filip K. Malinowski, Gerbold C. Ménard, Sebastian Pauka, Hung Nguyen, David M.T. van Zanten, Eoin C.T. O’Farrell, Judith Suter, Peter Krogstrup, Ferdinand Kuemmeth, and Charles M. Marcus. Radio-frequency methods for Majorana-based quantum devices: Fast charge sensing and phase-diagram mapping. *Physical Review Applied*, 11(6):064011, June 2019.
- [19] Sebastian Heedt, Marina Quintero-Pérez, Francesco Borsoi, Alexandra Fursina, Nick van Loo, Grzegorz P. Mazur, Michał P. Nowak, Mark Ammerlaan, Kongyi Li, Svetlana Korneychuk, Jie Shen, May An Y. van de Poll, Ghada Badawy, Sasa Gazibegovic, Nick de Jong, Pavel Aseev, Kevin van Hoogdalem, Erik P. A. M. Bakkers, and Leo P. Kouwenhoven. Shadow-wall lithography of ballistic superconductor–semiconductor quantum devices. *Nature Communications*, 12(1):4914, August 2021. Number: 1 Publisher: Nature Publishing Group.
- [20] David van Driel, Guanzhong Wang, Alberto Bordin, Nick van Loo, Francesco Zatelli, Grzegorz P. Mazur, Di Xu, Sasa Gazibegovic, Ghada Badawi, Erik P. A. M. Bakkers, Leo P. Kouwenhoven, and Tom Dvir. Spin-filtered measurements of Andreev bound states, December 2022. arXiv:2212.10241 [cond-mat].
- [21] M. G. House, I. Bartlett, P. Pakkiam, M. Koch, E. Peretz, J. van der Heijden, T. Kobayashi, S. Rogge, and M. Y. Simmons. High-Sensitivity Charge Detection with a Single-Lead Quantum Dot for Scalable Quantum Computation. *Physical Review Applied*, 6(4):044016, October 2016.
- [22] J. M. Hornibrook, J. I. Colless, A. C. Mahoney, X. G. Croot, S. Blanvillain, H. Lu, A. C. Gossard, and D. J. Reilly. Frequency multiplexing for readout of spin qubits. *Applied Physics Letters*, 104(10):103108, March 2014.

- [23] Ji-Yin Wang, Nick van Loo, Grzegorz P. Mazur, Vukan Levajac, Filip K. Malinowski, Mathilde Lemang, Francesco Borsoi, Ghada Badawy, Sasa Gazibegovic, Erik P. A. M. Bakkers, Marina Quintero-Pérez, Sebastian Heedt, and Leo P. Kouwenhoven. Parametric exploration of zero-energy modes in three-terminal InSb-Al nanowire devices. *Physical Review B*, 106(7):075306, August 2022.
- [24] Alexandre Assouline, Cheryl Feuillet-Palma, Alexandre Zimmers, Hervé Aubin, Marco Aprili, and Jean-Christophe Harmand. Shiba Bound States across the Mobility Edge in Doped InAs Nanowires. *Physical Review Letters*, 119(9):097701, August 2017.
- [25] J. Barański and T. Domański. In-gap states of a quantum dot coupled between a normal and a superconducting lead. *Journal of Physics: Condensed Matter*, 25(43):435305, October 2013. Publisher: IOP Publishing.
- [26] Eduardo J. H. Lee, Xiaocheng Jiang, Manuel Houzet, Ramón Aguado, Charles M. Lieber, and Silvano De Franceschi. Spin-resolved Andreev levels and parity crossings in hybrid superconductor–semiconductor nanostructures. *Nature Nanotechnology*, 9(1):79–84, January 2014. Number: 1 Publisher: Nature Publishing Group.
- [27] F. Persson, C. M. Wilson, M. Sandberg, G. Johansson, and P. Delsing. Excess Dissipation in a Single-Electron Box: The Sisyphus Resistance. *Nano Letters*, 10(3):953–957, March 2010.
- [28] L. DiCarlo, H. J. Lynch, A. C. Johnson, L. I. Childress, K. Crockett, C. M. Marcus, M. P. Hanson, and A. C. Gossard. Differential Charge Sensing and Charge Delocalization in a Tunable Double Quantum Dot. *Physical Review Letters*, 92(22):226801, June 2004.
- [29] Yongjie Hu, Hugh O. H. Churchill, David J. Reilly, Jie Xiang, Charles M. Lieber, and Charles M. Marcus. A Ge/Si heterostructure nanowire-based double quantum dot with integrated charge sensor. *Nature Nanotechnology*, 2(10):622–625, October 2007. Number: 10 Publisher: Nature Publishing Group.
- [30] MT Deng, S Vaitiekėnas, Esben Bork Hansen, Jeroen Danon, M Leijnse, Karsten Flensberg, Jesper Nygård, P Krogstrup, and Charles M Marcus. Majorana bound state in a coupled quantum-dot hybrid-nanowire system. *Science*, 354(6319):1557–1562, 2016.
- [31] Marco Valentini, Fernando Peñaranda, Andrea Hofmann, Matthias Brauns, Robert Hauschild, Peter Krogstrup, Pablo San-Jose, Elsa Prada, Ramón Aguado, and Georgios Katsaros. Nontopological zero-bias peaks in full-shell nanowires induced by flux-tunable andreev states. *Science*, 373(6550):82–88, 2021.
- [32] Jeroen Danon, Anna Birk Hellenes, Esben Bork Hansen, Lucas Casparis, Andrew P. Higginbotham, and Karsten Flensberg. Nonlocal Conductance Spectroscopy of Andreev Bound States: Symmetry Relations and BCS Charges. *Physical Review Letters*, 124(3):036801, January 2020.
- [33] G. C. Ménard, G. L. R. Anselmetti, E. A. Martinez, D Puglia, F. K. Malinowski, J. S. Lee, S Choi, M Pendharkar, C. J. Palmstrøm, K Flensberg, C. M. Marcus, L Casparis, and

- A. P. Higginbotham. Conductance-Matrix Symmetries of a Three-Terminal Hybrid Device. *Physical Review Letters*, 124(3):036802, January 2020.
- [34] Sebastian Miles, David van Driel, Michael Wimmer, and Chun-Xiao Liu. Kitaev chain in an alternating quantum dot-andreev bound state array. *arXiv preprint arXiv:2309.15777*, 2023.
- [35] William Samuelson, Viktor Svensson, and Martin Leijnse. A minimal quantum dot-based kitaev chain with only local superconducting proximity effect. *arXiv preprint arXiv:2310.03536*, 2023.
- [36] L. Yu. Bound state in superconductors with paramagnetic impurities. *Acta Phys. Sin.*, 21:75–91, 1965.
- [37] Hiroyuki Shiba. Classical spins in superconductors. *Progress of theoretical Physics*, 40(3):435–451, 1968.
- [38] A.I. Rusinov. Superconductivity near a paramagnetic impurity. *JETP Lett.*, 9, 1969.
- [39] K. Grove-Rasmussen, H. I. Jørgensen, B. M. Andersen, J. Paaske, T. S. Jespersen, J. Nygård, K. Flensberg, and P. E. Lindelof. Superconductivity-enhanced bias spectroscopy in carbon nanotube quantum dots. *Physical Review B*, 79(13):134518, April 2009.
- [40] Anders Jellinggaard, Kasper Grove-Rasmussen, Morten Hannibal Madsen, and Jesper Nygård. Tuning Yu-Shiba-Rusinov states in a quantum dot. *Physical Review B*, 94(6):064520, August 2016.
- [41] G. O. Steffensen, J. C. Estrada Saldaña, A. Vekris, P. Krogstrup, K. Grove-Rasmussen, J. Nygård, A. L. Yeyati, and J. Paaske. Direct transport between superconducting subgap states in a double quantum dot. *Physical Review B*, 105(16):L161302, April 2022.
- [42] Zhaoen Su, Alexandre B. Tacla, Moïra Hocevar, Diana Car, Sébastien R. Plissard, Erik P. A. M. Bakkers, Andrew J. Daley, David Pekker, and Sergey M. Frolov. Andreev molecules in semiconductor nanowire double quantum dots. *Nature Communications*, 8(1):585, September 2017. Number: 1 Publisher: Nature Publishing Group.
- [43] Olivér Kürtösy, Zoltán Scherübl, Gergő Fülöp, István Endre Lukács, Thomas Kanne, Jesper Nygård, Péter Makk, and Szabolcs Csonka. Andreev Molecule in Parallel InAs Nanowires. *Nano Letters*, 21(19):7929–7937, October 2021. Publisher: American Chemical Society.
- [44] Zoltán Scherübl, András Pályi, and Szabolcs Csonka. Transport signatures of an Andreev molecule in a quantum dot–superconductor–quantum dot setup. *Beilstein Journal of Nanotechnology*, 10(1):363–378, February 2019. Publisher: Beilstein-Institut.
- [45] J. C. Estrada Saldaña, A. Vekris, R. Žitko, G. Steffensen, P. Krogstrup, J. Paaske, K. Grove-Rasmussen, and J. Nygård. Two-impurity Yu-Shiba-Rusinov states in coupled quantum dots. *Physical Review B*, 102(19):195143, November 2020.

- [46] K. Grove-Rasmussen, G. Steffensen, A. Jellinggaard, M. H. Madsen, R. Žitko, J. Paaske, and J. Nygård. Yu–Shiba–Rusinov screening of spins in double quantum dots. *Nature Communications*, 9(1):2376, June 2018. Number: 1 Publisher: Nature Publishing Group.
- [47] Heidi Potts, Markus Aspegren, Rousan Debbarma, Sebastian Lehmann, and Claes Thelander. Large-bias spectroscopy of Yu-Shiba-Rusinov states in a double quantum dot. *Nanotechnology*, 34(13):135002, March 2023.
- [48] D. Z. Haxell, M. Coraiola, M. Hinderling, S. C. ten Kate, D. Sabonis, A. E. Svetogorov, W. Belzig, E. Cheah, F. Krizek, R. Schott, W. Wegscheider, and F. Nichele. Demonstration of nonlocal Josephson effect in Andreev molecules, July 2023. [arXiv:2306.00866 \[cond-mat\]](#).
- [49] Marco Coraiola, Daniel Z Haxell, Deividas Sabonis, Hannes Weisbrich, AE Svetogorov, Manuel Hinderling, Sofieke C ten Kate, Erik Cheah, Filip Krizek, Rüdiger Schott, et al. Hybridisation of andreev bound states in three-terminal josephson junctions. *arXiv preprint arXiv:2302.14535*, 2023.
- [50] Mátyás Kocsis, Zoltán Scherübl, Gergő Fülöp, Péter Makk, and Szabolcs Csonka. Strong nonlocal tuning of the current-phase relation of a quantum dot based Andreev molecule, March 2023. [arXiv:2303.14842 \[cond-mat\]](#).
- [51] Elsa Prada, Ramón Aguado, and Pablo San-Jose. Measuring Majorana nonlocality and spin structure with a quantum dot. *Physical Review B*, 96(8):085418, August 2017.
- [52] David J. Clarke. Experimentally accessible topological quality factor for wires with zero energy modes. *Physical Review B*, 96(20):201109, November 2017.
- [53] Andreas Pöschl, Alisa Danilenko, Deividas Sabonis, Kaur Kristjuhan, Tyler Lindemann, Candice Thomas, Michael J. Manfra, and Charles M. Marcus. Nonlocal signatures of hybridization between quantum dot and Andreev bound states. *Physical Review B*, 106(16):L161301, October 2022.
- [54] Jason R Petta, Alexander Comstock Johnson, Jacob M Taylor, Edward A Laird, Amir Yacoby, Mikhail D Lukin, Charles M Marcus, Micah P Hanson, and Arthur C Gossard. Coherent manipulation of coupled electron spins in semiconductor quantum dots. *Science*, 309(5744):2180–2184, 2005.
- [55] Athanasios Tsintzis, Rubén Seoane Souto, Karsten Flensberg, Jeroen Danon, and Martin Leijnse. Roadmap towards majorana qubits and nonabelian physics in quantum dot-based minimal kitaev chains. *arXiv preprint arXiv:2306.16289*, 2023.
- [56] Willemijn Uilhoorn, James G Kroll, Arno Bargerbos, Syed D Nabi, Chung-Kai Yang, Peter Krogstrup, Leo P Kouwenhoven, Angela Kou, and Gijs de Lange. Quasiparticle trapping by orbital effect in a hybrid superconducting-semiconducting circuit. *arXiv preprint arXiv:2105.11038*, 2021.
- [57] Arno Bargerbos, Marta Pita-Vidal, Jesús Ávila, Lukas J Splitthoff, Lukas Grünhaupt, Jaap J Wesdorp, Christian K Andersen, Yu Liu, Leo P Kouwenhoven, Ramón Aguado,

- et al. Singlet-doublet transitions of a quantum dot josephson junction detected in a transmon circuit. *PRX Quantum*, 3(3):030311, 2022.
- [58] M. S. Khalil, M. J. A. Stoutimore, F. C. Wellstood, and K. D. Osborn. An analysis method for asymmetric resonator transmission applied to superconducting devices. *Journal of Applied Physics*, 111(5):054510, March 2012.
- [59] C. Volk, A. M. J. Zwerver, U. Mukhopadhyay, P. T. Eendebak, C. J. van Diepen, J. P. Dehollain, T. Hensgens, T. Fujita, C. Reichl, W. Wegscheider, and L. M. K. Vandersypen. Loading a quantum-dot based “Qubyte” register. *npj Quantum Information*, 5(1):1–8, April 2019. Number: 1 Publisher: Nature Publishing Group.
- [60] A. R. Mills, D. M. Zajac, M. J. Gullans, F. J. Schupp, T. M. Hazard, and J. R. Petta. Shutting a single charge across a one-dimensional array of silicon quantum dots. *Nature Communications*, 10(1):1063, March 2019. Number: 1 Publisher: Nature Publishing Group.
- [61] Florian Luthi, Thijs Stavenga, OW Enzing, Alessandro Bruno, Christian Dickel, NK Langford, Michiel Adriaan Rol, Thomas Sand Jespersen, Jesper Nygård, P Krogstrup, et al. Evolution of nanowire transmon qubits and their coherence in a magnetic field. *Physical review letters*, 120(10):100502, 2018.
- [62] Han Zheng, Luk Yi Cheung, Nikunj Sangwan, Artem Kononov, Roy Haller, Joost Ridderbos, Carlo Ciaccia, Jann Hinnerk Ungerer, Ang Li, Erik PAM Bakkers, et al. Coherent control of a few-channel hole type gatemon qubit. *arXiv preprint arXiv:2312.06411*, 2023.
- [63] Sven Marian Albrecht, Andrew P Higginbotham, Morten Madsen, Ferdinand Kuemmeth, Thomas Sand Jespersen, Jesper Nygård, Peter Krogstrup, and CM Marcus. Exponential protection of zero modes in majorana islands. *Nature*, 531(7593):206–209, 2016.
- [64] J. Bauer, A. Oguri, and A. C. Hewson. Spectral properties of locally correlated electrons in a Bardeen–Cooper–Schrieffer superconductor. *Journal of Physics: Condensed Matter*, 19(48):486211, November 2007.
- [65] A. Martín-Rodero and A. Levy Yeyati. The Andreev states of a superconducting quantum dot: mean field versus exact numerical results. *Journal of Physics: Condensed Matter*, 24(38):385303, September 2012. Publisher: IOP Publishing.
- [66] Damaz de Jong, Christian G. Prosko, Daan M. A. Waardenburg, Lin Han, Filip K. Malinowski, Peter Krogstrup, Leo P. Kouwenhoven, Jonne V. Koski, and Wolfgang Pfaff. Rapid Microwave-Only Characterization and Readout of Quantum Dots Using Multiplexed Gigahertz-Frequency Resonators. *Physical Review Applied*, 16(1):014007, July 2021.

5

ROBUST POOR MAN'S MAJORANA ZERO MODES USING YU-SHIBA-RUSINOV STATES

5

If the doors of perception were cleansed every thing would appear to man as it is, Infinite.

- William Blake

The recent realization of a two-site Kitaev chain featuring “poor man’s Majorana” states demonstrates a path forward in the field of topological superconductivity. Harnessing the potential of these states for quantum information processing, however, requires increasing their robustness to external perturbations. Here, we form a two-site Kitaev chain using proximitized quantum dots hosting Yu-Shiba-Rusinov states. The strong hybridization between such states and the superconductor enables the creation of poor man’s Majorana states with a gap larger than $70\mu\text{eV}$. It also greatly reduces the charge dispersion compared to Kitaev chains made with non-proximitized quantum dots. The large gap and reduced sensitivity to charge fluctuations will benefit qubit manipulation and demonstration of non-abelian physics using poor man’s Majorana states.

INTRODUCTION

Kitaev chains based on quantum dots (QDs) coupled via a hybrid semiconductor-superconductor heterostructure are a promising avenue for the creation of Majorana bound states [1, 2]. Even a minimal chain, consisting of only two QDs, supports fine-tuned Majorana zero modes known as “poor man’s Majoranas” (PMMs) [3]. These PMM states do not benefit from topological protection, but already exhibit robustness to local perturbations and quadratic protection from global fluctuations in the chemical potential [3]. Moreover, PMM states obey non-abelian exchange statistics, thus providing a favourable platform for braiding and Majorana-based qubit experiments in the near future [4–7]. In Ref. [8], we have recently realized the two-site Kitaev chain by coupling two QDs formed in an InSb/Al hybrid nanowire. While providing the necessary proof of concept, the gap separating PMMs from excited states is not much higher than the electron temperature. Furthermore, appreciable noise in the measured spectra indicate sensitivity to charge fluctuations, making practical use of such states infeasible.

Insensitivity to charge noise has been successfully achieved in transmon qubits by increasing the ratio between superconducting coupling (Josephson energy) and charging energy, thereby suppressing the charge dispersion of the spectrum [9, 10]. We follow a similar approach by strongly coupling our QDs to the superconductor. This induces superconducting correlations on the QDs leading to energy eigenstates known as Yu-Shiba-Rusinov (YSR) states [11–20]. Spin-polarized YSR states can also serve as the sites of a Kitaev chain, as investigated theoretically [21–26] and experimentally using scanning tunneling microscopy [27–31]. In this work, we realize a two-site Kitaev chain using YSR states in a hybrid semiconducting InSb nanowire partly covered with a superconducting Al film. We show that the sensitivity of the resulting PMMs to charge fluctuations affecting the QDs decreases by two orders of magnitude compared to a QD-based Kitaev chain [8]. In addition, we measure a gap between ground and excited states of $E_{\text{gap}} = 76\mu\text{eV}$, a threefold increase compared to our previous report [8]. Complementary results are also reported in a parallel study on a 2D hybrid platform using an InAsSb/Al two-dimensional electron gas [32], demonstrating the wider applicability of our approach.

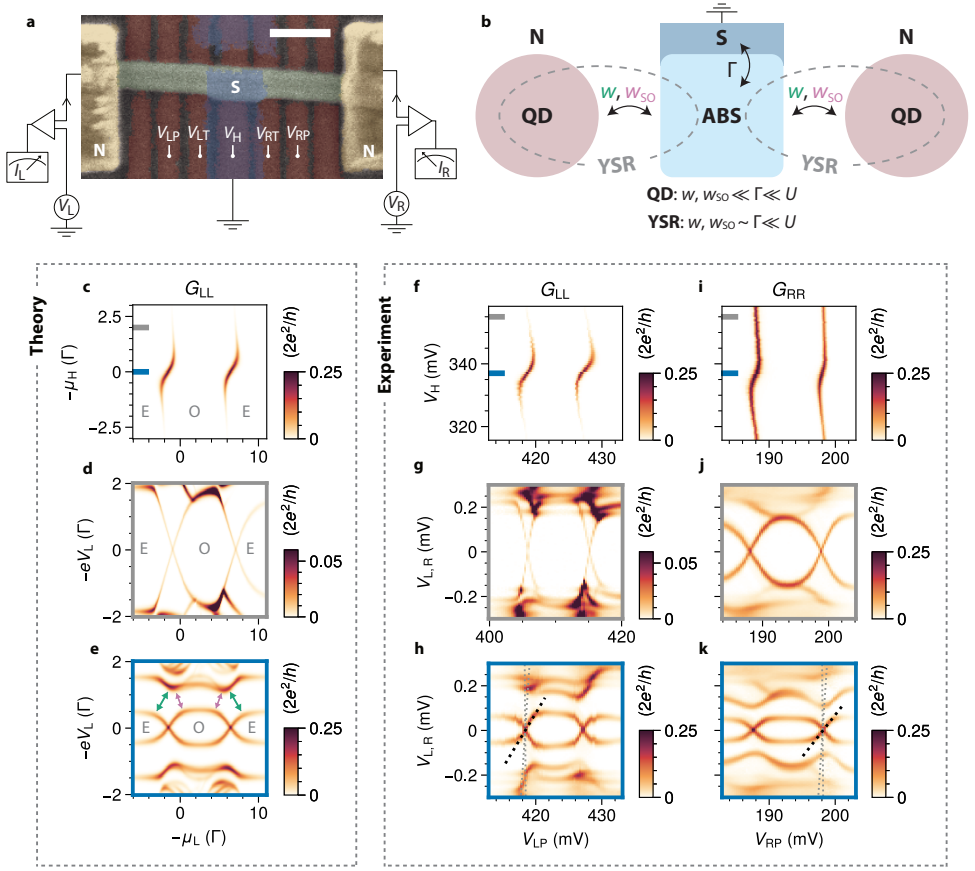


Figure 1: YSR states formed by hybridizing QDs with an ABS. **a**, False-colored scanning electron micrograph and measurement circuit of the device. Scale bar is 200 nm. **b**, Illustration of the QD-ABS-QD model. Two QDs are coupled to the same ABS via spin-conserving and spin-flipping tunneling. QD and YSR regimes are defined by the relative energy scales shown below the sketch. **c**, Numerical CSD using zero-bias conductance of a QD coupled to an ABS. “E”/“O” indicate even/odd occupation of the QD. **d**, **e**, Numerical conductance spectrum of a QD coupled to an ABS as a function of QD chemical potential when ABS is far (d) and close to its energy minimum (e). In **e**, green/pink arrows indicate avoided crossings due to spin-conserving/spin-flipping tunneling. **f**–**h**, Same as **c**–**e** for the left QD coupled to an ABS, experimentally measured using local conductance. Gray/blue ticks in **f** mark V_H values at which g/h are measured. The right QD is off resonance. In **h**, we extract a lever arm $\alpha \approx 0.05e$ by fitting the spectrum with the black dotted line at the zero-energy crossing. This procedure overestimates the actual lever arm since it does not account for capacitance to the normal lead. For comparison, we plot the profile of a typical Coulomb diamond in our device with gray dotted lines (see figure 7a). The V_{LP} range in **g** is shifted because of a gate jump affecting the left QD. **i**–**k**, Same as **f**–**h**, but for the right QD. The extracted lever arm is $\alpha \approx 0.04e$.

5.1 FABRICATION AND SETUP

figure 1a shows a scanning electron microscope image of the reported device. It consists of an InSb nanowire (green) placed on top of a series of bottom gates [33]. The middle part of the nanowire is covered by a thin Al shell (blue), forming a superconductor-semiconductor

hybrid whose electrochemical potential is controlled by a plunger gate (V_H). On both sides of the hybrid segment, QDs are formed in the nanowire using three gates each. The electrochemical potential of each QD is controlled by a plunger gate (V_{LP} and V_{RP} for the left and right QDs, respectively), and the couplings between the QDs and the hybrid are controlled by tunnel gates (V_{LT} and V_{RT} for the left and right QDs, respectively). A normal lead is attached to each QD, separated by another gate-defined tunnel barrier. The superconducting lead is kept grounded at all times. In addition, the two normal leads are connected to off-chip multiplexed resonators for fast RF reflectometry measurements [34], using the setup described in Ref. [35]. Each lead is voltage biased independently with respect to the grounded Al, with voltages V_L and V_R on the left and right leads, respectively. The currents (I_L and I_R on the left and right leads), the local conductances ($G_{LL} = dI_L/dV_L$, $G_{RR} = dI_R/dV_R$), and the non-local conductances ($G_{RL} = dI_R/dV_L$, $G_{LR} = dI_L/dV_R$) are measured simultaneously. When the full conductance matrix is measured, we correct for line resistance as described in the Methods section. Further fabrication and setup details can be found in our previous publications [36–38]. The experiment is conducted in a dilution refrigerator with a base temperature of 30 mK. A magnetic field of $B = 150$ mT is applied along the nanowire axis, inducing a Zeeman splitting of approximately 200 μ eV in the QDs (figure 5).

5.2 YSR STATES IN QUANTUM DOTS

We model our system using a three-site model in which the hybrid is considered as a single Andreev bound state (ABS) in the atomic limit [15, 16] tunnel-coupled to two QDs (see schematics in figure 1b) [26]. The QDs have charging energy U , Zeeman splitting E_Z , and chemical potentials μ_L, μ_R for the left and right QD, respectively. The ABS has an induced gap Γ , which in the atomic limit [15, 16] can be identified with its tunnel coupling to the bulk superconductor. Its charging energy is negligible due to the screening of the grounded Al film. It also has Zeeman splitting E_{ZH} , which is smaller than that of the QDs due to metallization of the ABS [39]. We ensure $E_{ZH} < \Gamma$ so that the ground state of the ABS is always a BCS singlet. The electron-hole composition of the ABS depends on its chemical potential μ_H .

In our model, the QDs are coupled to the ABS by spin-conserving and spin-flipping tunneling due to spin-orbit interaction, with amplitudes w and w_{SO} , respectively [26]. The hybridization between QDs and the ABS becomes significant when $w, w_{SO} \sim \Gamma$. As a consequence, the QDs become proximitized and form YSR states [20, 40], which we distinguish from ABSs because of their large charging energy [15–19, 41]. We refer readers to the Supplementary Information and the parallel work of Ref. [40] for theory models of the strong coupling regime investigated in this work.

To understand the nature of the YSR states formed in proximitized QDs, we first examine the coupling between a single QD and an ABS in the hybrid segment, following Ref. [20]. figure 1c shows the theoretical zero-bias conductance of a QD-ABS charge stability diagram (CSD), while the second QD is off-resonance. The two vertical features indicate parity transitions of the system, largely corresponding to the consecutive filling of a single orbital of the QD by two electrons. The S-shaped conductance features result from renormalization of the QD energy via hybridization with the ABS. The ABS reaches its energy minimum at charge neutrality, i.e., $\mu_H = 0$, where its excitation is equal-parts electron

and hole. The hybridization with the QD is also maximal here due to their minimal energy separation, evident in the enhanced zero-bias conductance as local Andreev reflection becomes stronger [20, 40]. The QD spectra in panels d and e further reveal its hybridization with the ABS. When the latter is away from charge neutrality, the QD spectrum as a function of μ_L (figure 1d) exhibits straight features reminiscent of Coulomb diamonds. As the ABS approaches $\mu_H = 0$ (figure 1e), such features evolve into an eye-shaped spectrum typical of YSR states [19, 42–45]. The arrows indicate avoided crossings in the excited states of the spectrum produced by spin-conserving (green) and spin-flipping (pink) tunneling between the ABS and the QD levels [40].

The hybrid segment of our device features multiple discrete ABSs well-separated from each other in V_H (figure 6). We operate in a V_H range containing a single ABS level. In figure 1f, we show the zero-bias conductance measured with the left lead as a function of V_{LP} and V_H . V_{RP} is fixed to keep the right QD off-resonance. We observe the QD-ABS charge stability diagram features described in panel c, indicating the presence of an ABS reaching its energy minimum at $V_H \approx 337$ mV. The QD-ABS hybridization is further confirmed by the QD spectrum being in agreement with the model when the ABS is away from (figure 1g) and at its energy minimum (figure 1h).

The YSR zero-energy excitations in figure 1h are our building blocks of a Kitaev chain. Compared to a non-proximitized QD zero-energy crossing, these YSR crossings have noticeably weaker energy dispersion as a function of gate (see dashed lines in panel h). To quantify this observation, we can estimate the lever arm of the YSR excitation at charge degeneracy using its gate-dispersion slope: $\alpha \equiv \partial E / \partial V_{LP}$. In contrast to the above-gap QD lever arm of $\alpha \approx 0.4e$ in our devices (figure 7a), this subgap lever arm reduces to $\alpha \approx 0.2e$ (figure 7b) when the ABS is detuned from its charge neutrality. Tuning the ABS to its energy minimum further reduces the lever arm to $\alpha \approx 0.05e$ (figure 1h). This signals a strong reduction in the effective charge of the fermionic excitation, attributable to charging energy renormalization, QD-ABS hybridization, and electron-hole superposition [46, 47], as detailed in figure 8.

The right QD shows similar behavior when coupled to the same ABS (figure 1i–k). However, when the ABS is away from charge neutrality, the subgap conductance is not significantly suppressed (figure 1i) and the QD spectrum still shows typical YSR features (figure 1h), albeit with a small superconducting coupling. This could be due to residual proximity resulting from direct coupling between the QD and the superconducting film since V_H does not affect it appreciably (figure 9).

5.3 COUPLED YSR STATES

Recent theoretical [25, 26] and experimental [8, 48, 49] works have shown that an ABS can mediate elastic co-tunneling (ECT) and crossed Andreev reflection (CAR) between QDs. These two processes implement the hopping and pairing terms of the original Kitaev chain model [1, 2]. To form PMM states in a two-site chain, the amplitudes of both terms must be equal [3]. Such control can be achieved by tuning the electrochemical potential of the ABS in the hybrid nanowire [8, 25, 26, 49].

Similar effective ECT and CAR couplings, with respective amplitudes t and Δ , also emerge between YSR states (figure 2a) formed by strongly coupling QDs to the same ABS [40, 50, 51]. To observe them, we turn to the CSD of two such YSR states, akin to

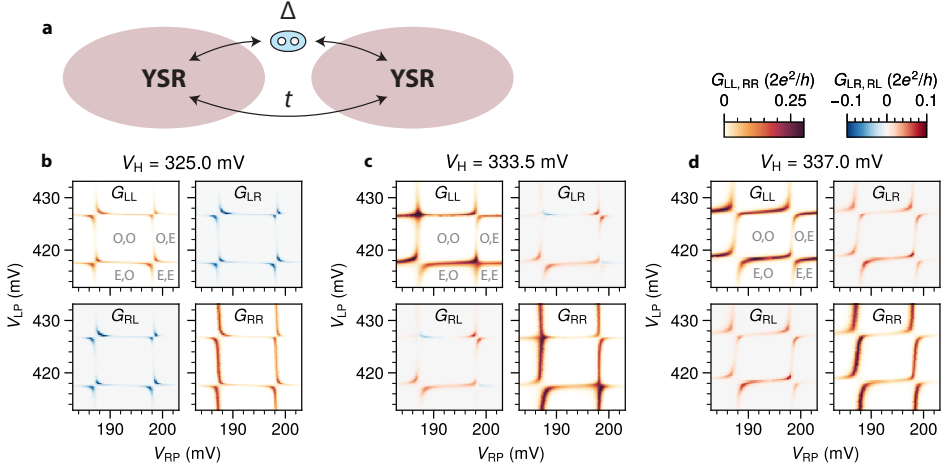


Figure 2: **ECT and CAR coupling between YSR states.** **a**, Illustration of the effective two-site system of YSR states coupled via ECT (t) and CAR (Δ). **b–d**, Conductance matrices of CSDs measured at different V_H . By tuning the electrochemical potential of the ABS in the hybrid, it is possible to continuously vary t and Δ . In **b**, avoided crossings along the anti-diagonal are observed, indicating $t > \Delta$. The opposite regime is shown in **d**, with all the avoided crossings along the diagonal, indicating $t < \Delta$. The crossover between these two regimes is shown in **c**, where two crossings indicate $t \approx \Delta$.

5

those explored in Refs. [52, 53]. In figure 2b, we show the zero-bias conductance matrix measured as a function V_{RP} and V_{LP} when the ABS is tuned away from its energy minimum. All elements of the conductance matrix show prominent resonances arising from the two charge transitions of each QD. The type of avoided crossings observed in the CSD serves as an indication of the coupled-YSR system's ground state [8, 26]. Avoided crossings along a negative diagonal, as seen in all four resonances in figure 2b, show hybridization between states with the same total charge. This is the ground state of the system when $t > \Delta$. This observation is further confirmed by the negative non-local conductance that is characteristic of ECT [8].

Increasing the value of V_H leads to a change in the CSD, shown in figure 2c. Here, the bottom-left and the top-right resonances show avoided crossings along a positive diagonal associated with $\Delta > t$. In the top-left and bottom-right, the resonance lines cross each other, indicating a PMM sweet spot, with $t \approx \Delta$. Finally, bringing the ABS close to its energy minimum by a further increase of V_H tunes all of the quadrants of the CSD to the $\Delta > t$ regime (Fig. 2d). The theoretical model reproduces the observed evolution of the CSDs (figure 10a–c).

5.4 GATE CONTROL OF CAR AND ECT

ABS-mediated ECT and CAR couplings between QDs are controlled by the chemical potential of ABS [25, 49]. At the energy minimum of the ABS, its excitation is equally electron- and hole-like, both parts interfering constructively to enhance CAR and destructively to quench ECT. Finite values of μ_H lead to an imbalance between the electron and hole parts of

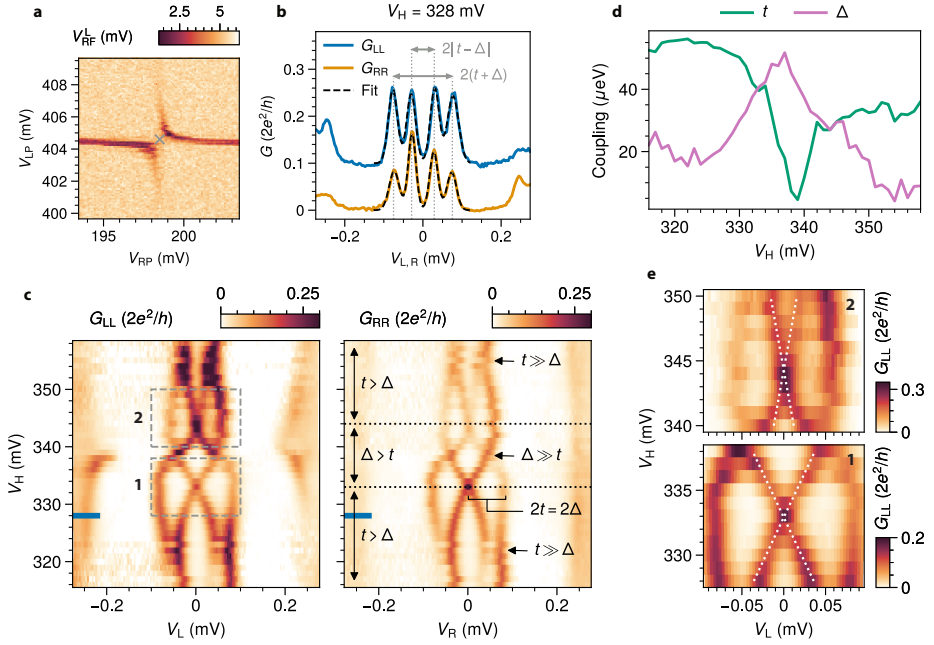


Figure 3: ECT and CAR coupling as a function of the ABS chemical potential. **a**, CSD measured using RF reflectometry. The center of the avoided crossing, marked with a gray cross, is identified as $\mu_L = \mu_R = 0$. **b**, Spectrum measured on both sides of the device at the center of the avoided crossing shown in **a**. The inner peaks correspond to excited states at $|t - \Delta|$, while the outer ones correspond to excited states at $t + \Delta$. By summing and subtracting these energies, it is possible to extract t and Δ for each V_H value. **c**, Spectrum as a function of V_H while $\mu_L = \mu_R = 0$. Each line of the spectrum was measured as described above. The blue tick indicates the V_H value at which **a** and **b** were measured. **d**, ECT and CAR couplings extracted from **c**. **e**, Zoom-in on the zero-energy crossings highlighted in **c**. The white dotted lines are fits to extract the slope of the linear splitting. The data reported here was collected for the bottom-right charge transition shown in figure 2. More details about data processing and data for all charge degeneracies are reported in figure 11.

the ABS, decreasing the value of the CAR coupling while enhancing ECT. This control over the ECT and CAR amplitudes guarantees a PMM sweet spot when the two QDs are coupled via a single ABS [25, 26, 49]. To demonstrate that this description can be extended to YSR states coupled via an ABS, we study how the couplings t and Δ vary as the electrochemical potential of the ABS changes.

The magnitudes of t and Δ can be extracted by measuring the excitation spectrum of the system at $\mu_L = \mu_R = 0$, when spectral splitting is determined by the couplings alone. We limit the discussion here to the bottom-right crossing of figure 2, noting that the other crossings exhibit qualitatively similar behavior (figure 11). At each fixed value of V_H , we measure a CSD (figure 3a) and set the QD gates to the center of an avoided crossing. There, the subgap spectrum exhibits two sets of electron-hole symmetric peaks at energies $|t - \Delta|$ and $t + \Delta$ (figure 3b), as detailed in Methods. By fitting the measured spectrum with two pairs of Gaussians symmetric around $V_{L,R} = 0$, we extract the energy of the excited states and calculate t and Δ . We repeat this procedure for different values of V_H and collect the

spectra in figure 3c, where each line was measured as described above.

figure 3d shows the extracted values of ECT and CAR amplitudes. At $V_H \approx 322$ mV and $V_H \approx 355$ mV, the outer peaks almost merge with the inner ones, indicating $|t - \Delta| \approx t + \Delta$. Inspecting the corresponding CSDs (see figure 2b for an example, all the CSDs are available in the online repository), we can see that ECT is dominant and, therefore, $t \gg \Delta$. Upon varying V_H , the two peaks split into four well-separated peaks, signaling that CAR is increasing although ECT still prevails. At $V_H \approx 333$ mV and 345 mV, the two inner peaks merge into a single zero-bias peak. These are two sweet spots where $t \approx \Delta$. In between them, CAR dominates, as the CSDs can confirm (see figure 2d). Around $V_H \approx 338$ mV, the outer peaks merge again, this time indicating $\Delta \gg t$. This feature is the peak in Δ and dip in t seen in figure 3d, because of the aforementioned interference effects [25, 49]. Finally, figure 10d shows that the same spectral features are reproduced by the theoretical model.

The zero-energy crossings in figure 3e allow us to characterize the robustness of the PMM sweet spots to charge fluctuations affecting the ABS and, consequently, t and Δ , causing a splitting of the zero-energy states. Indeed, we observe that each zero energy state splits with a linear dependence on V_H as predicted by theory, indicating the lack of protection against deviations from the condition $t = \Delta$ known for a two-site Kitaev chain [3]. We extract a slope of $\frac{\partial E}{\partial V_H} \approx 7 \mu\text{eV/mV}$ and $3 \mu\text{eV/mV}$ for the two crossings, comparable to what we measured in Ref. [8].

5.5 MAJORANA SWEET SPOT

Finally, we measure the spectrum and stability of the PMM states against perturbation of the QDs. We tune our device to the sweet spot at $V_H = 333.5$ mV, where $t \approx \Delta$. In figure 4a, we show the full conductance matrix of the CSD at the sweet spot. As expected, the resonance lines cross each other and non-local conductance alternates between positive and negative values. The spectrum measured at the sweet spot in the center of the CSD (figure 4b) shows, on both sides of the device, a zero-bias conductance peak clearly separated from the excited states. As a result of the much stronger coupling between YSR states, the first excited states reside at energies of $E_{\text{gap}} \approx 76 \mu\text{eV}$, three times larger than in our previous report [8] and significantly above the electron temperature.

One of the hallmarks of PMM states is their stability against local perturbations. In figure 4c, we measure the spectrum of the QDs varying V_{RP} while keeping the left QD on resonance. The observed zero-bias conductance peak persists within the range of the investigated charge degeneracy. Tuning V_{LP} while keeping the right QD on resonance (figure 12b) shows the same qualitative features. The same behavior can be reproducibly observed with other QD and ABS orbitals, as shown in figure 13.

If the electrochemical potentials of both QDs are detuned from the sweet spot, PMM states are expected to split quadratically. This is verified in figure 4d, where we measure the spectrum while detuning both QDs along the antidiagonal path shown in figure 4a. The spectrum taken along the diagonal path is shown in figure 12c. Numerical simulations reproducing these measurements are reported in figure 10e–i. For comparison, we plot the quadratic dispersion measurements of the QD-based vs YSR-based PMMs side by side in panels e and f. The curvature of the energy-gate dispersion close to the sweet spot is directly proportional to the dephasing rate resulting from charge noise affecting both QDs [54–57] and is therefore a measure of the Majorana states' robustness against it. Comparing the

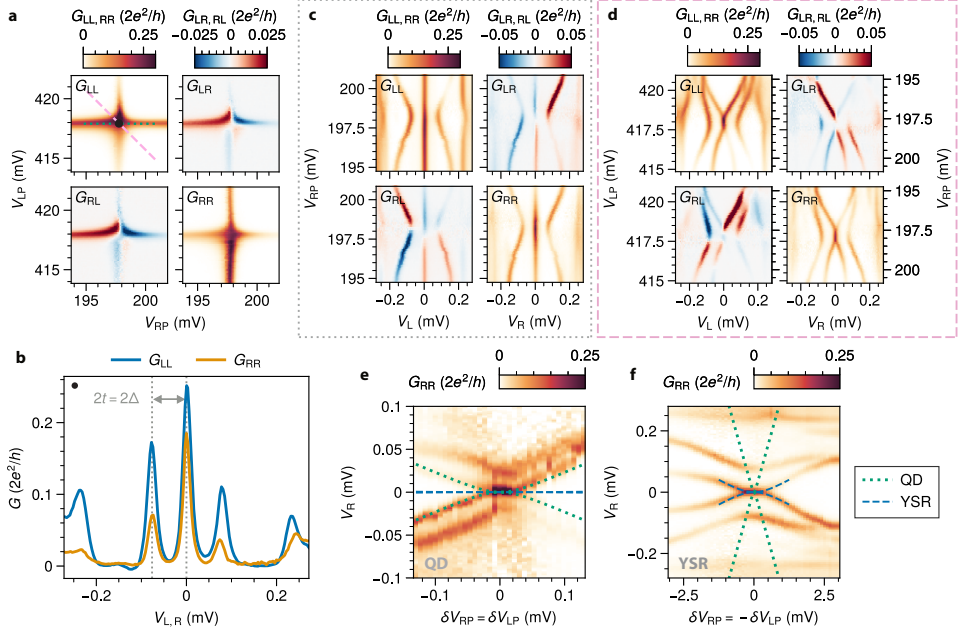


Figure 4: **Poor man's Majorana sweet spot for coupled YSR states.** **a**, Conductance matrix of a crossing in the CSD, when $t \approx \Delta$. **b**, Spectrum of both sides measured at the sweet spot in the center of the crossing of panel a. **c**, Conductance matrix of the spectrum as a function of V_{RP} (along the gray dotted line in a). The right QD is detuned across the sweet spot, while the left one is kept on resonance. **d**, Conductance matrix of the spectrum measured detuning both QDs simultaneously along the antidiagonal along the pink dashed line in a. **e, f**, G_{RR} as a function of the simultaneous detunings of both sites, δV_{LP} and δV_{RP} , away from the sweet spot, using QDs (e, replotted from Ref. [8]) and YSR states (f, from the same dataset presented in d). For comparison, we have plotted the two gate dispersions with the same scale in both plots. The green dotted lines correspond to the expected energy splitting of a PMM realized with QDs, the blue dashed lines to that of a PMM realized with YSR states, as detailed in the Methods section.

overlaid curves in figure 4e and f, we find the gate dispersion curvature reported in this work to be a factor of ~ 150 lower than the non-proximitized case (details in Materials and Methods). This striking reduction can be fully explained by the decreased lever arm of the YSR states, α and the increased E_{gap} , since the curvature expected from the theory model is α^2/E_{gap} (see Materials and Methods).

To illustrate the effect of reduced charge dispersion on the coherence of a potential poor man's Majorana qubit, we calculate the dephasing rates using realistic charge noise estimations and data presented above (see Supplementary Information). While perturbation of QDs' potentials is expected to be the dominant mechanism of energy splitting and thus dephasing for non-proximitized PMMs, the drastic reduction in gate dispersion of YSR-based PMMs makes it negligible compared to dephasing caused by deviations from the $t = \Delta$ condition. The estimated $T_2^* \sim 10$ ns is now limited by noise affecting the couplings t and Δ , nearly an order of magnitude higher than the charge-noise-limited T_2^* extracted from data in our previous report [8]. Importantly, the expected dephasing time is now also much longer than the adiabatic limit $\hbar/E_{\text{gap}} \sim 10$ ps, which sets an upper bound on how

fast Majorana states can be manipulated without populating the excited states [5, 54].

5.6 CONCLUSION

In conclusion, we have demonstrated the formation of YSR states by hybridizing QDs with a common ABS. The coupling between these YSR states can be controlled by varying the electrochemical potential of the ABS, thus realizing a fully tunable two-site Kitaev chain. The resulting PMM states have two significant improvements over those in a non-proximitized QD chain. First, the stronger coupling between the YSR states triples the gap between the PMM and excited states, protecting the former from finite temperature excitations [55] and enabling faster adiabatic operations [5, 54]. Second, the reduced charge dispersion of the YSR states enhances the robustness of the PMMs against charge noise affecting both QDs by more than 100. Thanks to these, even a two-site Kitaev chain realized using YSR states should suffice for a prototypical Majorana qubit and verification of non-abelian properties with fusion and braiding experiments. Despite the present lack of protection against tunnel-coupling noise, the expected coherence of Majorana qubits made from PMM states is increased by close to an order of magnitude compared to the first report [8]. In the future, increasing the number of sites can mitigate noise affecting the tunnel-coupling rates. Estimations using parameters of the YSR-based PMMs suggest that a Majorana qubit realized with Kitaev chains as short as 3 to 5 sites could already achieve dephasing times comparable to those predicted for continuous nanowires [2, 55].

5.7 MATERIALS AND METHODS

5.7.1 DEVICE FABRICATION

The InSb/Al hybrid nanowire device presented in this work was fabricated using the shadow-wall lithography technique [36, 37].

A substrate is patterned with Ti/Pd gates. 10 nm of AlO_x and 10 nm of HfO_x are deposited by ALD as gate dielectric. HSQ shadow-walls are then patterned. Nanowires are deposited and pushed next to the shadow-walls using an optical micro-manipulator. An 8 nm Al shell is deposited at alternating angles of 15° and 45° with respect to the substrate, followed by a capping layer of 20 nm of AlO_x . Normal leads in ohmic contact with the nanowire are fabricated by Ar milling and evaporation of Cr/Au.

Additional details about the substrate fabrication and the Al deposition are described in Ref. [38].

5.7.2 TRANSPORT MEASUREMENTS AND DATA PROCESSING

The measurements are done in a dilution refrigerator with a base temperature of 30 mK. A magnetic field of 150 mT is applied along the nanowire axis except in figure 5c,d.

The three-terminal setup used to measure the device is illustrated in figure 1a. The SC lead is always kept grounded. The two normal leads can be voltage-biased independently. When a bias is applied to one side, the other one is kept grounded. The currents I_L and I_R are measured separately. Digital multimeters and lock-in amplifiers are used to read the voltage outputs of the current meters. AC excitations of $5\text{ }\mu\text{V}$ RMS are applied on each side with different frequencies (39 Hz on the left and 29 Hz on the right), except for figure 6 and figure 9d–f, where excitations of $10\text{ }\mu\text{V}$ RMS were used.

Off-chip multiplexed resonators [34] connected to the two normal leads are used for fast RF reflectometry measurements. This measurement scheme was employed to speed up the tune-up of the device, for figure 3, and for figure 11, as explained in figure 3a. Additional details about the reflectometry setup are described in Ref. [35].

5.7.3 SPINLESS PMM SPECTRUM

The low-energy spectrum of the coupled YSR system arising from the model described in Supplementary Information can be reduced to that of a spinless PMM model [3, 6, 25, 26, 40].

In this simplified model, the non negative energy eigenvalues are [3]

$$E_{\pm} = \sqrt{\mu_+^2 + \mu_-^2 + t^2 + \Delta^2 \pm 2\sqrt{(\mu_+^2 + \Delta^2)(\mu_-^2 + t^2)}},$$

where $\mu_{\pm} = \frac{\mu_L \pm \mu_R}{2}$, μ_L and μ_R are the chemical potentials of the two sites, and t , Δ are the couplings. The spectrum is symmetric around zero energy because of particle-hole symmetry. If $\mu_L = \mu_R = 0$, the eigenvalues reduce to $E_+ = t + \Delta$ and $E_- = |t - \Delta|$. These are the excitation energies that we use to extract t and Δ from the measured spectra in figure 3.

The gate dispersion lines plotted in figure 4e,f are calculated using the lowest excitation energy. When $t = \Delta$ we obtain

$$E_- = \sqrt{\alpha^2 \delta V^2 + 2t^2 - 2\sqrt{t^2(t^2 + \alpha^2 \delta V^2)}},$$

where α is the lever arm converting voltage to chemical potential and δV is the simultaneous detuning of each gate away from the sweet spot. For the PMM realized with QDs, we have used $\alpha = 0.33e$ and $t = 12\mu\text{eV}$ [8]. For the PMM realized with YSR states we have used $\alpha = 0.05e$ (figure 5) and $t = 38\mu\text{eV}$ (figure 4b). Finally, the quadratic splitting of PMM states can be derived by expanding the expression above for small δV , which gives

$$E_- \approx \frac{\alpha^2}{2t} \delta V^2.$$

5.7.4 SERIES RESISTANCE CORRECTION

The effect of series resistance in the fridge line and other parts of the circuit on transport measurements of a three-terminal device of our type is described in Ref. [58], as well as how to correct for it. In our setup, the resistance of the voltage source is 100Ω and that of the current meter is 200Ω . Additional series resistance comes from the fridge lines and the ohmic contacts. Correcting for the voltage fall over these resistors in series to the device requires knowledge of the exact resistance values, which we presently cannot obtain before the next sample exchange. Therefore, we make use of the fact that the bulk Al superconducting gap in local conductance measurements should stay constant across all gate values to arrive at an estimation of the total series resistance in each fridge line.

In figure 14a,c it is possible to observe that the superconducting gap appears enlarged when there is finite subgap conductance, indicating unaccounted-for series resistance. To estimate it, we correct the G_{LL} measurement shown in figure 14a for different trial values of the series resistance. We extract the energies of the coherence peaks and calculate their variance. Finally, we choose the value that minimizes the variance as the optimal series resistance. We find an optimal value of $3.65\text{k}\Omega$, in addition to the resistance of the voltage

source and current meter. The corrected measurement is shown in figure 14b. All the data processing steps are available in the online repository. In figure 14c,d we show that the same series resistance value also corrects an analogous measurement on the right side. In the regimes relevant to this work, the voltage divider effect caused by the series resistance does not strongly affect local conductance. On the other hand, it can be more pronounced for non-local conductance, as discussed in figure 14e,f. Using the extracted resistance value, we apply the correction method described in Ref. [58] to the data presented in figure 2, figure 3, figure 4, figure 6, figure 9d, figure 11, figure 12, figure 13d–k, and figure 14b,d,f, where the full conductance matrix is measured.

5.7.5 DEVICE TUNE-UP

The device is controlled with seven bottom gates (figure 1a). To perform tunnel spectroscopy of the hybrid segment in figure 6 and figure 9, we use V_{LT} and V_{RT} to form a tunnel barrier and apply a large positive voltage to V_{LP} , V_{RP} , and the outer gates. V_H is used to control the electrochemical potential in the hybrid segment, where discrete states are confined because of the tunnel barriers. QDs are formed by reducing the voltage on the outer gates. This creates additional tunnel barriers next to the normal leads, thus shaping a confining potential. V_{LP} and V_{RP} control the electrochemical potential of the QDs. Finally, the coupling between the QDs and the ABS can be controlled using V_{LT} and V_{RT} . By increasing their voltage, we can achieve the strong coupling regime between the QDs and the ABS in the hybrid as explained in figure 1. For all the measurements presented in the main text, the gates defining the tunnel barriers were maintained at the same value.

5.8 SUPPLEMENTARY INFORMATION

5.8.1 THEORETICAL MODEL

The physical system of double QDs connected by a hybrid segment in the middle can be well described by a three-site model as below

$$\begin{aligned}
 H &= \sum_{i=L,H,R} H_i + H_T, \\
 H_i &= (\mu_i + E_{Zi})n_{i\uparrow} + (\mu_i - E_{Zi})n_{i\downarrow} + U_i n_{i\uparrow} n_{i\downarrow} + \Gamma_i (c_{i\uparrow}^\dagger c_{i\downarrow}^\dagger + c_{i\downarrow} c_{i\uparrow}), \\
 H_T &= w_L (c_{H\uparrow}^\dagger c_{L\uparrow} + c_{H\downarrow}^\dagger c_{L\downarrow}) + w_{SOL} (c_{H\downarrow}^\dagger c_{L\uparrow} - c_{H\uparrow}^\dagger c_{L\downarrow}) \\
 &\quad + w_R (c_{R\uparrow}^\dagger c_{H\uparrow} + c_{R\downarrow}^\dagger c_{H\downarrow}) + w_{SOR} (c_{R\downarrow}^\dagger c_{H\uparrow} - c_{R\uparrow}^\dagger c_{H\downarrow}) + h.c..
 \end{aligned} \tag{5.1}$$

Here H_i is the Hamiltonian for the QDs ($i = L, R$) or the ABS ($i = H$) in the hybrid, $n_{i\sigma} = c_{i\sigma}^\dagger c_{i\sigma}$ is the occupancy number of the QD orbital or normal state in the hybrid with spin σ , μ_i is the chemical potential energy, E_{Zi} is the induced Zeeman energy, U_i is the charging energy, and Γ_i is the induced superconducting gap. H_T is the tunnel Hamiltonian between the QDs and the ABS, where $w_{L/R}$ and $w_{SOL/SOR}$ are the amplitudes for the spin-conserving and spin-flipping single electron tunneling processes. The parameters used for the numerical simulations performed in this work, in unit of $\Gamma_H \equiv \Gamma$, the induced gap on the ABS, are: $E_{ZL} = E_{ZR} = 1.5\Gamma$, $E_{ZH} = 0.5\Gamma$ for Zeeman energy, $U_L = U_R = 5\Gamma$, $U_H = 0$ for charging energy, $w_L = \Gamma$, $w_{SOL} = w_L/2$, $w_R = 0.75\Gamma$, $w_{SOR} = w_R/2$ for tunneling amplitudes, and $\Gamma_L = 0, \Gamma_R = \Gamma$ for induced gaps on the QDs. Here the magnitude of the Zeeman energy on the ABS is weaker than that in the QDs owing to the g factor renormalization in the hybrid. Furthermore, an extra pairing gap is added on the right QD to explain the residual Andreev conductance when the ABS is far from its energy minimum, as shown in the measurement in figure 1. The sweet spot investigated in figure 10e-i corresponds to $\mu_H = 0.617\Gamma$, $\mu_L = 2.290\Gamma$, and $\mu_R = -5.879\Gamma$. Finally, in figure 8, we calculate the electron and hole character of an excitation between two states of different parity as

$$u_i^2 = \sum_{\sigma=\uparrow,\downarrow} |\langle o | c_{i\sigma}^\dagger | e \rangle|^2, \quad v_i^2 = \sum_{\sigma=\uparrow,\downarrow} |\langle o | c_{i\sigma} | e \rangle|^2, \tag{5.2}$$

where $|e\rangle$ is the even state and $|o\rangle$ the odd one.

In the experimental device, conductance spectroscopy of the hybrid system is measured in a three-terminal junction with two normal leads and one grounded superconducting lead. To numerically simulate the transport measurement, we attach two additional normal leads to the two QDs, respectively. The lead Hamiltonians are

$$H_{\text{lead}} = \sum_{a=L,R} \sum_{\sigma=\uparrow,\downarrow} \sum_k (\varepsilon_{ka} - \mu_{\text{lead},a}) f_{ak\sigma}^\dagger f_{ak\sigma}, \tag{5.3}$$

where $f_{ak\sigma}$ is the annihilation operator of a free electron with momentum k and spin σ in lead- a , ε_{ka} is the kinetic energy, and $\mu_{\text{lead},a}$ is the lead chemical potential. The tunnel Hamiltonian between leads and the QDs is

$$H_{T,\text{lead}} = \sum_{a=L,R} \sum_{\sigma=\uparrow,\downarrow} \sum_k w'_a f_{ak\sigma}^\dagger c_{a\sigma} + h.c., \tag{5.4}$$

where w'_a is the tunneling amplitude between QD- a and lead- a , and is assumed to be spin-diagonal and independent of k . A more useful physical quantity to characterize the lead coupling strength is $\gamma_a = 2\pi\rho w_a'^2$ with ρ being the density of states at the Fermi energy of the normal lead. Based on the model Hamiltonians introduced above, current and conductance matrices can be numerically calculated by solving a rate equation for the reduced density matrix of the hybrid system. We set the temperature $k_B T = 0.04\Gamma$ and tunneling strength $\gamma_a = 0.03\Gamma$ to be the same for both normal leads. Finally, when simulating the local Andreev conductance of a QD-ABS system, we are actually considering a two-terminal junction by removing the quantum dot and the normal lead on the other side.

5.8.2 ESTIMATION OF DEPHASING RATES

A minimal Majorana qubit consists of two subsystems, each hosting one pair of Majoranas: γ_{A1}, γ_{A2} , and γ_{B1}, γ_{B2} . It is possible to encode a qubit in the subspace of either even or odd global fermion parity. Without loss of generality, we focus on the even subspace. We define qubit states $|0\rangle \equiv |o_A, o_B\rangle$, with the fermion parity of each subsystem being odd, and $|1\rangle \equiv |e_A, e_B\rangle$, each being even. The qubit Pauli operator σ_z is then identified as $i\gamma_{A1}\gamma_{A2} = i\gamma_{B1}\gamma_{B2}$ and the effective Hamiltonian is [6, 54, 57]

$$H = \frac{i}{2} (E_A \gamma_{A1} \gamma_{A2} + E_B \gamma_{B1} \gamma_{B2}) = E \sigma_z, \quad (5.5)$$

where $E_{A,B} = E_{o_{A,B}} - E_{e_{A,B}}$ is the excitation energy of each subsystem and $E \equiv (E_A + E_B)/2$.

An ideal Majorana qubit has $E = E_A = E_B = 0$. Uncontrolled fluctuations of E lead to qubit dephasing [54–57]. If the typical amplitude of E fluctuation is δE , the dephasing rate is $1/T_2^* \sim \delta E/\hbar$ [9, 54]. In the following estimations, we assume the two subsystems are similar and omit details of the statistical distribution of the noise, so that $\delta E_A \sim \delta E_B \sim \delta E$. Thus, we use the typical energy fluctuations of one pair of PMM to estimate the dephasing rates of a qubit.

Energy splitting of a pair of PMM can occur due to two reasons: the degeneracy splits quadratically when the QDs are detuned simultaneously ($\mu_L = \pm\mu_R \neq 0$) and linearly when the ECT and CAR couplings are perturbed from the sweet spot ($t \neq \Delta$) [3]. Other types of noise, e.g., magnetic fluctuations, enter the Hamiltonian parametrically via these two mechanisms. In the main text, we have characterized the sensitivity of the degeneracy to each of them by intentionally tuning gate voltages away from the sweet spots. These gate dispersion results allow us to estimate the dephasing rate given typical noise amplitudes found in QD qubit devices. Concretely, we consider random fluctuations of the gate voltages controlling the electrochemical potential of the QDs (V_{LP}, V_{RP}) and ABS (V_H), the former causing on-site potential fluctuation and the latter that of the tunneling amplitudes.

We first focus on charge noise affecting the QDs. In figure 4f, we have measured the quadratic splitting of the PMM when the electrochemical potential of both QDs is detuned from the sweet spot. Given the vanishing first derivative of the gate dispersion, we extracted a second derivative of $\partial^2 E / \partial V_{LP}^2 \approx 30 \text{ e/V}$, two orders of magnitude smaller than the one measured in our previous report, $\partial^2 E / \partial V_{LP}^2 \approx 4500 \text{ e/V}$ [8]. In previous measurements of charge fluctuations of a QD [59–63], equivalent voltage noise on the gates is typically found to be $\delta V \sim 10 \mu\text{V}$ (after accounting for the gate lever arm). A worst-case estimation of maximally (anti)correlated gate noise on both QDs predicts a resulting energy fluctuation of

$\delta E \approx \frac{\partial^2 E}{\partial V_{LP}^2} \delta V^2$, yielding ~ 3 neV for the YSR-based PMM states in this work and ~ 450 neV for our previous work. These correspond to dephasing rates of $\delta E/\hbar \sim 5$ MHz and ~ 700 MHz for the two cases, a direct consequence of the two orders of magnitude of gate dispersion suppression.

We now turn to charge noise affecting the ABS and thereby the couplings between QDs, t and Δ . Given the charge sensitivity of the hybrid ABS and its key effect on modulating the tunneling amplitudes, we assume the primary source of $t - \Delta$ variation to be charge fluctuations of the ABS. In figure 3e, we have estimated the noise sensitivity of two PMM sweet spots against perturbation on V_H . We found $\partial E/\partial V_H \approx 3$ to $7 \mu\text{eV}/\text{mV}$, comparable to our previous work [8]. Although the exact sensitivity depends on microscopic details, we note that the superconducting lead, in general, strongly screens charge fluctuations. This explains the small lever arm for an ABS in the hybrid segment, which is $\sim 1/20$ that of a normal QD (see figure 6 and figure 7a). By considering the worst sensitivity and the same fluctuations as before, we estimate typical splittings of $\delta E \sim \frac{\partial E}{\partial V_H} \delta V = 70$ neV and a dephasing rate of ~ 100 MHz.

5

Comparing the dephasing rates, we find that on-site QD charge fluctuations likely dominated dephasing of PMM qubits made from non-proximitized QD states. With the introduction of YSR-based Kitaev chain and its strongly suppressed gate dispersion, the QD charge fluctuation will likely no longer be the main source of dephasing. Instead, tunneling amplitude variations, not suppressed by the formation of YSR states, becomes the more probable primary dephasing mechanism. While reducing sensitivity to tunneling amplitude fluctuations is beyond the scope of this paper, we remark here that a possible solution is to increase the number of sites of the Kitaev chain to at least 3 [2].

Finally, we comment on a few additional details not addressed by the discussions above. We estimated energy fluctuations only using equivalent gate fluctuations converted from previous charge noise measurements. This does not describe other sources of decoherence including that due to quasiparticles [55, 64] and electron-phonon coupling [55]. We do not expect our estimations to be drastically altered if these effects are included, given the low electron temperature and that electron-phonon dephasing rates measured in charge qubits realized in III/V semiconductors are on the order of 100 MHz [65, 66], comparable to our estimated dephasing rates due to tunneling-rate variations. Ultimately, a realistic quantitative noise model would require the measurement of the noise spectrum and dephasing times. Despite all these simplifications, the dephasing rate estimations indicate that there should be a reasonable time window where it is possible to adiabatically manipulate PMM states before they decohere significantly. This is a necessary condition to demonstrate qubit, fusion, and braiding protocols based on PMM states [4–6]. In the future, longer Kitaev chains are expected to increase the dephasing time, since the energy splitting is predicted to decrease exponentially with the number of sites [2].

DATA AVAILABILITY AND CODE AVAILABILITY

Raw data presented in this work, the data processing/plotting code, and code used for the theory calculations are available at <https://zenodo.org/records/10013728>.

5.9 EXTENDED DATA

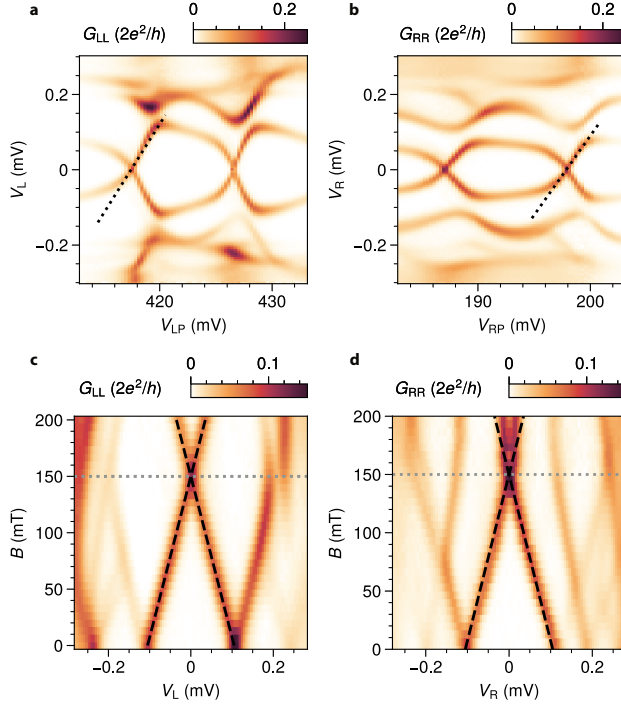


Figure 5: **Characterization of the YSR states at $t \approx \Delta$.** **a**, Local conductance measurement of the spectrum of the left YSR state when the right one is off-resonance. $V_H = 333.5$ mV is tuned such that $t \approx \Delta$ for the crossing showed in figure 4a. The lever arm at charge degeneracy is $\approx 0.05e$, extracted using the black dotted line. **b**, Same as panel a, but for the right YSR state. We extract a lever arm of $\approx 0.04e$. **c**, Local conductance measurement of the Zeeman splitting of the left YSR state, at the same value of V_H as above. The field is applied along the nanowire axis. The gray dotted line indicates the field at which all the other measurements were conducted. The left dot was positioned at the charge degeneracy point at $B = 150$ mT and the right one off-resonance. We extract a g-factor of ≈ 24 , consistent with previously measured values for strongly proximitized states in similar devices [38]. The corresponding Zeeman splitting at 150 mT is $\approx 200 \mu\text{eV}$. **d**, Same as panel c, but for the right YSR state. We extract the same g-factor as for the left YSR state.

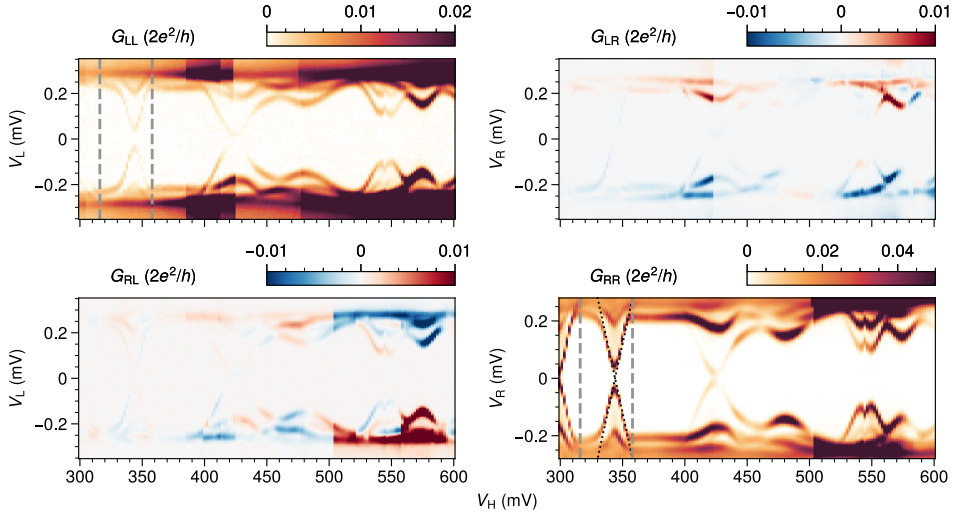


Figure 6: Spectroscopy of the hybrid segment. Conductance matrix of the hybrid spectrum as a function of V_H . The hybrid segment hosts separated ABS that can mediate the coupling between the QDs. The gray dashed lines indicate the range of V_H used for the measurements presented in the main text. The lever arm is $\alpha \approx 0.02e$ as extracted from the black dotted lines superimposed on the ABS in panel d, indicating a strong screening effect of the superconducting lead. For this measurement, the two sides are tuned as tunnel barriers as described in the Methods section. When QDs are formed, V_{LT} and V_{RT} are increased to reach the strong coupling regime between them and the ABS. This affects the ABS spectrum because of cross-coupling and modification to the confining potential. Therefore, the V_H values and the energy of the ABS in this measurement are slightly different from those presented in the main text.

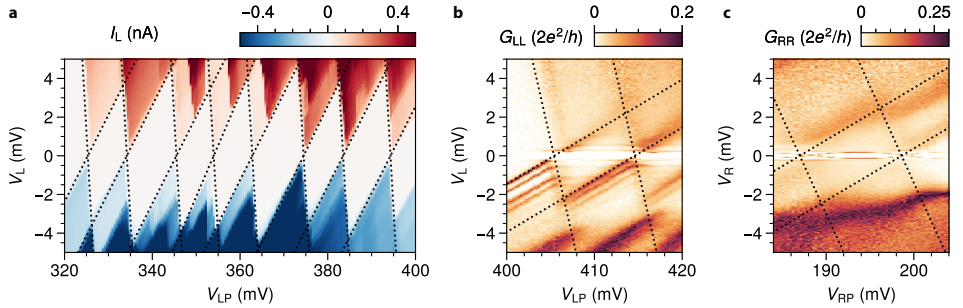


Figure 7: High-bias spectroscopy of the QDs. **a**, Coulomb diamonds for the left QD when it is not coupled to any ABS by closing V_{LT} and keeping ABSs off-resonance. From the overlaid black dotted lines, we extract typical charging energies of ≈ 3.5 meV and lever arms of $\alpha \approx 0.4e$. **b**, Local conductance spectroscopy of the left QD as a function of V_{LP} after V_{LT} is increased to strongly couple to an ABS. The measurement was taken in the same configuration as figure 1g, with the ABS off-resonance. We extract a charging energy of ≈ 2 meV and a lever arm of $\alpha \approx 0.2e$, which are renormalized because of the lowered tunnel barriers. **c**, Same as panel b, but for the right QD. Typical QD features are not as clearly visible since the state is significantly proximitized by the SC, as shown in figure 1j and in figure 9a–c. By overlaying the visible features, we extract a charging energy of ≈ 2 meV and a lever arm of $\alpha \approx 0.2e$. These measurements were taken applying a field of 150 mT along the nanowire axis.

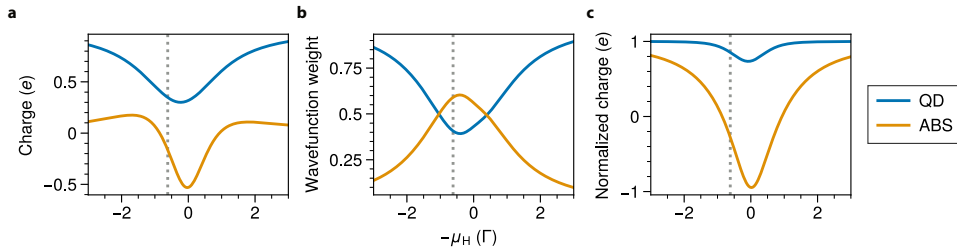


Figure 8: Properties of the YSR zero-energy excitation. **a**, Charge of the YSR excitation residing on the left QD (blue line) and on the ABS (orange line). The charge is calculated as $u_i^2 - v_i^2$, with $i = L$ for the QD and $i = M$ for the ABS, as defined in Supplementary Information. The gray dotted line corresponds to the μ_H value used for the sweet spot studied in figure 10e–i. The decrease of the charge residing on the QD explains part of the lever arm reduction observed for YSR states (figure 1h). A further reduction comes from charging energy renormalization. **b**, Weight of the YSR excitation wavefunction on the left QD (blue line) and on the ABS (orange line). The weight of the wavefunction on each site is defined as $u_i^2 + v_i^2$. When the ABS is close to its energy minimum at $\mu_H = 0$, the hybridization between the QD and the ABS becomes stronger and the excitation is delocalized on the two sites, thus reducing the charge residing on the QD. **c**, Charge of the YSR excitation normalized for the wavefunction weight residing on the left QD (blue line) and on the ABS (orange line). The normalized charge is defined as $(u_i^2 - v_i^2)/(u_i^2 + v_i^2)$ and it quantifies the mixed electron and hole character. It ranges from 1 to -1 when the excitation is purely electron- and hole-like, respectively. Although the charge of a YSR state is not a good quantum number while ECT/CAR is defined using charge states, the predominance of a charge character justifies our use of ECT and CAR in the main text, as investigated in more detail in Ref. [40].

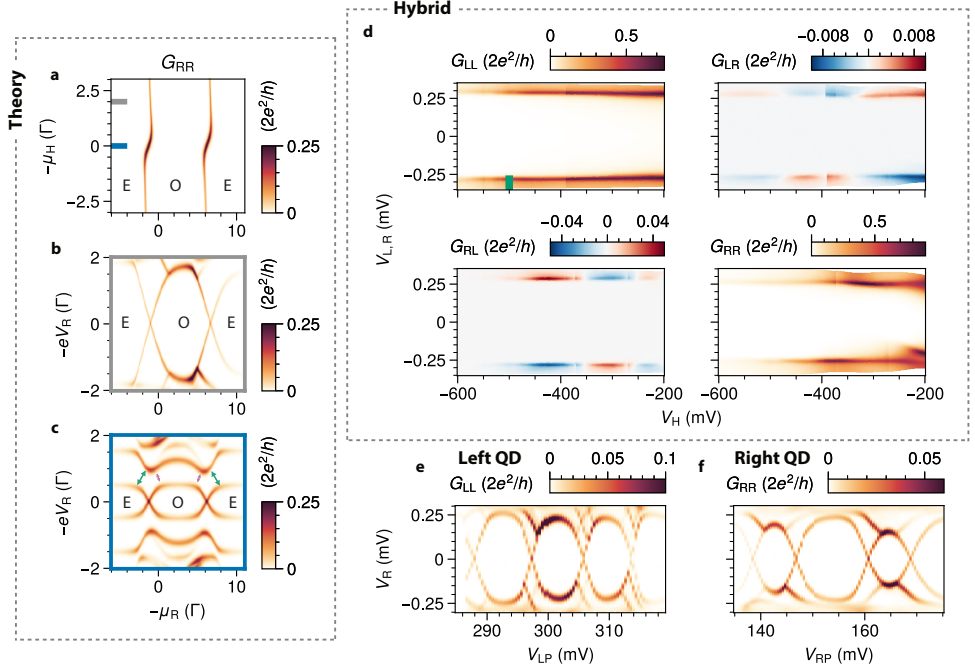


Figure 9: QDs directly proximitized by the superconducting film. **a–c**, Same as figure 1c–e, but with an additional gate-independent source of proximity for the QD, as discussed in Supplementary Information. **d**, Conductance matrix for tunnel spectroscopy of the hybrid section as a function of V_H . The green tick marks the value of V_H at which the measurements in e and f were taken. In this regime, there are no subgap states. **e, f**, Local tunnel spectroscopy of the left (**b**) and right (**c**) QDs at low V_H . Although there are no subgap states in the hybrid, it is possible to tune the QDs in a regime where a gap and subgap states appear. We interpret this as arising from the QDs being proximitized by the AI, indicating that the proximity of the QDs can be not exclusively due to subgap states in the hybrid. These measurements were taken applying a field of 150 mT along the nanowire axis.

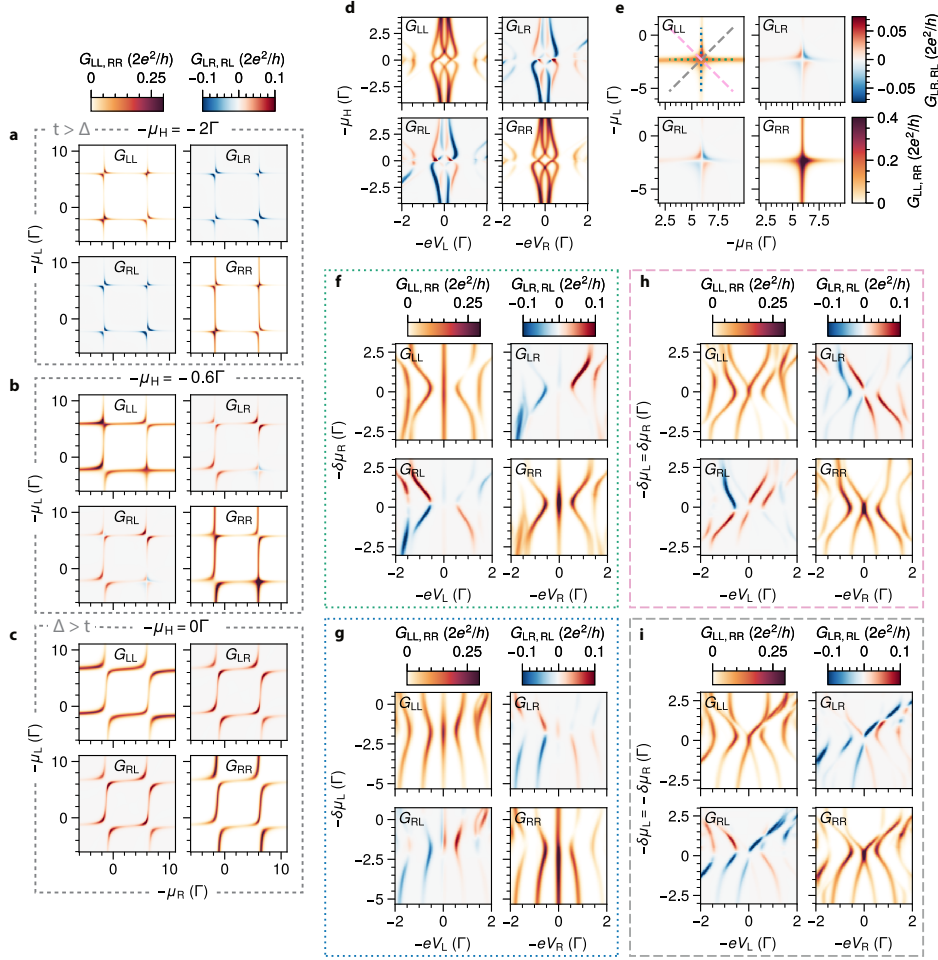


Figure 10: Numerical simulations of coupled YSR states **a-c** Numerical conductance matrix of the CSDs of coupled YSR states varying μ_H , reproducing figure 2. **d**, Numerical conductance spectrum of coupled YSR states as a function of the ABS chemical potential. The spectrum is calculated following the same approach discussed in figure 3 to maintain the chemical potentials of the QDs at the center of the crossing. The theoretical model reproduces the experimental findings presented in figure 3. **e**, Numerical conductance matrix of a crossing in the CSD, when $t \approx \Delta$, at $\mu_H = 0.617\Gamma$. **f, g**, Numerical conductance matrix of the spectrum as a function of the right (f)/left (g) QD detuning along the green/blue dotted line in panel a. The other QD is kept on resonance. The numerical results reproduce the measurement shown in figure 4c/figure 12b. **h, i**, Numerical conductance matrix of the spectrum calculated detuning both QDs simultaneously, along the pink/gray dashed line in panel e. The numerical results reproduce the measurements shown in figure 4d/figure 12c.

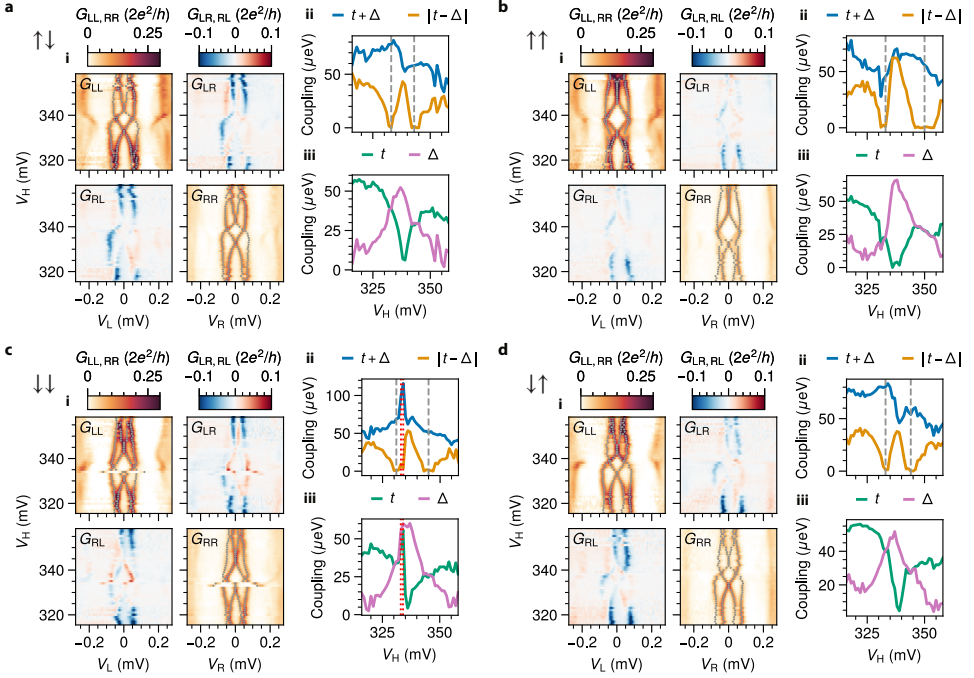


Figure 11: **ECT and CAR coupling for all the resonances.** a–d, (i) Conductance matrix of the spectrum of two coupled YSR states as a function of V_H , measured as described in figure 3. The extracted peaks are marked with gray dots. (ii) Energy of the excited states, calculated by averaging the peaks at positive and negative bias of both the left and the right spectrum. From the outer peaks we extract $t + \Delta$, from the inner ones $|t - \Delta|$. The gray dashed lines indicate a change of sign of $t - \Delta$. In particular, $t < \Delta$ within the lines and $t > \Delta$ outside. In c a gate jump affected the measurement of the spectrum for two values of V_H . These are highlighted with red dotted lines in c(ii) and c(iii). Parts of d were presented in figure 3.

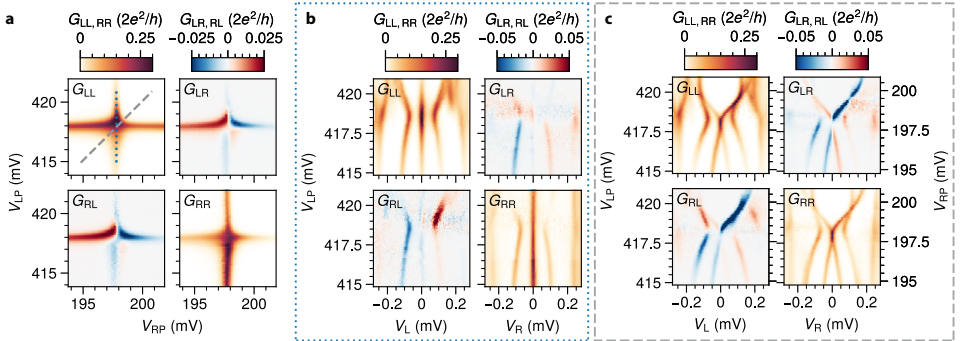


Figure 12: **Additional PMM spectra.** a, CSD for a PMM sweet spot. Same as figure 4a, but with different paths highlighted. b, PMM spectrum measured along the vertical path of panel a. The left QD is detuned, while the right one is kept on resonance. The asymmetry with respect to $\mu_L = 0$ can be attributed to the asymmetric energy dispersion of the left YSR state (see figure 5a). c, PMM spectrum measured detuning both QDs along the diagonal path of panel a. The asymmetry with respect to $\mu_L = \mu_R = 0$ can be explained as discussed in panel b.

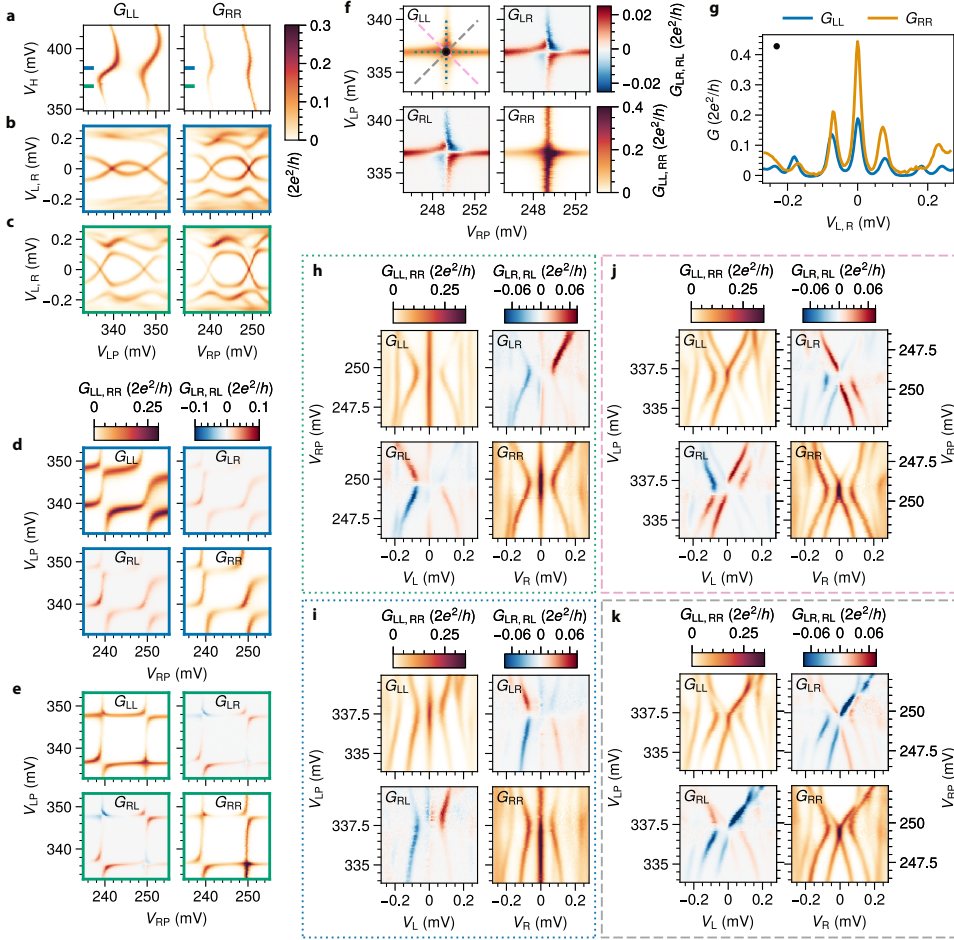


Figure 13: **PMM with different YSR and ABSs.** **a-c** Similarly to figure 1, QD-ABS CSDs (a), spectra of the YSR states when the ABS is at its minimum energy (b), and for a V_H corresponding to a $t = \Delta$ sweet spot (c), as described in the next panels. The colors of the frames correspond to the V_H values indicated in panel a. **d-e**, Conductance matrix for YSR states CSDs when the ABS is at its minimum energy (d) and slightly detuned (e), as discussed in figure 3. The color of the frames correspond to the V_H values indicated in panel a. **f**, Zoom-in on the bottom right crossing of panel e, corresponding to a PMM sweet spot. **g**, Left and right conductance spectra measured at the PMM sweet spot, corresponding to the black dot at the middle of the crossing in f. The gap between the ground and the first excited states is $E_{\text{gap}} \approx 71 \mu\text{eV}$. **h-k**, Conductance matrix of the PMM spectra along the paths in panel f, analogously to figure 4 and figure 12.

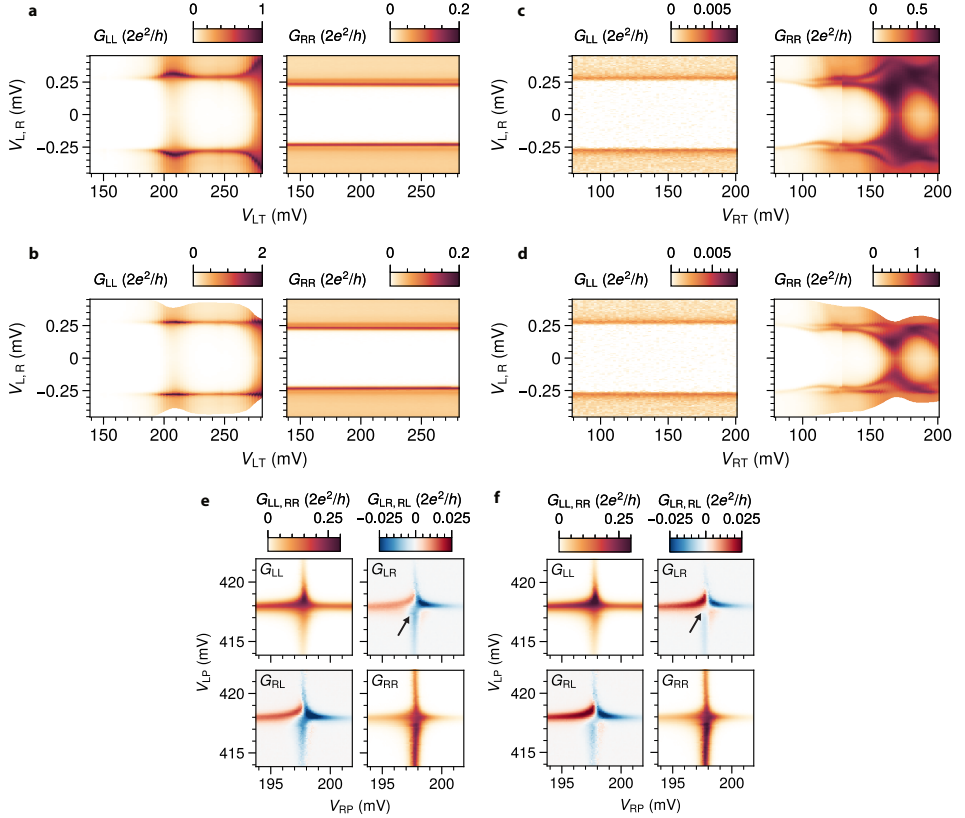


Figure 14: Estimation of series resistance. **a**, Tunnel spectroscopy of the hybrid spectrum from both sides varying V_{LT} . Whenever there is finite subgap conductance, the parent gap expands because of the voltage divider effect. **b**, Same measurement as in panel **a**, after correcting the voltage divider effect. We find that a series resistance of $R_{\text{series}} = 3.65 \text{ k}\Omega$ corrects the gap increase discussed above. In addition, we also considered a total resistance for the voltage source and current meter of 300Ω . **c**, **d**, Same as panels **a** and **b**, but for the right side. **e**, **f**, CSD presented in figure 4a, before (e) and after (f) correcting the voltage divider effect. The local signal is not significantly affected. On the other hand, the alternating positive and negative non-local signal becomes clearer after the correction. In particular, it approaches zero in the middle of the crossing, indicated by the black arrow. Without series resistance correction, the finite non-local signal at the center of the crossing in panel **e** could be misinterpreted as a signature of low Majorana polarization [26].

REFERENCES

- [1] A Yu Kitaev. Unpaired Majorana fermions in quantum wires. *Physics-Uspekhi*, 44(10S):131, 2001.
- [2] Jay D. Sau and S. Das Sarma. Realizing a robust practical Majorana chain in a quantum-dot-superconductor linear array. *Nature Communications*, 3(1):964, 2012.
- [3] Martin Leijnse and Karsten Flensberg. Parity qubits and poor man’s Majorana bound states in double quantum dots. *Physical Review B*, 86(13):134528, 2012.
- [4] Chun-Xiao Liu, Haining Pan, F. Setiawan, Michael Wimmer, and Jay D. Sau. Fusion protocol for Majorana modes in coupled quantum dots. *Physical Review B*, 108(8):085437, August 2023.
- [5] Péter Boross and András Pályi. Braiding-based quantum control of a Majorana qubit built from quantum dots. *arXiv*, may 2023.
- [6] Athanasios Tsintzis, Rubén Seoane Souto, Karsten Flensberg, Jeroen Danon, and Martin Leijnse. Roadmap towards Majorana qubits and nonabelian physics in quantum dot-based minimal Kitaev chains. *arXiv*, jun 2023.
- [7] D. Michel Pino, Rubén Seoane Souto, and Ramón Aguado. Minimal Kitaev-transmon qubit based on double quantum dots. *arXiv*, September 2023.
- [8] Tom Dvir, Guanzhong Wang, Nick van Loo, Chun-Xiao Liu, Grzegorz P. Mazur, Alberto Bordin, Sebastiaan L. D. ten Haaf, Ji-Yin Wang, David van Driel, Francesco Zatelli, Xiang Li, Filip K. Malinowski, Sasa Gazibegovic, Ghada Badawy, Erik P. A. M. Bakkers, Michael Wimmer, and Leo P. Kouwenhoven. Realization of a minimal Kitaev chain in coupled quantum dots. *Nature*, 614(7948):445–450, 2023.
- [9] Jens Koch, Terri M. Yu, Jay Gambetta, A. A. Houck, D. I. Schuster, J. Majer, Alexandre Blais, M. H. Devoret, S. M. Girvin, and R. J. Schoelkopf. Charge-insensitive qubit design derived from the Cooper pair box. *Physical Review A*, 76(4):042319, October 2007.
- [10] J. A. Schreier, A. A. Houck, Jens Koch, D. I. Schuster, B. R. Johnson, J. M. Chow, J. M. Gambetta, J. Majer, L. Frunzio, M. H. Devoret, S. M. Girvin, and R. J. Schoelkopf. Suppressing charge noise decoherence in superconducting charge qubits. *Physical Review B*, 77(18):180502, May 2008.
- [11] L Yu. Bound state in superconductors with paramagnetic impurities. *Acta Phys. Sin.*, 21:75–91, 1965.
- [12] Hiroyuki Shiba. Classical Spins in Superconductors. *Progress of Theoretical Physics*, 40(3):435–451, September 1968.
- [13] AI Rusinov. Superconductivity near a paramagnetic impurity. *JETP Lett.*, 9, 1969.

- [14] M. R. Buitelaar, T. Nussbaumer, and C. Schönenberger. Quantum dot in the Kondo regime coupled to superconductors. *Physical Review Letters*, 89(25):256801, December 2002.
- [15] J Bauer, A Oguri, and A C Hewson. Spectral properties of locally correlated electrons in a Bardeen–Cooper–Schrieffer superconductor. *Journal of Physics: Condensed Matter*, 19(48):486211, 2007.
- [16] Tobias Meng, Serge Florens, and Pascal Simon. Self-consistent description of Andreev bound states in Josephson quantum dot devices. *Physical Review B*, 79(22):224521, June 2009.
- [17] K. Grove-Rasmussen, H. I. Jørgensen, B. M. Andersen, J. Paaske, T. S. Jespersen, J. Nygård, K. Flensberg, and P. E. Lindelof. Superconductivity-enhanced bias spectroscopy in carbon nanotube quantum dots. *Physical Review B*, 79(13):134518, April 2009.
- [18] W. Chang, V. E. Manucharyan, T. S. Jespersen, J. Nygård, and C. M. Marcus. Tunneling spectroscopy of quasiparticle bound states in a spinful Josephson junction. *Physical Review Letters*, 110(21):217005, May 2013.
- [19] Anders Jellinggaard, Kasper Grove-Rasmussen, Morten Hannibal Madsen, and Jesper Nygård. Tuning Yu-Shiba-Rusinov states in a quantum dot. *Physical Review B*, 94(6):064520, aug 2016.
- [20] K. Grove-Rasmussen, G. Steffensen, A. Jellinggaard, M. H. Madsen, R. Žitko, J. Paaske, and J. Nygård. Yu–Shiba–Rusinov screening of spins in double quantum dots. *Nature Communications*, 9(1):2376, jun 2018.
- [21] Ion C Fulga, Arbel Haim, Anton R Akhmerov, and Yuval Oreg. Adaptive tuning of Majorana fermions in a quantum dot chain. *New Journal of Physics*, 15(4):045020, 2013.
- [22] S. Nadj-Perge, I. K. Drozdov, B. A. Bernevig, and Ali Yazdani. Proposal for realizing Majorana fermions in chains of magnetic atoms on a superconductor. *Physical Review B*, 88(2):020407, 2013.
- [23] Falko Pientka, Yang Peng, Leonid Glazman, and Felix von Oppen. Topological superconducting phase and Majorana bound states in Shiba chains. *Physica Scripta*, 2015(T164):014008, August 2015.
- [24] Michael Schechter, Karsten Flensberg, Morten H. Christensen, Brian M. Andersen, and Jens Paaske. Self-organized topological superconductivity in a Yu-Shiba-Rusinov chain. *Physical Review B*, 93(14):140503, April 2016.
- [25] Chun-Xiao Liu, Guanzhong Wang, Tom Dvir, and Michael Wimmer. Tunable superconducting coupling of quantum dots via Andreev bound states in semiconductor-superconductor nanowires. *Physical Review Letters*, 129(26):267701, 2022.

- [26] Athanasios Tsintzis, Rubén Seoane Souto, and Martin Leijnse. Creating and detecting poor man’s Majorana bound states in interacting quantum dots. *Physical Review B*, 106(20):L201404, 2022.
- [27] S. Nadj-Perge, I. K. Drozdov, J. Li, H. Chen, S. Jeon, J. Seo, A. H. MacDonald, B. A. Bernevig, and A. Yazdani. Observation of Majorana fermions in ferromagnetic atomic chains on a superconductor. *Science*, 346(6209):602–607, October 2014.
- [28] Michael Ruby, Falko Pientka, Yang Peng, Felix von Oppen, Benjamin W. Heinrich, and Katharina J. Franke. End states and subgap structure in proximity-coupled chains of magnetic adatoms. *Physical Review Letters*, 115(19):197204, November 2015.
- [29] Sangjun Jeon, Yonglong Xie, Jian Li, Zhijun Wang, B. Andrei Bernevig, and Ali Yazdani. Distinguishing a Majorana zero mode using spin-resolved measurements. *Science*, 358(6364):772–776, 2017.
- [30] Lucas Schneider, Philip Beck, Thore Posske, Daniel Crawford, Eric Mascot, Stephan Rachel, Roland Wiesendanger, and Jens Wiebe. Topological Shiba bands in artificial spin chains on superconductors. *Nature Physics*, 17(8):943–948, August 2021.
- [31] Lucas Schneider, Philip Beck, Jannis Neuhaus-Steinmetz, Levente Rózsa, Thore Posske, Jens Wiebe, and Roland Wiesendanger. Precursors of Majorana modes and their length-dependent energy oscillations probed at both ends of atomic Shiba chains. *Nature Nanotechnology*, 17(4):384–389, April 2022.
- [32] Sebastiaan L. D. ten Haaf, Qingzhen Wang, A. Mert Bozkurt, Chun-Xiao Liu, Ivan Kulesh, Philip Kim, Di Xiao, Candice Thomas, Michael J. Manfra, Tom Dvir, Michael Wimmer, and Srijit Goswami. Realizing Majorana bound states through interacting quantum dots in a two-dimensional electron gas. *arXiv*, 2023.
- [33] Ghada Badawy, Sasa Gazibegovic, Francesco Borsoi, Sebastian Heedt, Chien-An Wang, Sebastian Koelling, Marcel A. Verheijen, Leo P. Kouwenhoven, and E. P. A. M. Bakkers. High Mobility Stemless InSb Nanowires. *Nano Letters*, 19(6):3575–3582, June 2019.
- [34] J. M. Hornibrook, J. I. Colless, A. C. Mahoney, X. G. Croot, S. Blainvillain, H. Lu, A. C. Gossard, and D. J. Reilly. Frequency multiplexing for readout of spin qubits. *Applied Physics Letters*, 104(10):103108, March 2014.
- [35] Ji-Yin Wang, Nick van Loo, Grzegorz P. Mazur, Vukan Levajac, Filip K. Malinowski, Mathilde Lemang, Francesco Borsoi, Ghada Badawy, Sasa Gazibegovic, Erik P. A. M. Bakkers, Marina Quintero-Pérez, Sebastian Heedt, and Leo P. Kouwenhoven. Parametric exploration of zero-energy modes in three-terminal InSb-Al nanowire devices. *Physical Review B*, 106(7):075306, August 2022.
- [36] Sebastian Heedt, Marina Quintero-Pérez, Francesco Borsoi, Alexandra Fursina, Nick van Loo, Grzegorz P. Mazur, Michał P. Nowak, Mark Ammerlaan, Kongyi Li, Svetlana Korneychuk, Jie Shen, May An Y. van de Poll, Ghada Badawy, Sasa Gazibegovic, Nick de Jong, Pavel Aseev, Kevin van Hoogdalem, Erik P. A. M. Bakkers, and Leo P. Kouwenhoven. Shadow-wall lithography of ballistic superconductor–semiconductor quantum devices. *Nature Communications*, 12(1):4914, 2021.

- [37] Francesco Borsoi, Grzegorz P. Mazur, Nick van Loo, Michał P. Nowak, Léo Bourdet, Kongyi Li, Svetlana Korneychuk, Alexandra Fursina, Ji-Yin Wang, Vukan Levajac, Elvedin Memisevic, Ghada Badawy, Sasa Gazibegovic, Kevin van Hoogdalem, Erik P. A. M. Bakkers, Leo P. Kouwenhoven, Sebastian Heedt, and Marina Quintero-Pérez. Single-shot fabrication of semiconducting–superconducting nanowire devices. *Advanced Functional Materials*, 31(34):2102388, 2021.
- [38] Grzegorz P. Mazur, Nick van Loo, Ji-Yin Wang, Tom Dvir, Guanzhong Wang, Aleksei Khindanov, Svetlana Korneychuk, Francesco Borsoi, Robin C. Dekker, Ghada Badawy, Peter Vinke, Sasa Gazibegovic, Erik P. A. M. Bakkers, Marina Quintero Pérez, Sebastian Heedt, and Leo P. Kouwenhoven. Spin-Mixing Enhanced Proximity Effect in Aluminum-Based Superconductor–Semiconductor Hybrids. *Advanced Materials*, 34(33):2202034, 2022.
- [39] Christopher Reeg, Daniel Loss, and Jelena Klinovaja. Metallization of a Rashba wire by a superconducting layer in the strong-proximity regime. *Physical Review B*, 97(16):165425, April 2018.
- [40] Chun-Xiao Liu, A. Mert Bozkurt, Francesco Zatelli, Sebastiaan L. D. ten Haaf, Tom Dvir, and Michael Wimmer. Enhancing the excitation gap of a quantum-dot-based Kitaev chain. *arXiv*, October 2023.
- [41] Gediminas Kiršanskas, Moshe Goldstein, Karsten Flensberg, Leonid I. Glazman, and Jens Paaske. Yu-Shiba-Rusinov states in phase-biased superconductor–quantum dot–superconductor junctions. *Physical Review B*, 92(23):235422, December 2015.
- [42] J.-D. Pillet, C. H. L. Quay, P. Morfin, C. Bena, A. Levy Yeyati, and P. Joyez. Andreev bound states in supercurrent-carrying carbon nanotubes revealed. *Nature Physics*, 6(12):965–969, December 2010.
- [43] Eduardo J. H. Lee, Xiaocheng Jiang, Manuel Houzet, Ramón Aguado, Charles M. Lieber, and Silvano De Franceschi. Spin-resolved Andreev levels and parity crossings in hybrid superconductor–semiconductor nanostructures. *Nature Nanotechnology*, 9(1):79–84, 2014.
- [44] Zoltán Scherübl, Gergő Fülöp, Cătălin Pașcu Moca, Jörg Gramich, Andreas Baumgartner, Péter Makk, Tosson Elalaily, Christian Schönenberger, Jesper Nygård, Gergely Zaránd, and Szabolcs Csonka. Large spatial extension of the zero-energy Yu-Shiba-Rusinov state in a magnetic field. *Nature Communications*, 11(1), April 2020.
- [45] Zoltán Scherübl, Gergő Fülöp, Jörg Gramich, András Pályi, Christian Schönenberger, Jesper Nygård, and Szabolcs Csonka. From cooper pair splitting to nonlocal spectroscopy of a Shiba state. *Physical Review Research*, 4(2), May 2022.
- [46] J. Schindele, A. Baumgartner, R. Maurand, M. Weiss, and C. Schönenberger. Nonlocal spectroscopy of Andreev bound states. *Physical Review B*, 89(4):045422, 2014.
- [47] J. Gramich, A. Baumgartner, and C. Schönenberger. Andreev bound states probed in three-terminal quantum dots. *Physical Review B*, 96(19):1–14, 2017.

- [48] Guanzhong Wang, Tom Dvir, Grzegorz P. Mazur, Chun-Xiao Liu, Nick van Loo, Sebastiaan L. D. ten Haaf, Alberto Bordin, Sasa Gazibegovic, Ghada Badawy, Erik P. A. M. Bakkers, Michael Wimmer, and Leo P. Kouwenhoven. Singlet and triplet Cooper pair splitting in hybrid superconducting nanowires. *Nature*, 612(7940):448–453, December 2022.
- [49] Alberto Bordin, Guanzhong Wang, Chun-Xiao Liu, Sebastiaan L. D. ten Haaf, Nick van Loo, Grzegorz P. Mazur, Di Xu, David van Driel, Francesco Zatelli, Sasa Gazibegovic, Ghada Badawy, Erik P. A. M. Bakkers, Michael Wimmer, Leo P. Kouwenhoven, and Tom Dvir. Tunable crossed Andreev reflection and elastic cotunneling in hybrid nanowires. *Physical Review X*, 13(3):031031, September 2023.
- [50] Piotr Trocha and Ireneusz Weymann. Spin-resolved Andreev transport through double-quantum-dot cooper pair splitters. *Physical Review B*, 91(23), June 2015.
- [51] Zoltán Scherübl, András Pályi, and Szabolcs Csonka. Transport signatures of an Andreev molecule in a quantum dot–superconductor–quantum dot setup. *Beilstein Journal of Nanotechnology*, 10:363–378, February 2019.
- [52] J. C. Estrada Saldaña, A. Vekris, R. Žitko, G. Steffensen, P. Krogstrup, J. Paaske, K. Grove-Rasmussen, and J. Nygård. Two-impurity Yu-Shiba-Rusinov states in coupled quantum dots. *Physical Review B*, 102(19), November 2020.
- [53] Olivér Kürtösy, Zoltán Scherübl, Gergő Fülöp, István Endre Lukács, Thomas Kanne, Jesper Nygård, Péter Makk, and Szabolcs Csonka. Andreev molecule in parallel InAs nanowires. *Nano Letters*, 21(19):7929–7937, September 2021.
- [54] David Aasen, Michael Hell, Ryan V. Mishmash, Andrew Higginbotham, Jeroen Danon, Martin Leijnse, Thomas S. Jespersen, Joshua A. Folk, Charles M. Marcus, Karsten Flensberg, and Jason Alicea. Milestones toward Majorana-based quantum computing. *Physical Review X*, 6(3):031016, aug 2016.
- [55] Christina Knapp, Torsten Karzig, Roman M. Lutchyn, and Chetan Nayak. Dephasing of Majorana-based qubits. *Physical Review B*, 97(12):125404, March 2018.
- [56] Ryan V. Mishmash, Bela Bauer, Felix von Oppen, and Jason Alicea. Dephasing and leakage dynamics of noisy Majorana-based qubits: Topological versus Andreev. *Physical Review B*, 101(7):075404, feb 2020.
- [57] Péter Boross and András Pályi. Dephasing of Majorana qubits due to quasistatic disorder. *Physical Review B*, 105(3):035413, jan 2022.
- [58] Esteban A. Martinez, Andreas Pöschl, Esben Bork Hansen, May An Y. van de Poll, Saulius Vaitiekėnas, Andrew P. Higginbotham, and Lucas Casparis. Measurement circuit effects in three-terminal electrical transport measurements. April 2021.
- [59] K. D. Petersson, J. R. Petta, H. Lu, and A. C. Gossard. Quantum coherence in a one-electron semiconductor charge qubit. *Physical Review Letters*, 105(24):246804, December 2010.

- [60] O. E. Dial, M. D. Shulman, S. P. Harvey, H. Bluhm, V. Umansky, and A. Yacoby. Charge noise spectroscopy using coherent exchange oscillations in a singlet-triplet qubit. *Physical Review Letters*, 110(14):146804, apr 2013.
- [61] P. Scarlino, J. H. Ungerer, D. J. van Woerkom, M. Mancini, P. Stano, C. Müller, A. J. Landig, J. V. Koski, C. Reichl, W. Wegscheider, T. Ihn, K. Ensslin, and A. Wallraff. *In situ* tuning of the electric-dipole strength of a double-dot charge qubit: Charge-noise protection and ultrastrong coupling. *Physical Review X*, 12(3):031004, jul 2022.
- [62] Elliot J. Connors, J. J. Nelson, Lisa F. Edge, and John M. Nichol. Charge-noise spectroscopy of Si/SiGe quantum dots via dynamically-decoupled exchange oscillations. *Nature Communications*, 13(1):940, February 2022.
- [63] Guido Burkard, Thaddeus D. Ladd, Andrew Pan, John M. Nichol, and Jason R. Petta. Semiconductor spin qubits. *Reviews of Modern Physics*, 95(2):025003, June 2023.
- [64] Diego Rainis and Daniel Loss. Majorana qubit decoherence by quasiparticle poisoning. *Physical Review B*, 85(17):174533, may 2012.
- [65] A. Hofmann, C. Karlewski, A. Heimes, C. Reichl, W. Wegscheider, G. Schön, K. Ensslin, T. Ihn, and V. F. Maisi. Phonon spectral density in a GaAs/AlGaAs double quantum dot. *Physical Review Research*, 2(3):033230, August 2020.
- [66] Antti Ranni, Subhomoy Haldar, Harald Havir, Sebastian Lehmann, Pasquale Scarlino, Andreas Baumgartner, Christian Schönenberger, Claes Thelander, Kimberly A. Dick, Patrick P. Potts, and Ville F. Maisi. Dephasing in a crystal-phase defined double quantum dot charge qubit strongly coupled to a high-impedance resonator. *arXiv*, August 2023.

6

CROSS-PLATFORM MACHINE-LEARNING-ASSISTED CONTROL OF MINIMAL KITAEV CHAINS

6

There are no secrets about the world of nature. There are secrets about the thoughts and intentions of men.

- J. Robert Oppenheimer

The Kitaev model can be implemented by a chain of quantum dots (QDs) coupled together through interleaved semiconductor-superconductor hybrid segments hosting Andreev bound states (ABSs). Tuning the energy of the ABSs changes the tunneling rate between the QDs as well as the rate of Cooper pair splitting into the QDs. The system reaches a sweet spot when these two rates become equal, at which point Majorana zero modes appear at the system edges. However, for these emerging Majorana zero modes to be of use for braiding, anyon fusion and qubit experiments, it is required to tune up large chains to the sweet spot, which is an increasingly challenging as the system size increases. In this work, we report on an automated tuning algorithm that drives a minimal, two-site Kitaev chain into a sweet spot. The algorithm is based on a convolutional neural network that predicts the rates of tunneling and Cooper pair splitting from charge stability diagrams measured using differential conductance. These predictions are used in a gradient descent algorithm that changes the electrochemical potential of ABSs until a sweet spot is reached. We find that the algorithm converges within ± 1.5 mV of a sweet spot in 67.6% of the cases, and within ± 4.5 mV in 80.9% of the cases. On average, a sweet spot can be found in 45 minutes. Our work opens the door for automatically tuning up the longer Kitaev chains that are required for quantum information experiments using Majorana zero modes.

6.1 INTRODUCTION

Majorana zero modes (MZM) are predicted to manifest as emergent modes in a one-dimensional Kitaev chain [1]. MZMs not only represent a key milestone in defining the intersection of topology and condensed matter physics [2], but they also hold particular interest in the field of topological quantum computing [3]. This interest is largely due to their predicted resilience against certain types of experimental noise [4–7]. The Kitaev model can be implemented in a chain of quantum dots (QDs) with spin-orbit interaction, coupled to superconductors [8, 9]. In this implementation, the co-existence of electron hopping and superconducting pairing results in MZMs appearing at the chain ends. Even a two-site Kitaev chain is predicted to host MZMs in a parameter sweet spot, in which the elastic co-tunneling rate (ECT) is exactly equal to the crossed Andreev reflection rate (CAR) [10]. These transport processes are mediated by an Andreev bound state (ABS) that couples the two QDs. This minimal Kitaev chain was recently realized in quasi-one-dimensional nanowires [11] and two-dimensional electron gases [12].

MZMs in Kitaev chains are expected to host non-Abelian statistics, paving the way for quantum information processing, including fusion, braiding, and qubits [13–15]. These proposed experiments require tuning multiple pairs of QDs into the sweet spot where the ECT and CAR rates are equal, which amounts to changing the ABS energy using a gate voltage [16, 17]. Changing this gate voltage can affect other QDs through cross-coupling. As a result, tuning sweet spots in Kitaev chain devices is a complex iterative process that becomes lengthier and more complicated with each added QD. Furthermore, the qubit dephasing rate of Kitaev chains is predicted to be dominated by deviations of the ratio of ECT and CAR away from the sweet spot [18], which in turn demands strict temporal monitoring of the sweet spot condition.

Both tuning-up and monitoring sweet spots are essential algorithms that are currently performed manually and might benefit from automation to improve the speed and performance of complex measurements. Generally, a combination of quantum noise and

complex electronics makes algorithmic tuning of contemporary quantum devices a challenge. For this reason, many experiments rely on human operators for tuning and operation as automation is challenging. The generalization and fast application of machine learning methods, such as neural networks, introduced a new paradigm in the space of experimental control, tuning, and devices [19–23]. These efforts include various stages of tune-up of electrostatically defined quantum dots [24–31], optimizing electrostatic gate settings in semiconductor-superconductor nanowires [32], and Hamiltonian learning [33–38]. In our previous work, we have deployed a conditional generative adversarial neural network to learn the Hamiltonian of a two-site Kitaev chain and estimate the distance to the sweet-spot regime [39].

In the present work, we put forward a completely autonomous tune-up procedure for driving a Kitaev chain device into a sweet spot. First, we use a convolutional neural network (CNN) to determine whether a given measurement was taken in an ECT-, or CAR-dominated regime. The output of this classification is then used as an input for a gradient descent algorithm that minimizes the distance to sweet spots by adjusting device voltages. On average, we find that 67.6% of tuning runs converges within ± 1.5 mV, and 80.9% converges within ± 4.5 mV of a known sweet spot. We utilize two different device types in this work. Device A is an InSb-Al nanowire-based two-site Kitaev chain device. We apply the neural network algorithm to device A without utilizing any training examples specific to this device. Instead, we pre-train the model exclusively on transport data derived from a theoretical model, in addition to experimental data obtained from device B: an InAsSb-Al two-dimensional electron gas (2DEG) device.

6

6.2 DEVICE CHARACTERIZATION

In this work, we employ two devices: device A, which we use for the automated tuning algorithm, and device B, which we use for testing and retraining the neural network. Device A consists of QDs defined in an InSb nanowire as shown in figure 1a. The nanowire (green) is deposited on bottom finger gates (red), and contacted by normal Cr/Au (yellow) contacts at its ends. The middle section of the nanowire, the hybrid, is contacted by a grounded Al shell (blue). Further details pertaining to the device fabrication can be found in Refs. [40, 41]. The left and right normal leads can be biased with respect to the grounded Al with voltages V_L and V_R respectively. The current running through the left lead (I_L) and through the right lead (I_R) can be measured independently. Using standard lock-in detection, we obtain the local and non-local differential conductances [42]:

$$\begin{aligned} G_{LL} &= dI_L/dV_L, & G_{RR} &= dI_R/dV_R \\ G_{RL} &= dI_R/dV_L, & G_{LR} &= dI_L/dV_R \end{aligned}$$

Measurements of the local conductances, G_{LL} and G_{RR} , for varying V_{LP} and V_{RP} are used as an input for a CNN that predicts the rates of elastic co-tunneling (ECT) and crossed Andreev reflection (CAR) (see section 6.7.1 for details on the CNN architecture). This prediction is then fed into a gradient descent algorithm that adjusts V_{ABS} until the rates are equal, marking a sweet spot. While we could have equally used G_{RL} and G_{LR} as input for the CNN, measurements of non-local conductance require a multi-terminal set-up that does not scale well for longer Kitaev chains.

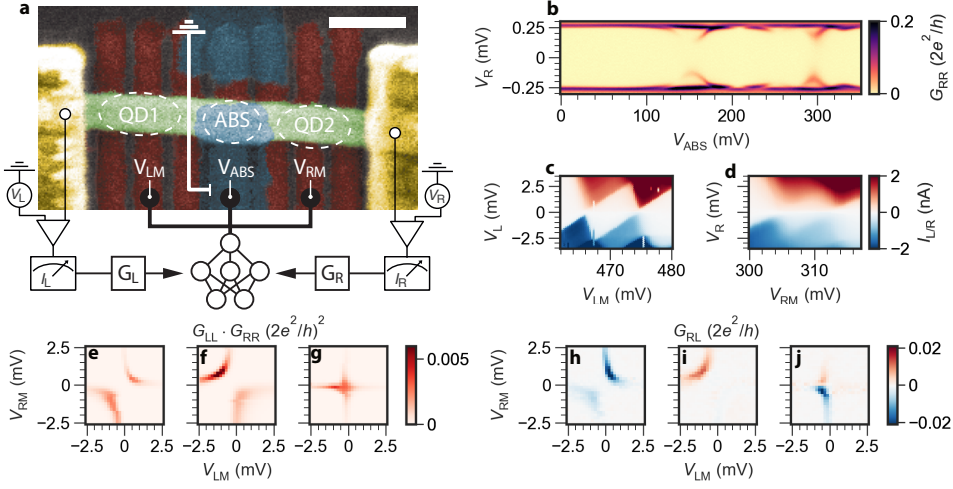


Figure 1: Device A set-up and characterization. **a.** False color SEM micrograph of our device, and the circuit. An InSb nanowire (green) is contacted by a grounded Al shell (blue) and two normal leads (yellow). The nanowire is placed on bottom gates (red). The relevant gate voltages are indicated by text. Both normal leads can be voltage biased independently with respect to the grounded Al. **b.** Local differential conductance measured from the right lead, G_{RR} , for varying hybrid plunger gate voltage, V_{ABS} , and V_R at $B = 0$ T. **c.** The current measured at the left lead, I_L , for varying plunger gate voltage of the left quantum dot (QD), V_{LP} , and bias voltage applied to the left lead, V_L . **d.** The current measured at the right lead, I_R , for varying plunger gate voltage of the right QD, V_{RP} , and bias voltage applied to the right lead, V_R . **e-g.** The product of the left and right differential conductance, $G_{LL} \cdot G_{RR}$, for varying V_{LP} and V_{RP} at $V_L = V_R = 0$ V. The measurements were performed at V_{ABS} values of 85 mV, 104 mV and 115 mV respectively. **h-j.** Non-local conductance, $G_{RL} = dI_R/dV_L$ for varying V_{LP} and V_{RP} . The data was measured simultaneously with panels e-g.

First, we characterize the spectrum of the hybrid segment by accumulating electrons in the InSb nanowire, and defining tunnel barriers using the two gates directly next to the hybrid segment. In figure 1b, we show G_{RR} for varying V_R and hybrid plunger gate voltage, V_{ABS} . A hard superconducting gap is observed over the entire gate voltage range. Multiple discrete states are observed in this range, whose gate dependence is typical for Andreev bound states (ABSs). Then, we change the tunnel gate voltages to define quantum dots (QDs) to the left and right of the hybrid. We control their electrochemical potentials by varying the plunger gate voltages V_{LP} and V_{RP} . We characterize the left QD by varying V_{LP} and V_L while measuring I_L as shown in figure 1c. For small bias voltage the current is fully suppressed due to the Coulomb blockade and as the bias increases we see current appearing in the form of Coulomb diamonds. Additionally, we notice that a gap has opened around the Fermi level due to the superconducting Al. We also perform an analogous measurement of the right QD as shown in figure 1d. Here, the Coulomb diamonds are more difficult to resolve than in figure 1c, which we attribute to a stronger tunnel-coupling to the superconductor [43].

After defining the QDs, we set $V_{ABS} = 85$ mV and measure charge stability diagrams (CSDs). figure 1e, shows the correlated local conductance, $G_{LL} \cdot G_{RR}$, for varying V_{LP} and V_{RP} . This correlated conductance is only finite when transport processes involve both

QDs. Therefore, it filters out features that are local to only one QD, such as Andreev reflection. We see an avoided crossing in figure 1a that indicates hybridization between the left and right QD levels. figure 3h shows the non-local conductance, G_{RL} , that was measured simultaneously. The negative sign of G_{RL} indicates that the ECT rate is greater than the CAR rate, $t > \Delta$, which is confirmed by the anti-diagonal avoided crossing [11]. figure 3f, i show $G_{LL} \cdot G_{RR}$ and G_{RL} respectively, for varying V_{LP} and V_{RP} at $V_{ABS} = 104$ mV. Here, the avoided crossing is now diagonal and the sign of G_{RL} is positive, indicating that CAR dominates over ECT. figure 3g, j show $G_{LL} \cdot G_{RR}$ and G_{RL} at $V_{ABS} = 115$ mV. There is no avoided crossing in the CSD anymore, and G_{RL} has both negative and positive values, which is characteristic of the sweet spot where the ECT and CAR rates are equal.

6.3 TUNING ALGORITHM

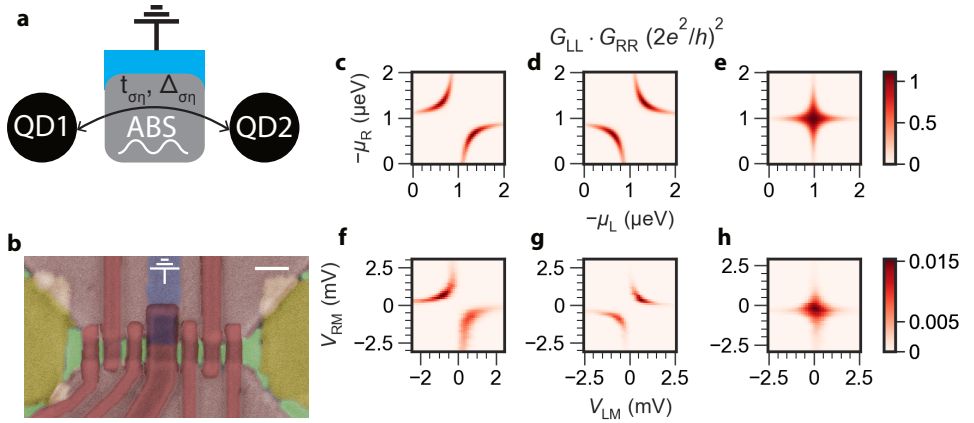


Figure 2: Device B charge stability diagrams and simulations. **a.** Schematic overview of the model system. Two quantum dots (QDs) are coupled by an Andreev bound state (ABS) in a semiconductor (gray) coupled to a grounded superconductor (blue). **b.** False color SEM image of device B. A 1D channel is defined in the InAsSb (green) using a top and bottom depletion gate (light red). The InAsSb is contacted in the middle by a grounded Al strip (blue). QDs are defined the left and right of this hybrid segment using finger gates (darker red). The InAsSb channel is contacted from the sides by two Ti/Au leads (yellow). Scale bar is 200 nm. **c-e.** Simulated conductance, $G_{LL} \cdot G_{RR}$ at zero energy, for varying chemical potential of the left and right quantum dots, μ_L and μ_R . These were generated for $(t - \Delta)/(t + \Delta) = \{-1/3, 1/3, 0\}$ respectively. **f-h.** Measured $G_{LL} \cdot G_{RR}$, for varying V_{LP} and V_{RP} at $V_L = V_R = 0$ V for device B. The CNN predicts $(t - \Delta)/(t + \Delta) = \{-0.31, 0.31, 0.01\}$ for these respectively.

6.3.1 THEORY MODEL

To train a convolutional network to predict the CAR and ECT rates from CSDs, we construct an effective model of the system to simulate transport data. We model the device in figure 1a as a 3-site system, where the semiconductor-superconductor hybrid segment gets treated as individual site, as shown in figure 2a. The couplings between the two QDs are mediated by ABSs in the hybrid segment. A more detailed description of the theory model and Hamiltonian can be found in section 6.7.2. We can write the effective Hamiltonian for the

QDs in the number basis as:

$$H_{\text{eff}} = \sum_{\sigma, \eta=\uparrow, \downarrow} \left(t_{\sigma\eta} c_{DL\sigma}^\dagger c_{DR\eta} + \Delta_{\sigma\eta} c_{DL\sigma}^\dagger c_{DR\eta}^\dagger \right) + h.c., \quad (6.1)$$

The operators $f_{L/R}^\dagger$ ($f_{L/R}$) create (annihilate) a quasiparticle in each QD, that is a superposition of electron and hole components. $t_{\sigma\eta}$ and $\Delta_{\sigma\eta}$ are the ECT and CAR couplings between electrons (holes) in the two QDs with corresponding spins σ and η . Coupling to the ABS results in an induced gap on each QD, leading us to model them as Yu-Shiba-Rusinov (YSR) states [44–46]. We perform a Bogoliubov transformation to account for the particle-hole symmetry on the QDs, and write an effective Hamiltonian for two coupled YSR states as:

$$H_{\text{eff}} = \delta\epsilon_L f_L^\dagger f_L + \delta\epsilon_R f_R^\dagger f_R + t \left(f_L^\dagger f_R + f_R^\dagger f_L \right) + \Delta \left(f_L^\dagger f_R^\dagger + f_L f_R \right) \quad (6.2)$$

Here, $\delta\epsilon_{L/R}$ are the energies of the YSR states and t and Δ are the generalized effective couplings for the odd-, and even-parity states respectively. While t and Δ correspond to ECT and CAR for normal QDs, this is no longer the case for YSR states. Due to local Andreev reflection, ECT can now also couple the global even-parity states, and CAR the odd states (see section 6.7.2 for details).

We note that equation (6.2) is a spinless Hamiltonian that is justified for infinite Zeeman energy, for which Majorana zero modes emerge at $t = \Delta$. We train the CNN on this model, and apply it to measurements taken both in the presence and absence of a magnetic field. At zero field, the odd states are spin-degenerate, and the system has a sweet spot at $t = \tilde{\Delta}(B) = \sqrt{2}\Delta$. Here, Majorana Kramer's pairs emerge that are protected against local perturbations but have an additional degeneracy (see [47] for details). The CSD in the sweet spot is identical for zero and infinite Zeeman energy. As a result, we can train the CNN on the spinless Hamiltonian, and recognize sweet spots in both the absence and presence of a magnetic field. We shall refer to the renormalized and field-dependent parameter $\tilde{\Delta}(B)$ as Δ , to ensure that $t = \Delta$ corresponds to a sweet spot for all magnetic field values.

equation (6.2) allows us to compute CSDs using the Mahaux-Weidenmuller formula and the scattering matrix formalism [48] (see. App. 6.7.2 for more details). We generate CSDs for varying values of t and Δ , and show three examples in figure 2c-e. We label each generated CSD with $(t - \Delta)/(t + \Delta)$ and train the CNN on 6000 examples (see section 6.7.2 for details on the training set). We use this ratio for labeling, as it is a dimensionless quantity and scales with the interaction strength $t + \Delta$ of the QDs. In principle, we could have used $(t - \Delta)$, which is directly proportional to the distance between the hyperbola's of the avoided crossing in the CSDs. However, there is a scaling factor that depends on the measurement resolution, the lever arm of the gates and the range of V_{LP} and V_{RP} . To eliminate the necessity to manually scale an absolute quantity, we choose the dimensionless ratio, $(t - \Delta)/(t + \Delta)$.

6.3.2 MODEL VALIDATION

As we want the CNN predictions to be transferable between different types of Kitaev chain devices, we first perform measurements on device B, which was fabricated on an InAsSb-Al

two-dimensional electron gas (2DEG), shown in figure 2b. Here, a quasi 1-D channel is defined by two large depletion gates. Gate-defined QDs are created on the left and right of a region proximitized by a thin Al strip (blue), using fabrication methods detailed in [49]. The same measurement set-up is used as for device A. In figure 2f-h, we show three example CSDs measured at different V_{ABS} values using device B. These CSDs are fed into our trained CNN, yielding predictions for $(t - \Delta)/(t + \Delta)$ of $-0.31, 0.31, 0.01$, respectively. The experimental CSDs closely resemble the generated ones in figure 2c-e, which we manually matched with the experimental ones by setting: $(t - \Delta)/(t + \Delta) = \{-1/3, 1/3, 0\}$ respectively. As t and Δ represent the ECT and CAR rates, validating the CNN predictions requires determining these rates quantitatively. We extract them by performing bias spectroscopy at the $V_{\text{LP}}, V_{\text{RP}}$ values corresponding to the center of the (avoided) crossing of the CSDs (see section 6.7.6 for details on the labeling procedure).

figure 3a compares the $(t - \Delta)/(t + \Delta)$ values obtained experimentally with those predicted by the CNN for a range of V_{ABS} values. The CNN predictions (red markers) generally match the experimentally extracted values (black markers), with small deviations around $(t - \Delta)/(t + \Delta) = 0$. We stress that the CNN has not been trained on any experimental data for these predictions. To improve the accuracy of the CNN, we retrain it on a part of the experimental data that we manually labeled (see section 6.7.2 for details). For retraining, we use 51 labeled CSDs that were randomly sampled from figure 3a.

The orange markers in figure 3b show the predictions of the retrained CNN applied to a test set of 24 previously unseen experimental CSDs. We observe that the predicted values of $(t - \Delta)/(t + \Delta)$ are closer to the values extracted from spectroscopy compared to the predictions of the CNN that was trained on the simulated data only. In figure 3c-e we show the CSDs measured for device B for V_{ABS} values indicated by the colored marks in panel b. We see that the avoided crossings in panels c. and e. have reversed direction, which agrees with the predicted sign change of $(t - \Delta)/(t + \Delta)$ shown in figure 3b. The Coulomb resonances form a cross in figure 3d, which is consistent with the predicted $(t - \Delta)/(t + \Delta) \approx 0$ and indicates a sweet spot.

6

6.3.3 TRANSFER LEARNING

Before discussing the CNN's performance on Device A, it is crucial to note that we only retrained it on experimental data from Device B. The ability of machine learning algorithms to generalize is vital, making them highly effective for analyzing noisy experimental datasets. In figure 3a, we assessed the performance of a CNN that was trained on a theoretical model only, which may not fully capture the nuances of experimental data. By retraining the CNN with 51 experimental examples, we observed notable improvements, as illustrated in figure 3b. We now consider a different type of generalization, namely the machine learning model's ability to adapt from one device to another. Eliminating the need for device-specific retraining offers a significant advantage in time.

We now apply the CNN that was trained on theory simulations and re-trained on all 75 experimental datasets from device B (2DEG) to device A (nanowire) that is shown in figure 1a. The blue markers in figure 3f show the $(t - \Delta)/(t + \Delta)$ values that we have extracted experimentally from device A using the same method as for device B. The red markers show the corresponding predictions of the CNN. We see excellent agreement with the experimental data for small $(t - \Delta)/(t + \Delta)$. Most importantly, there is good agreement

for the values of V_{ABS} at which the $(t - \Delta)/(t + \Delta)$ ratio changes sign, indicating a sweet spot. Around $V_{\text{ABS}} \approx 50$ mV, the CNN predicts values close to 0, which is not in agreement with the labeled data. We attribute this to the left QD interacting strongly with the ABS, which exceeds the simplified model used for generating training data (see section 6.7.7 for details).

The CNN predictions diverge from the labeled data around $V_{\text{ABS}} \approx 130$ mV as well. We attribute this to a low interaction strength, $(t + \Delta)$, which causes the ratio $(t - \Delta)/(t + \Delta)$ to become large. As the CNN was trained and retrained predominantly on strongly interacting QDs, it generalizes less well to the device with low $(t + \Delta)$. To mitigate the fact that the CNN identifies sweet spots in the weakly interacting regime, we regularize the predictions of $(t - \Delta)/(t + \Delta)$ based on the total conductance of each CSD (see section 6.7.8 for details). As seen from the gray markers in figure 3f, the regularization increases the predicted value of $(t - \Delta)/(t + \Delta)$ around $V_{\text{ABS}} = 130$ mV. We use the regularized predictions in the automated tuning algorithm to avoid regions of low interaction strength. We conclude that the CNN can correctly identify $t \approx \Delta$ at intermediate QD-ABS couplings and non-negligible QD-QD couplings.

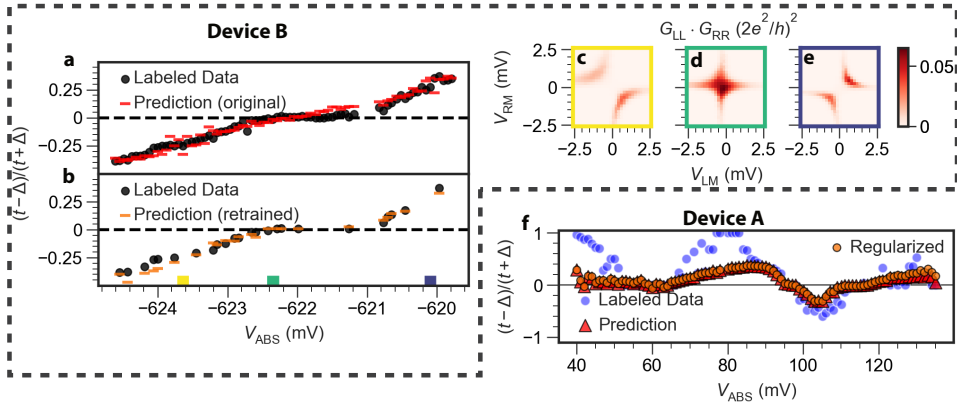


Figure 3: **Convolutional neural network (CNN) retraining and predictions.** **a.** The weighted ratio of elastic co-tunneling (t) and crossed Andreev reflection (Δ) rates, $(t - \Delta)/(t + \Delta)$, for varying V_{ABS} for device B. The black markers indicate experimentally-labeled data and the red markers are the CNN predictions. **b.** $(t - \Delta)/(t + \Delta)$ of a subset of test data of panel a after retraining the CNN on experimental data. The black markers indicate experimentally labeled data and the orange markers are the predictions of the retrained CNN. **c.-e.** The product of the left and right differential conductance, $G_{\text{LL}} \cdot G_{\text{RR}}$, for varying V_{LP} and V_{RP} at $V_{\text{L}} = V_{\text{R}} = 0$ V for device B. The measurements were performed at the V_{ABS} values indicated by colored marks in panel b. **f.** $(t - \Delta)/(t + \Delta)$ for varying V_{ABS} for device A. The blue markers indicate experimentally labeled data, and the red markers are the retrained CNN predictions. The orange markers are the retrained CNN predictions after performing a data regularization step.

6.3.4 GRADIENT DESCENT VOLTAGE OPTIMIZATION

Each CNN prediction of $(t - \Delta)/(t + \Delta)$ is incorporated into a gradient descent algorithm that sets a new value of the voltage V_{ABS} . The algorithm minimizes the cost function $f(V_{\text{ABS}}) = |(t - \Delta)/(t + \Delta)|$ until it reaches a value below a set tolerance. In each step, n , the algorithm computes the following quantities [50]:

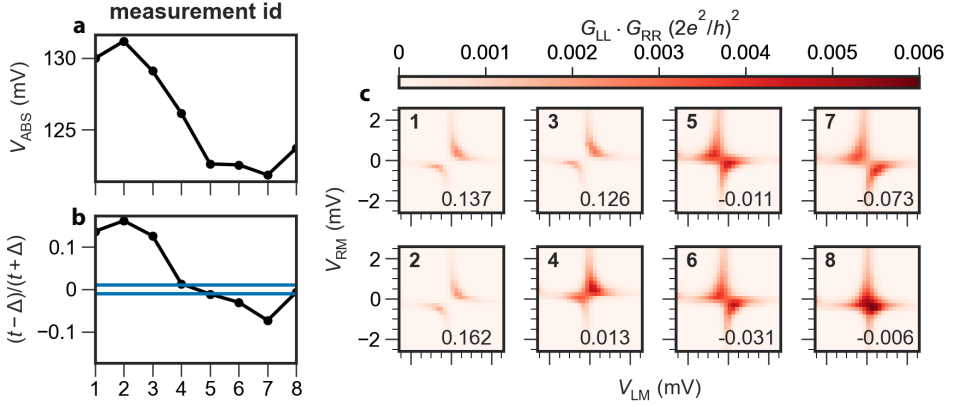


Figure 4: **Example of an automated tuning run of device A.** **a.** The hybrid plunger gate voltage, V_{ABS} , for each measurement. **b.** Prediction of the weighted ratio of elastic co-tunneling and crossed Andreev reflection, $(t - \Delta)/(t + \Delta)$, for each measurement. The horizontal, blue lines indicate the tolerance set before the run. **c.** $G_{\text{LL}} \cdot G_{\text{RR}}$, for varying V_{LP} and V_{RP} for subsequent measurements. The measurement ids are indicated by the bold text in the top left corner. The predicted value of $(t - \Delta)/(t + \Delta)$ is indicated in the bottom right corner.

6

$$\begin{aligned}
 \langle g \rangle_n &= \frac{1}{N} \sum_{i=n-N}^n \frac{f(V_{\text{ABS}})_i - f(V_{\text{ABS}})_{i-1}}{V_{\text{ABS}}^i - V_{\text{ABS}}^{i-1}} \\
 v^{n+1} &= kv^n + (1-k)\langle g \rangle_n \\
 V_{\text{ABS}}^{n+1} &= V_{\text{ABS}}^n - \eta v^{n+1}
 \end{aligned} \tag{6.3}$$

Here, $\langle g \rangle_n$ is the gradient of the objective function which is computed after the n th measurement, averaged over the past N measurements. The velocity v^{n+1} is a mixture of the previous velocity v^n , and gradient $\langle g \rangle_n$, weighted by the momentum, k . The change in V_{ABS} is then determined by v^{n+1} , scaled by the learning rate η . These steps are repeated until $f(V_{\text{ABS}}) < \tau$, where τ is the tolerance set for each run. We note that in the first step of the algorithm, V_{ABS} is changed by a pseudo-random number drawn from a Gaussian distribution with a standard deviation of 1, and an amplitude of 1.2 mV. This first step is on the order of typical V_{ABS} changes made by the algorithm. The minimal change of V_{ABS} is set by the 60 μV resolution of our digital-analog converters. We limit the maximal change to 5 mV, to prevent large shifts of the QD levels due to cross-capacitance. See section 6.7.9 for details on the algorithm, the choices of τ and η , and the algorithm pseudocode.

We now apply the automated tuning algorithm to device A. figure 4a shows the gate voltages, V_{ABS} , set by the algorithm for a run that converged below tolerance in 8 steps. figure 4b shows the values of $(t - \Delta)/(t + \Delta)$ predicted by the CNN. Here, the blue horizontal lines indicate the ideal tolerance, $\tau = 0.01$, set before the run. We show the charge stability diagrams for each step in figure 4c, and see that the direction of the avoided crossing reverses between steps 4 and 5. This indicates that $(t - \Delta)/(t + \Delta)$ changes sign, which is confirmed by the CNN predictions in panel b. Due to the momentum term k in the gradient descent algorithm (equation (6.3)), the algorithm first proceeds to lower V_{ABS} values before

the velocity term changes sign. The CNN converges below the tolerance at measurement 8, which we can confirm as a sweet spot by identifying a cross in panel figure 4j. In this run, the automated tuning was able to correctly identify the sweet spot, as well as vary V_{ABS} to find it. We show an example of a run that did not converge successfully in section 6.7.13.

6.4 TUNING ALGORITHM PERFORMANCE

6.4.1 ZERO FIELD ALGORITHM PERFORMANCE

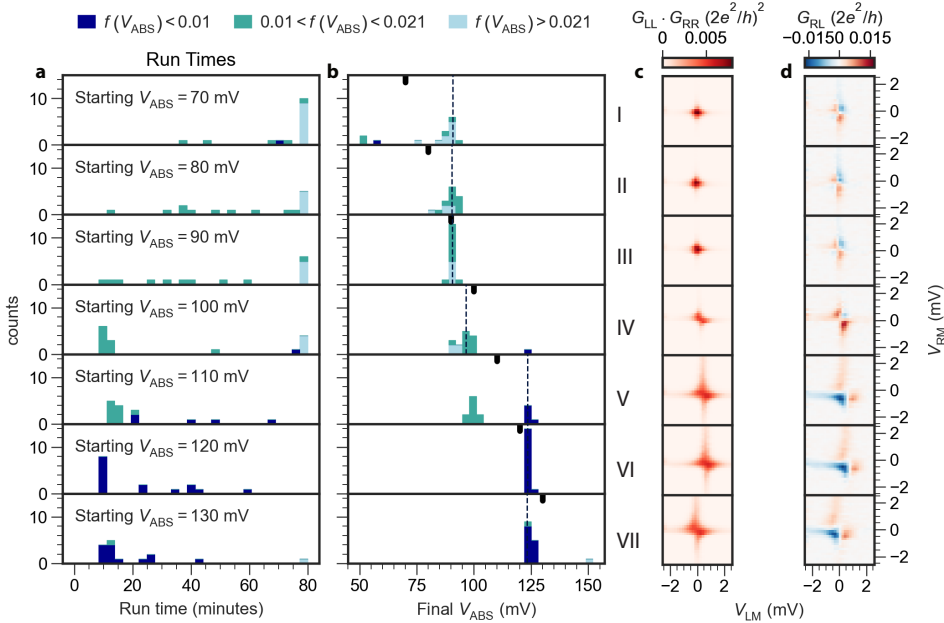


Figure 5: Run times and V_{ABS} values at which the algorithm converges for zero applied magnetic field We set a learning rate $\eta = 2 \times 10^{-4}$, a momentum $k = 0.5$ and a tolerance $\tau = 1 \times 10^{-2}$. **a.** Histograms of the run time of the gradient descent algorithm, for different starting V_{ABS} values. The dark blue bars indicate which runs converged with an objective function $f(V_{\text{ABS}}) = |(t - \Delta)/(t + \Delta)| < 0.01$. The sea green bars indicate convergence with $0.01 < f(V_{\text{ABS}}) < 0.021$. Light blue bars indicate runs that did not converge with $f(V_{\text{ABS}}) < 0.021$ within 25 iterations. **b.** Histograms of the V_{ABS} values for which the algorithm found the lowest $f(V_{\text{ABS}})$, for different starting V_{ABS} values. The black marks at the top of the figures indicate the starting V_{ABS} value. The dashed, vertical line indicates the V_{ABS} value closest to the greatest histogram peak with the lowest $f(V_{\text{ABS}})$. **c.** $G_{\text{LL}} \cdot G_{\text{RR}}$, for varying V_{LP} and V_{RP} , measured at the V_{ABS} value indicated by the dashed, vertical line in panel b. **d.** $G_{\text{RL}} = dI_{\text{R}}/dV_{\text{L}}$ for varying V_{LP} and V_{RP} , for different starting V_{ABS} values. The data was measured simultaneously with $G_{\text{LL}} \cdot G_{\text{RR}}$ in panel c.

The example run shown in figure 4 converged in 8 steps and was chosen as a representative example. To assess the performance of the algorithm more quantitatively, we repeat the tuning procedure 15 times and initialize it at different starting values of voltage V_{ABS} . We limit each run to a maximum of 25 measurements (not including the initial measurement) in order to restrict the total run time of the experiment. We chose the number of iterations based on the operation time of the presented experiment. In general, this variable can be

set by the user and will be specific to the data collection time and other experimental time scales.

We calculate the time elapsed between the start and end of each run and plot histograms for different starting V_{ABS} values in figure 5a. The dark blue bars indicate runs where the algorithm identified a sweet spot, by finding $f(V_{\text{ABS}}) < 0.01$ within 25 measurements. The sea green bars indicate runs where the algorithm identified a sweet spot, with higher tolerance, $0.01 < f(V_{\text{ABS}}) < 0.021$, within 25 measurements. For the light blue bars, the algorithm did not converge with $f(V_{\text{ABS}}) < 0.021$ within 25 measurements. We note that this does not exclude a sweet spot, as will be discussed below. Most of the runs that start from $V_{\text{ABS}} = 70 \text{ mV}$ do not converge within 25 measurements. In contrast, nearly all runs starting from $V_{\text{ABS}} = 130 \text{ mV}$ do converge, most of them within 20 minutes. This can be explained by the distance of each starting V_{ABS} to the nearest sweet spot.

In figure 5b, we show histograms of the V_{ABS} values for which the algorithm found the lowest $f(V_{\text{ABS}})$. For starting V_{ABS} values of 70 mV, 80 mV and 90 mV (rows I-III), most runs end at $V_{\text{ABS}} \approx 90.5 \text{ mV}$. We can inspect the charge stability diagrams measured at these gate values to determine whether they correspond to sweet spots. figure 5c shows $G_{\text{LL}} \cdot G_{\text{RR}}$, for varying V_{LP} and V_{RP} at ending V_{ABS} values indicated by the vertical dashed lines in panel b. We see that for figure 5c.I-III, the QD levels hybridize to form a cross, which is consistent with a sweet spot. The corresponding G_{RL} measurements in figure 5d show both signs of non-local conductance, which confirms that $t = \Delta$ [11]. Most of the runs starting from $V_{\text{ABS}} = 100 \text{ mV}$ (row IV) converge in 20 minutes, with the majority ending at $V_{\text{ABS}} = 96.5 \text{ mV}$. From panels c and d, we see that the QD levels do not form a cross, and the non-local conductance is mostly positive. We conclude that the algorithm incorrectly identifies this charge stability diagram as a sweet spot.

Runs that start from $V_{\text{ABS}} = 110 \text{ mV}$ (row V) converge with $0.01 < f(V_{\text{ABS}}) < 0.021$ at $V_{\text{ABS}} = 99.5 \text{ mV}$ and with $f(V_{\text{ABS}}) < 0.01$ at $V_{\text{ABS}} = 123.5 \text{ mV}$. We can see that the latter is close to a sweet spot, with $t \gtrsim \Delta$, as seen from the predominantly negative values of G_{RL} . The peak at $V_{\text{ABS}} = 99.5 \text{ mV}$ is close to the V_{ABS} ending values of the runs that started at $V_{\text{ABS}} = 100 \text{ mV}$ runs, and does not correspond to a sweet spot. We define 90.5 mV and 123.5 mV as sweet spots, based on the charge stability measurements. We note that the runs that did not converge with $f(V_{\text{ABS}})$ below tolerance (light blue) are clearly peaked around the sweet spot at 90.5 mV. We attribute the higher value of $f(V_{\text{ABS}})$ here to a weaker interaction strength than at the other sweet spot at 123.5 mV. Averaging all runs over the varying starting V_{ABS} values, 67.6% of runs converges within $\pm 1.5 \text{ mV}$, and 80.9% of runs converges within $\pm 4.5 \text{ mV}$ of an independently verified sweet spot. Averaging over all starting V_{ABS} values, the algorithm converges within $\pm 4.5 \text{ mV}$ of a sweet spot in 45 minutes. This is considerably faster than an experimentalist would find a sweet spot in an unknown V_{ABS} range.

6.4.2 FINITE FIELD ALGORITHM PERFORMANCE

In the previous section, we found sweet spots in the absence of an external magnetic field. In this case, the emerging Majorana zero modes are Kramers' pairs, which retain the protection against local perturbations, but have an additional degeneracy due to time-reversal symmetry [47]. This degeneracy has no impact on the demonstration of the automated tuning algorithm in the previous section, as the CSDs look identical to the

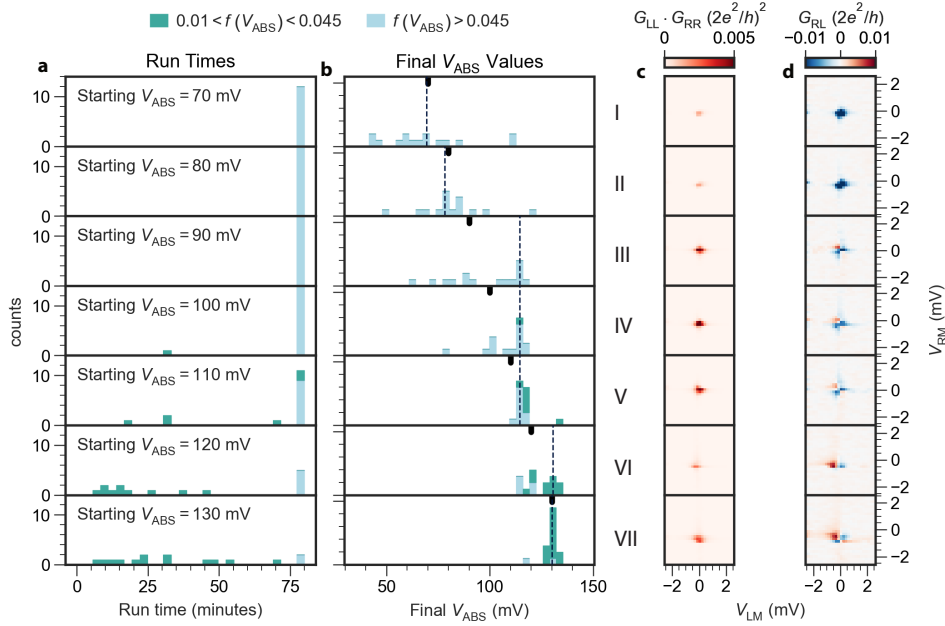


Figure 6: **Run times and V_{ABS} values at which the algorithm converged for $B = 150$ mT.** We set a learning rate $\eta = 2 \times 10^{-4}$, a momentum $k = 0.5$ and a tolerance $\tau = 1 \times 10^{-2}$. **a.** Histograms of the run time of the gradient descent algorithm, for different starting V_{ABS} values. The sea green bars indicate which runs converged with an objective function $0.01 < f(V_{\text{ABS}}) < 0.021$. The light blue bars indicate runs that did not converge with $f(V_{\text{ABS}}) < 0.021$ within 25 iterations. **b.** Histograms of the V_{ABS} values for which the algorithm found the lowest $f(V_{\text{ABS}})$, for different starting V_{ABS} values. The black marks at the top of the figures indicate the starting V_{ABS} value. The dashed, vertical line indicates the V_{ABS} value closest to the greatest histogram peak with the lowest $f(V_{\text{ABS}})$. **c.** $G_{\text{LL}} \cdot G_{\text{RR}}$, for varying V_{LP} and V_{RP} , measured at the V_{ABS} value indicated by the dashed, vertical line in panel b. **d.** $G_{\text{RL}} = dI_{\text{R}}/dV_{\text{L}}$ for varying V_{LP} and V_{RP} , for different starting V_{ABS} values. The data was measured simultaneously with $G_{\text{LL}} \cdot G_{\text{RR}}$ in panel c.

spin-polarized result. We now break time-reversal symmetry by applying an external field $B = 150$ T along the nanowire axis, to test whether our algorithm works both in the absence and presence of magnetic field. The magnetic field Zeeman-splits the ABSs in addition to the QDs and lowers their energy. To compensate for the resulting increased hybridization between the QDs and ABS, we raise the tunnel barriers between them using electrostatic gates.

We repeat the automated tuning algorithm for 15 times at different starting values of voltage V_{ABS} each. We limit each run to a maximum of 25 measurements (not including the initial measurement) in order to restrict the total run time of the experiment, and show histograms of the run times in figure 6a. In figure 6a.I-III, we see that none of the runs converge with $f(V_{\text{ABS}}) < 0.045$ within 80 minutes. The corresponding histograms in figure 6b show a broader distribution than for $B = 0$ T, as seen in figure 5b. The runs that start from V_{ABS} values of 110 mV, 120 mV and 130 mV (rows V-VII) converge with $0.01 < f(V_{\text{ABS}}) < 0.045$ more frequently, and the resulting histograms in figure 6b are more clustered.

From the charge stability diagrams in figure 6c,d, we see that the interaction between the QDs is significantly weaker than for $B = 0$ T. We attribute this to the stronger tunnel barriers we had to set to compensate for the lower ABS energy. This leads to generally larger values of $(t - \Delta)/(t + \Delta)$, as the denominator becomes smaller. In addition, our regularization procedure of the CNN predictions leads to a larger $f(V_{\text{ABS}})$ when the conductance is low. We attribute the poor convergence of the algorithm to the weaker QD-QD interaction. Nonetheless, we see from figure 6d that a number of peaks of the histograms in panel b correspond to sweet spots. We further note that $G_{\text{LL}} \cdot G_{\text{RR}}$ is the input for the CNN, which does not have the added information of G_{RL} . Based on the CSDs measured using $G_{\text{LL}} \cdot G_{\text{RR}}$ in figure 6c alone, it is not possible for an experimentalist to identify a sweet spot. Defining 114.26 mV and 130.44 mV as sweet spots based on the measurements of G_{RL} , we find that 45.7% of the runs converge within ± 1.62 mV, and 60% converge within ± 4.85 mV of these sweet spots. While this is worse than the algorithm's performance at $B = 0$ T, we note that the CNN was trained only on strongly interacting data (see section 6.7.2). We also note that we chose the same tolerance for $f(V_{\text{ABS}})$ as for figure 5, while the QD-QD interaction was weaker. This means that the algorithm will find less $f(V_{\text{ABS}})$ values below tolerance than before. We conclude that the algorithm can partially generalize to previously unseen experimental data in the weakly interacting regime.

6.5 DISCUSSION

Currently, the algorithm converges within ± 4.5 mV of a sweet spot in 45 minutes at zero field, which is generally faster than the time duration for manually tuning to a sweet spot. Because the CNN predictions and gradient descent algorithm calculations are nearly instantaneous, the run time is dominated by the DC conductance measurements. Performing RF reflectometry measurements is significantly faster and was used to explore a multidimensional parameter space in semiconductor-superconductor devices before [51]. We believe that the algorithm can converge significantly faster, provided that it is possible to train the CNN on RF reflectometry data generated from theoretical models instead of DC conductance presented here. Also, we note that we start the algorithm from tuned-up QDs in a region of V_{ABS} with ABSs. Ideally, the algorithm should also include tuning the QDs and ABSs to have interaction, which also takes a significant amount of time. We note that there are several automated tuning algorithms for forming double quantum dots in literature [26, 27, 30, 52]. Adapting these algorithms and integrating them into the tuning routine presented here would additionally increase speed of Kitaev chain devices tune-up.

6.6 CONCLUSION

We have shown that a supervised machine learning algorithm can predict $(t - \Delta)/(t + \Delta)$ from the charge stability diagrams of a minimal Kitaev chain. The algorithm was first trained on data generated from a theoretical model, and was shown to generalize reasonably well to conductance measurements of a two-dimensional electron gas device. After retraining on a part of this experimental data, the predictions of $(t - \Delta)/(t + \Delta)$ became significantly closer to the experimentally extracted values. The retrained algorithm demonstrated strong generalization to conductance measurements obtained from a nanowire device, achieving good accuracy across different architectures.

A gradient descent algorithm was then used to drive the nanowire device into a sweet spot by changing V_{ABS} , based on the predictions of $(t - \Delta)/(t + \Delta)$. When the QD-QD interaction is strong, the algorithm converges at two sweet spots with different $t + \Delta$ values, which is reflected in the value of $f(V_{\text{ABS}})$ at convergence. At finite external magnetic field, we had to decrease the QD-QD interaction because of the lower ABS energy. As a result fewer runs converged, which we attribute to the bias towards strong QD-QD interaction in the training and retraining data. However, a number of peaks in the ending V_{ABS} histogram coincide with sweet spots, which shows that the CNN does, to a degree, generalize to weak interaction.

Our automated tuning algorithm can successfully drive a minimal Kitaev chain into a sweet spot. Tuning and monitoring multiple sweet spots is required for quantum information experiments involving Majorana zero modes. Our work paves the way for tuning up more complicated Kitaev chain devices that are required for braiding, anyon fusion and other quantum information experiments.

DATA AVAILABILITY

All raw data in the publication and the analysis code used to generate figures are available at <https://doi.org/10.5281/zenodo.10900882>.

6.7 SUPPLEMENTARY INFORMATION

6

6.7.1 CNN ARCHITECTURE

Convolutional Neural Networks (CNNs) are designed for efficient data analysis, especially for visual tasks such as image recognition. Unlike traditional fully-connected neural networks (NNs), CNNs utilize convolutions to process information in image-like datasets. These enhance their capacity to handle spatially-correlated information present among pixels in image-like datasets [53, 54]. The architectural framework of CNNs leverages spatial relations within the data through locally-connected layers that improve the computational efficiency by neglecting correlations between distant data points.

At the foundation of CNNs are trainable convolutional filters that are crucial for capturing spatial correlations in the data set. The filter size is a hyperparameter of the network architecture and, therefore, adaptable to specific problem sets. Furthermore, to reduce the complexity and number of parameters, CNNs integrate dimensionality reduction techniques such as pooling operations [55]. These operations allow us to preserve essential features and increase computational efficiency at the same time.

The architecture of the CNN to make prediction in this work is shown in table 6.1. The network architecture employed in this study comprises a total of 9 layers. The initial 6 layers constitute the convolutional segment of the network, followed by a flattening operation and the subsequent utilization of a fully-connected NN. The initial 6 layers operate within a dual-input framework, where two independent and unconnected CNNs can process different images, such as G_{LL} and G_{RR} (or non-local conductance $G_{LR/RL}$), and integrate them in the subsequent NN segment. Notably, in the current research, the dual-input framework is not exploited, as we pre-process the data by multiplying G_{LL} with G_{RR} . However, the dual-input framework is kept for the sake of generalization that allows us to adapt the CNNs and tuning algorithm to different inputs in future research.

Table 6.1: Architecture of the CNN.

*we are using a dual-input framework for the first 6 layers

CNN Classifier	
Layer	Output shape
Input	(28,28,1)
Conv2D	(28, 28, 32)
MaxPooling2D	(14, 14, 32)
Conv2D	(14, 14, 64)
MaxPooling2D	(7, 7, 64)
Flatten	(3136)
Concatenate *	(6272)
Dense	(128)
Dense	(1)
total parameters	840,705

6.7.2 CNN TRAINING

In this work, we are utilizing a two-step training process for the CNN. The first step involves training with a dataset generated through numerical calculations, while the second step involves re-training using a smaller set of experimental conductance data.

6.7.3 KITAEV CHAIN EFFECTIVE MODEL

We are modeling the double quantum dot system coupled by a semiconductor-superconductor hybrid segment as a two-site Kitaev chain. The couplings between the quantum dots are mediated by ABSs in the hybrid segment. From a theory point, the system can be seen as 3-site model where the hybrid segment gets treated as site. We are following the work of Ref [56] and refer there for a more detailed description of the theory model. The corresponding Hamiltonian of the 3-site model takes the form [57–59]

$$\begin{aligned}
H &= H_D + H_S + H_T \\
H_D &= \sum_{a=L,R} (\varepsilon_{Da} + E_{ZDa}) n_{Da\uparrow} + (\varepsilon_{Da} - E_{ZDa}) n_{Da\downarrow} \\
&\quad + U_{Da} n_{Da\uparrow} n_{Da\downarrow} \\
H_S &= \varepsilon_A (n_{A\uparrow} + n_{A\downarrow}) + \Delta_0 (c_{A\uparrow} c_{A\downarrow} + c_{A\downarrow}^\dagger c_{A\uparrow}^\dagger) \\
H_T &= \sum_{\sigma=\uparrow,\downarrow} (t_L c_{A\sigma}^\dagger c_{DL\sigma} + \sigma t_{Lso} c_{A\sigma}^\dagger - c_{DL\sigma} \\
&\quad + t_R c_{DR\sigma}^\dagger c_{A\sigma} + \sigma t_{Rso} c_{DR\sigma}^\dagger - c_{A\sigma}) + h.c..
\end{aligned} \tag{6.4}$$

The Hamiltonian can be split into three parts, the quantum dot Hamiltonian, H_D , the hybrid segment with the ABSs, H_S , and the tunnel coupling between ABS and quantum dots, H_T . H_D contains the orbital energy, ε_{Da} , the electron occupation, $n_{Da\sigma}$, the Zeeman energy, E_{ZDa} , and Coulomb repulsion, U_{Da} . The index a defines the left/right quantum dot. The hybrid Hamiltonian H_S contains the normal state energy ε_A and an induced pairing gap Δ_0 .

The tunnel Hamiltonian H_T includes two couplings between the quantum dot and ABS: a spin-conserving, t , and a spin-flipping process, t_{so} . The spin-orbit interaction determines the ratio of t_{so}/t .

Proximity effects of the semiconductor-superconductor hybrid transform the quantum dot orbitals into Yu-Shiba-Rusinov states (YSR) [44–46] and create a new basis of spinless fermions for a Kitaev chain model. The YSR states are a superposition of electron and hole components and in this basis, the Kitaev chain has more generalized effective couplings, describing the interaction between the two YSR states. We can write the effective Hamiltonian describing the interaction between these two states as

$$H_{\text{eff}}^{\text{coupling}} = \sum_{\sigma, \eta=\uparrow, \downarrow} \left(t_{\sigma\eta} c_{DL\sigma}^\dagger c_{DR\eta} + \Delta_{\sigma\eta} c_{DL\sigma}^\dagger c_{DR\eta}^\dagger \right) + h.c., \quad (6.5)$$

where we consider different ECT and CAR amplitudes, $t_{\sigma\eta}$ and $\Delta_{\sigma\eta}$ between electron and hole components of the quantum dots. Considering that the YSR states have electron and hole components, the couplings $t_{\sigma\eta}$ and $\Delta_{\sigma\eta}$ have to be generalized. The ground states of a single proximitized quantum dot are a spin singlet and a spin-down state in the even- and odd-parity subspace:

$$\begin{aligned} |S\rangle &= u|00\rangle - v|11\rangle, \quad |\downarrow\rangle = |01\rangle \\ u^2 &= 1 - v^2 = \frac{1}{2} + \frac{\xi}{2E_0} \\ \xi &= \varepsilon + \frac{U}{2}, \quad E_0 = \sqrt{\xi^2 + \Delta_{\text{ind}}^2}. \end{aligned} \quad (6.6)$$

This allows us to define the YSR state as $|\downarrow\rangle = f_{YSR}^\dagger |S\rangle$ and the effective coupling of Eq.(B2) written in terms of YSR states becomes

$$H_{\text{eff}} = \sum_{a=L,R} \delta\varepsilon_a f_a^\dagger f_a + \Gamma_o f_L^\dagger f_R + \Gamma_e f_L^\dagger f_R^\dagger + h.c., \quad (6.7)$$

where $\delta\varepsilon_a = E_\downarrow - E_S$ is the excitation energy of the YRS state and $\Gamma_{o/e}$ are odd/even generalized effective couplings between the YSR states. The odd coupling is defined as

$$\begin{aligned} \Gamma_o &= \langle S_\downarrow | H_{\text{eff}}^{\text{coupling}} | \downarrow S \rangle \\ &= -t_{\uparrow\uparrow} v_L v_R + t_{\downarrow\downarrow} u_L u_R + \Delta_{\uparrow\downarrow} v_L u_R - \Delta_{\downarrow\uparrow} u_L v_R, \end{aligned} \quad (6.8)$$

where $|\downarrow S\rangle$ and $|S \downarrow\rangle$ are odd parity tensor states and Γ_o is a linear combination of spin-conserving couplings, namely equal spin ECT and opposite spin CAR processes. The even-parity coupling

$$\begin{aligned} \Gamma_e &= \langle SS | H_{\text{eff}}^{\text{coupling}} | \downarrow\downarrow \rangle \\ &= -\Delta_{\uparrow\uparrow} v_L v_R + \Delta_{\downarrow\downarrow} u_L u_R + t_{\uparrow\downarrow} v_L u_R - t_{\downarrow\uparrow} u_L v_R \end{aligned} \quad (6.9)$$

couple states with total spin zero and one, i.e. breaks spin conservation. These odd- and even-parity couplings can be seen as more generalized effective t and Δ parameter from

the poor man's Majorana Kitaev chain model [10]. To obtain the differential conductance, we employ the Mahaux–Weidenmuller formula to compute the scattering matrix [48]. For this, we rewrite the derived effective Hamiltonian of Eq.(B4) in the Bogoliubov-de Gennes formalism, solve the corresponding eigenequation, and obtain the W -, scattering matrix and conductance matrix. In this work, we focus on the diagonal elements of the conductance matrix G_{LL} and G_{RR} .

6.7.4 NUMERICAL TRAINING DATA

After introducing the theory model, we create the theoretical training data by generating a diverse set of Hamiltonians of Eq. (B1) leading to an effective Hamiltonian in the YSR basis of Eq.(B4), incorporating random variations within of parameters in the model in specified intervals:

- induced Zeeman energy in each quantum dot $E_{ZDa} \in I = [-0.2, 0.2]$
- induced pairing gap $\Delta_0 \in I = [0.2, 0.6]$
- tunneling couplings $t_{L/R} \in I = [0.05, 0.4]$
- $t's$ and $\Delta's \in I = [0.01, 0.48]$
 $\rightarrow \Gamma_{odd/even} \in I = [0.01, 0.48]$
- temperature $T \in I = [0.02, 0.03]$
- left/right lead coupling $\Gamma_{L/R} \in I = [0.04, 0.06]$

While we include a Zeeman energy on the QDs, we do not consider the up state of the QDs. As a result, the Zeeman energy only lowers the energy of the down states. The theoretical data, depicted in Fig. 7(c), closely resembles the experimental conductance data including, e.g., variations in lead couplings, background noise, and interaction strengths across a broad parameter range spanning from the ECT- to the CAR-dominated region. We illustrate in Fig. 7(a) the training/test loss for the initial training step. The loss function shows the expected behavior, with the test-loss consistently higher than the training-loss, reaching saturation at around 75 epochs. We have chosen a training set of 6000 samples and trained the CNN with a batch size of 16 for the 100 epochs. The fluctuations during the training can be related to the stochastic nature of the gradient descent algorithm [60], the small batch size, and randomly-chosen training/test data.

6.7.5 EXPERIMENTAL TRAINING DATA

We show the training/test loss for the re-training with an experimental training set in Fig. 7(b). The test-loss is again consistently higher than the training-loss and saturates at around 20 epochs. For the re-training, we only train the CNN for 25 epochs, starting from the already-trained CNN parameters and fine-tuning the parameters to experimental data.

In Figs. 3(a,b), we compare the CNN predictions for the experimental dataset. In (a), we show the predictions of the initial theory-only CNN. The predictions show a constant gradient for increasing V_{ABS} capturing the experimental values overall with good accuracy. However, the theory CNN does not predict the sweet spot region around $V_{ABS} = -622$ mV

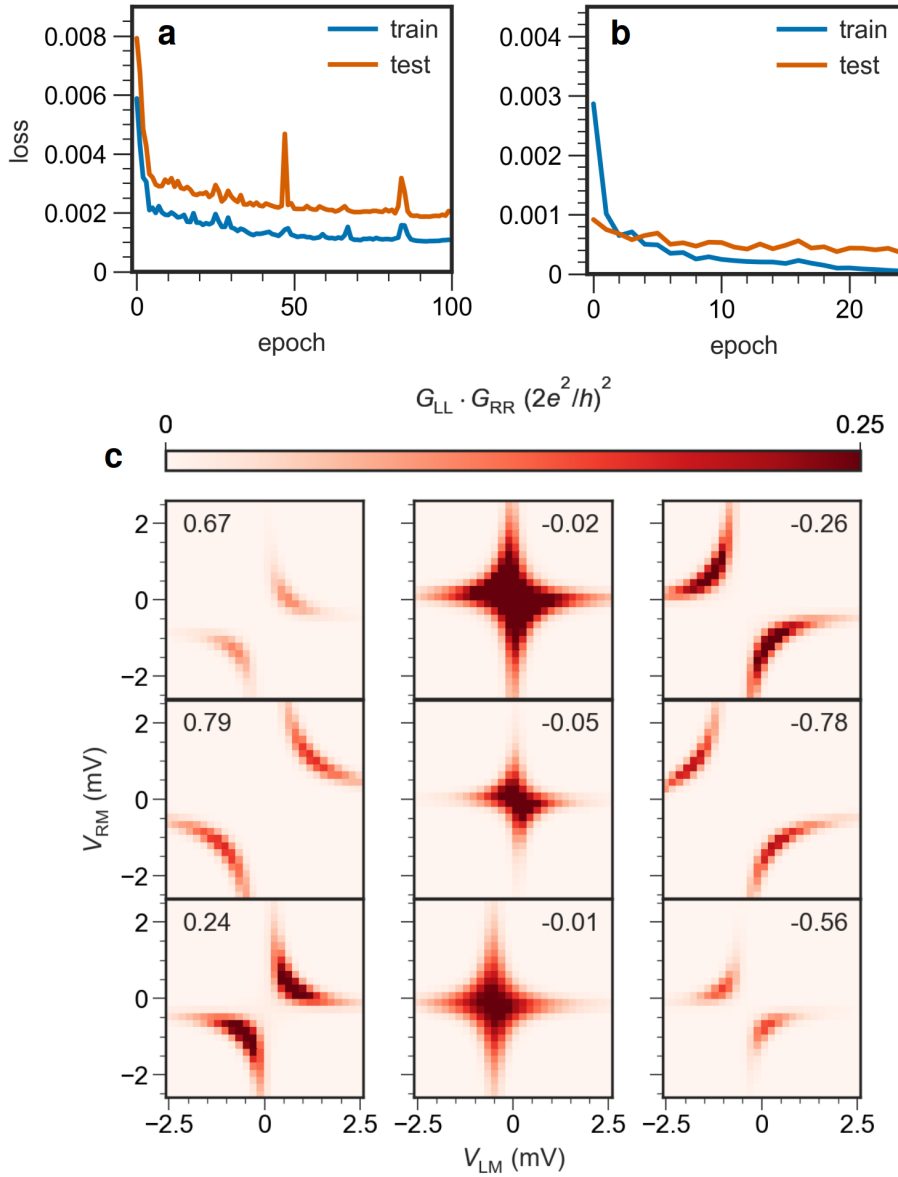


Figure 7: Training evaluation and numerical training data of the convolutional neural network (CNN)
a. The train- and test-loss during the initial training of the CNN with the numerical data set (shown in c). **b.** The train- and test-loss during the re-training of the CNN with labeled experimental data, as shown in Fig. 3(a-e)
c. Numerical calculations of the product of the left and right differential conductance, $G_{LL} \cdot G_{RR}$, for varying $(t - \Delta)/(t + \Delta)$, including the ECT-dominated, sweet spot, and CAR-dominated regime.

well which possibly can lead to convergence problems when approaching the sweet spot

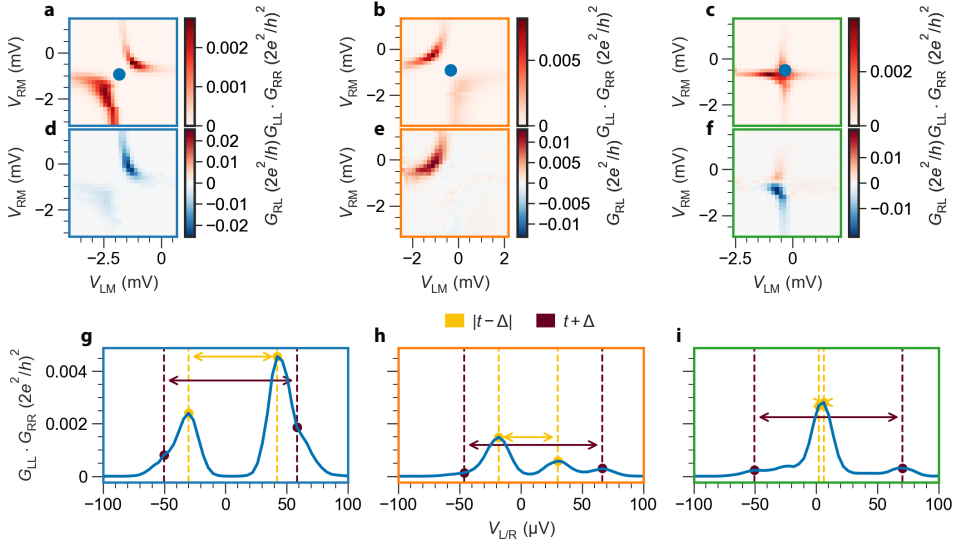


Figure 8: **Extraction of labels using tunnel spectroscopy.** a.-c. The product of the left and right differential conductance, $G_{LL} \cdot G_{RR}$, for varying V_{LP} and V_{RP} . The measurements were performed at V_{ABS} values of 85 mV, 104 mV and 115 mV respectively. e.-g. Non-local conductance, $G_{RL} = dI_R/dV_L$ for varying V_{LP} and V_{RP} . The data was measured simultaneously with panels b-d. g.-i. $G_{LL} \cdot G_{RR}$ for varying left/right lead bias, $V_{L/R}$, measured at the V_{LP} and V_{RP} values indicated by the blue marker in panels a-c. The purple, dashed lines indicate the outer peaks. The yellow, dashed lines indicate the inner peaks.

with the gradient descent algorithm. Figure 3(b) shows the prediction of the re-trained CNN for the experimental test-data. In this case, the CNN captures the sweet spot region well. The gradient towards the sweet spot coincides well with the labeled data which is one of the most important factors for CNN-tuning algorithm. In Fig. 3(c-e) we show three conductance measurements for the ECT, CAR, and sweet spot regime taken at specific V_{ABS} from above.

6.7.6 DATA LABELING PROCEDURE

figure 8a,c show the charge stability diagrams as presented in figure 3a-c. We use python code to interpolate the center of the avoided crossings, which is indicated by the blue markers. At the V_{LP} and V_{RP} values corresponding to these markers, we measure G_{LL} for varying V_L , and G_{RR} for varying V_R , and show the resulting $G_{LL} \cdot G_{RR}$ in figure 8g-i. Each spectrum consists of two inner peaks separated by $|t - \Delta|$ and two outer peaks separated by $t + \Delta$ (see methods section of [18] for details on the model). These are indicated by the yellow and purple arrows in panels g-i. We label the $V_{L/R}$ values corresponding to the peaks manually, since $G_{LL} \cdot G_{RR}$ can be too low for a peak-finding algorithm to work. Because the inner peaks do not provide information on the sign of $t - \Delta$, we extract it from the non-local conductance. When $t > \Delta$, elastic co-tunneling dominates over crossed Andreev reflection, and the sign of non-local conductance will be negative [11]. Likewise, G_{RL} will be predominantly positive for $t < \Delta$, so we extract the sign from:

$$\text{sgn}(t - \Delta) = \begin{cases} 1 & -\min(G_{RL}) > \max(G_{RL}) \\ -1 & \max(G_{RL}) > -\min(G_{RL}) \end{cases}$$

We combine the sign found from the non-local conductance measurements with the inner and outer peak spacing to calculate $(t - \Delta)/(t + \Delta)$ for each V_{ABS} value in figure 3g.

We note that directly relating the peak spacings to the CAR and ECT rates is only justified in the infinite Zeeman limit. At zero magnetic field, in limit of large charging energy on the QDs, the sweet spot condition becomes $t = \sqrt{2}\Delta$ as a result of the larger Hamiltonian basis that now includes both spin species [47]. At this sweet spot, there is still a peak at the Fermi level and two peaks that indicate the gap. While the distance between the outer peaks is then no longer $t + \Delta$, we continue to use this form of labeling for the CNN. The direct relation with the CAR and ECT rates is then severed. This means that we are not training the CNN on transport rates, but rather on peak spacings. For our purposes this is not problematic, as minimizing $(t - \Delta)/(t + \Delta)$ will still correspond to finding the sweet spot. We note that there can be additional excited states in spectroscopy at zero field [12]. These are only visible at one bias polarity. As we look for particle-hole symmetric peaks in $G_{LL} \cdot G_{RR}$, we filter out these low-Zeeman excited states.

6.7.7 CNN PREDICTION LIMITATIONS

As discussed in section 6.7.2, the CNN was mainly trained on an effective model for the two QDs, that integrates out the ABS coupling them. When the QD-ABS coupling becomes on the order of the ABS energy, this model does not accurately describe the system anymore. In figure 9a we see that the CNN predicts a sweet spot around $V_{ABS} = 45$ mV, while the labeled data indicates that $(t - \Delta)/(t + \Delta) \approx 1$. The weighted ratio approaches 1 when $\Delta \rightarrow 0$, as the numerator and denominator will be equal. From the corresponding CSD in figure 9b we see that the correlated conductance vanishes, which points to weak interaction between the QDs. However, the corresponding non-local conductance in figure 9e has both signs, which is usually a sign of a sweet spot. The features in panels b and e depend less on V_{RP} than on V_{LP} , which suggests that the transport is dominated by the left QD. We interpret the presence of positive and negative non-local conductance as a sign of direct transport between the left QD and the ABS. From the tunnel spectroscopy in figure 1b, we see that

the ABS at the lowest V_{ABS} values comes close to zero-energy at its minimum. This is consistent with our interpretation of an increased QD-ABS interaction at low V_{ABS} values.

In figure 9c and f, we see both signs of non-local again, together with a cross in the correlated conductance. The non-local features depend mostly on V_{LP} , which suggests strong QD-ABS interaction as in panels b and e. It is hard to tell whether this is an actual sweet spot, and might be related to low Majorana polarization as detailed in Ref. [61]. We note that the CNN predictions and experimentally extracted values of $(t - \Delta)/(t + \Delta)$ agree at this V_{ABS} value.

Finally, we see that the labeled data becomes noisier around $V_{\text{ABS}} = 135$ mV in figure 9a. From panels d and g, we see that the QD-QD interaction is very weak. Accurately labeling the data becomes challenging for low interaction, as the peaks are hard to find due to low conductance. The CNN predictions are greater than the experimental labels here due to the regularization procedure. We conclude that the CNN performs well when the QD-ABS interaction is smaller than the ABS energy. Also, it does not perform well when the conductance becomes low due to weak QD-QD interaction.

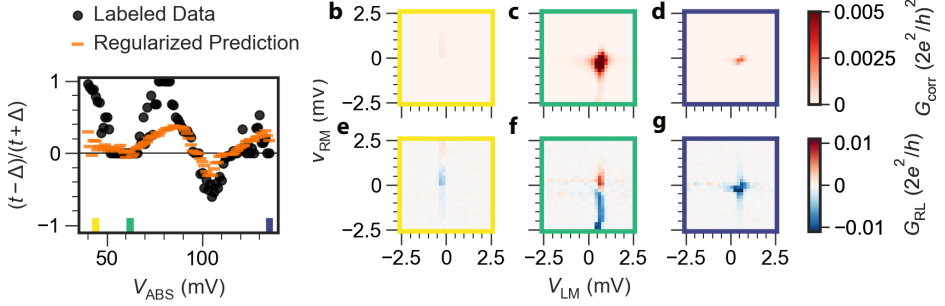


Figure 9: **Selected charge stability diagrams.** **a.** $(t - \Delta)/(t + \Delta)$ for varying V_{ABS} for device A. The black markers indicate experimentally-labeled data and the orange markers are the retrained and regularized CNN predictions. **b.-d.** The product of the left and right differential conductance, $G_{\text{LL}} \cdot G_{\text{RR}}$, for varying V_{LP} and V_{RP} . The measurements were performed at V_{ABS} values of 44 mV, 62 mV and 135 mV respectively. **e.-g.** Non-local conductance, $G_{\text{RL}} = dI_{\text{R}}/dV_{\text{L}}$, for varying V_{LP} and V_{RP} . The data was measured simultaneously with panels b.-d.

6.7.8 REGULARIZATION

There are three cases that can lead to a vanishing $(t - \Delta)/(t + \Delta)$ ratio. In the first case, $(t + \Delta)$ becomes very large. The interaction strength is ultimately limited by the ABS energy and the superconducting parent gap. Second, $(t + \Delta)$ is finite, but $t \approx \Delta$, which is the desired sweet spot condition. In the third case, both t and Δ become vanishingly small, but are not equal in size. While this should be mitigated by scaling $t - \Delta$ with $1/(t + \Delta)$, the CNN can incorrectly identify weak QD interaction as a sweet spot. To penalize low interaction, we add a correction to the objective function based on the mean conductance of a measurement. When the QDs have low interaction, the differential conductance will be negligible. First, we compute the average conductance of a charge stability diagram:

$$\langle G \rangle = \frac{1}{N} \sum_{i=1}^N \left(\frac{1}{M} \sum_{j=1}^M G_{\text{LL}} \cdot G_{\text{RR}}(V_{\text{LP}}^i, V_{\text{RP}}^j) \right)$$

Then we count the number of pixels of a measurement that have a conductance value greater than $\langle G \rangle$:

$$N_{>} = \sum_{i,j}^{N,M} \Theta[G_{LL} \cdot G_{RR}(V_{LP}^i, V_{RP}^j) - \langle G \rangle]$$

Where Θ is the Heaviside function. Finally, we offset the objective function based on the ratio of above-average conductance pixels:

$$f(V_{ABS}) = \frac{|t - \Delta|}{t + \Delta} + \left(\frac{N}{2N_{>}} \right)^3 \quad (6.10)$$

Where $N_{>}$ is limited by $0 \leq N_{>} \leq N^2$, assuming $M = N$. As $N_{>} \rightarrow \infty$, this correction disappears. As $N_{>} \rightarrow 0$, the correction becomes very large and a minimum of the objective function cannot be found. We use this regularization procedure for all the automated tuning runs.

6.7.9 GRADIENT DESCENT ALGORITHM

As detailed in equation (6.3), we use a gradient descent algorithm to find sweet spots where $t = \Delta$. While most gradient descent algorithms use the slope as a condition for convergence, we use the objective function. The reason is that we cannot compute the gradient at each given point, but need discrete points between which we can approximate the gradient using finite differences:

$$g_i = \frac{f(V_{ABS})_i - f(V_{ABS})_{i-1}}{V_{ABS}^i - V_{ABS}^{i-1}}$$

We use a momentum term, k , to update the velocity with the average of the past 5 gradients in each step:

$$v^{n+1} = kv^n + (1-k)\langle g \rangle_n$$

Considering QD-based devices are mesoscopic in nature, predictions of the CNN at the same V_{ABS} can differ. This can result from gate jumps, gate hysteresis, off-centered measurements, etc. The momentum term helps to overcome local maxima of $f(V_{ABS})$ and find the global minimum. We update V_{ABS} using the velocity scaled by a learning rate, η :

$$V_{ABS}^{n+1} = V_{ABS}^n - \eta v^{n+1}$$

This procedure is repeated until the objective function is below the predefined tolerance, τ :

$$f(V_{ABS}) = \frac{|t - \Delta|}{t + \Delta} + \left(\frac{N}{2N_{>}} \right)^3 < \tau$$

where the final term penalizes low QD-QD interaction, see section 6.7.8 for details.

Considering the algorithm directly controls gate voltages on the device, we include some extra constraints. First, the minimal change in V_{ABS} is limited to $60 \mu\text{V}$ by our digital-analog converter resolution. Second, we limit the maximal change in V_{ABS} to 10 mV . A larger change will shift the Coulomb resonance out of the measurement window. In each iteration, we center the measurements by taking linecuts of V_{LP} and V_{RP} at the extrema of

a charge stability diagram, and interpolate their intersection. Furthermore, we limit the algorithm with ± 50 mV from each starting V_{ABS} to confine it to the known region. If the algorithm proposes a V_{ABS} value across this boundary, we reverse the sign of the velocity. In the first iteration, we change V_{ABS} by a value drawn from a Gaussian distribution:

$$f(\Delta V_{\text{ABS}}) = \frac{1.2 \text{ mV}}{\sqrt{2\pi}} e^{-\Delta V_{\text{ABS}}^2/2}$$

While g_i values are generally linear close to the sweet spot, they change sign at the sweet spot. If the CNN identifies a sign change of $t - \Delta$, we change the sign of the velocity -before updating it with the gradients- and reduce the learning rate by a factor of 2. We also increase the learning rate by 50% every 5 steps.

6.7.10 CHOICE OF LEARNING RATE

For a single ABS in the infinite parent gap limit, we can write the elastic co-tunneling (t) and crossed Andreev reflection (Δ) rates as [16]:

$$t = \frac{\Gamma^2 I_0 \mu^2}{(\Gamma^2 + \mu^2)^2} \quad \Delta = \frac{\Gamma^4 I_0}{\Gamma^4 + 2\Gamma^2 \mu^2 + \mu^4}$$

Where Γ is the induced gap of the ABS, μ is its electrochemical potential and I_0 is a proportionality constant. We can then write the sum and differences of t and Δ , as well as their ratio as:

$$\begin{aligned} t + \Delta &= \frac{\Gamma^2 I_0}{\Gamma^2 + \mu^2} \\ t - \Delta &= \frac{\Gamma^2 I_0 (-\Gamma^2 + \mu^2)}{\Gamma^4 + 2\Gamma^2 \mu^2 + \mu^4} \\ \Lambda &= \frac{t - \Delta}{t + \Delta} = \frac{\mu^2 - \Gamma^2}{\mu^2 + \Gamma^2} \end{aligned} \tag{6.11}$$

At $\mu = \pm\Gamma$, we obtain $t = \Delta$ and calculate the derivative:

$$\begin{aligned} \frac{d\Lambda}{d\mu} &= \frac{4\mu\Gamma^2}{(\mu^2 + \Gamma^2)^2} \\ \left. \frac{d\Lambda}{d\mu} \right|_{\mu=\pm\Gamma} &= \frac{1}{\Gamma} \end{aligned} \tag{6.12}$$

In a device, we are tuning μ indirectly using a gate voltage V_{ABS} . We can write the slope in terms of V_{ABS} using:

$$\left. \frac{d\Lambda}{dV_{\text{ABS}}} \right|_{\text{sweet spot}} = \left. \frac{d\Lambda}{d\mu} \right|_{\mu=\pm\Gamma} \frac{d\mu}{dV_{\text{ABS}}} \tag{6.13}$$

$$= \frac{1}{\Gamma} \frac{d\mu}{dV_{\text{ABS}}} = \frac{\alpha}{\Gamma} \tag{6.14}$$

Where α is the lever arm. Bottou et al. recommend a learning rate which matches the slope at the objective function minimum [50]. Using a lever arm $\alpha = 0.05e$ and an induced gap

$\Gamma = 100 \mu\text{eV}$, we obtain $\eta_{\text{opt}} = \Gamma/\alpha = 2 \times 10^{-3} \text{ V}$, which is 10 times larger than the learning rate used in the experiments. We lower the learning rate to prevent large changes of V_{ABS} , as cross-capacitance can shift the Coulomb resonances of the QDs.

We also note that we chose a relatively low learning rate, η , compared to the optimal value (see section 6.7.9 for details). This η was chosen to prevent large changes in V_{ABS} , which also affects the electrochemical potential of the QDs. The centering of the QD measurements is important for having accurate CNN predictions. This can be improved by using “virtual gates”, which are linear combinations of V_{LP} , V_{RP} and V_{ABS} that compensate for cross-capacitance. Additionally, the CNN could be trained on more off-centered theory data.

6.7.11 CHOICE OF TOLERANCE

At $t = \Delta$, the QD levels intersect perfectly. As t and Δ move away from the sweet spot, an avoided crossing of magnitude $D = \sqrt{8|t^2 - \Delta^2|}$ opens between the two hyperbolas (see page 4 of the supplementary materials of [12]). If this magnitude is smaller than the broadening of conductance, an avoided crossing cannot be observed. We can define a tolerance based on broadening and the expected interaction strength $t + \Delta$. First, we rewrite the distance between parabola's as:

$$D = 2(t + \Delta) \sqrt{2 \frac{|t - \Delta|}{t + \Delta}}$$

If we demand that the distance is below thermal broadening, $D < 3.5k_{\text{B}}T$, we can write:

$$\frac{|t - \Delta|}{t + \Delta} < \frac{1}{8} \left(\frac{3.5k_{\text{B}}T}{t + \Delta} \right)^2 = \tau$$

Using a temperature of $T = 30 \text{ mK}$ and an interaction strength $t + \Delta = 80 \mu\text{eV}$ we obtain a tolerance $\tau = 1.6 \times 10^{-3}$. While this quantity is smaller than the value we used in experiments, we note that our conductance broadening is significantly larger than the $9 \mu\text{eV}$ we can expect from thermal processes. Substituting the thermal term by a broadening of $20 \mu\text{eV}$ yields a tolerance $\tau = 1 \times 10^{-2}$, which is the value we used in the experiments. Therefore, we recommend using a tolerance:

$$\tau = \frac{1}{32} \left(\frac{\gamma}{\Delta^*} \right)^2$$

Where Δ^* is the desired gap at the sweet spot and γ is the linewidth of the Coulomb resonances observed from bias spectroscopy. We note that in principle this allows us to select sweet spots based on their gap by choosing τ . This is seen in figure 5b, where the algorithm converges on the weaker sweet spot at $V_{\text{ABS}} = 99.5 \text{ mV}$ with a higher tolerance than on the stronger one at $V_{\text{ABS}} = 123.5 \text{ mV}$. Although this implies that we can reject weakly-interacting sweet spots, they are still minima of the objective function. A possible improvement of the algorithm could be lowering the tunnel barriers when the objective function does not converge below tolerance, or penalizing the objective function for weak sweet spots, as in figure 6.

6.7.12 PSEUDOCODE

In algorithm 1 we show the pseudocode for the automated tuning algorithm.

Algorithm 1 Sweet Spot Optimization Algorithm

Require: $V_ABS_parameter$, $learning_rate$, $epochs$, min_step_size , $tolerance$, N , $momentum$, $damping_term$, max_step_size , V_ABS_min , V_ABS_max

```

1: Assert  $min\_step\_size > 1e-6$ 
2: for  $epoch = 1$  to  $epochs$  do
3:   if  $epoch == 1$  then
4:      $V\_ABS \leftarrow handle\_first\_epoch(V\_ABS, min\_step\_size)$ 
5:   else
6:     if  $epoch \bmod 5 == 0$  then
7:        $learning\_rate \leftarrow learning\_rate \times 1.5$ 
8:     end if
9:     Compute gradients
10:    Update  $V\_ABS$  and  $v$  using gradients
11:  end if
12:  Set gate value using  $V\_ABS\_parameter(V\_ABS)$ 
13:  Precenter measurement
14:   $dbx \leftarrow measure\_func(measure\_func\_kwargs)$ 
15:  Update  $\delta_{min\_t\_values}$ ,  $obj\_fun\_values$ ,  $V\_ABSs$ ,  $dbxs$ 
16:  if Overshoot detected then
17:    Reverse  $v$ , reduce  $learning\_rate$ , log overshoot
18:  end if
19:  if  $|current\_obj\_val| < tolerance$  then
20:    Log convergence, break
21:  end if
22: end for
23: if Non-convergence after all epochs then
24:   Log non-convergence details
25: end if
26: Close log return  $V\_ABSs$ ,  $obj\_fun\_values$ ,  $current\_obj\_val$ ,  $epoch$ 

```

6.7.13 NON-CONVERGED RUN EXAMPLE

In figure 10a, we show the V_{ABS} values visited by a run that did not converge. Just as in figure 4, the run started from $V_{ABS} = 130$ mV. For the first 14 measurements, the algorithm visits increasing values of V_{ABS} . We see from figure 10b that $(t - \Delta)/(t + \Delta)$ does not change significantly in this gate range. From the charge stability diagrams in figure 10c, we see that the interaction between the QDs becomes weaker for increasing V_{ABS} . Eventually, the algorithm reverses direction and returns to the starting $V_{ABS} = 130$ mV. As we limit the number of measurements per run to 26, the algorithm stops here. This non-converged run highlights that the CNN does not predict $(t - \Delta)/(t + \Delta)$ accurately if $t + \Delta$ is small, as can be seen from the superimposed CNN predictions in the charge stability diagrams. We attribute this to the bias toward strong interaction in our theoretical and experimental

training set. We note that this run ended with a velocity in the right direction and might have converged given more steps.

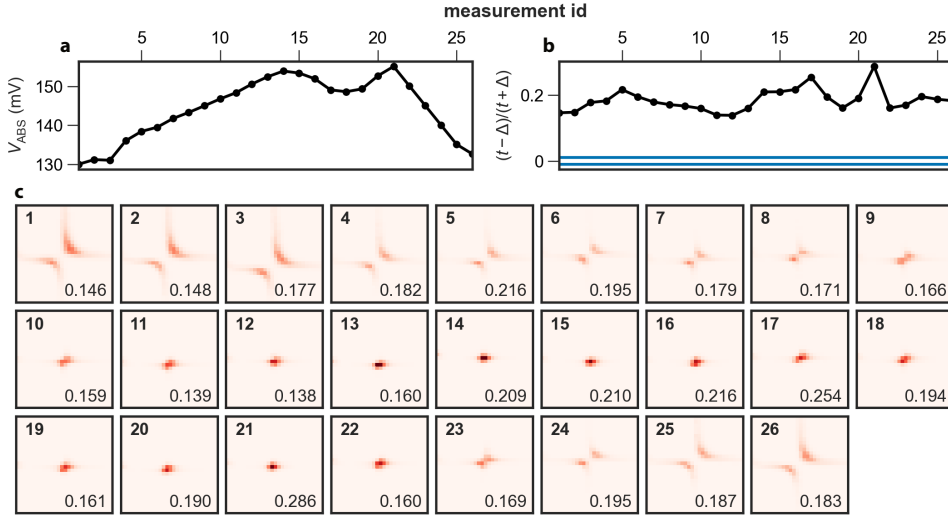


Figure 10: **Example of a non-converged automated tuning run.** **a.** The hybrid plunger gate voltage, V_{ABS} , for each measurement. **b.** Prediction of the weighted ratio of elastic co-tunneling and crossed Andreev reflection, $(t - \Delta)/(t + \Delta)$, for each measurement. The horizontal, blue lines indicate the tolerance set before the run. **c.** The product of the left and right differential conductance, $G_{\text{LL}} \cdot G_{\text{RR}}$, for varying V_{LP} and V_{RP} for subsequent measurements. The measurement ids are indicated by the bold text in the top left corner. The predicted value of $(t - \Delta)/(t + \Delta)$ is indicated in the bottom right corner.

REFERENCES

- [1] A Yu Kitaev. Unpaired majorana fermions in quantum wires. *Physics-uspekhi*, 44(10S):131, 2001.
- [2] Liang Fu and Charles L Kane. Superconducting proximity effect and majorana fermions at the surface of a topological insulator. *Physical review letters*, 100(9):096407, 2008.
- [3] A Yu Kitaev. Fault-tolerant quantum computation by anyons. *Annals of physics*, 303(1):2–30, 2003.
- [4] Ryan V Mishmash, Bela Bauer, Felix von Oppen, and Jason Alicea. Dephasing and leakage dynamics of noisy majorana-based qubits: Topological versus andreev. *Physical Review B*, 101(7):075404, 2020.
- [5] Christina Knapp, Torsten Karzig, Roman M Lutchyn, and Chetan Nayak. Dephasing of majorana-based qubits. *Physical Review B*, 97(12):125404, 2018.
- [6] Manuel J Schmidt, Diego Rainis, and Daniel Loss. Decoherence of majorana qubits by noisy gates. *Physical Review B*, 86(8):085414, 2012.
- [7] Christina Knapp, Michael Beverland, Dmitry I Pikulin, and Torsten Karzig. Modeling noise and error correction for majorana-based quantum computing. *Quantum*, 2:88, 2018.
- [8] Jay D Sau and S Das Sarma. Realizing a robust practical majorana chain in a quantum-dot-superconductor linear array. *Nature communications*, 3(1):964, 2012.
- [9] Ion C Fulga, Arbel Haim, Anton R Akhmerov, and Yuval Oreg. Adaptive tuning of majorana fermions in a quantum dot chain. *New journal of physics*, 15(4):045020, 2013.
- [10] Martin Leijnse and Karsten Flensberg. Parity qubits and poor man’s majorana bound states in double quantum dots. *Physical Review B*, 86(13):134528, 2012.
- [11] Tom Dvir, Guanzhong Wang, Nick van Loo, Chun-Xiao Liu, Grzegorz P Mazur, Alberto Bordin, Sebastiaan LD Ten Haaf, Ji-Yin Wang, David van Driel, Francesco Zatelli, et al. Realization of a minimal kitaev chain in coupled quantum dots. *Nature*, 614(7948):445–450, 2023.
- [12] Sebastiaan LD ten Haaf, Qingzhen Wang, A Mert Bozkurt, Chun-Xiao Liu, Ivan Kulesh, Philip Kim, Di Xiao, Candice Thomas, Michael J Manfra, Tom Dvir, et al. Engineering majorana bound states in coupled quantum dots in a two-dimensional electron gas. *arXiv preprint arXiv:2311.03208*, 2023.
- [13] Chun-Xiao Liu, Haining Pan, F Setiawan, Michael Wimmer, and Jay D Sau. Fusion protocol for majorana modes in coupled quantum dots. *Physical Review B*, 108(8):085437, 2023.
- [14] Péter Boross and András Pályi. Braiding-based quantum control of a Majorana qubit built from quantum dots, May 2023. arXiv:2305.08464 [cond-mat, physics:quant-ph] version: 1.

- [15] Athanasios Tsintzis, Rubén Seoane Souto, Karsten Flensberg, Jeroen Danon, and Martin Leijnse. Roadmap towards majorana qubits and nonabelian physics in quantum dot-based minimal kitaev chains. *arXiv preprint arXiv:2306.16289*, 2023.
- [16] Chun-Xiao Liu, Guanzhong Wang, Tom Dvir, and Michael Wimmer. Tunable superconducting coupling of quantum dots via andreev bound states in semiconductor-superconductor nanowires. *Physical review letters*, 129(26):267701, 2022.
- [17] Alberto Bordin, Guanzhong Wang, Chun-Xiao Liu, Sebastiaan LD Ten Haaf, Nick Van Loo, Grzegorz P Mazur, Di Xu, David Van Driel, Francesco Zatelli, Sasa Gazibegovic, et al. Tunable crossed andreev reflection and elastic cotunneling in hybrid nanowires. *Physical Review X*, 13(3):031031, 2023.
- [18] Francesco Zatelli, David van Driel, Di Xu, Guanzhong Wang, Chun-Xiao Liu, Alberto Bordin, Bart Roovers, Grzegorz P Mazur, Nick van Loo, Jan Cornelis Wolff, et al. Robust poor man’s majorana zero modes using yu-shiba-rusinov states. *arXiv preprint arXiv:2311.03193*, 2023.
- [19] Anna Dawid, Julian Arnold, Borja Requena, Alexander Gresch, Marcin Płodzień, Kaelan Donatella, Kim A Nicoli, Paolo Stornati, Rouven Koch, Miriam Büttner, et al. Modern applications of machine learning in quantum sciences. *arXiv preprint arXiv:2204.04198*, 2022.
- [20] Juan Carrasquilla. Machine learning for quantum matter. *Advances in Physics: X*, 5(1):1797528, January 2020.
- [21] Justyna P Zwolak, Jacob M Taylor, Reed Andrews, Jared Benson, Garnett Bryant, Donovan Buterakos, Anasua Chatterjee, Sankar Das Sarma, Mark A Eriksson, Eliška Greplová, et al. Data needs and challenges of quantum dot devices automation: Workshop report. *arXiv preprint arXiv:2312.14322*, 2023.
- [22] Florian Marquardt. Machine learning and quantum devices. *SciPost Phys. Lect. Notes*, page 29, 2021.
- [23] Justyna P Zwolak and Jacob M Taylor. Colloquium: Advances in automation of quantum dot devices control. *Reviews of modern physics*, 95(1):011006, 2023.
- [24] Renato Durrer, Benedikt Kratochwil, Jonne V Koski, Andreas J Landig, Christian Reichl, Werner Wegscheider, Thomas Ihn, and Eliska Greplova. Automated tuning of double quantum dots into specific charge states using neural networks. *Physical Review Applied*, 13(5):054019, 2020.
- [25] Jonas Schuff, Miguel J Carballido, Madeleine Kotzagiannidis, Juan Carlos Calvo, Marco Caselli, Jacob Rawling, David L Craig, Barnaby van Straaten, Brandon Severin, Federico Fedele, et al. Fully autonomous tuning of a spin qubit. *arXiv preprint arXiv:2402.03931*, 2024.
- [26] Justyna P Zwolak, Thomas McJunkin, Sandesh S Kalantre, JP Dodson, ER MacQuarrie, DE Savage, MG Lagally, SN Coppersmith, Mark A Eriksson, and Jacob M Taylor.

- Autotuning of double-dot devices in situ with machine learning. *Physical review applied*, 13(3):034075, 2020.
- [27] Sandesh S Kalantre, Justyna P Zwolak, Stephen Ragole, Xingyao Wu, Neil M Zimmerman, MD Stewart Jr, and Jacob M Taylor. Machine learning techniques for state recognition and auto-tuning in quantum dots. *npj Quantum Information*, 5(1):6, 2019.
 - [28] Dominic T Lennon, Hyungil Moon, Leon C Camenzind, Liuqi Yu, Dominik M Zumbühl, G Andrew D Briggs, Michael A Osborne, Edward A Laird, and Natalia Ares. Efficiently measuring a quantum device using machine learning. *npj Quantum Information*, 5(1):79, 2019.
 - [29] V Nguyen, SB Orbell, Dominic T Lennon, Hyungil Moon, Florian Vigneau, Leon C Camenzind, Liuqi Yu, Dominik M Zumbühl, G Andrew D Briggs, Michael A Osborne, et al. Deep reinforcement learning for efficient measurement of quantum devices. *npj Quantum Information*, 7(1):100, 2021.
 - [30] Jana Darulová, SJ Pauka, Nathan Wiebe, Kok W Chan, GC Gardener, Michael J Manfra, Maja C Cassidy, and Matthias Troyer. Autonomous tuning and charge-state detection of gate-defined quantum dots. *Physical Review Applied*, 13(5):054005, 2020.
 - [31] Stefanie Czischek, Victor Yon, Marc-Antoine Genest, Marc-Antoine Roux, Sophie Rochette, Julien Camirand Lemyre, Mathieu Moras, Michel Pioro-Ladrière, Dominique Drouin, Yann Beilliard, et al. Miniaturizing neural networks for charge state autotuning in quantum dots. *Machine Learning: Science and Technology*, 3(1):015001, 2021.
 - [32] Matthias Thamm and Bernd Rosenow. Conductance based machine learning of optimal gate voltages for disordered majorana wires. *Physical Review B*, 109(4):045132, 2024.
 - [33] X. Turkeshi, T. Mendes-Santos, G. Giudici, and M. Dalmonte. Entanglement-guided search for parent hamiltonians. *Physical Review Letters*, 122(15), April 2019.
 - [34] Eyal Bairey, Itai Arad, and Netanel H. Lindner. Learning a local hamiltonian from local measurements. *Physical Review Letters*, 122(2), January 2019.
 - [35] Agnes Valenti, Guliuxin Jin, Julian Léonard, Sebastian D. Huber, and Eliska Greplova. Scalable hamiltonian learning for large-scale out-of-equilibrium quantum dynamics. *Physical Review A*, 105(2), February 2022.
 - [36] Netta Karjalainen, Zina Lippo, Guangze Chen, Rouven Koch, Adolfo O. Fumega, and Jose L. Lado. Hamiltonian inference from dynamical excitations in confined quantum magnets. *Physical Review Applied*, 20(2), August 2023.
 - [37] Maryam Khosravian, Rouven Koch, and Jose L Lado. Hamiltonian learning with real-space impurity tomography in topological moiré superconductors. *Journal of Physics: Materials*, 7(1):015012, January 2024.

- [38] Jozef Bucko, Frank Schäfer, František Herman, Rebekka Garreis, Chuyao Tong, Annika Kurzmann, Thomas Ihn, and Eliska Greplova. Automated reconstruction of bound states in bilayer graphene quantum dots. *Physical Review Applied*, 19(2):024015, 2023.
- [39] Rouven Koch, David Van Driel, Alberto Bordin, Jose L Lado, and Eliska Greplova. Adversarial hamiltonian learning of quantum dots in a minimal kitaev chain. *Physical Review Applied*, 20(4):044081, 2023.
- [40] Sebastian Heedt, Marina Quintero-Pérez, Francesco Borsoi, Alexandra Fursina, Nick van Loo, Grzegorz P. Mazur, Michał P. Nowak, Mark Ammerlaan, Kongyi Li, Svetlana Korneychuk, Jie Shen, May An Y. van de Poll, Ghada Badawy, Sasa Gazibegovic, Nick de Jong, Pavel Aseev, Kevin van Hoogdalem, Erik P. A. M. Bakkers, and Leo P. Kouwenhoven. Shadow-wall lithography of ballistic superconductor–semiconductor quantum devices. *Nature Communications*, 12(1):4914, August 2021. Number: 1 Publisher: Nature Publishing Group.
- [41] David van Driel, Guanzhong Wang, Alberto Bordin, Nick van Loo, Francesco Zatelli, Grzegorz P. Mazur, Di Xu, Sasa Gazibegovic, Ghada Badawi, Erik P. A. M. Bakkers, Leo P. Kouwenhoven, and Tom Dvir. Spin-filtered measurements of Andreev bound states, December 2022. arXiv:2212.10241 [cond-mat].
- [42] GC Ménard, GLR Anselmetti, EA Martinez, D Puglia, FK Malinowski, JS Lee, S Choi, M Pendharkar, CJ Palmstrøm, K Flensberg, et al. Conductance-matrix symmetries of a three-terminal hybrid device. *Physical Review Letters*, 124(3):036802, 2020.
- [43] Anders Jellinggaard, Kasper Grove-Rasmussen, Morten Hannibal Madsen, and Jesper Nygård. Tuning yu-shiba-rusinov states in a quantum dot. *Physical Review B*, 94(6):064520, 2016.
- [44] YU LUH. Bound state in superconductors with paramagnetic impurities. *Acta Physica Sinica*, 21(1):75, 1965.
- [45] Hiroyuki Shiba. Classical spins in superconductors. *Progress of Theoretical Physics*, 40(3):435–451, September 1968.
- [46] AI Rusinov. Theory of gapless superconductivity in alloys containing paramagnetic impurities. *Sov. Phys. JETP*, 29(6):1101–1106, 1969.
- [47] A. M. Bozkurt. Poor man’s strong zero modes in interacting quantum dot chains [forthcoming]. *arxiv*, 7(1):100, 2021.
- [48] T J Christiansen and M Zworski. A mathematical formulation of the mahaux–weidenmüller formula for the scattering matrix. *Journal of Physics A: Mathematical and Theoretical*, 42(41):415202, September 2009.
- [49] Christian M. Möhle, Prasanna K. Rout, Nayan A. Jainandunsing, Dibyendu Kuri, Chung Ting Ke, Di Xiao, Candice Thomas, Michael J. Manfra, Michał P. Nowak, and Srijit Goswami. Controlling Andreev bound states with the magnetic vector potential. *Nano Letters*, 22(21):8601–8607, 2022.

- [50] Léon Bottou. Stochastic gradient descent tricks. In *Neural Networks: Tricks of the Trade: Second Edition*, pages 421–436. Springer, 2012.
- [51] Ji-Yin Wang, Nick Van Loo, Grzegorz P Mazur, Vukan Levajac, Filip K Malinowski, Mathilde Lemang, Francesco Borsoi, Ghada Badawy, Sasa Gazibegovic, Erik PAM Bakkers, et al. Parametric exploration of zero-energy modes in three-terminal insb-al nanowire devices. *Physical Review B*, 106(7):075306, 2022.
- [52] Hyungil Moon, Dominic T Lennon, James Kirkpatrick, Nina M van Esbroeck, Leon C Camenzind, Liuqi Yu, Florian Vigneau, Dominik M Zumbühl, G Andrew D Briggs, Michael A Osborne, et al. Machine learning enables completely automatic tuning of a quantum device faster than human experts. *Nature communications*, 11(1):4161, 2020.
- [53] Zewen Li, Fan Liu, Wenjie Yang, Shouheng Peng, and Jun Zhou. A survey of convolutional neural networks: Analysis, applications, and prospects. *IEEE Transactions on Neural Networks and Learning Systems*, 33(12):6999–7019, December 2022.
- [54] Keiron O’Shea and Ryan Nash. An introduction to convolutional neural networks, 2015.
- [55] Naila Murray and Florent Perronnin. Generalized max pooling. In *Proceedings of the IEEE Conference on Computer Vision and Pattern Recognition (CVPR)*, June 2014.
- [56] Chun-Xiao Liu, A Mert Bozkurt, Francesco Zatelli, Sebastiaan LD ten Haaf, Tom Dvir, and Michael Wimmer. Enhancing the excitation gap of a quantum-dot-based kitaev chain. *arXiv preprint arXiv:2310.09106*, 2023.
- [57] Chun-Xiao Liu, Guanzhong Wang, Tom Dvir, and Michael Wimmer. Tunable superconducting coupling of quantum dots via andreev bound states in semiconductor-superconductor nanowires. *Physical Review Letters*, 129(26), December 2022.
- [58] Athanasios Tsintzis, Rubén Seoane Souto, and Martin Leijnse. Creating and detecting poor man’s majorana bound states in interacting quantum dots. *Physical Review B*, 106(20), November 2022.
- [59] Fernando Domínguez and Alfredo Levy Yeyati. Quantum interference in a cooper pair splitter: The three sites model. *Physica E: Low-dimensional Systems and Nanostructures*, 75:322–329, January 2016.
- [60] Léon Bottou. *Large-Scale Machine Learning with Stochastic Gradient Descent*, page 177–186. Physica-Verlag HD, 2010.
- [61] Rubén Seoane Souto, Athanasios Tsintzis, Martin Leijnse, and Jeroen Danon. Probing majorana localization in minimal kitaev chains through a quantum dot. *Physical Review Research*, 5(4):043182, 2023.

7

CONCLUSIONS AND OUTLOOK

Once in a while, you get shown the light in the strangest of places if you look at it right.

- The Grateful Dead

Most of the work in this thesis is dedicated to quantum dots (QDs) coupled to Andreev bound states (ABSs) in semiconductor-superconductor hybrids. These can be capacitively coupled, to allow for charge sensing of ABSs. The QDs can be weakly tunnel-coupled to allow for spin-filtered spectroscopy of ABSs. When the coupling is intermediate for multiple QDs coupled to the same ABS, a Kitaev chain can be realized based on elastic co-tunneling and crossed Andreev reflection processes. When one QD is strongly coupled to an ABS, a minimal Kitaev chain can be implemented through direct spin-conserving, and flipping transport processes. The tunability of semiconductors allows for the engineering of Kitaev chains in many geometries. Here, we propose a single, flexible platform for researching Kitaev chains.

7.1 EXTENDING KITAEV CHAINS WITH A SINGLE SUPERCONDUCTOR

A minimal Kitaev chains consists of two quantum dots (QDs) that are coupled by crossed Andreev reflection (CAR), indicated by Δ and elastic co-tunneling (ECT), indicated by t . These two transport processes are mediated by Andreev bound states (ABSs) that couple the QDs. At $t = \Delta$, the chain is in a sweet spot, and separated Majorana zero modes (MZMs) emerge on each of the two QDs. Adding more QDs and ABSs to the chain improves the robustness of the MZMs to electrostatic perturbations, if the condition $t = \Delta$ is satisfied between each pair of QDs. The chain can be expanded by adding QDs and interleaving each pair of QDs by a semiconductor-superconductor segment which hosts an ABS that mediates ECT and CAR. However, a phase difference between each pair of superconductors results in a phase differences between the tunneling phases of t and Δ of different pairs of QDs [1]. If this tunneling phase difference is π between two pairs of QDs, the tunneling rates in the sweet spot between QDs 1 and 2, and 2 and 3 become:

$$\begin{aligned} t_{12} &= \Delta_{12} \\ t_{23} &= -\Delta_{23} \end{aligned}$$

Which results in a gapless bulk that decreases the isolation of the MZMs at the system ends. When the phase is not fixed, it can change over time, resulting in a time-average of 0-, and π -junctions [2]. While the stability of a zero-energy state is maintained, a changing phase is a potential source of dephasing for a Kitaev chain. One can fix the phase by threading a flux through a loop connecting the superconductors. However, the need to fix the phase externally can be obviated by having a single, bulk superconductor that couples to all QDs. The superconductor can be phase-coherent over its entire length, which prevents phase factors from appearing in the ECT and CAR rates. In s-wave superconductors such as Al, the penetration depth is lower than the coherence length. This means that the gap is small compared to the superfluid stiffness, which sets the energy cost of spatial variations of the phase [3]. As this cost is very high in Al, we expect to be able to extend the superconductor to accommodate as many QDs as desired.

An example geometry of a multi-site Kitaev chain with a single superconductor is sketched in figure 1a. Here, four tunnel gates are used to confine three QDs in the semiconductor. Three gates are used to tune their coupling to the superconductor, denoted by

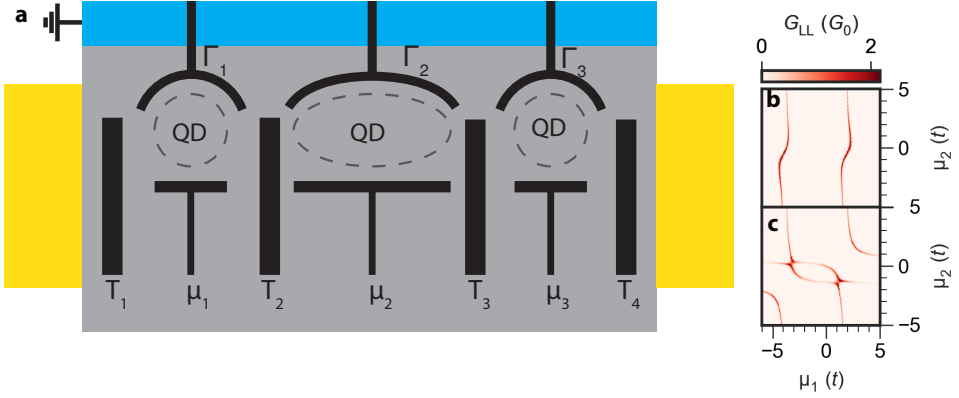


Figure 1: **Extending Kitaev chains with a single superconductor.** **a.** Top view schematic of a semiconductor (gray) coupled to a grounded superconductor (blue). Top gates (black) are used to confine quantum dots (QDs) and tune their coupling. Normal leads (yellow) can be used to measure differential conductance. **b.** Simulated conductance of the left lead, G_{LL} , for varying chemical potential of the left and middle QDs, $\mu_{1,2}$. Here, the middle QD is strongly coupled to the superconductor and does not have an odd parity ground state. **c.** G_{LL} for varying μ_1 and μ_2 . Here, the middle QD is less strongly coupled to the superconductor, meaning its levels cross zero.

Γ_i . Finally, the electrochemical potential of each QD (μ_i) can be tuned using three plunger gates. The middle, extended QD can then be operated as either a coupler or a direct part of the Kitaev chain. If its coupling is stronger than the charging energy, $\Gamma_2 > 2E_C$, the middle QD levels do not cross zero-energy in the absence of magnetic field. Its virtual occupation can then be used to mediate ECT and CAR between QD 1 and 2. A charge stability diagram of QD1 and QD2 in the limit of $\Gamma_2 \gtrsim 2E_C$ is shown in figure 1b, that was computed using the model provided in Ref. [4]. Here, we see the “S-shapes” that are characteristic of QD levels coupling to an ABS. When similar S-shapes are observed between the middle and right QDs, the system can be tuned to a sweet spot between the left and right QDs under the correct conditions.

For $\Gamma_2 < 2E_C$, the middle QD levels cross zero-energy in the absence of field, and it becomes a site in the chain. We show a charge stability diagram of the left and middle QDs in figure 1c. Here, we see an anti-diagonal avoided crossing of the levels, which is associated with a dominant coupling of the odd states. The ratio of the even and odd couplings can be tuned by varying $\Gamma_{1,2}$, the external magnetic field, or T_2 [4]. The curvature in the levels of the middle QD originates from its strong coupling to the superconductor.

The device of figure 1a can be extended by adding more gates that define T , Γ and μ between neighboring QDs. More tunnel probes can also be added to probe each QD, which assists the tuning up of the system. The condition $t = \Delta$ can then be satisfied between each pair of QDs using electrostatic gates. We note that this can also be performed automatically using machine learning, as detailed in chapter 6. An extended version of this system is comparable to the ABS chain of Fulga et al. and Samuelson et al. [1, 5] without phase differences, the QD-ABS-QD chain of Miles et al. [4] with on-site pairing of the QDs, or a discrete implementation of the Lutchyn-Oreg model [6, 7]. A comparison to the latter is especially interesting, as the Lutchyn-Oreg implementation prescribes the need for only

a single gate controlling the global electrochemical potential of the hybrid segment. The spatial differences of the gate voltages required to tune the device of figure 1a into a global sweet spot reveal the amount of disorder in the system.

7.2 BEYOND III-V SEMICONDUCTORS

The system of figure 1a can be implemented in two-dimensional III-V semiconductors, such as InAs/InSb, coupled to an s-wave superconductor. However, another option is to implement it in a two-dimensional hole gas (2DHG) such as germanium. This material can be isotopically purified, has strong spin-orbit interaction, low effective mass and is being used successfully in quantum information experiments. Germanium-superconductor hybrids have been studied experimentally and theoretically before. Laubscher et al. proposed germanium hole nanowires as a platform for realizing the Lutchyn-Oreg model [8]. Tossato et al. found that superconductivity could be induced in germanium using diffused superconductors [9]. Lakič et al. demonstrated that germanium hole QDs can host sub-gap states by coupling to superconductors [10]. Finally, Schwarze and Flensberg explored the possibility of coupling two QDs through a superconductor to form a two-site Kitaev chain [11]. We suggest adapting the device geometry of figure 1a to Ge/SiGe planar heterostructures.

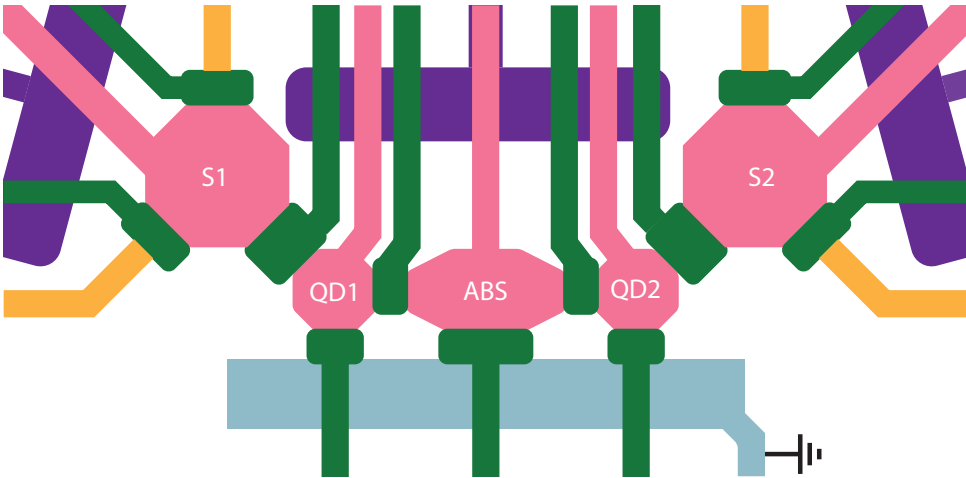


Figure 2: **A minimal Kitaev chain with parity readout in Germanium.** Top view schematic of a two-site Kitaev chain device fabricated on a Ge/SiGe planar heterostructure. Screening gates are purple, plunger gates are pink, and tunnel gates are green. The yellow lines indicate ohmic contacts, the grounded superconductor is indicated in light blue. The quantum well is buried beneath a top layer of SiGe and gate dielectric.

Germanium can be confined into a 2DHG by encapsulating it in two SiGe barrier layers. The resulting strain from the lattice mismatch lowers the effective mass of the germanium quantum well and splits the heavy hole and light hole bands in energy [12]. The top SiGe layer separates the 2DHG from the surface of the heterostructure, which can greatly improve its charge noise [13]. As charge noise is expected to be the biggest source of decoherence in Kitaev chain-based qubits, removing this top layer is detrimental to the coherence time [14]. This provides a challenge for interfacing the 2DHG with a

superconductor, as directly contacting it using ion milling or hydrogen cleaning removes the top barrier. Depositing a superconductor on top of the 2DHG might affect the compressive strain which results from a carefully engineered SiGe layer. Furthermore, it removes the possibility of tuning the coupling to the superconductor using an electrostatic gate. We therefore propose to proximitize the 2DHG from the side, as shown in the device sketched in figure 2. This sketch is based on the design of a 2×4 Ge/SiGe QD array, see Ref. [15]. The pink plunger gates are used to define QDs in the quantum well below the top SiGe layer. The green tunnel gates can tune the coupling between the QDs and other parts of the system. The purple screening gates prevent the accumulation of holes beneath the gate electrodes close to the QDs. The elongated plunger gate in the middle of figure 2 is used to confine an ABS that couples the two neighboring QDs. This ABS can be strongly coupled to the grounded superconductor by accumulating holes using the tunnel gate between the two.

We note that the electronic g -factor is highly anisotropic for Ge/SiGe heterostructures, with in-plane values of $g_{\parallel} < 1$ and out-of-plane values of $g_{\perp} > 10$ [12]. As the Kitaev chain is based on spin-polarized QDs, the large out-of-plane g -factor motivates applying an external magnetic field along it. However, due to the large surface area of evaporated thin-film superconductors, the parent gap will close at low fields due to orbital depairing. If the field is applied in-plane instead, large fields are required obtain a substantial Zeeman splitting. However, common metallic superconductors such as Al have a g -factor of 2 [16]. This implies that the superconducting parent gap will close at lower fields than the ABS and QD states can Zeeman split at. This can potentially be circumvented by covering the superconductor in heavy atoms that cause spin-mixing, such as Pt [17]. However, we propose to use a thin strip of a diffused germanosilicide superconductor that also allows the 2DHG to remain buried as discussed above. As the lateral extent of the strip is small, the superconductor has a low cross-section with an out-of-plane field. This suppresses orbital depairing and can increase the critical magnetic field [17]. Finally, we note that the g factor anisotropy of Ge/SiGe QDs can be tuned by changing their shape [18]. This was suggested in the original two-site Kitaev chain proposal, as having non-collinear spin quantization axes helps in engineering the two coupling magnitudes [19].

We have proposed an implementation of a two-site Kitaev chain in Ge/SiGe planar heterostructures. This implementation benefits from the existing expertise in fabricating QD arrays in this material platform. Charge noise has been minimized in these systems to reduce the decoherence in spin qubit experiments [20]. As charge noise is expected to be the main source of decoherence in Kitaev chains, Ge/SiGe could be a good platform for these systems as well. While the large g -factor of III-V semiconductors is superior, engineering of the superconductor in Ge/SiGe heterostructures might compensate for the material's lower g -factor.

7.3 TUNING A MINIMAL KITAEV CHAIN WITHOUT NORMAL LEADS

As the device in figure 2 does not have normal leads coupled to the QDs forming the Kitaev chain, it cannot be tuned up using transport measurements. The charge sensors S1 and S2 can however be used to tune the device based on the charge of QD1 and QD2. We propose

to weakly tunnel couple S1 to QD1, such that it acts as a connection to an electron reservoir. Then, S2 can be used to charge sense QD2 for tuning up. In figure 3a, we show a charge stability that was computed using the model introduced in Ref. [21]. Here, we plot the global fermion parity of the ground state. We see three avoided crossings that arise from elastic co-tunneling and crossed Andreev reflection involving the ABS. Finally, there is a crossing in the bottom left corner of figure 3a, indicated by a dashed, orange circle. While crossing QD levels usually indicate a lack of tunnel coupling in a double QD, here they are a result of equal elastic co-tunneling and crossed Andreev reflection rates.

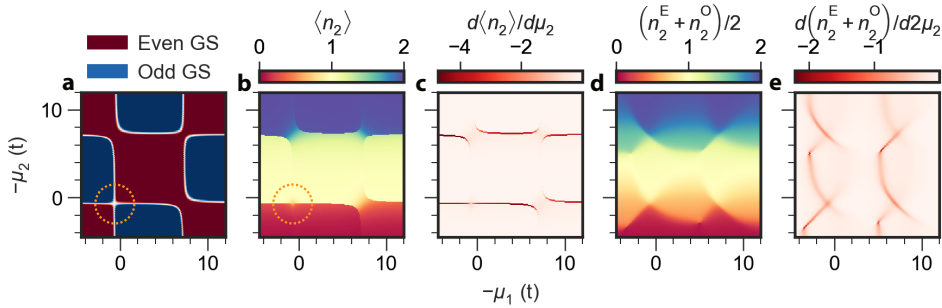


Figure 3: Differential charge sensing a QD-ABS-QD system. **a.** Ground state parity for varying electrochemical potential of the left QD μ_1 and the right QD μ_2 . The superimposed orange, dashed circle highlights a sweet spot. **b.** Charge expectation value of the right QD, $\langle n_2 \rangle$, for varying μ_1 and μ_2 . The superimposed orange, dashed circle highlights a sweet spot. **c.** Differential charge expectation value of the right QD $d\langle n_2 \rangle / d\mu_2$ for varying μ_1 and μ_2 . **d.** Parity-averaged charge expectation value of the right QD, $(n_2^E + n_2^O)/2$, for varying μ_1 and μ_2 . Here, $n_2^E = \langle E | n_2 | E \rangle$ and $n_2^O = \langle O | n_2 | O \rangle$, where E and O are the lowest-energy even and odd states respectively. **e.** Differential charge expectation value of the right QD, averaged over parity, $d(n_2^E + n_2^O) / d\mu_2$, for varying μ_1 and μ_2 .

In figure 3b, we show the ground state charge expectation value of QD2, $\langle n_2 \rangle$. When QD1 is off-resonance, the charge changes abruptly around the charge degeneracy points of QD2. When QD1 is on-resonance, the two QDs hybridize and the charge changes gradually. We see that there is a small region where $\langle n_2 \rangle = 1/2$, as highlighted by the dashed, orange circle. This is the signature of the two-site Kitaev chain sweet spot, where the crossed Andreev reflection and elastic co-tunneling rates are equal and both QDs are at the Fermi level.

In figure 3c, we show the differential charge of QD2. Here, we obtain a finite signal at points of μ_2 where $\langle n_2 \rangle$ changes abruptly due to a change of μ_{QD}^R . As charge sensor S2 in Figure 2 has two normal leads, a differential conductance measurement can be performed, which probes the differential charge. Alternatively, $d\langle n_2 \rangle / d\mu_2$ can be probed directly using gate sensing measurements [22]. This can be done by attaching a resonator to the plunger gate of QD2, which can measure capacitive shifts due to the quantum capacitance of the double QD. A switch in the orientation of the avoided crossing signals a change from even, to odd-dominated coupling of the QDs. Furthermore, the differential charge vanishes at the sweet spot considering $d\langle n_2 \rangle / d\mu_2 = 0$ [19].

Once a sweet spot is reached, S1 has to be decoupled from QD1, as it serves as an electron reservoir that effectively poisons the parity of the Kitaev chain. In this case, the system is not coupled to any normal leads anymore and its parity can only be changed

by quasiparticle poisoning from the superconductor. When the system is connected to a normal lead, the Fermi-Dirac distribution of the metal forces the system to remain in the ground state for the majority of the time. When quasiparticle poisoning is the only mechanism that flips parity, this is not necessarily true. The charge sensor signal will then depend on the fraction of time spent in each charge state [23]. A measurement that is longer than the quasiparticle poisoning time will measure the charge averaged over the even-, and odd-parity states. While the exact dynamics of quasiparticle poisoning are hard to model, we approximate the time spent in the even and odd states as being equal, and write the average measured charge, Q_{avg} as:

$$-\frac{Q_{\text{avg}}}{e} = \frac{n_2^E + n_2^O}{2} = \frac{\langle E|n_2|E \rangle + \langle O|n_2|O \rangle}{2}$$

We show this parity-averaged charge expectation value, $(n_2^E + n_2^O)/2$, in figure 3d. We note that the charge stability diagram looks significantly different from the one shown in panel b. Notably, the gradual change of charge, together with an avoided crossing is no longer observable in figure 3d. As a result, it is hard to distinguish which of the avoided crossings corresponds to a sweet spot.

In figure 3e, we show the differential parity-averaged charge of QD2. Here, finite signal is no longer associated with a degenerate even-odd state. Instead, we see four lines that intersect pairwise each time QD1 and QD2 are both on resonance. We note that the relative amplitude of each pair of lines seems to be related to the dominant type of interaction. However, it is not easy to recognize which of the four resonances corresponds to a sweet spot. Ideally, one would measure a single quantity that can be used to identify both $t = \Delta$, and distinguish the ground state parity.

7

7.4 READING OUT PARITY USING NON-LOCAL QUANTUM CAPACITANCE

In a two-site Kitaev chain, we can detune one QD without splitting the zero-energy state. The wave function will redistribute across the system due to detuning. When varying the electrochemical potential of the right QD, μ_2 for $\mu_1 = 0$, the even and odd ground states have the same local charge expectation value: $\langle E|n_2|E \rangle = \langle O|n_2|O \rangle$. Detuning the right QD does result in a parity-dependent charge expectation value for the left QD: $\langle E|n_1|E \rangle \neq \langle O|n_1|O \rangle$ (see section 2.4.4 for details). We can capture this effect by defining the non-local quantum capacitance, $C_q^{\text{NL}} = d\langle n_1 \rangle / d\mu_2$. For convenience, we will consider a two-site Kitaev chain based on normal QDs (see section 2.4.1 for details). We fix the electrochemical potential of the left QD at the Fermi level ($\mu_1 = 0$) and limit ourselves to weak detuning of the right QD ($\mu_2 \ll 2t$). Then, we can approximate the non-local quantum capacitance as:

$$C_q^{\text{NL}} = \left. \frac{d\langle n_1 \rangle}{d\mu_2} \right|_{\mu_1=\mu_2=0} = \frac{P}{4} = \frac{1}{4} \begin{cases} -\frac{1}{\Delta} & \text{even GS} \\ \frac{1}{t} & \text{odd GS} \end{cases}$$

Where Δ is the crossed Andreev reflection (CAR) rate and t is the elastic co-tunneling (ECT) rate. P is a parity-dependent factor stemming from the (anti)-symmetric response of the left QD charge due to a change in charge of the right QD. C_q^{NL} can be estimated by

measuring a charge stability diagram using a charge sensor, and performing a numerical derivative along the non-sensed QD: $dQ_1/d\mu_2$. However, C_q^{NL} can be measured directly using differential charge sensing. In figure 4a, we show a sketch of a measurement setup that can be used to measure C_q^{NL} , based on the device described in section 7.2.

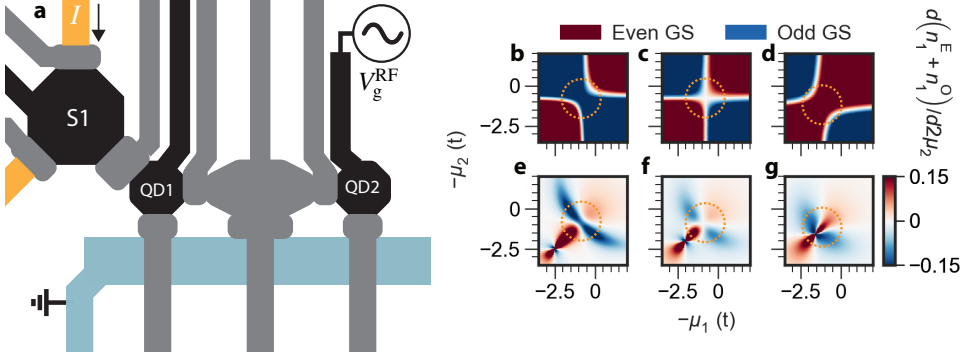


Figure 4: **Reading out parity using the non-local quantum capacitance.** **a.** Top view schematic of a two-site Kitaev chain device fabricated on a Ge/SiGe planar heterostructure. The yellow lines indicate ohmic contacts, the grounded superconductor is indicated in light blue. An RF gate voltage is applied to QD2 while the current, I , through charge sensor S1 is measured. **b-d.** Ground state parity for varying electrochemical of the left QD μ_1 and the right QD μ_2 . These were computed for different energies of the Andreev bound state that mediates elastic co-tunneling and crossed Andreev reflection. The superimposed orange, dashed circles highlight the center of the (avoided) crossings. **e-g.** Non-local quantum capacitance averaged over parity, $d(n_1^E + n_1^O)/d\mu_2$, for varying μ_1 and μ_2 . The superimposed orange, dashed circles highlight the center of the (avoided) crossings.

Here, we apply an RF voltage to the plunger gate of QD2: $V_g = V_g^0 + V_g^{\text{RF}} \sin(\omega t)$, where V_g^0 is the constant gate voltage, V_g^{RF} is the RF voltage amplitude and ω is the angular frequency. The effect of the gate voltage on $\langle n_1 \rangle$ can be written as:

$$\frac{d\langle n_1 \rangle}{dV_g} = \frac{d\langle n_1 \rangle}{d\mu_2} \frac{d\mu_2}{dV_g} = -e\alpha C_q^{\text{NL}}$$

Where α is the lever arm of the plunger gate of QD2. We can apply a voltage bias to the normal leads of S1, which results in a current I running through the sensor. We assume that the plunger gate voltage of S1 is chosen such that the electrochemical potential corresponds to the linear slope of a Coulomb resonance. As QD1 effectively gates S1, we can roughly approximate the effect on the current as: $I \propto -C_m \langle n_1 \rangle$, where C_m is the mutual capacitance. We can then demodulate the measured current, I , with the V_g^{RF} signal using a lock-in amplifier to obtain the differential conductance:

$$G \propto \frac{dI}{dV_g} = -C_m \frac{d\langle n_1 \rangle}{dV_g} = e\alpha C_m C_q^{\text{NL}}$$

G is then directly proportional to C_q^{NL} , resulting in a parity-dependent conductance of S1.

In figure 4b-d, we show the ground state parity of the system sketched in panel a, that was computed using the model introduced in Ref. [21]. The energy of the ABS is varied between the plots, which tunes the relative rates of ECT and CAR. These rates are equal in

figure 4c, which corresponds to a sweet spot. In figure 4e-g we show C_q^{NL} averaged over the parity:

$$\bar{C}_q^{\text{NL}} = \frac{d(n_1^{\text{E}} + n_1^{\text{O}})}{2d\mu_2} = \frac{d(\langle E|n_1|E\rangle + \langle O|n_1|O\rangle)}{2d\mu_2}$$

At $\mu_1 = \mu_2 = 0$, this reduces to $\bar{C}_q^{\text{NL}} = (\Delta - t)/(8\Delta t)$. We see that \bar{C}_q^{NL} is negative at the center of the avoided crossing in figure 4e. This correctly indicates that $t > \Delta$, as seen from the direction of the avoided crossing in figure 4b. In figure 4g, \bar{C}_q^{NL} is positive, which is consistent with the diagonal avoided crossing seen in figure 4d. In figure 4f, we see that $\bar{C}_q^{\text{NL}} = 0$ in a cross-shaped region close to $\mu_1 = \mu_2 = 0$. The non-local quantum capacitance of the even and odd states is equal and opposite here, which causes the average to cancel. If $d\langle n_1 \rangle / dV_g$ is measured faster than the quasiparticle poisoning time, the parity can be inferred from measurements of C_q^{NL} . This implies that parity readout can be performed at $\mu_1 = \mu_2 = 0$, at which point the zero-energy state is most robust to charge noise. In contrast, reading out the parity using a charge sensor requires detuning at least one QD (see section 2.4.4). The advantages of the present method are threefold. First, it can be used for tuning a Kitaev chain into the sweet spot without normal leads by measuring slower than quasiparticle poisoning. Second, it can read out the parity of the two-site Kitaev chain by measuring faster than quasiparticle poisoning. Third, it does not require any voltage pulses, as the SNR is highest for $\mu_1 = \mu_2 = 0$, where $d\langle n_1 \rangle / d\mu_2$ is maximal.

To recognize a sweet spot based on \bar{C}_q^{NL} , it is crucial for the charge sensor response to be linear. If S1 is tuned close to Coulomb blockade, a chemical potential shift in one direction will not result in a significant change in response. A shift in the other direction brings S1 closer to Coulomb resonance, which results in a larger change of I . Averaging over parity does not result in $\bar{C}_q^{\text{NL}} = 0$ then. We demonstrated how to read out the non-local capacitance using a single-electron transistor for convenience, as it does not require readout resonators. In one-dimensional nanowires, experimentalists are often limited to using a single-lead charge sensor or “single-electron box” (SEB). In this case, the measured quantity is the reflected amplitude or phase of the SEB. Predicting the response of \bar{C}_q^{NL} is more challenging in this case, as there is now a readout signal on the SEB as well as a drive signal on QD2. Effectively, this becomes a two-tone measurement, as the RF gate voltage changes the reflected amplitude and phase of the SEB over time [24]. Modeling the full time dependence is challenging, as it also depends on the exact relaxation processes of the SEB. We hypothesize that driving the SEB with an angular frequency ω_0 may result in signal resonances at $\omega_0 \pm \omega$, where, ω is the angular frequency of the RF gate voltage of QD2. If ω is lower than the bandwidth of the readout resonator of the SEB, the mixed signal can be detected using reflectometry measurements. This relies on wave-mixing in the system, which we have not investigated presently.

7.5 YU-SHIBA-RUSINOV SINGLET-TRIPLET QUBITS

In section 2.2.3, we discussed the formation of zero-bandwidth Yu-Shiba-Rusinov (ZBW-YSR) states on a QD coupled to a single superconducting orbital. We concluded that the system’s two-electron states resemble those of double QDs [25]. In both systems, singlet and triplet states can be formed by the hybridization of spatially-separated spins. Qubit states have been encoded into these singlet and triplet states in double QDs [26]. In this section,

we explore the possibility of extending singlet-triplet qubits to YSR states. In these states, a single spin in a QD is screened by a screening cloud in a bulk superconductor [27]. This implies that the QD spin can form a singlet or triplet with quasiparticles in a superconductor. A nuclear field in either the QD or the superconductor could then cause coherent singlet-triplet oscillations, as it does for double QDs [28]. Observing the YSR singlet state evolve into a triplet is then a direct confirmation of a screening cloud in the superconductor. If there is no singlet-triplet mixing, there is no screening cloud, which indicates a BCS singlet ground state.

To model the system, we use the perturbative zero-bandwidth Hamiltonian defined in equation (2.25). We then consider all even-parity states that do not include the high-energy $|S_+\rangle$ state of the superconductor and write the states in the $|N_{\text{QD}}, N_{\text{SC}}\rangle$ basis:

$$\{|0, S\rangle, |2, S\rangle, |\uparrow, \downarrow\rangle, |\downarrow, \uparrow\rangle, |\uparrow, \uparrow\rangle, |\downarrow, \downarrow\rangle\}$$

Here, $|S\rangle = u|0\rangle - v|2\rangle$ is the BCS singlet state of the superconducting orbital. We now include a Zeeman energy, E_Z , on both the QD and the superconducting orbital and transform the basis to account for exchange coupling:

$$\{|0, S\rangle, S(1, 1), |2, S\rangle, T_- = |\downarrow, \downarrow\rangle, T_0, T_+ = |\uparrow, \uparrow\rangle\}$$

We obtain exchange-coupled singlet and triplet states, with a single electron in the QD, and a single quasiparticle in the superconductor:

$$\begin{aligned} S(1, 1) &= \frac{1}{\sqrt{2}}(|\downarrow, \uparrow\rangle - |\uparrow, \downarrow\rangle) & E_S &= \mu - 2J \\ T_0 &= \frac{1}{\sqrt{2}}(|\downarrow, \uparrow\rangle + |\uparrow, \downarrow\rangle) & E_{T_0} &= \mu \end{aligned} \quad (7.1)$$

As these are the single-orbital equivalent of YSR states, we shall refer to them as zero-bandwidth YSR (ZBW-YSR) states. We then write the Hamiltonian as:

$$H_{\text{ST}} = \begin{bmatrix} -\Delta & -t & 0 & 0 & 0 & 0 \\ -t & \mu - 2J & t & 0 & 0 & 0 \\ 0 & t & E_C - \Delta + 2\mu & 0 & 0 & 0 \\ 0 & 0 & 0 & -2E_Z + \mu & 0 & 0 \\ 0 & 0 & 0 & 0 & \mu & 0 \\ 0 & 0 & 0 & 0 & 0 & 2E_Z + \mu \end{bmatrix} \quad (7.2)$$

Where Δ is the superconducting parent gap, t is the hopping between the QD and the superconductor, E_C is the charging energy of the QD and μ its electrochemical potential. J is the exchange coupling that emerges from virtual processes, which we can approximate as $J = t^2/(\Delta + E_C)$ for $\mu \approx -E_C/2$. We do not include spin-orbit interaction. The Hamiltonian consists of three triplet states, T_- , T_0 , T_+ , that do not interact with any other states, and three singlet states, $|0, S\rangle$, $S(1, 1)$, $|2, S\rangle$, that are mutually coupled. For more discussion on the model, see section 2.2.4. We diagonalize the Hamiltonian and show the eigenstates in figure 5b.

The triplet states are split by the Zeeman energy and intersect the singlet states. The three singlet states hybridize due to the spin-conserving tunnel coupling. The resulting

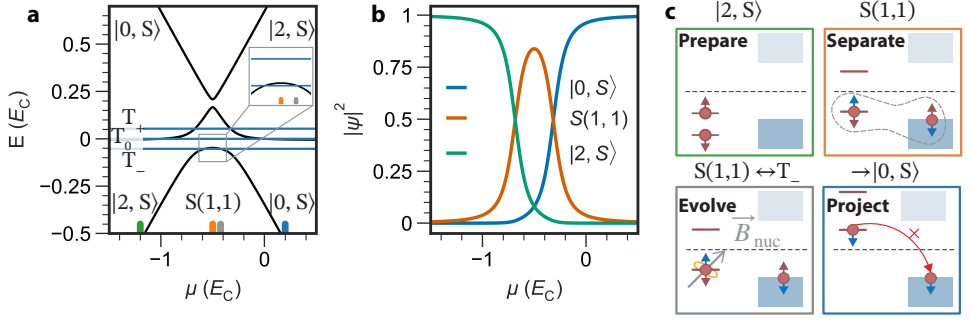


Figure 5: **Singlet-triplet mixing in a QD coupled to a single superconducting orbital.** **a.** Singlet (black) and triplet (blue) eigenstates of the Yu-Shiba-Rusinov zero-bandwidth model for varying electrochemical potential μ . These were computed for $E_C = 15t$, $\Delta = 5t$, $E_Z = 0.4t$. The inset shows a zoom-in of the low-energy manifold around $\mu = -E_C/2$. The colored ticks at the bottom indicate values of μ for the preparation (green), separation (orange), evolution (gray) and measurement (blue) of the system. **b.** Wave function components of the singlet ground state for varying μ . **c.** Schematic illustration of a protocol to measure singlet-triplet oscillations. The colors of the frames correspond to the colors of the ticks in panel a.

ground state is a mixture of the $|0, S\rangle$, $S(1,1)$, $|2, S\rangle$ states, and is shown in figure 5c. At large detuning, the BCS singlet states $|0, S\rangle$ and $|2, S\rangle$ dominate the ground state. At half-occupancy ($\mu = -E_C/2$) of the QD, the ground state is predominantly $S(1,1)$, which is the single-orbital equivalent of the YSR “screening cloud”. If there is a hyperfine interaction in either the QD or the superconductor, nuclear fields can mix the $S(1,1)$ and triplet states [26] when they are close to degeneracy. This implies that the spin in the QD or the superconducting orbital can precess over time. If the system remains in the $S(1,1)$ state, it can be unloaded to the $|0, S\rangle$ or $|2, S\rangle$ BCS singlet states, which represents the creation or annihilation of a Cooper pair respectively. If the $S(1,1)$ state has evolved into a triplet state, it cannot be projected onto the BCS singlet states due to spin blockade. This blockade can be lifted by the formation of a triplet Cooper pair, which is not possible in s-wave superconductors. We can utilize this “Cooper spin blockade” as a readout mechanism of the two-electron spin state, similarly to Pauli spin blockade in double QDs.

In figure 5c, we schematically show a protocol for measuring singlet-triplet oscillations, which can be performed by varying the electrochemical potential of the QD using gate voltage pulses. The system is prepared in the $|2, S\rangle$ state, where the QD orbital is doubly-occupied and the superconductor is in the BCS singlet state. Then, the QD is pulsed to half-occupancy at $\mu = -E_C/2$ using rapid adiabatic passage, to form the $S(1,1)$ state. The voltage pulse has to be slow compared to the $|2, S\rangle - S(1,1)$ energy splitting to prevent Landau-Zener transitions. The pulse has to be fast compared to the singlet-triplet mixing time due to nuclear fields, as the $S(1,1) - T_{\pm}$ degeneracy is crossed (see inset of figure 5a). Afterwards, the system is kept at the $S(1,1) - T_{\pm}$ degeneracy for a time τ to evolve the $S(1,1)$ state into the T_{\pm} state. Then, the state is projected onto $|0, S\rangle$ using rapid adiabatic passage again. Depending on the spin state, the electron in the QD will form a Cooper pair with the quasiparticle in the superconductor or not. The QD occupancy can be monitored using a charge sensor to detect a possible tunneling event. A jump in the charge sensor signal points to the $S(1,1)$ state, while a constant response indicates the T_{\pm} state.

Repeating this experiment for varying τ while measuring the singlet probability, P_S , can then be used to estimate T_2^* of the spin states [26]. If $P_S = 1$ regardless of τ , there is no singlet-triplet evolution. A likely interpretation then is that the wave function weight in the $S(1, 1)$ state is small, as the nuclear fields do not couple the $|2, S\rangle$, $|0, S\rangle$ states to the triplet states. Both the QD and superconductor have even occupancy in the BCS singlet states, which precludes spin precession. Observing $P_S = 1$ regardless of τ would then disprove the formation of a YSR state, as there is no spatially separated singlet or triplet state. The system is then an ABS, as the ground state is a BCS singlet. If P_S does depend on τ , the ground state has to (partially) be an exchange singlet, as nuclear fields can only mix the exchange singlet and triplet states. For $\tau \gg T_2^*$ in double QD singlet-triplet qubits, P_S will saturate at a non-unity value that depends on the magnetic field strength [28]. Observing $P_S < 1$ regardless of τ then still confirms the formation of a YSR singlet, which decoheres faster than one can measure. We note that this protocol has to be performed faster than the quasiparticle poisoning time, as it would flip the parity of the system.

The singlet-triplet evolution relies on a difference in the nuclear fields in the QD and superconductor. Singlet-triplet evolutions were first observed in GaAs double QDs, where the nuclear fields resulted in a T_2^* on the order of 10 ns [26]. In the present system, one of the spins is located in a bulk superconductor, and is presumably spatially-extended as it forms a screening cloud. It is unknown how nuclear fields will affect this spatially extended spin state. Quay et al. measured a spin coherence time of ~ 100 ps for the spin of quasiparticles that were injected into Al, which they compared to the previously measured spin relaxation time of ~ 10 ns [29]. We note that these measurements were carried out in non-equilibrium conditions of an irradiated superconductor, which are significantly different from coherent single-spin YSR states. Nonetheless, they found that the Elliott-Yafet spin-orbit interaction was responsible for the decoherence of quasiparticle spin states in Al [30]. We note that if the spin in the superconductor is rotated or flipped, it cannot fully screen the QD spin anymore. The exchange coupling between the two makes this energetically expensive, as it favors antiparallel spins. The singlet-triplet energy difference might prevent spin relaxation due to spin-orbit interaction in the superconductor. To probe whether there is also spin precession in the superconductor of our system, we can repeat the protocol in figure 5c without tuning to the $S(1, 1) - T_-$ degeneracy. The singlet-triplet mixing due to precession of the QD spin is then suppressed. If P_S is still time-dependent, it could indicate spin-precession in the superconductor.

To conclude, we propose an experiment that directly probes the formation of YSR states on a QD coupled to a superconductor. We exploit the exchange coupling of the screened state to induce singlet-triplet mixing using nuclear fields. We have assumed equal Zeeman splitting in the QD and the superconductor for convenience. A difference in g-factor is not problematic, as the external magnetic field only serves to split the triplet states. We can estimate the necessary energy scales based on the parameters used for figure 5. Starting from the superconducting gap of Al ($\Delta = 270 \mu\text{eV}$), we find: $t = 54 \mu\text{eV}$, $E_C = 0.8 \text{ meV}$ and $E_Z = 22 \mu\text{eV}$. We conclude that these are experimentally accessible parameters for state-of-the-art devices.

REFERENCES

- [1] Ion C Fulga, Arbel Haim, Anton R Akhmerov, and Yuval Oreg. Adaptive tuning of majorana fermions in a quantum dot chain. *New journal of physics*, 15(4):045020, 2013.
- [2] Alberto Bordin, Chun-Xiao Liu, Tom Dvir, Francesco Zatelli, Sebastiaan LD ten Haaf, David van Driel, Guanzhong Wang, Nick van Loo, Thomas van Caekenberghe, Jan Cornelis Wolff, et al. Signatures of majorana protection in a three-site kitaev chain. *arXiv preprint arXiv:2402.19382*, 2024.
- [3] Pratap Raychaudhuri and Surajit Dutta. Phase fluctuations in conventional superconductors. *Journal of Physics: Condensed Matter*, 34(8):083001, 2021.
- [4] Sebastian Miles, David van Driel, Michael Wimmer, and Chun-Xiao Liu. Kitaev chain in an alternating quantum dot-andreev bound state array. *arXiv preprint arXiv:2309.15777*, 2023.
- [5] William Samuelson, Viktor Svensson, and Martin Leijnse. Minimal quantum dot based kitaev chain with only local superconducting proximity effect. *Physical Review B*, 109(3):035415, 2024.
- [6] Roman M Lutchyn, Jay D Sau, and S Das Sarma. Majorana fermions and a topological phase transition in semiconductor-superconductor heterostructures. *Physical review letters*, 105(7):077001, 2010.
- [7] Yuval Oreg, Gil Refael, and Felix Von Oppen. Helical liquids and majorana bound states in quantum wires. *Physical review letters*, 105(17):177002, 2010.
- [8] Katharina Laubscher, Jay D Sau, and Sankar Das Sarma. Majorana zero modes in gate-defined germanium hole nanowires. *Physical Review B*, 109(3):035433, 2024.
- [9] Alberto Tosato, Vukan Levajac, Ji-Yin Wang, Casper J Boor, Francesco Borsoi, Marc Botifoll, Carla N Borja, Sara Martí-Sánchez, Jordi Arbiol, Amir Sammak, et al. Hard superconducting gap in germanium. *Communications Materials*, 4(1):23, 2023.
- [10] Lazar Lakic, Will Lawrie, et al. A proximitized quantum dot in germanium [forthcoming]. *arXiv preprint arXiv:2402.19382*, 2024.
- [11] Oliver Holmegaard Schwarze. Finite element modeling of germanium spin devices. Master's thesis, University of Copenhagen, 2023.
- [12] Giordano Scappucci, Christoph Kloeffel, Floris A Zwanenburg, Daniel Loss, Maksym Myronov, Jian-Jun Zhang, Silvano De Franceschi, Georgios Katsaros, and Menno Veldhorst. The germanium quantum information route. *Nature Reviews Materials*, 6(10):926–943, 2021.
- [13] Mario Lodari, Nico W Hendrickx, William IL Lawrie, Tzu-Kan Hsiao, Lieven MK Vandersypen, Amir Sammak, Menno Veldhorst, and Giordano Scappucci. Low percolation density and charge noise with holes in germanium. *Materials for Quantum Technology*, 1(1):011002, 2021.

- [14] Francesco Zatelli, David van Driel, Di Xu, Guanzhong Wang, Chun-Xiao Liu, Alberto Bordin, Bart Roovers, Grzegorz P Mazur, Nick van Loo, Jan Cornelis Wolff, et al. Robust poor man's majorana zero modes using yu-shiba-rusinov states. *arXiv preprint arXiv:2311.03193*, 2023.
- [15] Xin Zhang, Elizaveta Morozova, Maximilian Rimbach-Russ, Daniel Jirovec, Tzu-Kan Hsiao, Pablo Cova Fariña, Chien-An Wang, Stefan D Oosterhout, Amir Sammak, Giordano Scappucci, et al. Universal control of four singlet-triplet qubits. *arXiv preprint arXiv:2312.16101*, 2023.
- [16] Nick van Loo, Grzegorz P Mazur, Tom Dvir, Guanzhong Wang, Robin C Dekker, Ji-Yin Wang, Mathilde Lemang, Cristina Sfiligoj, Alberto Bordin, David van Driel, et al. Electrostatic control of the proximity effect in the bulk of semiconductor-superconductor hybrids. *Nature Communications*, 14(1):3325, 2023.
- [17] Grzegorz P Mazur, Nick van Loo, Ji-Yin Wang, Tom Dvir, Guanzhong Wang, Aleksei Khindanov, Svetlana Korneychuk, Francesco Borsoi, Robin C Dekker, Ghada Badawy, et al. Spin-mixing enhanced proximity effect in aluminum-based superconductor-semiconductor hybrids. *Advanced Materials*, 34(33):2202034, 2022.
- [18] Stefano Bosco, Mónica Benito, Christoph Adelsberger, and Daniel Loss. Squeezed hole spin qubits in ge quantum dots with ultrafast gates at low power. *Physical Review B*, 104(11):115425, 2021.
- [19] Martin Leijnse and Karsten Flensberg. Parity qubits and poor man's majorana bound states in double quantum dots. *Physical Review B*, 86(13):134528, 2012.
- [20] Brian Paquelet Wuetz, Davide Degli Esposti, Anne-Marije J Zwerver, Sergey V Amitonov, Marc Botifoll, Jordi Arbiol, Amir Sammak, Lieven MK Vandersypen, Maximilian Russ, and Giordano Scappucci. Reducing charge noise in quantum dots by using thin silicon quantum wells. *Nature communications*, 14(1):1385, 2023.
- [21] Chun-Xiao Liu, A Mert Bozkurt, Francesco Zatelli, Sebastiaan LD ten Haaf, Tom Dvir, and Michael Wimmer. Enhancing the excitation gap of a quantum-dot-based kitaev chain. *arXiv preprint arXiv:2310.09106*, 2023.
- [22] Florian Vigneau, Federico Fedeale, Anasua Chatterjee, David Reilly, Ferdinand Kuemmeth, M Fernando Gonzalez-Zalba, Edward Laird, and Natalia Ares. Probing quantum devices with radio-frequency reflectometry. *Applied Physics Reviews*, 10(2), 2023.
- [23] Alexander Comstock Johnson, JR Petta, CM Marcus, MP Hanson, and AC Gossard. Singlet-triplet spin blockade and charge sensing in a few-electron double quantum dot. *Physical Review B*, 72(16):165308, 2005.
- [24] A Wallraff, DI Schuster, A Blais, JM Gambetta, J Schreier, L Frunzio, MH Devoret, SM Girvin, and RJ Schoelkopf. Sideband transitions and two-tone spectroscopy of a superconducting qubit strongly coupled to an on-chip cavity. *Physical Review Letters*, 99(5):050501, 2007.

- [25] Ronald Hanson, Leo P Kouwenhoven, Jason R Petta, Seigo Tarucha, and Lieven MK Vandersypen. Spins in few-electron quantum dots. *Reviews of modern physics*, 79(4):1217, 2007.
- [26] Jason R Petta, Alexander Comstock Johnson, Jacob M Taylor, Edward A Laird, Amir Yacoby, Mikhail D Lukin, Charles M Marcus, Micah P Hanson, and Arthur C Gossard. Coherent manipulation of coupled electron spins in semiconductor quantum dots. *Science*, 309(5744):2180–2184, 2005.
- [27] Gorm Ole Steffensen and Jens Paaske. *Yu-Shiba-Rusinov bound states in quantum dots*. Niels Bohr Institute, Copenhagen University, 2017.
- [28] WA Coish and Daniel Loss. Singlet-triplet decoherence due to nuclear spins in a double quantum dot. *Physical Review B*, 72(12):125337, 2005.
- [29] CHL Quay, M Weideneder, Y Chiffaudel, Christoph Strunk, and M Aprili. Quasiparticle spin resonance and coherence in superconducting aluminium. *Nature Communications*, 6(1):8660, 2015.
- [30] Annamária Kiss, Lénard Szolnoki, and Ferenc Simon. The elliott-yafet theory of spin relaxation generalized for large spin-orbit coupling. *Scientific Reports*, 6(1):22706, 2016.

ACKNOWLEDGMENTS

A man alone in the desert is sovereign and free. He is also powerless.

Michael Heseltine

The only thing that interests me more than quantum mechanics is the nature, personality, and socializing of people. I am lucky to know and have known an amazing variety of them.

First of all, **Leo**, I'd like to recall the exact moment when and where you asked me whether I'd be interested in doing a PhD in your group; the toilets in the Microsoft wing, after a meeting. I'm most grateful for you teaching me to "bet my house", as Richard Feynman puts it. I have wide interests and was planning to do about 6 parallel projects throughout my PhD, which would have left me with 3 unfinished preprints. You taught me how to focus, give everything you have and learn everything you can about a single topic. You are a gifted physicist and know very well which concepts are understood and which aren't; in physics and in people. **Tom**, I came into your orbit at some point in my second or third year. This was a chaotic time with people, teams and topics being reshuffled into the new field of Kitaev chain physics that you and Guan founded. You approach experiments with the mindset and joy of a child, complete with questions like "*what does it mean?*" or "*why?*". You are a naturally creative person, and it was an honor and pleasure to work with you. You taught me that physics is play. **Greg**, you are a natural-born leader. I was very grateful for you to welcome me into the UTS team (where I did my masters, of course). Us being the early birds, I really enjoyed our serious, funny or just lighthearted coffee chats around 08:15. I congratulate you for carrying the Olympic torch of hybrids to Oxford, and feel science would be much less interesting without you being part of it. **Michael W.**, I have you to thank ultimately for drawing me into QuRe and Leo's group. I met you while following computational physics, which I TA'd for you with pleasure for 2 years. I really wish more PI's were like you, as you're very gentle and funny. The academic world could learn a lot from you. **Andrey**, thanks for taking a chance in me, and trusting me with path integrals, even though I had never heard of a Green's function. My stay in Santa Barbara was magical and I will never forget it. You're a very cool guy. Also if you ever get bored of your Martin guitar I'd be happy to take it from you. **Anasua**, first of all, thanks a lot for inviting me to your lab back in Copenhagen. I had a really good time (see what I wrote about Will and Lazar). Before my exchange, I considered physics mainly from a DC, condensed matter point of view. When I was in Copenhagen, I learned to think in terms of

single-shot readout, impedances and electron loading. These hadn't really been applied much to hybrids before, and it heavily influenced my thinking of them. I owe a lot to you, especially for my charge sensing paper. **Eliška** you convinced me that quantum matter and AI are in fact a match made in heaven. You have a particular way of attacking problems and approaching physics, from which I've learned a lot. From lurking deep within the Mattermost, I could see that you created a research group that is not only brilliant but also a lot of fun. **Ferdinand**, thank you for hosting me in your lab! **Bas t.H.**, this might be the first time the phrase "boxershort-cocktail VAP" has appeared in print, but that is where I first met you in 2015. We went to Kenya together, made an almanac and had some alcoholic beverages well before you started a PhD at QuTech. It was so much fun to have a friend around at all times during the days in the lab. **Francesco**, you are the student who teaches the teacher. You were my master student during the toughest part of my PhD, with the perfect storm of Covid lockdowns, retractions, SAG, ESD and worst of all: nanocrosses. I really like you as a person, and was delighted to continue working with you when you stayed around for a PhD. If you do decide to stay in academia, I think you'll make a brilliant professor someday. **Alberto**, if only 3% of the world was like you, there would be no more war. You are genuinely a very sweet person and it was so much fun to be basically starting our PhD's at the same time. Whenever someone around me announces that they are having a baby or getting married I just hear you saying "**WOW, that's amazing!!!**" including the dramatic gesticulation. **Bart**, you are the eye of the hurricane. Even in the face of disaster, stressful periods or after major disappointments you can remain calm and cheerful with your signature Bart smile ©. Bas and I used to joke that I could make you say at least one negative thing during your masters, but I lost the bet. Whether you'll stay in academia or not, I'm pretty sure you'll be both happy and successful. **Guan**, you are a gifted physicist, but you know that already, so I'm just going to write other stuff. I'd call you a connoisseur of science, who talks about preprints like fine glasses of Barolo. I think you once referred to a certain qubit coupling as "unnatural", and said that my colormap looked like food. Your laugh and high-pitch "*Oh my gosh!*" are unforgettable. **Nick**, you always reminded me that science is after all a human affair. You led me through the snake pit that is semiconductor-superconductor physics like a fish swims through water. You knew all the scoops, including academic hate triangles (and love triangles!!). It was a lot of fun to work with you. You are very reliable and "just get stuff done", even if that may be very hard. Unlike some other people (Bart), people like you and me get stuff done and complain about it constantly. **Di**, it was a lot of fun to have worked with you at the very start (SAG) and very end (robust paper) of my PhD. You live a very cultured life of which I'm honestly a bit jealous. **Alex**, good lord did we spent a lot of time in the STM dungeon. This was a very challenging project, as we faced a completely new sample prep technique, limited machine time, Covid restrictions and GAFAM bullshit. Despite these, we had a lot of fun thanks to your colorful and elated personality. I am very happy that your talents were recognized, as you strongly deserve your role as assistant professor. I am also happy that you are teaching ethics in the field of quantum technology, cause *dang gurl* it's needed. **Rouven**, you were a solution looking for a problem, where I was a problem looking for a solution. Somehow, we found each other in Delft at exactly the right time, looking to attack Kitaev chains using neural nets. It was an absolute pleasure to work with you. You are the only person who I've collaborated successfully with using zoom, and it was very nice

to have you visit Delft so often. **Gunjan**, I'd first of all like to thank you for welcoming a nearly absolute stranger into your home. There are not so many people in this world who have the heart to do something like this. I really enjoyed going out and about in Copenhagen with you in the weekends and evenings. I feel like I've learned a lot from hanging out with you. I wish you a lot of happiness! **Will** and **Lazar**, doing physics with you feels like hanging out in a half pipe, recording a new mixtape, and shooting dice in an abandoned stairway. I think it's a miracle we did anything at all in our month together, let alone gather enough data for a paper. I think both of you are amazing human beings who happen to be very good physicists too. Life cannot be boring in a 5 km radius of either of you. Please continue your existence! **Alisa**, meeting you coincided with the turning point in my PhD where I actually felt good about my research and started having fun. I always felt connected to you simply because we did exactly the same research, and were basically neighbors in the crazy world of topology in condensed matter. Our resolution to not scoop each other and keep in touch was formative for the rest of my PhD, and affected the way I think about sharing success, inviting discussion and keeping science an open playing field. **Andreas**, you beautiful young man. While Sankar may not have liked your work particularly much, I really did! **Charrold**, **Charri** or **Harry**, we'd actually already collaborated on InSb + Pb nanowires at the very start of my PhD. It was a nice surprise to see that you were still in Copenhagen when I was also there! You are unforgettable and a super fun guy! **Jie**, by the time I was your master student, I was convinced of a future in consultancy or some tech firm. I just had to survive 8 months working in Leo's group under your supervision, and the rest of my future would be easy street. This turned out a little different, and I have you to thank for getting me hooked on doing physics research. I feel a weird sort of nostalgia about super-semi islands now, as they remind me of my master research. **Sebastian H. and Gijs**, though our collaboration had to end prematurely, I did enjoy working with you very much and appreciate the effort you put in making it work. **Jiyin** after working with you during my masters, it was especially fun to succeed you on B2, and of course we also did some highly experimental measurements of noise. **Cristina**, it was nice to have you in the group, as you provided a nice refreshing take on everything we did from a different area of physics. **Jan Cornelis** it was a lot of fun getting to know each other better while training in the clean room. I'll never forget our aggressive run-in with an unnamed Italian in the clean room, after which you loudly declared: "I'm never eating pizza again!!". **Anton**, I enjoy your high-level understanding of physics and the way you communicate it. At some point I was asking myself why I didn't like Floquet physics and you said: "it's too *ephemeral*. The physics stops when you turn off the lights". Now that's some real physics poetry. **Chunxiao**, we were very lucky to have you around to guide us and explain what we could not in Kitaev physics. I feel like at every given moment you probably have 10 interesting projects to look into, but have to prioritize some from sheer lack of time. **Mert**, you are a very knowledgeable and fun person. I am very impressed by your zero-field Majorana work, and feel certain there will be some interesting outcome from it in the end. For a basketball player, I would have expected you to land a napkin in a trash bin at least once during my PhD, but it never happened. I also really liked your story of the liquor smugglers during your interrail travels. **Juan**, I knew you and Francesco from computational physics and both of you impressed me a lot. Briefly, I thought you were Francesco, and that you might be my future master student. While it

didn't turn out that way, I'm happy that both of us worked on Kitaev physics. **Sebastian M.**, you are an experimentalist in the body of a theorist. You join Friday drinks, take the physical world seriously, and literally wore a resistor on your wrist at some point. It's nice to have a casual train enthusiast close by. It was a lot of fun hanging around over the years and even being authors on a paper together. **Rik**, we are like two circles in a Venn diagram that overlap in the Otte lab. I really enjoyed our discussions about Shiba, and including a semi-open 2D substrate into a single atom as a self-energy. This to me is the ability "To see a World in a Grain of Sand". **Hélène**, it was really cool to TA computational physics with you, and find someone who could out-internet me. Many congratulations on your marriage! **Florian and Xiang**, I'm happy Alberto convinced you to do projects in our group. **Thomas and Tijl**, it was nice to see a Belgian takeover of our labs! **Vincent**, I formally count you as Belgian too, seeing as $\frac{\text{France} + \text{Belgian}}{2} = \text{Dutch}$. Without you, I would have never finished my final paper. You're also an extremely fun person to be around. I'll never forget the time you microwaved a frozen pizza, rolled it up, and ate it in front of the flabbergasted Italians. **Arjen and Mark**, you were great additions to the group. Nowadays, it seems you're quite happy in Sydney, of which I am slightly jealous. **Praveen**, you are also a really fun guy who would make a great scientist. **Srijit** you are ultimately a grand debater who got tenured in physics. It is amazing to see your involvement in the day-to-day work of your students. It's also a lot of fun to have beer with you, cheers! **Yining, Wietze and Eoin**, it was really cool to discuss charge sensing of hybrids with you when you got it to work. You had a good start, I wish you a nice and fruitful PhD research! **Ivan** you are a beast. I don't know anyone who could juggle 6 chips from 3 wafers and manage to write on the correct one. I wish you a lot of fun at ASML! **Qing**, you deserve a lot of respect for getting Kitaev to work so quickly in 2DEGs. Best of luck in your further career! **Sebas**, you are a blast from the past, having been Jaap's bachelor student. Good luck to you! **DJ and Rebecca**, you really are working on the next-gen experiments on 2DEGs. While this requires significant initial investment, it will benefit you in the long term. Especially once, having done everything yourself, you learn that more senior researchers will not be more experienced than you are. **Christian P.**, everything I knew was DC and you taught me a lot about RF. Your knowledge of physics is very broad, exact and precise. You're super fun to hang out with, big congrats on your marriage and enjoy Norway! **Damaz**, we really should have started that fountain pen club back in the B wing. **Filip**, you are nearly peerless in knowledge in what you worked on. I hope you can share this knowledge with the people around you. **Lin**, I was very impressed by the connection you made from floating islands to Kitaev chains. Good luck after the PhD! **Michael C.** I secretly wish we could have worked together on Kitaev chains in germanium. I'm happy you found other interesting projects in Menno's group. **Jaap**, I will never ever forget your tequila-empanada party. You're a real fun guy and a SAG man at heart. **Lukas S.**, you are a very sweet person who has his own clear ideas about physics and research, never change! **Marta**, you are a brilliant researcher and a really fun person. I enjoyed the few weeks we actually both worked on germanium. **Arno**, it seems that we are the same person. We live in Leiden, have girlfriends that studied clinical neuropsychology, and started as quantum measurement engineers after our PhD. Whenever we run into each other I have a lot of fun! **Lukas G.**, you are a very cool physicist who gets a lot done. I wish you great success back in Germany. **Christian A.** you are a very balanced and knowledgeable PI. I'm very

happy you joined at QuTech, you set up a fantastic group. **Daniël** it was cool to be office buddies with you in 2020, and now again in 2024! I hope you'll build a tea castle once more! **Michael B., Joris C. and Brecht S.** Thanks for all the fun times, especially at TPKV. **Anne-Marije and Nico**, thanks for taking a chance in me! Let's get these germanium spin qubits Grooving! **Achilleas and Davide**, it's been a lot of fun to work with the Greco-Italian alliance so far! **Jason**, first of all, your child is very lucky to have you as a father. You are super kind and helpful, and it's always fun to chat with you. Enjoy the family life! **Olaf**, every once in a while, I learn new stuff about you, like the fact that you are a golf enthusiast. Though I did stupid stuff, I never vented any mixture, so I don't think you'll consider me stupid. I got the impossible task of succeeding the dream team on B2, which you'll agree with me was no easy game. Without you QuTech would literally be a hot mess. **Raymond**, I made one working device in my PhD, which I almost discarded because it looked terrible. Then you came with your ghostbusters electromagnetic detector. You showed that the line broadening I observed was actually due to 13.7 kHz noise from the cheap power supply of a Leiden Cryogenics motor. Lately, I'm wondering how much of the problems we ascribe to chips are actually from wiring, connectors, power supplies, etc. Delft is very lucky to have you in any case, as your knowledge of electronics is astounding. Also, your hobby projects are very fun, you are a cool person! **Roy B.**, also you helped me a lot in debugging stuff in the lab, thanks a lot! **Yannick**, when I first talked to you, I had no idea how bias tee's worked or what an SMP connector was. I think it's impressive how you guys help everyone at QuTech with such varying demands. I can proudly say that the PCB you made for Leo's group is now actively in use. **Csilla** thanks a lot for arranging all the contract stuff and negotiations on our behalf. You are a very effective programme manager. **Delphine**, thank you for providing us with TNO support, clarity in focus when our fabrication broke down completely. You are a very nice person and a true connector. **Jenny** you are a really cool and spontaneous person. Also, I would have probably failed my PhD without you for various reasons. I always enjoyed chatting with you very much. **Bas van A.**, you are a very sweet and fun person. You helped us a lot when we had huge issues in the clean room. You are naturally curious and helpful, and I'm very grateful to have worked with you. **Roald**, it was really insightful to learn about ellipsometry and thin films from you. You are naturally excited and listen to 50 languages of metal, which I find impressive if anything. **Martin and Karsten** thank you for writing the paper that started a field. 10 years later you are still an active part of Majorana bound states in Kitaev chains. I very much liked discussing with you in person in both Copenhagen and Lund. **Gorm**, whereas I am an average Andreev enthusiast, you are a chad Shiba appreciator. Your passion is quite infectious, I am now also looking for a problem that Shiba states can solve. **Rubén Seoane Souto, Thanos Tsintzis, András Pályi, Ramon Aguado, Alfredo Levy Yeyati and Jeroen Danon**, I am very grateful that there are people outside of Delft who also research Kitaev chains, from a different perspective. Also, I had very interesting discussions with you about Majorana physics. **Charlie Marcus**, we had a number of lively exchanges in different parts of the world. In a dive bar in Santa Barbara ("I'll have your famous old fashioned please"), to Copenhagen ("this natural phenomenon *only* occurs in Denmark or Holland"), and San Sebastian ("are you really gonna give me shit for my beautiful data?"). I think science would be a lot more amusing if everyone had a touch of drama like you (and probably me too). **Dirk Bouwmeester**, thank you for sparking my

interest in quantum mechanics during my bachelors in Leiden. It was also really cool to talk to you in Santa Barbara when I was there. **Sasa, Ghada, Jason, Roy, and Erik**, thank you for the suite of high-quality semiconductors you have provided for us over the years!

Natuurkunde is prachtig, maar er is ook een leven erbuiten. Het is voor mij altijd belangrijk geweest om mij een “ingebed mens” te voelen. Dat er touwtjes aan je hangen waar anderen aan trekken als je valt. Zoals Levinas schreef: “Ik ben pas vrij in het gelaat van de Ander”. Ik wil graag deze anderen bedanken.

Te beginnen met **Daan, Stef, Derk en Boray**. Waar veel mensen tijdens de studie hun vrienden van herkomst uit het oog verliezen, hebben wij dat nooit laten gebeuren. We zijn een onwaarschijnlijke groep die uit het niets bij elkaar was. We deden echt heel veel samen; stappen, sporten, LAN parties, etc. Ik ben heel dankbaar dat ik goede vrienden heb kunnen maken op de middelbare school die ik nog steeds zie. In het bijzonder **Boray**, mijn oudste vriend. Er zijn golven dat we elkaar meer of minder zien, maar onze relatie blijft altijd steady. Jij leert mij nog steeds dat ik niet moet vergeten om te “chillen”.

Dan mijn niet-musketiers **Sietze, Gerwin, Joris en Sjoerd**. Tegenwoordig schijnt ons ding te zijn om (on)ironisch naar ADO Den Haag te gaan, terwijl niemand van voetbal houdt. Behalve Joris. En schijnbaar Sjoerd, maar dat gelooft niemand. Maar zeker niet Gerwin, ook al kijkt hij alle wedstrijden en SMS'te hij vragen naar VI. Ik denk dat er weinig mannelijke vriendengroepen zijn die het concept van “achter de schermen” zo goed begrijpen als wij. Ook wij zijn ooit willekeurig bij elkaar gezet, maar ik ben heel dankbaar dat ik jullie mijn vrienden mag noemen. Het unieke aan jullie is dat 10 jaar geleden hetzelfde voelt als gister. “weet je nog toen Luka te laat was”, ‘ja man, augustus 2014’. **Sietze**, ik waardoor jouw ondernemende geest enorm. Dit zal ongetwijfeld ooit leiden tot je eigen bedrijf, maar in onze studententijd leidde het tot veel ludieke ongein. DS Sinchon, Gerwin's Skyrim treasure hunt, en een literaire canon aan ingezonden stukken. Hoogtepunt voor mij: “1947, naoorlogs Praag. Freek v.H. wordt wakker in zijn vernielde appartement”. Daarnaast ben ik blij dat je verloofd bent met **Heather** en vind ik jullie een heel leuk stel. **Gerwin**, ik kan met jou de meest simpele gesprekken (“heerlijk, HEERlijck, HEERLIJKCCC”) en de meest complexe gesprekken (“*je zou maar in Transsiberië geboren worden man, daar is echt helemaal niets hè*”) hebben. Vooruit, nog een paar mooie voorbeelden: “Napoleon was 24 toen hij generaal werd hè. VIER en TWINTIG, wat deden wij toen?”. Of over twee emails van een markant persoon: “deze email is de declaration of independence, en deze is dan de bill of rights.” **Joris**, jij hebt echt een waanzinnig gevoel voor stijl. Alles van architectuur, tot schilderijen, muziek en boeken. Je bent ook creatief, met bijvoorbeeld het bedenken van een gitaar riffje, een clip over Mark Rutte op youtube zetten en je instagram pagina over oude & nieuw foto's in Den Haag. Het is ook heel leuk om met jou in het buitenland te zijn, waar je gevoel voor avontuur echt opbloeit. Met name de signature “links rechts” weg van de hoofdstraat. **Sjoerd**, mijn beste vriend. Wij spraken elkaar voor het eerst echt op een zaterdag in 2014 bij Van Der Werff. Sindsdien ben jij eigenlijk familie geworden. Ook in letterlijke zin, omdat het vaak over je gaat aan tafel in Acht en je wel eens kerst hebt meegevierd. Je bent heel bijzonder voor me en ik ben dankbaar dat je een grote rol in mijn leven speelt.

Jona, Ysbrand, Max, Sjoerd, ook van jullie weet ik niet heel goed hoe we een groep zijn geworden. Ik denk dat **Ysbrand** hoopte op een soort Herenclub zoals Harry Mulisch had. Wat het is geworden is 5 luidsprekers zonder microfoons. Na iedere avond zeggen

we trots en ironisch: “wat hebben we weer goed naar elkaar geluisterd”. Je kan het ook zo zien: wat hebben we een hoop tegen elkaar te zeggen! Ik ben altijd dankbaar geweest dat ik mensen van de publieke sector, politiek of Europa (en pensioen risicobereidheid) om me heen heb. Dit is een goede tegenhanger voor de ietwat robotische wereld van de techniek. **Eric**, je bent een fantastisch persoon en een ware verbinder der mensen. Ik heb veel van je geleerd en waardeer je oprechte interesse heel erg. Daarnaast geniet ik altijd van je gespreksavonden en ben ik vereerd dat ik ooit inleider mocht zijn. **Cathelijne**, jij noemde mij ooit jouw “broertje” tot het genoeg van veel mensen 10 jaar later. Je bent een hilarisch persoon, ook al vraag je jezelf misschien af waarom. Ik vind het heel leuk om met je te eten en “CIDER” te drinken. Niet te verwarren met “Ceder” gym, of “Don Ceder” van de Christenunie. **Hugo**, wij waren geen vrienden op de middelbare school, laten we dat voorop stellen. Later gelukkig wel! Je bent een intelligent mens met heel goede humor. Ik hoop van harte dat we ooit nog de beach party gaan organiseren. **Lisa d.P.** toen we nog huisgenoten waren hadden we wel eens andere ideeën over hoe dingen zouden moeten zijn in een studentenhuus. Nu ik wat ouder ben zie ik hoe onnozel dat was en zie ik je als een goede vriendin. Je bent heel creatief en een fijn persoon om mee om te gaan. **Sebas, Sjali, Bob, Casper, Célestine, Daniëlle, Jochem, Lisa v.d.V., Maxim, Sabine, Suus en Tim**, het was episch om met jullie te wonen. Ik weet niet eens waar ik moet beginnen met deze nevelige en chaotische tijd beschrijven. Hoogtepunten: domme jongens weekend, drrrrrie oktoberrrrt, tour du chambre, huisthuisweekend. Het cooldowncafé, Sneekweek (zonder naar Sneekweek te gaan), MexicanOS, cursus mindfulness (en de mensen die liever gingen darten), date diners. Mijn gesprek met Sebas over Satésaus, waarna wij hem saté noemden: “ik hou echt van satésaus” ‘je weet dat satésaus niks is, alles wat je over saté doet is satésaus’ “dus ook Remoulade, beurre blanc, curry kruidenketchup, hollandaise..” ‘ja, allemaal in potentie satésaus’.

Dieptepunten: “ik ga je laten verdwijnselen”, die keer dat Max een ongesneden rode ui in de pastasalade deed, sociaal beheerder Rie-Sjaar, die keer dat ik van de fusie weer een fietsenstalling wilde maken, de -7 winter toen de boiler kapot ging.

Lieve **familie**, bedankt voor een fantastische jeugd met verjaardagen, bezoeken aan de Belgische kust, dekenforten en belletje lellen. **Harry en Margriet**, al heel lang, maar nog meer na ons huwelijk zijn jullie echt als ouders voor me. Het is ook heel makkelijk om te zien welke eigenschappen Nienke van ieder van jullie heeft overgenomen. De verschillen met Han en Janny zijn soms ook grappig, denk aan uitslapen in Acht en vroeg op (“tijdig” volgens Nienke) bij jullie. Ik vond het heel bijzonder om met jullie mee te gaan naar Italië en Champéry en hoop dat nog vaker te mogen doen! **Wouter**, mijn mededuft. Jij bent een hilarische bonamigo die duidelijk zijn wereldje gevonden heeft. Ik vind het cool hoeveel je de wereld over reist om boten in elkaar te zetten (ofziets). Je bent een stoere bink met uiteindelijk een erg klein hartje. **Jasper**, ik vind het dapper dat je hebt besloten dat het 9-tot-5 leven in Nederland niet voor jou is weggelegd. Ik heb geen idee waar je over een paar jaar bent, jij zelf waarschijnlijk ook niet. Je bent uiteindelijk een erg zorgzaam persoon die het goede in mensen wil zien. **Doortje**, wat houd ik toch van jouw bulderlach. En wat heb je een prachtig haar, maar dat hoeft ik je niet te vertellen. Ik vind het altijd heel gezellig met je en hoop nog op vele avondjes chillen!

Marianne, ik wil je bedanken voor het zijn van de meest geweldige moeder die ik me kan voorstellen. Als kind moest ik altijd mee met shoppen, waar ik vervolgens met het

grootste ongeduld chagrijnig ging wachten op een stoel tot je klaar was met passen. We bespraken alles wat ik meemaakte en te vertellen had. Mijn liefde voor mensen heb ik dankzij jou. Mijn passie voor kunst en vormgeving ook. De weekendjes naar De Haan waren ook heel belangrijk voor me. Was het ons maar gegund dat je langer in ons leven was geweest. **Han**, ik weet niet waar ik moet beginnen met jou bedanken. Je hebt me in feite in je eentje opgevoed. Dit begon met horten en stoten, toen we als avondeten overgingen op kant-en-klare (en zeer goed verteerbare!) seniorenmaaltijden. Later ging je zelf koken, en ik deed het ook af en toe om je te ontlasten. Ik ken weinig mensen die zonder schromen hun goede baan opzeggen als hun vrouw zieker wordt, dat spreekt voor je. Ik heb heel veel van je geleerd, maar ben desalniettemin ook mijn eigen persoon geworden. Je hebt mijn interesse in natuurkunde gevoed met je eigen verhalen. Ik hou van je! **Janny**, jij en Han waren heel voorzichtig naar mij toen jij in mijn leven kwam. Er komt veel op een kind af bij het vormen van een samengesteld gezin. Voor mij hofde het echter nooit langzaam te gaan. Je bent een geweldig en zorgzaam persoon en ik zou heel ongelukkig zijn geweest als je niet in ons leven was. Je bent en blijft als een moeder voor me! **Philippe**, op papier zouden we niet meer kunnen verschillen. Soldaat en wetenschapper, lang en kort, Arnhem en Leiden. Toch vind ik dat we heel erg op elkaar lijken op veel gebieden, vooral qua humor. Ik ga niet oprakelen hoe je Aimée aan het teisteren was op de trampoline toen ik je ontmoette. Ik denk dat we binnen zo'n 5 minuten al maatjes waren. Je bent mijn broer en ik ben heel trots op je. **Aimée**, ik wilde als kind altijd een jonger zusje. Met jou ging die wens in vervulling. We keken in de lange weekenden in Vught naar dingen zoals Phineas en Ferb, taarten van Abel, of gewoon MTV. Naarmate je ouder werd ontstond er een nieuwe Aimée. Deze Aimée staat sterk in haar schoenen, fixt shit gewoon en is heel trouw. Ik vond die keren dat we tijdens Covid afspraken heel bepalend voor onze relatie. Je mag heel trots zijn op de persoon die je geworden bent en hoe je je eigen pad hebt bewandeld. Ik ben heel dankbaar hoe mij toch een zusje gegund is. **Lieve**, onze relatie heeft de grootste groei doorgemaakt over de jaren. Geheel per toeval gingen we allebei in Leiden studeren en bij dezelfde studentenvereniging. Ik denk dat we het toen wel fijn vonden dat we elkaar ook enige privacy gunden, omdat we allebei een eigen wereld nodig hadden. Gelukkig hebben we elkaar snel daarna echt gevonden. Ik vind de spelletjesavonden met jou en Rob altijd heel gezellig. Maar ook simpele dingen als carpoolen naar Acht en gewoon kletsen. Ik gun je een heel gelukkig gezinsleven met Rob en jullie zoontje. Ik ben heel blij dat ik jou ook mijn oudere zus kan noemen. **Anne-Roos, Rob en Damin**, Jullie zijn de dakopbouw op ons Vila Volta gezin. Het is heel mooi om te zien hoe jullie Philippe, Lieve en Aimée ieder op jullie eigen manier aanvullen. Ik ben heel blij dat ook jullie mijn familie zijn en dat we samen echt een groot gezin vormen.




Lieve **Nienke**, waar kan ik zelfs beginnen met jou bedanken? Zelfs terwijl ik dit schrijf heb je door mijn gehele dankwoord geploegd om te kijken of er ongepaste dingen in staan. Ik heb ongelooflijk veel van je geleerd over de jaren, want er valt heel veel van je te leren. Je houdt altijd rekening met anderen, soms teveel. Je bent geduldig, zeker naar mij toe. Ik heb met name van jou geleerd dat het openbaren van jezelf en je emoties naar anderen toe een teken van kracht is, dat kon ik niet zo goed toen ik je net kende. Je grapt altijd dat ik je in feite in 2015 al ten huwelijk heb gevraagd. Ik grap dan altijd dat ik het toen al wist. Je bent mijn eerste en laatste relatie en ik houd zielsveel van je. Ik ben ook heel trots op je.


CURRICULUM VITÆ

David VAN DRIEL

- 01/02/1996 Born in Eindhoven, The Netherlands.
- 2008-2013 **Bilingual Atheneum**
Stedelijk College Henegouwenlaan, Eindhoven
- 2013-2016 **Bachelor of Science in physics**
Leiden University
- Bachelor research project in the group of Prof. dr. D. Bouwmeester:
"Magnetic-field enhanced coherence in Ytterbium-doped ring resonators at millikelvin temperatures"
- Honours College Béta and Life Sciences
- 2016-2020 **Master of Science in Applied Physics**
Delft University of Technology
- Master research project in the group of Prof. dr. ir. L.P. Kouwenhoven:
"Parity-Dependent Majorana Signatures for Advanced Superconductor -Semiconductor Nanodevices"
- Internship at Microsoft Station Q, Santa Barbara:
"Constructing Elements of Tunneling Hamiltonians Using the Mahaux-Weidenmüller Formula"
- Leiden Leadership Programme
- 2020-2024 **Ph. D. in Experimental Physics**
Delft University of Technology
- Doctoral research in the group of Prof. dr. ir. L.P. Kouwenhoven:
"Quantum Dots Coupled to Andreev Bound States"

LIST OF PUBLICATIONS

18.  **David van Driel**, R. Koch, V. P. M. Sietses, S. L. D. ten Haaf, C.-X. Liu, F. Zatelli, B. Roovers, A. Bordin, N. van Loo, G. Wang, J. C. Wolff, G. P. Mazur, T. Dvir, I. Kulesh, Q. Wang, A. M. Bozkurt, S. Gazibegovic, G. Badawy, E. P. A. M. Bakkers, M. Wimmer, S. Goswami, J. L. Lado, L. P. Kouwenhoven, E. Greplova (2024). Cross-Platform Autonomous Control of Minimal Kitaev Chains. *arXiv preprint arXiv:2405.04596*.
17. L. Lakic[†], W. I. L. Lawrie[†], **David van Driel**, L. E. A. Stehouwer, M. Veldhorst, G. Scappucci, F. Kuemmeth, & A. Chatterjee. (2024). A proximitized quantum dot in germanium. *arXiv preprint arXiv:2405.02013*.
16. A. Bordin, C.-X. Liu, T. Dvir, F. Zatelli, S. L. D. ten Haaf, **David van Driel**, G. Wang, N. van Loo, T. van Caekenberghe, J. C. Wolff, Y. Zhang, G. Badawy, S. Gazibegovic, E. P. A. M. Bakkers, M. Wimmer, L. P. Kouwenhoven, G. P. Mazur (2024). Signatures of Majorana protection in a three-site Kitaev chain. *arXiv preprint arXiv:2402.19382*.
15. A. Bordin, X. Li, **David van Driel**, J. C. Wolff, Q. Wang, S. L. D. Ten Haaf, G. Wang, N. van Loo, L. P. Kouwenhoven, & T. Dvir. (2024). Crossed Andreev reflection and elastic cotunneling in three quantum dots coupled by superconductors. *Physical Review Letters*, 132(5), 056602.
14. A. Bordin[†], F. J. B. Everts[†], G. O. Steffensen[†], T. Dvir, G. P. Mazur, **David van Driel**, N. van Loo, J. C. Wolff, E. P. A. M. Bakkers, A. L. Yeyati, L. P. Kouwenhoven (2024). Supercurrent through an Andreev trimer. *arXiv preprint arXiv:2402.19284*.
13.  **David van Driel**, B. Roovers, F. Zatelli, A. Bordin, G. Wang, N. van Loo, J. C. Wolff, G. P. Mazur, S. Gazibegovic, G. Badawy, E. P. A. M. Bakkers, L. P. Kouwenhoven, T. Dvir (2024). Charge sensing the parity of an Andreev molecule. *PRX Quantum*, 5(2), 020301.
12. S. Miles, **David van Driel**, M. Wimmer, & C.-X. Liu. (2024). Kitaev chain in an alternating quantum dot-Andreev bound state array. *Physical Review B*, 110(2), 024520.
11.  F. Zatelli[†], **David van Driel**[†], D. Xu[†], G. Wang[†], C.-X. Liu, A. Bordin, B. Roovers, G. P. Mazur, N. van Loo, J. C. Wolff, A. M. Bozkurt, G. Badawy, S. Gazibegovic, E. P. A. M. Bakkers, M. Wimmer, L. P. Kouwenhoven, T. Dvir (2023). Robust poor man's Majorana zero modes using Yu-Shiba-Rusinov states. *arXiv preprint arXiv:2311.03193*.
10. A. Bordin[†], G. Wang[†], C.-X. Liu, S. L. D. ten Haaf, N. van Loo, G. P. Mazur, D. Xu, **David van Driel**, F. Zatelli, S. Gazibegovic, G. Badawy, E. P. A. M. Bakkers, M. Wimmer, L. P. Kouwenhoven, T. Dvir (2023). Tunable crossed Andreev reflection and elastic cotunneling in hybrid nanowires. *Physical Review X*, 13(3), 031031.
9. Y. Chen[†], **David van Driel**[†], C. Lampadaris, S. A. Khan, K. Alattallah, L. Zeng, E. Olsson, T. Dvir, P. Krogstrup, & Y. Liu. (2023). Gate-tunable superconductivity in hybrid InSb-Pb nanowires. *Applied Physics Letters*, 123(8).
8. R. Koch, **David van Driel**, A. Bordin, J. L. Lado, & E. Greplova. (2023). Adversarial Hamiltonian learning of quantum dots in a minimal Kitaev chain. *Physical Review Applied*, 20(4), 044081.

7.  **David van Driel**[†], G. Wang[†], A. Bordin, N. van Loo, F. Zatelli, G. P. Mazur, D. Xu, S. Gazibegovic, G. Badawy, E. P. A. M. Bakkers, L. P. Kouwenhoven, T. Dvir[†] (2023). Spin-filtered measurements of Andreev bound states in semiconductor-superconductor nanowire devices. *Nature Communications*, 14(1), 6880.

6. N. van Loo, G. P. Mazur, T. Dvir, G. Wang, R. C. Dekker, J.-Y. Wang, M. Lemang, C. Sfiligoj, A. Bordin, **David van Driel**, G. Badawy, S. Gazibegovic, E. P. A. M. Bakkers, L. P. Kouwenhoven (2023). Electrostatic control of the proximity effect in the bulk of semiconductor-superconductor hybrids. *Nature Communications*, 14(1), 3325.

5. T. Dvir[†], G. Wang[†], N. van Loo[†], C.-X. Liu, G. P. Mazur, A. Bordin, S. L. D. ten Haaf, J.-Y. Wang, **David van Driel**, F. Zatelli, X. Li, F. K. Malinowski, S. Gazibegovic, G. Badawy, E. P. A. M. Bakkers, M. Wimmer, L. P. Kouwenhoven (2023). Realization of a minimal Kitaev chain in coupled quantum dots. *Nature*, 614(7948), 445-450.

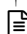
4. G. P. Mazur[†], N. van Loo[†], **D. van Driel**, J.-Y. Wang, G. Badawy, S. Gazibegovic, E. P. A. M. Bakkers, & L. P. Kouwenhoven. (2022). The gate-tunable Josephson diode. *arXiv preprint arXiv:2211.14283*.

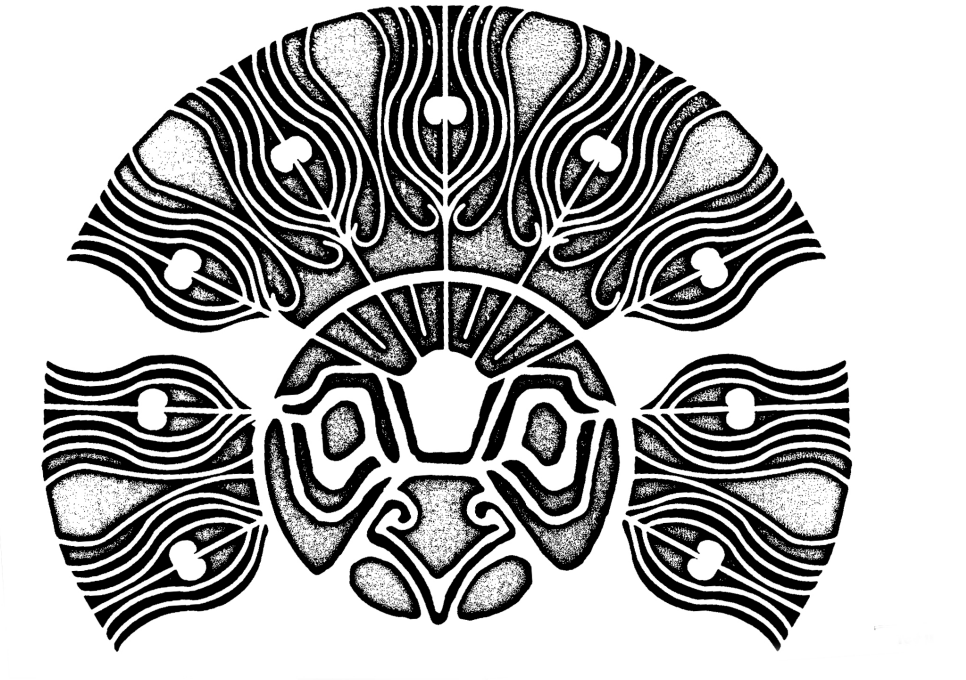
3. J.-Y. Wang, C. Schrade, V. Levajac, **David van Driel**, K. Li, S. Gazibegovic, G. Badawy, R. L. M. Op het Veld, J. S. Lee, M. Pendharkar, C. P. Dempsey, C. J. Palmstrøm, E. P. A. M. Bakkers, L. Fu, L. P. Kouwenhoven, J. Shen (2022). Supercurrent parity meter in a nanowire Cooper pair transistor. *Science Advances*, 8(16), eabm9896.

2. J. Shen, G. W. Winkler, F. Borsoi, S. Heedt, V. Levajac, J.-Y. Wang, **D. van Driel**, D. Bouman, S. Gazibegovic, R. L. M. Op Het Veld, D. Car, J. A. Logan, M. Pendharkar, C. J. Palmstrøm, E. P. A. M. Bakkers, L. P. Kouwenhoven, B. van Heck (2021). Full parity phase diagram of a proximitized nanowire island. *Physical Review B*, 104(4), 045422.

1. D. Ding, **David van Driel**, L. M. C. Pereira, J. F. Bauters, M. J. R. Heck, G. Welker, M. J. A. de Dood, A. Vantomme, J. E. Bowers, W. Löffler, D. Bouwmeester (2020). Probing interacting two-level systems with rare-earth ions. *Physical Review B*, 101(1), 014209.

[†] Equal Contribution

 Included in this thesis.



ISBN: 978-94-6384-618-9

1 μm